

**Integrated Photonics with Colloidal Semiconductor Nanocrystals:
Optoelectronic Devices and Quantum Applications**

**Geïntegreerde fotonica met colloïdale kwantumdots:
opto-elektronische componenten en kwantumfotonische toepassingen**

Lukas Elsinger

**Promotoren: prof. dr. ir. D. Van Thourhout, prof. dr. ir. Z. Hens
Proefschrift ingediend tot het behalen van de graad van
Doctor in de ingenieurwetenschappen: fotonica**



**Vakgroep Informatietechnologie
Voorzitter: prof. dr. ir. B. Dhoedt
Faculteit Ingenieurwetenschappen en Architectuur
Academiejaar 2019 - 2020**

ISBN 978-94-6355-409-1
NUR 959, 926
Wettelijk depot: D/2020/10.500/86



Universiteit Gent
Faculteit Ingenieurswetenschappen en Architectuur
Vakgroep Informatietechnologie

Promotoren:

prof. dr. ir. Dries Van Thourhout

prof. dr. ir. Zeger Hens

Examencommissie:

prof. dr. ir. Filip de Turck (chair) Universiteit Gent

prof. dr. ir. Roel Baets Universiteit Gent

prof. dr. ir. Iwan Moreels Universiteit Gent

dr. ir. David Cheyns imec

dr. Thilo Stöferle IBM Research Zürich

Universiteit Gent
Faculteit Ingenieurswetenschappen en Architectuur
Vakgroep Informatietechnologie
Technologiepark-Zwijnaarde 126 iGent B-9052 Gent, België
Tel.: +32 (0) 9264 3316
Fax.: +32 (0) 9264 3593

Acknowledgements

Starting a PhD in the Photonics Research Group was an easy decision for me, even though retrospectively I realize how little information I had when I made this choice. It has definitely not always been an easy journey, but still I never regretted coming to Ghent, which I literally knew nothing about in the beginning. Now that I'm finally finishing this book during a worldwide pandemic, there are many people I want to thank, who have given me invaluable support over the years.

First of all I want to thank my promoters *Dries* and *Zeger* for believing in me and hiring me for an ambitious project, which was part of an exciting Marie Curie network. You always gave me the freedom to explore new ideas, even if those didn't lead anywhere at times. I value your deep insight into all aspects of integrated photonics, semiconductor device physics and the intricate properties of colloidal nanocrystals. Your approachability and the numerous discussions we've had have really helped me to grow.

Being part of a large research group it is impossible to name everyone, who I've learned from and had interesting conversations with over coffee, lunch or while having a drink after one of our group meetings. I think it is really impressive how *Roel* and the other professors manage to create a welcoming atmosphere, where research and personal relations can flourish!

Luckily, I didn't have to start completely from scratch and in the beginning I learned a lot from *Weiqiang*, *Yunpeng*, *Chen* and *Suzanne*, who developed a lot of techniques I could build on. With a research topic at the intersection of integrated photonics and colloidal QDs, I spent a lot of time cycling in-between different campuses and I've had to rely on many colleagues to help me out with things, I never got the training for. Thanks to *Emile*, *Jorick* and *Natalia* for providing me with QDs and everyone else from the PCN group, who helped me out in the lab or with finding people. I've had many inspiring discussions with *Jakob* and later also *Robin* from CoCooN, who have been great at providing me with thin ALD layers. Thanks to *Michiel* from LCP for getting me started with the fabrication and characterization of QD-LEDs and later also *Frederik* for depositing many

organic layers. The closest collaboration I've had was with *Ronan* from Single Quantum, thanks for being a great host during my short stay in Delft and measuring countless samples. There have also been many fruitful discussions in all the QD meetings thanks to *Pieter, Iwan, Vignesh, Ivo, Felipe, Carmelita* and everyone else with a passion for QD physics.

The opportunity to join the Marie Curie training network Phonsi was a great experience with many eye-opening seminars, workshops and meetings, as well as amazing trips to places around Europe. I want to thank everybody who was involved in making that happen and especially my fellows *Adam, Annalisa, Bogdan, Darius, Federico, Joanna, Maryam, Michael, Nayyera, Niall, Renu, Ronan, Vignesh and Ye* for creating an unforgettable atmosphere. A special thanks should also go to *Michael, Darius, Thilo* and *Rainer*, who have welcomed me during my secondment at IBM Research Zurich.

As will become apparent in this thesis, I spent a lot of my time in the cleanroom, trying out new processes and I want to especially thank *Steven, Liesbet* and *Muhammad* for their great support. I've also been lucky to have many amazing office mates at the Photonics Research Group: *Camiel, Herbert, Isaac, Kasper, Koen, Maximilien, Nina, Pieter, Stijn, Stijn, Utsav and Zuyang*. When writing my thesis from home it became apparent to me, how much I appreciate those caffeine-fueled discussions at the whiteboard.

Koen and *Pieter*, thanks for introducing me to Belgian cycling culture. I really enjoyed all the rides we did together, even when it was a struggle to carry my bike upstairs afterwards. It has also been great to cycle with all the other colleagues of our informal photonics cycling team: *Daan, Antonio, Jasper, Stijn, Geert* and *Lieselotte*, who convinced me to join a proper Belgian cycling club. *Sören*, I gotta say, I'm a little upset that you only got yourself a racing bike after you moved to California.

Most importantly I want to thank my family, especially my parents *Georg* and *Monika*, who have always supported me with their unconditional love. Unfortunately my grandfather is not here anymore to see me finally finish "school". *Jéssica*, meu amor, I couldn't have done this without your help. Thank you for giving me a perspective on what is important.

Ghent, June 2020
Lukas Elsinger

Table of Contents

Acknowledgements	i
Samenvatting	xxv
Summary	xxxix
1 Introduction	1-1
1.1 Integrated photonics	1-1
1.2 Fundamentals of colloidal QDs	1-4
1.3 Structure of this thesis	1-8
1.4 Publications	1-9
1.4.1 Publications in international journals	1-9
1.4.2 Patent applications	1-9
1.4.3 Publications in international conferences	1-9
References	1-12
2 Nano-patterned colloidal quantum dot light emitting diodes	2-1
2.1 Introduction	2-1
2.2 Single-photon emission from colloidal CdSe/CdS QDs	2-3
2.3 Nano-patterning of a QD layer	2-5
2.4 Colloidal QD light emitting diodes	2-8
2.5 Nano-patterned QD-LED	2-13
2.6 Properties of QD monolayers	2-23
2.7 Nano-patterned structures with directional PL	2-27
2.8 Conclusion and outlook	2-30
References	2-32
3 Waveguide-coupled colloidal quantum dot light emitting diodes and detectors on a silicon nitride platform	3-1
3.1 Introduction	3-2
3.2 Design and simulation	3-3
3.3 Fabrication process development	3-7
3.3.1 Silicon nitride waveguides	3-7
3.3.2 Atomic layer deposition of ZnO	3-9

3.3.3	Patterning of the n-contact metal and ZnO	3-10
3.3.4	SiO ₂ planarization etch and QD deposition	3-11
3.3.5	Organic layers and p-contact metal	3-14
3.4	LED characterization	3-15
3.5	Detector characterization	3-22
3.6	Estimation of the gain threshold	3-25
3.7	Including distributed feedback	3-26
3.8	Optimization for lasing	3-29
3.9	Conclusion and outlook	3-32
	References	3-33
4	Integration of colloidal PbS/CdS quantum dots with plasmonic antennas and superconducting detectors on a silicon nitride photonic platform	4-1
4.1	Introduction	4-2
4.2	Antenna design and simulation	4-3
4.3	Waveguide-coupled nanowire detectors	4-9
4.4	Colloidal PbS/CdS QDs	4-13
4.5	Fabrication process	4-14
4.6	Measuring the antenna enhancement	4-17
4.7	Scaling to single emitters	4-24
4.8	On-chip lifetime spectroscopy	4-26
4.9	Spectrally resolved antenna enhancement	4-30
4.10	Conclusion and outlook	4-32
	References	4-33
5	Conclusions and perspectives	5-1
5.1	Optoelectronic devices	5-1
5.2	Quantum photonic applications	5-5
	References	5-8
A	Detailed fabrication processes	A-1
A.1	E-beam fabricated SiN waveguides	A-1
A.1.1	Low-frequency PECVD SiN deposition	A-1
A.1.2	E-beam lithography	A-1
A.1.3	SiN RIE recipe	A-3
A.1.4	PECVD SiO ₂ cladding layer	A-3
A.1.5	SiO ₂ RIE recipe	A-3
A.2	Synthesis of CdSe/CdS QDs	A-3
A.3	Synthesis of PbS/CdS QDs	A-3
A.4	Atomic layer deposition	A-5
B	Characterization details	B-1
B.1	Transient absorption spectroscopy	B-1
	References	B-2

List of Figures

- 1.1 Available wavelengths of different laser solutions from Toptica Photonics [17] 1-3
- 1.2 Size-dependent band-edge absorption energies of different colloidal semiconductor QDs. Data for CdS, PbS, PbSe nanocrystals was taken from reference [22], the sizing curve for CdSe cores was reported in [23], data for InAs QDs is from reference [24]. 1-3
- 1.3 (a) Solution absorption and photoluminescence (PL) emission of the CdSe/CdS QD sample used for the experiments described in Chapter 3. (b) Bright-dark excitation model introduced to explain the Stokes shift under resonant excitation and long excited state lifetimes at cryogenic temperatures [47] 1-5
- 1.4 Neutral and negatively charged QD ground states and their respective excited states, namely the neutral exciton (X), the bi-exciton (XX), the negative trion (T^-) and the doubly charged negative trion (T^{-2}) 1-7

- 2.1 Properties of individual CdSe/CdS QDs. (a) Comparison of the PL emission spectrum of a single QD with an ensemble of QDs, exhibiting inhomogeneous broadening. (b) Sketch of a Hanbury-Brown-Twiss set-up used for the characterization of the second-order auto-correlation function $g^2(t)$, comprising a single-photon source (SPS) and two avalanche photo-diode detectors (APDs). Unlike the sketch indicating a delay in the optical path, we used an electrical delay in the experimental implementation. (c) Second-order auto-correlation function for an individual CdSe/CdS QD, measured using CW and (d) pulsed excitation. 2-4

-
- 2.2 Nano-patterning of a colloidal QD monolayer. (a) Sketch of the Langmuir-Blodgett deposition technique, which allows to coat uniform QD monolayers on both sides of a sample. (b) SEM top-view of a nano-patterned layer of monodisperse CdSe/CdS QDs, showing the logo of the Ghent University Department of Information Technology. The technique allows to reliably pattern feature sizes down to 20 nm, with a limiting line edge roughness determined by the size of the QDs. 2-6
- 2.3 Single-dot patterning of colloidal CdSe/CdS QDs. (a) SEM top-view of an array with individual patterned QDs with magnified insets showing (1) a single QD and (2) two QDs. (b) Patterning statistics showing a probability of 40% for patterning of single QDs and a corresponding fit with a binomial distribution. 2-7
- 2.4 Nano-patterning of QDs using spin-coating. (a) SEM top-view of a patterned CdSe/CdS QD structure with two different feature sizes. (1) Large area with a uniform QD layer. (2) Nano-patterned grating of QDs, the bright regions originate from pronounced charging of the QDs and indicate areas with a thicker QD layer. (b) Array of nano-patterned PbS/CdS QDs, with the inset showing an individual 75 nm diameter QD pillar. 2-8
- 2.5 (a) Emission energies of the QD-LED device for different bias voltages on a logarithmic scale. (b) Theoretical band alignment of the different layers in the QD-LED stack with reference to the vacuum level and energy levels denoted in units of eV. 2-9
- 2.6 (a) 2-Theta XRD scan revealing the preferential c-axis orientation of the deposited ZnO layer. (b) Complex refractive index (n,k) from ellipsometry measurements with the dashed line indicating the ZnO band gap at 3.3 eV. 2-10
- 2.7 Bright and uniform emission from a QD-LED device for a bias of 7 V observed under ambient light. The emissive area has a size of approximately 2 mm × 3 mm and the sample was mounted on a microscopy glass slide to ease the handling. 2-11
- 2.8 Turn-on behavior of the QD-LED. (a) Comparison of the photoluminescence (PL) emission spectrum and electroluminescence (EL) for a bias voltage of 2.8 V. Dashed lines indicate Gaussian fits and the extracted central wavelengths. (b) Electrical turn-on behavior, obscured by a leakage current due to issues with the processing of the electrodes. A resistance of 4.1 kΩ was extracted for the parasitic channel, through a linear fit of the current for a bias voltage up to 2 V. (c) Optical turn-on behavior of the QD-LED. 2-12

2.9	Shift of the QD-LED emission spectrum for larger bias voltages. (a) Comparison of the EL emission spectrum for a bias voltage of 3 V and 7 V. Dashed lines indicate Gaussian fits and the extracted central wavelengths. (b) Shift of the emission peak energy (quadratic fit represented by the dashed line) and (c) the full width at half-maximum (FWHM) extracted from Gaussian fits. Reference values in (b) and (c) were measured on a monolayer (ML) of the same QD sample deposited on SiO ₂	2-14
2.10	Main processing steps to fabricate nano-patterned QD-LEDs. (a) E-beam lithography with a thin positive resist on a glass sample coated with a sputtered ITO n-contact and an ALD layer of ZnO and Al ₂ O ₃ . (b) Selective wet-etch of the dielectric Al ₂ O ₃ layer. (c) Langmuir-Blodgett deposition of a monolayer of CdSe/CdS QDs. (d) Lift-off results in QDs selectively deposited in the etched areas. (e) Thermal evaporation of organic layers for hole transport (NPB) and hole generation (HAT-CN), as well as an aluminum p-contact.	2-15
2.11	SEM micrographs of a dummy sample on a silicon substrate after different processing steps. (a) Top-view after the wet-etch of the dielectric Al ₂ O ₃ ALD layer. (b) Angled view showing the self-aligned deposition of a CdSe/CdS QD monolayer in the etched area.	2-15
2.12	(a) Schematic layout of the nano-patterned QD-LED sample, showing a common ITO n-contact and four individual Al p-contacts for different areas containing patterned QDs. The active device area was encapsulated using a cover glass and UV-curable epoxy resin incorporating getter materials. (b) Schematic cross-section outlining the device characterization using a high-resolution oil immersion objective lens.	2-16
2.13	Emission from a nano-patterned QD-LED. (a) Large-area emission observed with an optical microscope with low magnification and a large working distance for a bias voltage of 7 V. (b) Emission energies plotted on a logarithmic scale for different forward bias voltages.	2-17
2.14	Turn-on behavior of the nano-patterned QD-LED. (a) Comparison of the emission spectrum for a bias voltages of 5 V and 7V. Dashed lines indicate Gaussian fits and the extracted central wavelengths. (b) Electrical turn-on behavior, obscured by a leakage current. A resistance of 330 Ω was extracted for the parasitic channel, through a linear fit of the current for a bias voltage up to 2 V. (c) Optical turn-on behavior of the QD-LED.	2-18

-
- 2.15 EL blinking observed with a high-resolution (x50) objective. (a) Emission for a bias voltage of 5 V showing part of the nano-patterned QD-LED in a low-emission (off) state. (b) Same part of the device a few seconds later in a high-emission (on) state. 2-19
- 2.16 Comparison of the PL and EL emission of a nano-patterned QD-LED, observed with a high-resolution (x50) objective. (a) Photoluminescence of patterned CdSe/CdS QDs used for orientation as well as emission from re-deposited emitters in the center of the square. (b) Electroluminescence for a 5 V bias from the same device area, revealing emitters patterned on a 5 μm grid. 2-19
- 2.17 Comparison of the of the PL second-order auto-correlation function under pulsed excitation for (a) CdSe/CdS QD emission from the nano-patterned QD-LED and (b) an individual CdSe/CdS QD on a SiO₂ substrate. The lifetimes were extracted by a single-exponential fit of the respective peaks. . . 2-21
- 2.18 Photoluminescence decay measured for two different unbiased QD-LEDs, plotted on a (a) double-logarithmic and (b) the commonly used semi-logarithmic scale. The QD-LED comprising 2-3 layers of CdSe/CdS QDs clearly exhibits a slower PL decay than the monolayer QD-LED. 2-21
- 2.19 Parameters extracted from a stretched exponential fit of the PL decay for two different QD-LED samples, depending on the applied bias voltage. Mean lifetime (a) for the monolayer QD-LED and (b) the sample comprising 2-3 layers of QDs. Stretching exponent β for (a) monolayer and (b) multilayer QD-LED. 2-23
- 2.20 Wavelength-dependent PL decay of a CdSe/CdS QD monolayer on different surfaces. (a) Double-logarithmic and (b) semi-logarithmic plot for a SiO₂ substrate. (c) Double-logarithmic and (d) semi-logarithmic plot for the same QD sample on top of a thin layer of ALD ZnO. The data was fitted with stretched exponentials. 2-25
- 2.21 Spectroscopic analysis of the effect of QD shelling. (a) PL spectra of a dense CdSe/CdS QD monolayer on SiO₂ and on ZnO. The dashed lines represent a Gaussian fit and the extracted central wavelength. (b) Respective spectra for a CdSe/CdS/ZnS QD monolayer. (c) Mean lifetime extracted from a stretched exponential fit for the CdSe/CdS and (d) CdSe/CdS/ZnS QD sample. (e) Corresponding stretching exponent for the CdSe/CdS and (f) CdSe/CdS/ZnS QD sample. 2-26

-
- 2.22 Influence of PECVD on a QD monolayer. (a) PL emission spectrum of a CdSe/CdS QD monolayer on a SiO₂ substrate, before and after the deposition of a 30 nm thin layer of PECVD SiN. (b) Wavelength-dependent mean lifetime of the CdSe/CdS QDs extracted from a stretched exponential fit of the PL decay and (c) corresponding stretching exponent. . . . 2-28
- 2.23 (a) Sketch of the device stack, resembling a QD-LED, but with an Al₂O₃ dielectric instead of the organic layers. (b) SEM micrograph of a FIB cross-section through a dummy sample revealing the nano-patterned QD layer on top of ZnO. The image in (b) is turned upside down with respect to the sketch in (a). 2-29
- 2.24 (a) Angled SEM top-view of CdSe/CdS QDs patterned in the form of a bulls eye grating. (b) The red color channel in the image plane visualized with a x10 objective shows an increased brightness of the structures with a grating period of 375 nm and 400 nm. 2-29
- 2.25 (a) Unprocessed Fourier plane images from a x50 0.8 NA objective for different grating periods (b) Angular dependence of the far field intensity $I(\theta)$ after correction for the transmission function of the microscope system and integration over $d\phi$ 2-30
- 3.1 (a) Schematic model of the waveguide-coupled quantum dot light emitting diode (QD-LED), consisting of a silicon nitride waveguide covered with a low-loss ZnO electron transport and injection layer. Colloidal CdSe/CdS QDs are used as active material and organic layers for hole transport and injection. (b) Band alignment of the different layers used in the waveguide-coupled QDLED referenced to the vacuum level. 3-3
- 3.2 Simulation results of coupling efficiency and waveguide loss for different geometries. (a) Mode profile of the fundamental TE mode for the fabricated geometry and a simulation wavelength of 650 nm. (b) Figure of merit for the power coupled to the fundamental TE mode, for a given organics thickness of $t = 600$ nm. (c) Waveguide loss originating from the p-contact metal for a given width ($w = 1 \mu\text{m}$) and height ($h = 300$ nm) of the silicon nitride. (d) Dependence of the passive waveguide loss on the geometry, for a given organics thickness of $t = 600$ nm. First-order interpolation of the simulation results was used for the display in (b) and (d), the dashed lines represent the cut-on of higher order modes for the simulation wavelength. 3-5

- 3.3 Extraction of the loss induced by the p-contact metal. (a) Grating coupler transmission spectrum. (b) Transmission measured for different device lengths. 3-6
- 3.4 Main processing steps for fabricating waveguide-coupled QD-LEDs. (a) Low-frequency PECVD of a 300 nm SiN waveguide layer on a silicon sample with 1 μm thermal SiO₂. (b) Patterning of the waveguides using electron-beam lithography and a dry etch. (c) Atomic layer deposition (ALD) of the ZnO electron injection layer and Al₂O₃ passivation. (d) Local removal of Al₂O₃ and patterning of the Ti/Au/Ti n-contact metal using optical lithography and a lift-off process. (e) Patterning of the ZnO layer using optical lithography and a wet etch. (f) High-frequency PECVD of a 350 nm SiO₂ layer. (g) Local removal of SiO₂ using electron-beam lithography and a dry etch, wet removal of the Al₂O₃ layer to expose the ZnO electron injection layer. (h) Local deposition of CdSe/CdS colloidal quantum dots using a lift-off process. (i) Thermal evaporation of organic hole injection and hole transport layers, as well as an aluminum p-contact. 3-8
- 3.5 Material characterization of the optimized ZnO layer. (a) Cut-back measurements show a drastic reduction of the waveguide loss after the rapid thermal annealing (RTA) step. (b) Result of a typical transfer length measurement (TLM) to extract the sheet resistance of the 10 nm ZnO layer, before and after RTA. 3-10
- 3.6 Reflected laser intensity recorded by the etch monitor during the removal of SiO₂ on top of the waveguide. A slight change in the slope indicates when the etch reaches the Al₂O₃ etch-stop layer. 3-12

-
- 3.7 SEM top-view of different samples after the SiO₂ planarization etch. (a) Sample after successful RIE, before the Al₂O₃ wet-removal. The SiN waveguide appears bright due to the conformal ZnO coating and the etched area is aligned well to the underlying waveguide. (1) SiO₂ residue on top of the waveguide is only present near the edge of the etched area. (2) SiO₂ side-cladding next to the waveguide. (3) SiO₂ residue re-deposited next to the waveguide. (b) Sample after an incomplete RIE, before the Al₂O₃ wet-removal. The dark pattern on top of the waveguide indicates the presence of dielectric SiO₂. (4) Etch residue likely due to insufficient chamber cleaning. (5) Etched SiO₂ side-cladding due to an overly wide developed area. (c) Sample after successful removal wet-removal of the Al₂O₃ etch-stop layer. (6) Only minor imperfections are present in the ZnO layer. (d) Sample after a failed SiO₂ planarization etch due to incorrect etch parameters. The ZnO layer exhibits many holes and likely a significantly reduced conductivity. 3-13
- 3.8 SEM images of the sample at different stages of the fabrication process. (a) Top-view of a SiN waveguide after the SiO₂ planarization etch, showing the boundary of the patterned ALD layers. The SiN waveguide appears damaged in the area, where it is not covered with ZnO and Al₂O₃. (b) Side-clad SiN waveguide covered with CdSe/CdS colloidal QDs. (c) Focused ion-beam (FIB) cross-section of a completed device showing the surroundings of the SiN waveguide. A slight misalignment in the electron-beam lithography step prior to the SiO₂ planarization etch caused the SiO₂ side-cladding to be etched next to the waveguide. In the subsequent QD deposition step the etched trench was partly filled. (d) FIB cross-section of the n-contact metal on a completed device. The step in the surface profile due to the SiN waveguide etch and the deposition of the n-contact metal directly translates to the p-contact metal, leading to pinholes in the evaporated aluminum layer. 3-16
- 3.9 (a) Schematic top-view of the devices. (b) SEM top-view of a finished device showing the aluminum p-contact and the buried n-contact. (1) Part of the waveguide, where the SiO₂ top cladding was etched using the process described above. (2) Boundary of the large-area QD pattern. (3) Remaining SiO₂ on top of the SiN waveguide. (c) FIB cross-section of a finished device, outlining the different layers. 3-17
- 3.10 Finite element simulation of (a) the electric potential and (b) the current density in the organic layers for a forward bias voltage of 100 V. 3-18

-
- 3.11 Waveguide-coupled QD-LED operated with a high bias voltage. (a) Current density recorded for the device with the highest optical output power, with an inset detailing the electrical turn-on behavior. (b) Normalized emission spectrum collected from the grating coupler output for different bias voltages. 3-19
- 3.12 Bias voltage limitation for the waveguide-coupled QD-LED. (a) Irreversible destruction of the device was observed for a forward bias voltage above 120 V, with a reported maximum current density of 100 A/cm². (b) SEM top-view showing the visibly damaged device. 3-19
- 3.13 (a) Optical turn-on behavior of the waveguide-coupled QD-LED with the power collected from the grating coupler output. (b) Comparison of the EL emission collected from the end facet of a cleaved sample to the PL spectrum of the same CdSe/CdS QD sample in solution. 3-20
- 3.14 Saturation of the QD-LED output power. (a) Measured on-chip optical power in a single-mode waveguide and (b) normalized quantum efficiency as a function of the current density. 3-21
- 3.15 Waveguide loss induced by the CdSe/CdS QD layer. (a) Waveguide transmission measured for two different devices. (b) Extracted loss due to the QDs, compared to values calculated from a measurement of the CdSe/CdS QDs in solution. 3-23
- 3.16 Detector characterization using an external LED. (a) Transmission spectrum of a device without QDs, used to estimate the power coupled into a single-mode waveguide. (b) Photo-current measured for different optical input powers for a 500 μm long device. 3-23
- 3.17 Detector performance of the waveguide-coupled QD-LED devices. (a) Photo-current after subtraction of the dark current and (b) detector quantum efficiency, for a reverse bias of 7 V and different optical input powers. Solid lines represent a fit of the data to Equation 3.5 and 3.6. 3-24
- 3.18 Transient absorption (TA) spectroscopy was used to characterize the CdSe/CdS QD sample in solution. (a) Gain spectrum after 3 ps, for different excitation $\langle N \rangle$ (b) Total absorption as a function of time, for a probe wavelength of 650 nm. 3-26
- 3.19 (a) Spectrum of the external laser used to monitor the waveguide transmission. (b) Excess loss for increasing forward bias extracted from a 2 mm long device. 3-27

-
- 3.20 SEM top-view of structures with a grating for distributed feedback. (a) After the SiO₂ planarization etch. (1) Corrugated sidewalls of the SiN waveguide. (2) Conformal ZnO and Al₂O₃ ALD coating of the waveguide. (3) Selective growth of the PECVD SiO₂ used as a side-cladding. (b) Sidewall-corrugated waveguide after the deposition of a ~ 30 nm layer of CdSe/CdS QDs. 3-28
- 3.21 Sidewall-corrugation with a period of 178 nm. (a) Transmission spectrum of a SiN waveguide with a SiO₂ top- and side-cladding. (b) Lasing lines observed for a side-clad waveguide covered with ZnO and CdSe/CdS QDs, using ns-pulsed excitation at 520 nm. 3-29
- 3.22 Finite element simulations for different width w and height h of the SiN waveguide and a constant thickness $t = 600$ nm of the organic layers. (a) Waveguide loss α on a linear scale. (b) Mode confinement Γ in a 20 nm QD layer on top of the SiN waveguide. The dashed black lines show the onset of higher order TE modes in the SiN waveguide. 3-30
- 3.23 Figure of merit for a waveguide-coupled QD laser. (a) Modal gain calculated for a material gain of $g_i = 500$ cm⁻¹ of a 20 nm QD layer with a fill-factor of 50%. (b) Modal gain for $g_i = 750$ cm⁻¹. (c) Modal gain for $g_i = 1000$ cm⁻¹. (d) Modal gain for $g_i = 1500$ cm⁻¹. 3-31
- 4.1 Optical microscope image of the SiN photonic chip. There are areas with colloidal QD emitters and plasmonic antennas (I), filters for pump rejection (II), a Planar Concave Grating (PCG) spectrometer (III) of which four channels are connected to waveguide-coupled SNSPD detectors (III). All components are connected by waveguides which are surrounded by metal strips to suppress stray light coupling (V). For measurements with SNSPDs the chip was cooled down in a helium bath cryostat to a temperature of 4.2 K. 4-4
- 4.2 False-color SEM pictures of the main components. (a) SiN waveguide with a plasmonic bowtie antenna and a patch of colloidal QDs patterned on top of it. (b) The QD emission was detected by U-shaped superconducting detectors placed underneath the SiN waveguides. 4-4

4.3	The map of the LRDOS in (a) results from Finite Difference Time Domain (FDTD) simulation of a dipole emitter with displacement vector \mathbf{d} . The SEM micrograph of the fabricated bowtie antenna with a small patch of PbS/CdS QDs deterministically positioned in the antenna gap (b) was colored to highlight the different materials. (c) Spectrum of the excitation laser and the QD PL emission at 4.2 K. (d) Comparison of the simulated LDOS for an emitter in the center of the antenna gap and the LRDOS for an empty antenna as well as for an antenna with a QD pillar placed in the gap.	4-6
4.4	FDTD simulation of the plasmonic bowtie antenna. (a) SEM top-view of a fabricated antenna (30 nm evaporated gold and a gap width of 25 nm). (b) Simulated antenna quantum efficiency $QE = LRDOS/LDOS$ for the center wavelength of the QD emission. (c) Polarization dependent excitation enhancement for a pump wavelength of 700 nm, parallel and (d) perpendicular to the antenna dipole axis.	4-7
4.5	(a) Transmission spectrum of an array of plasmonic bowtie antennas fabricated on a glass substrate. (b) Simulation of the coupling efficiency to the TE and TM waveguide mode for an emitter in the gap of a plasmonic antenna.	4-9
4.6	Mode profile for an oxide-clad SiN waveguide on top of superconducting NbTiN wires. (a) The fundamental transverse electric (TE) and (b) the fundamental transverse magnetic (TM) mode.	4-10
4.7	Simulated absorption of the waveguide-coupled SNSPD. (a) Absorption from FDTD simulations for the fundamental TE and TM mode of a 1 μm wide and 300 nm high SiN waveguide. (b) SEM top-view of a fabricated structure, showing a slight misalignment of the U-shaped nanowire and the SiN waveguide.	4-11
4.8	Estimation of the SNSPD internal detection efficiency for two different nanowires in (a) and (b). The dark counts were subtracted from the counts observed with illumination and an error function was fitted for the normalization where the saturation regime could not be reached. For a bias current corresponding to a Dark Count Rate (DCR) of 100 cps the extracted internal detection efficiency for the first detector in (a) is between 95% and 99% for the wavelength range of interest. The second detector in (b) has a significantly lower internal efficiency between 70% and 95%.	4-12
4.9	For the extraction of the SNSPD time jitter the binned data was fitted with a Gaussian for the normalization (a). The decay pulse in (b) was fitted with an exponential to extract the recovery time of the detector.	4-13

-
- 4.10 Comparison of the photoluminescence emission spectrum of the PbS/CdS QD sample in solution and a drop-casted film at room temperature and at cryogenic temperatures. Dashed lines represent Gaussian fits and the extracted central wavelengths. 4-14
- 4.11 Main processing steps for the fabrication. (a) Patterning of Cr/Au contacts on top of a Si samples coated with thermal SiO₂ and a 9.5 nm layer of NbTiN. (b) Definition of the nanowires by e-beam lithography and RIE. (c) deposition of a 300 nm low-fluorescence PECVD SiN layer. (d) Patterning of plasmonic bowtie antennas using e-beam lithography and a lift-off process. (e) SiN waveguide definition with e-beam lithography and RIE. (f) Overlay of the PbS/CdS QDs in the antenna gap using e-beam lithography and a lift-off process. (g) Room-temperature PECVD of the SiO₂ top-cladding. (h) Creation of openings to access the metal contacts employing optical contact lithography and RIE. (i) The finalized sample is glued to a printed circuit board (PCB) with silver paste and electrically connected via wire bonds. 4-15
- 4.12 Instrument response function (IRF) and PL decay signal from CdSe/CdS QDs and PbS/CdS QDs on top of SiN waveguides. The normalized data was fitted with a stretched exponential after subtraction of the background. (b) Analysis of the countrate contributions for PbS/CdS QDs in the gap of a plasmonic bowtie antenna for an excitation power of $P_{ant} = 800$ nW. 4-18
- 4.13 (a) Power dependence of the pulsed and CW contribution of the QD emission. The shaded areas show the 1- σ confidence intervals from the fit displayed as a dashed line. Excitation power dependence of the (b) estimated quantum efficiency and the (b) mean lifetime extracted from a stretched exponential fit. 4-20
- 4.14 SEM micrographs of patterned colloidal PbS/CdS QDs used to estimate the number of excited dots in the experiments. The collapsed pillar in (a) was fabricated using 10 μ M concentration of the QD dispersed in toluene. The QD pillar in (b) on top of a silicon nitride waveguide was fabricated with a 7.5 μ M concentration and is still standing upright. 4-21

-
- 4.15 PL lifetime from different freestanding pillars of PbS/CdS QDs (a) and PbS/CdS QDs placed in the gap of plasmonic bowtie antennas (b) extracted from measurements with different SNSPDs. The quantum efficiency with an antenna ϕ_{ant} normalized to an isolated pillar ϕ_0 in (c) correspond to the lifetime measurements above. The dashed lines and shaded areas show the respective mean value and standard deviation, the displayed error bars are the $1-\sigma$ confidence intervals from the fit. The PL decay traces in (d) and (e) were normalized after subtraction of the background, the experimental data is overlaid with fitted stretched exponential functions. The circled data points in (a) and (b) were extracted from the respective decay traces in (d) and (e). 4-23
- 4.16 Corrugated sidewall grating filter designed to reject the 700 nm pump laser. (a) Transmission spectrum measured for a cleaved sample, compared to the spectrum of the pump laser. (b) SEM top-view of the sidewall-corrugated waveguide, with absorbing metal lines next to the trenches. 4-25
- 4.17 (a) Schematic chip layout for the on-chip lifetime spectroscopy experiment. PbS/CdS QDs were excited from the top by a 700 nm pulsed laser, the emission coupled to SiN waveguides. A corrugated sidewall grating filter rejects light from the pump laser. The planar concave grating (PCG) spectrometer with four output arms connected to waveguide-coupled SNSPDs allows for a wavelength-resolved characterization of the PL decay. (b) SEM micrograph of the distributed Bragg reflector (DBR) elements making up the blazed mirror grating of the spectrometer. (c) SEM micrograph of the in- and output waveguide tapers, interfacing the single-mode SiN waveguides with the slab mode section of the spectrometer. . 4-27
- 4.18 (a) Simulated TE reflection spectrum of the DBR mirror designed for the spectrometer. (b) Transmission measurements from all 6 channels. Channels 1-4 were connected to waveguide-coupled SNSPD. Channels 5 and 6 were used to characterize the fabricated spectrometers at room temperature, prior to the cool-down. 4-28
- 4.19 (a) Position dependence of the lifetime extracted from a stretched exponential fit, measured with a single SNSPD. (b) SEM top-view of part of a single-mode SiN waveguide covered with multiple layers of PbS/CdS QDs, before the deposition of the SiO₂ top-cladding. 4-28

-
- 4.20 On-chip lifetime spectroscopy of PbS/CdS QDs. (a) The PL decay traces measured with SNSPDs connected to the spectrometer channels, fitted with a stretched exponential. (b) Extracted lifetimes for the respective spectrometer channels (c) The emission spectrum of an embedded layer of PbS/CdS QDs at 4.2 K. 4-29
- 4.21 (a) Simulated radiative local density of states (LRDOS) in the gap of a plasmonic antenna with the inset showing a corresponding 2D map for a wavelength of $\lambda = 1150$ nm. (b) Rate enhancement measured using the four channels of an on-chip spectrometer and an inset showing a false-color SEM image of a fabricated structure. (c) Average lifetimes extracted from a stretched exponential fit of the PL decay. (d) Transmission measured through the four spectrometer channels connected to SNSPDs. Error bars represent $1-\sigma$ confidence intervals. 4-31
- 5.1 Schematic rendering of the waveguide-coupled colloidal QD light emitting diode developed in Chapter 3 and the emission spectrum collected for a voltage bias of 5 V. 5-2
- 5.2 Sketch of an integration scheme for further work on chip-based quantum photonics. Mature epitaxial quantum dots can be pre-selected and transfer printed on top of foundry processed SiN passives. Pure phase modulators should be compatible with operation at cryogenic temperatures, which are required for the high-performance waveguide-coupled SNSPDs. 5-7

List of Tables

2.1	Comparison of different room-temperature single-photon emitters under electrical excitation.	2-2
2.2	Comparison of the extracted central wavelengths λ_c , stretching exponents β and mean PL lifetimes $\bar{\tau}$ for QD monolayers on different substrates.	2-25
3.1	Estimated waveguide loss contributions for the fundamental TE mode with the fabricated dimensions, assuming QD absorption in absence of electrical or optical pumping.	3-7

List of Acronyms

ASE	Amplified spontaneous emission
AWG	Arrayed waveguide grating
ALD	Atomic layer deposition
APD	Avalanche photo diode
CMP	Chemical mechanical polishing
QD-LED	Colloidal quantum dot light emitting diode
CW	Continuous wave
DCR	Dark count rate
DEZ	Diethylzinc
DI	De-ionized
dc,DC	Direct current
DBR	Distributed Bragg reflector
DFB	Distributed feed-back
EL	Electroluminescence
FBMS	Fixed beam moving stage
FIB	Focused ion beam
FRET	Förster resonant energy transfer
FWHM	Full width at half-maximum
GC	Grating coupler
HAT-CN	1,4,5,8,9,11-Hexaazatriphenylenehexacarbonitrile
HOMO	Highest occupied molecular orbital
HSQ	Hydrogen silsesquioxane
ICP	Inductively coupled plasma
IPA	Isopropyl alcohol
IR	Infrared
IRF	Instrument response function
ITO	Indium tin oxide
LB	Langmuir-Blodgett
LED	Light-emitting diode
LUMO	Lowest unoccupied molecular orbital
ML	Monolayer
NPB,NPD	N,N'-Di(1-naphthyl)-N,N'-diphenyl-(1,1'-biphenyl)-4,4'-diamine
OLED	Organic light emitting diode

OPA	Optical parametric amplifier
PL	Photoluminescence
PCR	Photon count rate
PCG	Planar concave grating
PECVD	Plasma-enhanced chemical vapor deposition
PCB	Printed circuit board
QCSE	Quantum confined Stark effect
QD	Quantum dot
QKD	Quantum key distribution
RF	Radio frequency
RTA	Rapid thermal annealing
RIE	Reactive ion etching
RT	Room temperature
SEM	Scanning electron microscopy
SOI	Silicon on insulator
SM	Single-mode
SPS	Single-photon source
SNSPD	Superconducting nanowire single-photon detector
TCSPC	Time-correlated single photon counting
TLM	Transfer length measurement
TA	Transient absorption
TE	Transverse electric
TM	Transverse magnetic
TCTA	Tris(4-carbazoyl-9-ylphenyl)amine
UV	Ultraviolet
VIS	Visible
WG	Waveguide
WDM	Wavelength division multiplexing
XRD	X-ray diffraction
XRR	X-ray reflection
ZPL	Zero phonon line

Samenvatting

Geïntegreerd fotonica combineert verschillende geminiaturiseerde optische elementen op kleine chips om geavanceerde functionaliteiten en nieuwe toepassingen mogelijk te maken. Deze toepassingen zouden onmogelijk of economisch onhaalbaar zijn met discrete componenten. Toepassingen variëren van zenderontvangers voor glasvezel-telecommunicatie, chip gebaseerde bio-sensing en spectroscopie tot geminiaturiseerde atoomklokken en lineaire optische kwantumcomputers. Colloïdale kwantumdots (QD's) zijn halfgeleiderkristallen van enkele nanometers groot. In deze kleine 'dots' treedt kwantumopsluiting van de elektronen op, waardoor ze een emissie- en absorptiespectrum krijgen dat bepaald wordt door hun grootte. Een kosteneffectieve productie van deze QDs is mogelijk dankzij natte-chemie synthese van verschillende halfgeleidermaterialen. Op deze wijze kunnen colloïdale QDs verkregen worden met absorptie- en emissie-energieën doorheen het zichtbare en infrarode spectrum. Deze QD's zijn een aantrekkelijke lichtbron voor fotonische toepassingen bij zichtbare golflengtes, dankzij hun smalle emissielijnbreedtes en luminescentie-kwantumopbrengsten die 100% benaderen. Bovendien maken hybride integratiemethodes zoals spin-coaten en inkjetprinten een schaalbare productie mogelijk van QD-gebaseerde apparaten. Hoewel onderzoeksgroepen talrijke concepten op basis van colloïdale QD's hebben aangetoond, is het commerciële succes tot nu toe grotendeels beperkt gebleven tot de beeldschermindustrie.

In dit proefschrift onderzoeken we nieuwe concepten in de combinatie van colloïdale halfgeleider QD's met passieve geïntegreerde fotonische schakelingen. Deze combinatie maakt zowel conventionele opto-elektronische apparaten mogelijk, alsook nieuwe concepten voor single-foton bronnen. Deze laatste zijn van cruciaal belang in kwantumfotonische toepassingen.

Licht-emiterende diode gebaseerd op nanogestructureerde kwantumdots

Single-foton bronnen zijn onmisbare bouwstenen voor veel opkomende kwantum-optische technologieën. Lange tijd waren de meest gebruikte monofotonische bronnen gebaseerd op spontane parametrische down-conversie. Door gebruik te maken van een aankondigingsproces (heralding) biedt deze tech-

niek pure en niet te onderscheiden enkelvoudige fotonen. Deze enkelvoudige fotonen worden echter op willekeurige tijdstippen uitgezonden. De overgang van deze probabilistische single-foton-emissie naar een deterministische emissie is lange tijd een aanzienlijke uitdaging geweest. Slechts zeer recent is de fabricage van epitaxiale kwantumdots dusdanig verbeterd dat hun toepassingen in verschillende kwantumfotonische technologieën mogelijk is geworden. Vanwege hun relatief ondiepe kwantumopsluitingspotentialaal moeten deze QD-bronnen echter bij cryogene temperaturen worden gebruikt. Voor praktische toepassingen zou het nuttig zijn om alternatieve single-foton bronnen te ontwikkelen die zowel deterministisch zijn én bij hogere temperaturen kunnen worden gebruikt.

Door hun grotere opsluitingspotentialaal zijn colloïdale QD's beloftevol als efficiënte single-foton bronnen op kamertemperatuur. Het eerste deel van dit proefschrift handelt over een nanogestructureerde, QD-gebaseerde licht-emitterende diode (QD-LED). Met deze QD-LEDS trachten we single-foton emissie te verkrijgen via gelijkstromige elektrische excitatie, in plaats van de gebruikelijke optische aandrijving. We demonstreren de emissie van enkele CdSe/CdS core-shell QD's, gepositioneerd in een rechthoekige rooster. Het signaal van deze QDs was evenwel te zwak om zogenaamde anti-bunching op te meten, een kenmerkende eigenschap in de tijdsspanne tussen opeenvolgende single-foton emissies. Uit verder onderzoek blijkt de vorming van negatieve trionen verantwoordelijk voor deze verminderde kwantumopbrengst op vlak van luminescentie. Voor deze trionen - aangeslagen toestanden met een overtollige ladingsdrager - is niet-radiatieve Auger recombinatie het primaire ontbindingsmechanisme. We bespreken in het eerste hoofdstuk verder de verschillende noodzakelijke wijzigingen aan het apparaat die tot een heldere elektroluminescentie zouden kunnen leiden. In de literatuur is aangetoond dat het vervlakken van de opsluitingspotentialaal in de kern van QD's door middel van een gelegeerd omhulsel de niet-radiatieve Auger recombinatie aanzienlijk vertraagd kan worden. Dit kan de interne kwantumopbrengst van QD-LED's te verhogen. Het verminderen van de Auger rate vermindert echter ook de zuiverheid van de single-foton emissie van QDs. Dit treedt in het bijzonder op bij gebruik van een hoger excitatievermogen. Technieken gericht op het behoud van een neutrale ladingstoestand van de emitters zijn daarom geschikter. Het introduceren van een nanometer-dunne isolatielaag tussen de QD's en de elektroneninjectielaag kan de injectie van positieve en negatieve ladingen in de QD's balanceren. Deze zogenaamde tunnelbarrière vertraagt de efficiënte elektroneninjectie tot een niveau dat door de elektronengat-injectielagen kan worden geëvenaard. Een andere mogelijkheid om ladingsinjectie in evenwicht te houden, is het introduceren van verschillende QD-schillen. Deze schillen veranderen het geleidingsvermogen en de banduitlijning van de verschillende lagen. Voor onze apparaten vonden we dat CdSe/CdS/ZnS QD's met een dikkere ZnS-shell efficiënte single-foton bronnen kunnen zijn onder elektrische excitatie.

Terwijl de single-fotonemissie onder gelijkstroming elektrisch aandrij-

ven werd aangetoond door een concurrerende onderzoeksgroep, onderzochten wij apparaten met een gemanipuleerde uitstraalrichting als alternatieve toepassing van de ontwikkelde technieken. De verworven expertise in het nanostructureren van de quantum dots stelde ons bovendien in staat om golfgeleider-gekoppelde elementen te ontwikkelen. Deze worden in het tweede deel van dit proefschrift behandeld.

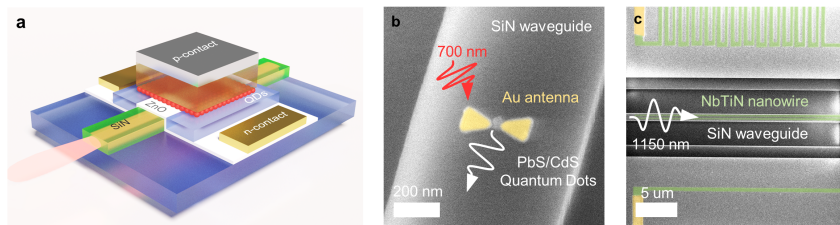
Golfgeleider-gekoppelde QD-LED's en detectoren

De tweede onderzoeksvraag richt zich op het elektrisch aanslaan van colloïdale QD's. Dit is reeds geruime tijd een struikelblok binnen de onderzoeksgemeenschap. In deze thesis presenteren we een nieuw concept dat enkele belangrijke problemen van eerder gepubliceerde implementaties uit de weg ruimt. De recente demonstratie van optische winst uit colloïdale QD's met behulp van een gelijkstromige elektrische bias maakt duidelijk dat deze QD's in principe geschikt zijn voor het bouwen van lasers. De huidige beschikbare QD-LED lagen zijn echter ontwikkeld voor toekomstige beeldschermapplicaties. Het is zeer moeilijk gebleken om in deze lagen een optische caviteit te ontwikkelen met voldoende laag verlies. Eerdere pogingen trachtten indexgeleiding van de optische mode in het actieve materiaal te bereiken, in combinatie met een periodisch gestructureerde ladingstransportlaag voor een verdeelde terugkoppeling van deze mode. Deze benadering lijdt echter onder een fundamentele beperking van efficiënte hybride anorganische/organische QD-LED concepten. Door het gebruik van de organische elektrongat-transportmaterialen is de bereikbare stroomdichtheid beperkt tot ongeveer 1 A/cm^2 in vlakke lagen. Een hoger stroomverbruik is noodzakelijk om optische winst van een elektrische bias waar te nemen, met gerapporteerde maxima tot 20 A/cm^2 . Terwijl een dunne QD-laag vereist is om zulke stroomdichtheden te bereiken, is een dikke QD-laag nodig om de optische mode te kunnen geleiden. Bijgevolg lijden implementaties die gebruik maken van indexopsluiting in dunne QD lagen aan hoge passieve optische verliezen. Deze verhinderen de lasing operatie in sterke mate.

Als alternatief hebben we een nieuw ontwerp ontwikkeld met een QD-LED-structuur in het evanescente veld van de geleide optische modus. Dit vermindert aanzienlijk de passieve optische verliezen ten gevolge van dunne QD-lagen, en maakt bovendien verschillende implementaties voor optische terugkoppeling mogelijk. Dankzij deze nieuwe apparaatarchitectuur hebben we een recordstroomdichtheid van 100 A/cm^2 aangetoond. Deze hoge stroomdichtheid maakt gestimuleerde emissie mogelijk, en dus uiteindelijk lasing operatie. De golfgeleider-gekoppelde QD-LED's zijn evenwel nog beperkt door enkele zijeffecten die optische transparantie belemmeren. Toch zijn we sterk overtuigd dat onze aanpak een belangrijke uitdaging oplost in het bouwen van een elektrisch aangedreven laser met behulp van colloïdale QD's. We rapporteren verder een maximaal on-chip vermogen van bijna 2 nW voor de QD-LED gekoppeld in een single-mode golfgeleider. Boven-

dien tonen we foton-detectie aan via dezelfde implementatie, met een lage donkere stroom van 1.5^{-6} A/cm² bij een omgekeerde bias van 7 V.

Op voorwaarde dat verder onderzoek leidt tot een sprong in de prestaties, verwachten we dat deze apparaten toepassingen zullen vinden in chip-gebaseerde absorptiespectroscopie en bio-sensing. Cruciaal voordeel hierbij is dat deze chips op grote schaal en aan lage kost kunnen gemaakt worden in bestaande halfgeleiderfabrieken. We hebben dan ook een Europese octrooiaanvraag ingediend ter valorisatie van deze colloïdale nanokristal-technologieën voor geïntegreerde fotonica-toepassingen.



Figuur 1: (a) Golfgeleider-gekoppelde QD-LED's en detectoren. (b) Colloïdale PbS/CdS QD's geplaatst in de antennespleet. (c) Golfgeleider-gekoppelde supergeleidende-nanodraad detector.

Integratie met supergeleidende detectoren

Het derde deel van dit proefschrift handelt over de ontwikkeling van een nieuw integratieplatform. Dit bestaat uit de combinatie van colloïdale QD single-foton stralers met een plasmonische antenne, supergeleidende-nanodraad single-foton detectoren (SNSPD's) én hoogwaardige siliciumnitride passieve fotonische componenten op één enkele chip.

De ongeëvenaarde prestaties van SNSPD's op het gebied van systeem-detectie-efficiëntie, donkerstroom en tijdsresolutie maken ze onmisbaar voor vele kwantumoptica-experimenten. Er is vooruitgang geboekt bij de integratie van epitaxiale QD's met SNSPD's op dezelfde chip, maar het vrij grote optische verlies in de golfgeleiders is een belangrijk obstakel voor de ontwikkeling van complexere optische circuits. Daarom is hybride integratie met geschikte single-foton stralers en laag-verlies golfgeleiders noodzakelijk om te voldoen aan de strenge eisen van kwantumoptische protocollen. Een korte stralingslevensduur van QD emitters is noodzakelijk voor een hoge single-foton emissiesnelheid. Hiertoe maken we gebruik van zogenaamde Purcell enhancement, waarbij deze emitters op een plaats met hoge lokale toestandsdichtheid (LDOS) gezet worden. Deze verhoogde LDOS treedt bijvoorbeeld op in diëlektrische holtes of nabij plasmonische antennes en

vermindert de stralingslevensduur zonder enige wijziging aan te brengen aan de emitter zelf.

Het is welgekend dat de Purcell enhancement zeer sterk is in de nanometer-grootte spleet tussen een plasmonische vlinderantenne. We gebruiken deze structuur om de microseconde-lange stralingslevensduur van IR-stralende colloïdale PbS/CdS QD's te verbeteren, vervolgens de foton-emissie rechtstreeks te koppelen aan siliciumnitride golfgeleiders en ten slotte het tijdsverval van de fotoluminescentie te meten met SNSPD's die zich op dezelfde chip bevinden. Dankzij deze meting op één chip hebben we een maximale stralingstoestandsdichtheid (LRDOS) van 200 ± 50 gedemonstreerd voor QD's die specifiek in de antennespleet zijn geplaatst. Bovendien zijn we er in geslaagd om het spectrum van het tijdsverval van de fotoluminescentie afkomstig van de PbS/CdS quantum dots uit te meten bij cryogene temperaturen. Hiertoe maakten we gebruik van planaire concave rooster-spectrometer, die eveneens geïntegreerd zit in de siliciumnitride chip.

In toekomst zullen echter betere emitters dan deze colloïdale PbS/CdS QDs nodig zijn. Een hogere kwantumefficiëntie op vlak van fotoluminescentie is nodig om met individuele single-foton bronnen te kunnen werken. Gelukkig is het hier ontwikkelde on-chip platform eenvoudig aan te passen naar nieuw ontwikkelde kwantumstralers.

Toekomstige onderzoeksperspectieven

Perovskiet nanokristallen bieden een alternatieve oplossing voor integreerbare single-foton stralers. Recent is men erin geslaagd om via foton-correlatie Fourier spectroscopie een defaserings-tijd op te meten die gelijkaardig is aan de radiatieve levensduur van deze kristallen. Dit maakt coherente single-fotonstraling mogelijk. De meeste kwantum-optische protocollen vereisen namelijk niet-onderscheidbare enkelvoudige fotonen, en dit is momenteel niet haalbaar met colloïdale QD emitters.

Toekomstig onderzoek gebaseerd op de ontwikkelingen in dit proefschrift kan leiden tot een chip-gebaseerd platform dat de nano-gestructureerde LEDs combineert met de Purcell enhancement van plasmonische antennes bovenop siliciumnitride golfgeleiders. Op deze manier kan de elektroluminescentie van perovskiet nanokristallen gekoppeld worden aan siliciumnitride golfgeleiders met een laag verlies. De enkelvoudige fotonen kunnen dan gemanipuleerd en gedetecteerd worden op dezelfde chip. Elektrische excitatie van deze fotonen biedt bovendien het grote voordeel dat er geen aandrijf-laser aanwezig is. De fotonen van deze laatste moeten dus ook niet onderdrukt moeten worden, verdwaalde fotonen vormen namelijk een groot struikelblok voor chip-gebaseerde kwantumoptica.

Belangrijke uitdaging om grotere circuits voor lineaire optische kwantumcomputers mogelijk te maken blijft dan nog de onderlinge coherentie tussen verschillende single-foton bronnen. In tegenstelling hiermee lijkt het demonstreren van elektrisch aangedreven lasing uit colloïdale QD's binnen

handbereik te liggen.

Naast het oplossen van de resterende problemen in de huidige ontwerpen, kan toekomstig onderzoek zich richten op het aanpassen van de ladingstoestand van de QD's om lasing te bereiken. Het is eerder aangetoond dat bij negatief geladen QD's de laserdrempel aanzienlijk kan worden verlaagd. Transiënte absorptiespectroscopie kan dan wel gebruikt worden om de optische winst van nanokristallen in oplossing te meten, de exacte landings- toestand en injectiemechanismes van QD emitters gekoppeld aan een vaste stof golfgeleider blijft ongekeerd terrein. Fotoluminescente levensduurspec- troscopie bij tot voorkort ongekeerde stroomdichtheden kan een waardevol hulpmiddel bieden om de QD-lading te op te meten en een geschikt wer- kingsregime voor een elektrisch aangedreven colloïdale QD-laser te vinden.

Summary

Integrated photonics research is aimed at combining miniaturized optical elements on small chips, to achieve advanced functionality or applications, which would not be possible, or economically unfeasible with discrete components. Applications range from transceivers for fiber-optic telecommunication, chip-based bio-sensing and spectroscopy to miniaturized atomic clocks and linear optical quantum computing. Colloidal quantum dots (QDs) are nanometer-sized semiconductor crystals with a characteristic size-dependent emission and absorption spectrum, which originates from the quantum confinement effect. Scalable wet-chemical synthesis allows for a cost-effective production and based on different semiconductor materials, colloidal QDs can span a wide range of absorption and emission energies in the visible and infrared. Especially for visible photonics, these QDs have become an attractive light source, with narrow emission linewidths and luminescence quantum yields approaching 100%. Straight-forward hybrid integration methods such as spin-coating or ink-jet printing enable scalable device fabrication. Yet, while research groups have demonstrated numerous device concepts based on colloidal QDs, commercial success has so far largely been limited to the display industry.

In this thesis we explore a new approach, combining colloidal semiconductor QDs with passive integrated photonic circuits, to demonstrate both conventional optoelectronic devices and also concepts for single-photon emitters, necessary for quantum photonic applications.

Nano-patterned QD light emitting diodes

Single-photon sources are indispensable building blocks for many emerging quantum-optical technologies. For a long time, the most commonly used single-photon sources were based on spontaneous parametric down-conversion. By utilizing a heralding process, this technique offers pure and indistinguishable single photons, however at random points in time. Moving from probabilistic single-photon emission to more practical deterministic emitters, has been a considerable challenge. Only recently, epitaxial quantum dots have reached a sufficient maturity level, enabling applications in several quantum photonic technologies. However, due to their relatively

shallow confinement potential, these QD sources have to be operated at cryogenic temperatures. For practical applications it would be beneficial, to develop alternative single-photon sources which are deterministic, but can also be operated without an expensive cryostat.

Owing to a larger confinement potential, colloidal QDs can be efficient room-temperature single-photon emitters. In the first part of this thesis we report on a nano-patterned QD light emitting diode (QD-LED), with the aim of achieving single-photon emission from dc electrical pumping, instead of commonly used optical excitation. We demonstrate emission from few CdSe/CdS core-shell QDs, patterned in a rectangular array. But due to a weak signal it was not possible to measure anti-bunching, characteristic of single-photon emission. Investigating the device physics, we identified the formation of negative trions as the reason for the reduced luminescence quantum yield. For these excited states with an excess charge carrier, non-radiative Auger recombination is the primary decay mechanism. We then discuss several modifications to the device, that could be implemented to mitigate the issue and retain bright electroluminescence.

In literature, it has been shown that smoothing the confinement potential in core-shell QDs by means of an alloyed shell can significantly slow down non-radiative Auger recombination. This can be used to increase the internal quantum yield of QD-LEDs. However, reducing the Auger rate also reduces the purity of the single-photon emission from QDs, when using higher excitation powers. Therefore, alternative techniques, aimed at preserving the neutral charge state of the emitters are more suitable. One possibility to balance the injection of positive and negative charges into the QDs, is to introduce a nanometer-thin insulating layer between the QDs and the electron-injection layer. This tunneling barrier slows down the efficient electron injection, to a level which can be matched by the hole injection layers. Alternatively, modifying the conductivity and band alignment of the layers and introducing different QD shells can help to balance the charge-injection. For our devices we found that CdSe/CdS/ZnS QDs with a thicker ZnS shell could be efficient single-photon emitters under electrical excitation.

While single-photon emission from dc electrical pumping was demonstrated by a competing research group, we also explored devices with engineered emission directionality as an alternative applications of the developed techniques. In addition, lessons learned from the nano-patterning process benefited the development of waveguide-coupled devices presented in the second part of this thesis.

Waveguide-coupled QD-LEDs and detectors

As a second research objective, we targeted electrically pumped lasing from colloidal QDs, which has long been sought after by the research community. While further improvements are needed to reach this goal, we present a

new device concept, which solves several issues of previous implementations found in literature.

The recent demonstration of optical gain from colloidal QDs using a dc electrical bias, has shown the feasibility of building a laser. Yet, it has proven difficult to engineer a low-loss optical cavity around established QD-LED stacks, developed for next-generation display applications. Previous attempts have used index confinement in the active material, combined with a patterned charge transport layer providing distributed feedback. However, this approach suffers from a fundamental limitation of efficient hybrid inorganic/organic QD-LED concepts. Due to the use of organic hole transport materials, the attainable current density is limited to approximately 1 A/cm^2 in planar devices. Moderate current focusing is necessary to observe optical gain from an electrical bias, with a previously reported maximum of 20 A/cm^2 . While it is possible to invert only thin QD layers with the available current density, a thick QD film is needed to support a confined optical mode. Consequently, devices employing index confinement in thin QD layers suffer from increasing passive optical losses, which strongly compromise lasing operation.

As an alternative, we developed a novel design with a QD-LED structure in the evanescent field of a guided optical mode, allowing to significantly reduce passive optical losses for thin QD layers and enabling multiple means of optical feedback. Importantly, thanks to the inherent current focusing architecture of the devices, we achieved a record current density of 100 A/cm^2 , putting stimulated emission within reach. While the waveguide-coupled QD-LEDs are currently still limited by adverse effects hampering the observation of optical transparency, we believe that our approach solves a key challenge in building an electrically pumped laser using colloidal QDs.

We further report a maximum on-chip power of almost 2 nW in a single-mode waveguide for the QD-LED and also demonstrate photo-detection with the same devices, with a low dark current of $1.5 \times 10^{-6} \text{ A/cm}^2$, at a reverse bias of 7 V . Provided that further improvements are going to lead to a leap in performance, we anticipate that these devices will find applications in chip-based absorption spectroscopy and bio-sensing, as they can be post-processed on foundry-fabricated waveguide platforms, at a low cost. Consequently, a European patent application was filed to facilitate the valorization of colloidal nanocrystal technologies for integrated photonics applications.

Integration with superconducting detectors

In the third part of this thesis we developed an integration platform to combine colloidal nanocrystal single-photon emitters with plasmonic antennas, state-of-the-art superconducting nanowire single-photon detectors (SNSPDs) and high-performance silicon nitride passive photonic components on a single chip.

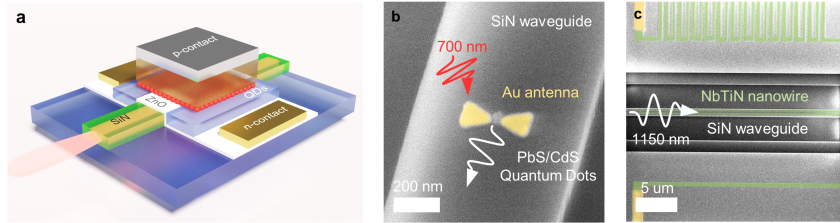


Figure 1: (a) Sketch of a waveguide-coupled QD-LED. (b) SEM image of colloidal PbS/CdS QDs placed in the gap of a plasmonic bowtie antenna. (c) SEM image of a waveguide-coupled superconducting nanowire detector.

The unrivaled performance of SNSPDs in terms of system detection efficiency, dark count rate and temporal resolution makes them indispensable for many quantum optics experiments. Progress has been made in integrating epitaxial QDs with SNSPDs on the same chip, but the rather large waveguide loss is a main hindrance to the development of more complex photonic circuits. Therefore, hybrid integration approaches with suitable single-photon emitters and low-loss waveguides are necessary to fulfill the stringent requirements of quantum optics protocols. A short radiative lifetime of QD emitters is further crucial for a high single-photon emission rate and Purcell enhancement of emitters placed in dielectric cavities or in the high local density of states (LDOS) field of plasmonic antennas is a common way to reduce the radiative lifetime, without the need for engineering the emitter itself. In this work we used the widely studied plasmonic gap antenna in a bowtie shape to improve the microsecond radiative lifetime of IR-emitting colloidal PbS/CdS QDs, coupling the emission directly to silicon nitride waveguides and measuring the photoluminescence decay trace with SNSPDs located on the same chip. With this chip-based measurement we demonstrated a maximum radiative local density of states (LRDOS) enhancement of 200 ± 50 for QDs deterministically placed in the antenna gap. In addition, using a silicon nitride planar concave grating spectrometer, we performed on-chip lifetime spectroscopy of the PbS/CdS QDs at cryogenic temperatures.

However, more suitable emitters than the colloidal PbS/CdS QDs in the present implementation, crucially with a higher PL quantum yield would be needed to work with individual single-photon emitters. Importantly, the developed chip-based platform is flexible to changes and newly developed emitters can be readily integrated.

Future research perspectives

Alternative solution-processable single-photon emitters could be perovskite nanocrystals. Recently, photon-correlation Fourier spectroscopy has been used to reveal dephasing times on the order of the radiative lifetime for these particles, which enables coherent single-photon emission. The indistinguishability of the emitted single photons is required for many quantum optic protocols, but currently still out of reach for other colloidal QD emitters.

As future research, based on the developments presented in this thesis, one could imagine a chip-based platform that combines the nano-patterned LED devices with the Purcell enhancement from plasmonic antennas on top of silicon nitride waveguides. This way, the electroluminescence from perovskite nanocrystals could be coupled to low-loss silicon nitride components, manipulated and detected on the same chip. Electrical excitation has the advantage that it eliminates the need for an effective suppression of the pump laser, which otherwise is a major hurdle for quantum optics on a single chip. Still, to create the envisioned large-scale circuits for linear optical quantum computing, another major challenge is to establish mutual coherence between many individual single-photon sources.

In contrast to that, the goal of demonstrating electrically pumped lasing from colloidal QDs seems within reach. Next to solving remaining issues in the current devices, future research could be aimed at deliberately modifying the charge state of the QDs to achieve lasing. It has been shown in literature that in negatively charged QDs the lasing threshold can be significantly reduced. While solution based transient absorption spectroscopy can be used to identify suitable nanocrystal gain materials, the exact charge state and injection mechanism of the emitters in our waveguide-coupled QD-LEDs remains unexplored. Photoluminescence lifetime spectroscopy at previously unavailable current densities could be a valuable tool to discern the QD charging and identify a suitable operation regime for an electrically pumped colloidal QD laser.

Chapter 1

Introduction

This dissertation explores new integration concepts, combining colloidal semiconductor QDs with passive photonic circuits, demonstrating both conventional optoelectronic devices and also concepts for single-photon emitters, necessary for quantum photonic applications. This introductory chapter provides a brief overview of integrated photonics research and the photophysics of semiconductor QDs.

1.1 Integrated photonics

In analogy to the omnipresent electronic integrated circuits (ICs), which have revolutionized many aspects of modern society, integrated photonics is aimed at combining miniaturized optical elements on small chips to achieve advanced functionality or applications, which would not be possible with discrete components. [1]

To date, research and commercialization opportunities for integrated photonics are vast, spanning a broad range of topics from chip-based spectroscopy [2] to miniature atomic clocks. [3] The biggest success however has been the use of integrated photonics for fiber-based optical telecommunication with millions of deployed units. [4, 5] Similar to the use of different process technologies for diverse applications of electronic ICs, a variety of integrated photonics platforms have been established, each with distinct advantages and drawbacks. [6] Native III-V platforms allow for a facile integration of lasers and waveguides, while silicon and silicon nitride platforms benefit from mature fabrication technologies previously developed for electronic ICs, but rely on the heterogeneous integration of suitable light sources. Due to its broad transparency range and low waveguide loss, [7] silicon nitride has recently received a renewed interest for applications both

in the visible and infrared. Other emerging platforms include lithium niobate on insulator, which features low waveguide losses and fast pure phase modulators. [8]

Depending on the application requirements, different advantages of integrated photonic circuits can make the difference. For bio-sensing and spectroscopy using disposable chips and cost effective mass manufacturing is of the essence. [2] Specialised quantum photonic applications on the other hand especially benefit from the inherent phase stability and miniaturization of components. Large-scale experiments become possible on a small chip, which would otherwise fill a room, when implemented with discrete components. [9] Commonly though, heterogeneous integration becomes necessary, when components from different photonic platforms are required. For example, quantum photonic applications may need a 2-level system emitting non-classical states of light and low-loss passive components, but also a suitable pump laser to drive the system. Single-use bio-sensors based on spectroscopy at visible wavelengths could benefit from cost-effective post-processing of light sources and detectors on silicon nitride photonic waveguides. [2]

In the past, the majority of research has been focused on the heterogeneous integration of established epitaxial III-V materials. [10, 11] This is an obvious choice for many wavelength ranges, since there are efficient diode lasers available for infrared wavelengths based on InP [12] and GaAs, [13] as well as in the visible based on GaN [14, 15] and AlGaInP. [16] However, as can be seen from Figure 1.1, summarizing the available light sources from a major commercial supplier, [17] for a range of wavelengths in the visible, efficient diode lasers (DL) are not available and second harmonic generation (SHG) is the only option. Hence, there is a need for a novel gain material, which can close this gap.

Colloidal semiconductor nanocrystals also known as colloidal quantum dots (QDs) are a possible alternative to conventional epitaxial III-V materials. These nanometer-sized crystals have a characteristic size-dependent emission and absorption spectrum, which originates from the quantum confinement effect. Scalable wet-chemical synthesis allows for a cost-effective production [18, 19] and based on different semiconductor materials, colloidal QDs can span a wide range of absorption and emission energies in the visible and IR, as shown in Figure 1.2. Colloidal QDs are especially efficient emitters for visible wavelength ranges, and photoluminescence (PL) quantum yields approaching 100% have been achieved for different material systems. [20, 21] The combination of a narrow emission spectrum and the high PL quantum yield has enabled the use of colloidal QDs as efficient color converters in displays, [25] which is currently the biggest market.

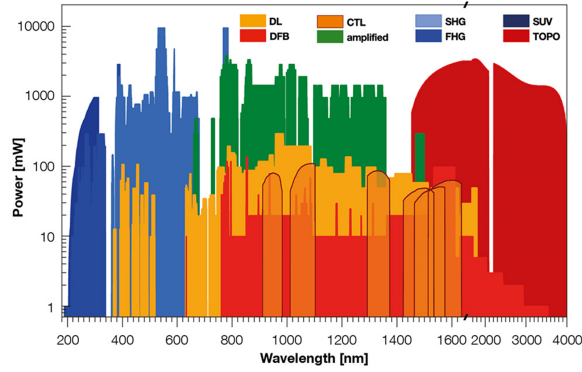


Figure 1.1: Available wavelengths of different laser solutions from Toptica Photonics [17]

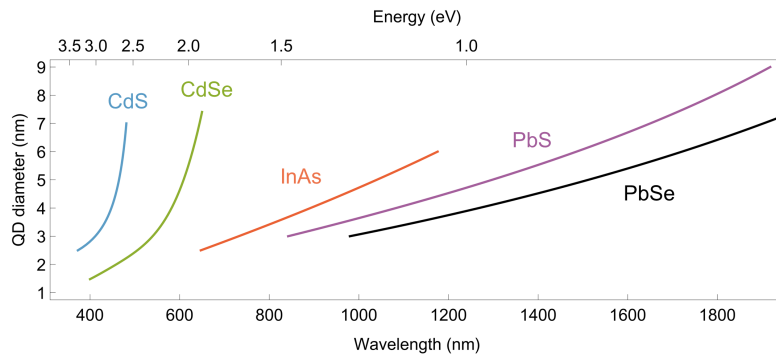


Figure 1.2: Size-dependent band-edge absorption energies of different colloidal semiconductor QDs. Data for CdS, PbS, PbSe nanocrystals was taken from reference [22], the sizing curve for CdSe cores was reported in [23], data for InAs QDs is from reference [24].

While electroluminescence from QD light emitting diodes has been an active area of research for a quite a while, [26] these devices have not reached the maturity for a commercial application yet. Apart from applications in the display industry, colloidal QDs have also been successfully employed for many other purposes. The improved photostability of QDs compared to traditional organic fluorophores has aided fluorescence microscopy [27] and the tuneable absorption spectrum has enabled efficient photo-detectors [28] and other spectroscopic applications. [29]

There have also been significant developments with respect to lasing from colloidal QDs, which are of particular interest for integrated photonics. Starting from early demonstrations of lasing using femtosecond optical pumping [30, 31] an improved understanding of the synthesis and QD physics has led to the demonstration of nanosecond [32], microsecond [33] and continuous wave lasing. [34, 35] Recently, also optical gain from direct current electrical pumping has been shown. [36] Yet, until now an electrically pumped laser using colloidal QDs is still missing. While for many of the optically pumped devices an application for integrated photonics is not straightforward, the demonstration of a disc laser with the emission coupled to a silicon nitride waveguides [37] has been a major achievement.

1.2 Fundamentals of colloidal QDs

An in-depth understanding of the QD synthesis and photo-physics has proven essential to reach the performance required for many advanced applications. This brief overview is aimed at providing a basis for the research presented in Chapter 2-4, but is in no way meant to be complete. A more extensive review can be for instance found in references [38, 39].

Since the first observation of a blue-shift of the absorption spectrum of CuCl nanocrystals in a glass matrix [40] and the subsequent development of a theoretical model, [41] the research field has progressed tremendously. The introduction of synthesis techniques based on the pyrolysis of organometallic precursors by injection into a hot coordinating solvent, allowed for a controlled nucleation and growth of nanocrystals, resulting in narrow size distribution of the QDs. [42] Organic ligands covering the surface of the nanocrystal are used to control the reaction and prevent agglomeration, when the QDs are dispersed in a solvent. In addition, the ligands passivate trap states at the surface and help to suppress the commonly observed photoluminescence blinking. [43] The development of shelling procedures, where the semiconductor nanocrystal core is embedded in a shell material with a wider bandgap, reduced the influence of the nanocrystal surface on the photophysical properties of colloidal QDs. [44, 45] As a result, photoluminescence quantum yields approaching 100% and virtually blinking-free emission can be achieved, [20, 21] which is a key requirement for many applications of colloidal QD emitters.

In a first approximation, the QD band-edge absorption energy E differs from the bulk bandgap $E_{g,bulk}$ by the quantum confinement of both electrons and holes as well as the Coulomb interaction [46]

$$E(r) = E_{g,bulk} + \frac{\hbar^2\pi^2}{2r^2} \left(\frac{1}{m_e^*} + \frac{1}{m_h^*} \right) - \frac{1.8e^2}{\epsilon r}, \quad (1.1)$$

where r is the radius of the semiconductor nanocrystal, m_e^* and m_h^* are the electron and hole effective mass, e is the elementary charge \hbar is the reduced Plack constant and ϵ is the dielectric constant of the semiconductor material.

In practice, already to explain the absorption and emission spectrum of the colloidal CdSe/CdS QDs in Figure 1.3a, this model needs to be extended. Clearly, there is a pronounced red-shift of the photoluminescence peak compared to the lowest energy absorption feature of about 50 meV, which is commonly referred to as Stokes shift. While the data in Figure 1.3a was acquired using non-resonant excitation at 400 nm and also suffers from inhomogeneous broadening of the spectra due to the QD size distribution, this effect persists for resonant excitation in fluorescence line narrowing (FLN) experiments. In addition, for colloidal nanocrystals, the excited state lifetime increases significantly at cryogenic temperatures. [47] These observations can be explained by the existence of an optically passive “dark” exciton state, for which the direct optical excitation or emission is spin-forbidden. [48, 49] In fact, in most semiconductor systems the ground

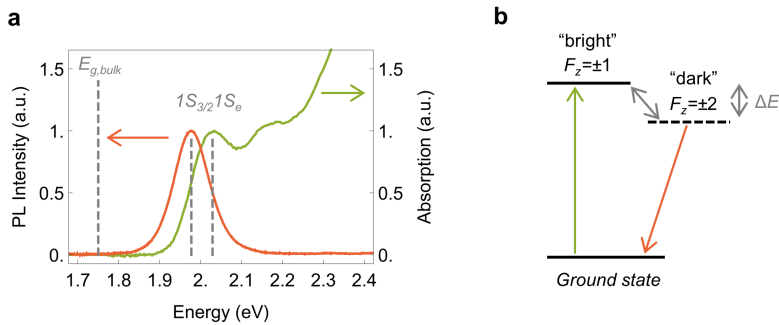


Figure 1.3: (a) Solution absorption and photoluminescence (PL) emission of the CdSe/CdS QD sample used for the experiments described in Chapter 3. (b) Bright-dark excitation model introduced to explain the Stokes shift under resonant excitation and long excited state lifetimes at cryogenic temperatures [47]

state is a “dark” exciton, [49] however usually the bright-dark splitting is smaller than the thermal energy, even at liquid helium temperatures, leading to an equal population of the states. The strong spatial confinement in colloidal QDs increases the splitting energy ΔE , which can be theoretically explained in the framework of a multiband effective mass theory. [50] In this framework, for spherically symmetric crystals, the first quantum size level of electrons is a doubly degenerate $1S_e$ state and the first quantum size level of the holes is a $1S_{3/2}$ state, which is fourfold degenerate with respect

to the projection of its total angular momentum. This results in a 8-fold degenerate $1S_{3/2}1S_e$ exciton ground state for spherical nanocrystals with a symmetric crystal structure. The electron-hole exchange interaction splits this 8-fold degenerate state in an upper optically active exciton state (total angular momentum $F = 1$) with 3-fold degeneracy and a lower optically passive state (total angular momentum $F = 2$) with 5-fold degeneracy. In addition, for deviations from a spherical symmetry, due a crystal structure without spherical symmetry, or a non-spherical shape of the QD, a further splitting occurs. For CdSe-based QDs this results in a 2-fold degenerate optically passive “dark” exciton state with a total angular momentum projection $F_z = \pm 2$ and an optically active “bright” state with $F_z = \pm 1$ split by ΔE as visualized in Figure 1.3b. Conservation of the angular momentum projection for the transition to ground state accounts for the $F_z = \pm 2$ states to be optically passive in the dipole approximation, because emitted or absorbed photons cannot have an angular momentum projection of ± 2 . However, the “dark” exciton can still recombine via a phonon assisted, momentum-conserving transition, albeit with a significantly longer associated lifetime. [47–49]

The radiative lifetime of an excited state, or the equivalent spontaneous emission rate γ_{rad} can be derived from “Fermi’s golden rule” [51, 52]

$$\gamma_{rad} = \frac{2e^4 n}{\pi \epsilon_0 m_0^3 c^3} |F_{loc}|^2 \underbrace{\frac{2m_0 \Theta^2 E}{3e^2 \hbar^2} |\langle 1S_{3/2} | p | 1S_e \rangle|^2}_f, \quad (1.2)$$

where e is the elementary charge, n is the refractive index, ϵ_0 is the vacuum permittivity, m_0 is the electron rest mass, c is the speed of light, F_{loc} is the local field correction factor, Θ is the overlap integral between electron and hole wave functions, E is the transition energy and $|\langle 1S_{3/2} | p | 1S_e \rangle|$ is the Kane interband matrix element. A transition between two states is also commonly characterized by the associated oscillator strength f . Generally, upon non-resonant excitation of a higher energy state, rapid phonon-assisted cooling brings the conduction band electron down to the lowest energy excited states, resulting in a thermal population of the band-edge exciton states. While for a neutral exciton only radiative recombination to the ground state is possible, which enables PL quantum yields approaching 100%, for other excited states sketched in Figure 1.4, also non-radiative Auger recombination pathways exist. [53, 54]

These excited states and their respective radiative and non-radiative recombination pathways are especially important when considering stimulated emission from colloidal QDs. Due to the 2-fold degeneracy of the band-edge exciton in CdSe-based QDs an excitation level of $\langle N \rangle > 1$ is necessary for

stimulated emission to overcome absorption. Hence, a fraction of QDs needs to have two excitations, which is commonly referred to as bi-exciton gain. The bi-exciton can also decay non-radiatively though, via Auger processes in which a remaining charge carrier takes up the energy instead of a photon. Similar to the case of non-resonant excitation, rapid cooling subsequently brings the QD back to its band-edge exciton state. Since the efficiency of Auger processes scales with the cube of the charge carrier density, the effect is significantly enhanced in colloidal nanocrystals, compared to their bulk semiconductor counterparts, leading to fast non-radiative decay of the bi-exciton state. It has been shown that while the Auger rate generally scales with the inverse volume of a QD, [53] this limitation can be overcome by modifying the shape of the confinement potential. [55] Alloying the interface of a core/shell QD to create a smooth confinement potential can significantly reduce the Auger recombination rates, [56] which greatly benefits LED [57] and lasing applications. [36]

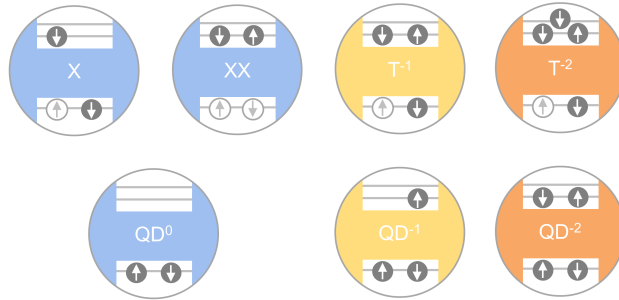


Figure 1.4: Neutral and negatively charged QD ground states and their respective excited states, namely the neutral exciton (X), the bi-exciton (XX), the negative trion (T^-) and the doubly charged negative trion (T^{-2})

While charged QDs are detrimental for applications which rely on a high PL quantum yield, such as the colloidal QD light emitting diodes discussed in Chapter 2, charging of QDs can actually benefit lasing applications. [58] Figure 1.4 focuses on QDs with one or two excess electrons in the conduction band, since those are relevant for the discussion in the subsequent chapters. A negatively charged trion T^- can recombine non-radiatively via an Auger process, which reduces the quantum yield and observed PL decay rate. [54] Yet, since there are fewer Auger pathways available, the non-radiative decay is slower than for the bi-exciton. Considering stimulated emission, the theoretical threshold excitation is reduced to $\langle N \rangle > 0.5$. For the doubly charged negative trion the Auger rate is closer to the bi-exciton, but since band-edge absorption is already forbidden for the ground

state QD^{-2} , thresholdless gain has been predicted. [58] The effect of QD charging on the gain threshold has successfully been used to demonstrate low-threshold optically pumped lasers, [59] and will be further discussed in Chapter 3 and 5.

1.3 Structure of this thesis

Following this brief introduction of the research background and fundamental physical processes in colloidal QDs, the remainder of this thesis is organized in three main chapters. Each of these chapters concerns a different application of colloidal QDs, requiring the development of advanced integration processes.

In Chapter 2 we discuss the fabrication and characterization of a nano-patterned light-emitting diode (QD-LED), aimed at showing single-photon emission from electrically pumped individual QDs. We demonstrate emission from few QDs, patterned in a rectangular array and identify weak emission from negatively charged trions as a main hindrance to observing photon anti-bunching, characteristic of single-photon emission. We further discuss several modifications to the device that could be implemented to mitigate the issue and retain bright electroluminescence from neutral excitons.

As a second research objective, the developments presented in Chapter 3 target electrically pumped lasing from colloidal QD, which has long been sought after by the research community. While further improvements are needed to reach this goal, we present a new device concept, which solves several issues of previous implementations found in literature. Importantly, we achieved a record current density of 100 A/cm^2 for the waveguide-coupled QD-LEDs and also demonstrate photo-detection with the same devices, which show a low dark current of $1.5 \times 10^{-6} \text{ A/cm}^2$, at a reverse bias of 7 V.

Thirdly, in Chapter 4 we developed an integration platform to combine colloidal nanocrystal single-photon emitters with state-of-the-art superconducting nanowire single-photon detectors (SNSPDs) and high-performance silicon nitride passive photonic components, as well as plasmonic bowtie antennas to enhance the radiative rate of the emitters. We show a maximum radiative local density of states (LRDOS) enhancement of 200 ± 50 for QDs deterministically placed in the antenna gap and further performed wavelength-resolved lifetime spectroscopy on a single chip.

The concluding Chapter 5 aims to put the work presented in this thesis in perspective, compared to the current state-of-the-art found in literature. This includes a discussion of the prospects of colloidal nanocrystal single-

photon sources for quantum photonic applications and an outlook on further research towards electrically pumped lasing from colloidal QDs.

1.4 Publications

1.4.1 Publications in international journals

L. Elsinger, R. Petit, F. Van Acker, N. K. Zawacka, I. Tanghe, K. Neyts, C. Detavernier, P. Geiregat, Z. Hens and Dries Van Thourhout. *Waveguide-Coupled Colloidal Quantum Dot Light Emitting Diodes and Detectors on a Silicon Nitride Platform*. (submitted)

L. Elsinger, R. Gourgues, I. E. Zadeh, J. Maes, A. Guardiani, G. Bulgarini, S. F. Pereira, S. N. Dorenbos, V. Zwiller, Z. Hens, and D. Van Thourhout. *Integration of Colloidal PbS/CdS Quantum Dots with Plasmonic Antennas and Superconducting Detectors on a Silicon Nitride Photonic Platform*. *Nano Letters*, 19(8), 5452–5458, (2019)

C. Op de Beeck, B. Haq, **L. Elsinger**, A. Gocalinska, E. Pelucchi, B. Corbett, G. Roelkens, and B. Kuyken. *Heterogeneous III-V on silicon nitride amplifiers and lasers via microtransfer printing*, *Optica* 7, 386-393 (2020)

S. Bisschop, P. Geiregat, **L. Elsinger**, E. Drijvers, D. Van Thourhout, Z. Hens, and E. Brainis. *Fabrication and characterization of SiNx/Au cavities with colloidal nanocrystals*, *Opt. Express* 26, 6046-6055 (2018)

1.4.2 Patent applications

A European patent application has been filed (EP20172462.2), based on the innovative device concepts presented in Chapter 3.

1.4.3 Publications in international conferences

L. Elsinger, I. Tanghe, F. Van Acker, N. K. Zawacka, R. Petit, K. Neyts, C. Detavernier, P. Geiregat, Z. Hens, and D. Van Thourhout. *A Waveguide-Coupled Colloidal Quantum Dot LED on a Silicon Nitride Platform*. in Conference on Lasers and Electro-Optics, OSA Technical Digest (online) (Optical Society of America, 2020), paper STh1J.8

L. Elsinger, R. Gourgues, I. E. Zadeh, J. Maes, A. Guardiani, G. Bulgarini, S. F. Pereira, S. N. Dorenbos, V. Zwiller, Z. Hens, and D. Van

Thourhout. *Wavelength-resolved Purcell enhancement of PbS/CdS quantum dots measured on a chip-based platform*. In Photonic and Phononic Properties of Engineered Nanostructures X, volume 11289, page 1128914. International Society for Optics and Photonics, 2020.

C. Op de Beeck, **L. Elsinger**, B. Haq, G. Roelkens, and B. Kuyken. *Heterogeneously Integrated Laser on a Silicon Nitride Platform via Micro-Transfer Printing*. in Frontiers in Optics + Laser Science APS/DLS, OSA Technical Digest (Optical Society of America, 2019), paper FTu6B.1.

C. Op de Beeck, **L. Elsinger**, B. Haq, G. Roelkens, and B. Kuyken. *Towards the Integration of C-band Amplifiers on Silicon Nitride Waveguides via Transfer Printing*. in Frontiers in Optics + Laser Science APS/DLS, OSA Technical Digest (Optical Society of America, 2019), paper FTu5C.6.

L. Elsinger, R. Gourgues, I. E. Zadeh, J. Maes, V. Chandrasekaran, G. Bulgarini, V. Zwiller, Z. Hens, and D. Van Thourhout. *Onchip Spectroscopy of PbS/CdS Colloidal QDs using Superconducting Nanowire Single Photon Detectors (SNSPDs) on a Silicon Nitride Photonic Platform*. Poster presented at nanoGe Fall Meeting in Torremolinos, Spain, 2018.

L. Elsinger, T. Vandekerckhove, N. K. Zawacka, N. Le Thomas, Z. Hens, and D. Van Thourhout. *Nano-patterned quantum dot-LED structures with enhanced photoluminescence emission directionality*. In 23rd Annual symposium of the IEEE Photonics Benelux Chapter, 2018.

L. Elsinger, R. Gourgues, I. E. Zadeh, J. Maes, V. Chandrasekaran, G. Bulgarini, V. Zwiller, Z. Hens, and D. Van Thourhout. *Integration of colloidal QDs with plasmonics and superconducting nanowire detectors on a silicon photonic platform*. Poster presented at the Tenth International Conference on Quantum Dots in Toronto, Canada, 2018.

L. Elsinger, Y. Zhu, W. Xie, I. Tanghe, S. Bisschop, V. Chandrasekaran, E. Brainis, P. Geiregat, Z. Hens, and D. Van Thourhout. *A Hybrid SiN-QDOT Platform for Visible Photonics*. in Conference on Lasers and Electro-Optics, OSA Technical Digest (online) (Optical Society of America, 2018), paper SW4I.4.

L. Elsinger, E. Drijvers, V. Chandrasekaran, W. Xie, Z. Hens, and D. Van Thourhout. *Incorporation of colloidal quantum dots into the gap of plasmonic bowtie antennas*. In Proceedings Symposium IEEE Photonics

Society Benelux, pages 297–300, 2016.

L. Elsinger, M. Callens, J. Kuhs, V. Chandrasekaran, E. Drijvers, K. Neyts, C. Detavernier, E. Brainis, W. Xie, Z. Hens, and D. Van Thourhout. *Progress towards an electrically driven single photon source with colloidal quantum dots*. In 4th international workshop on Engineering of Quantum Emitter properties, Ireland, page 26, 2016.

References

- [1] S. E. Miller. *Integrated optics: An introduction*. The Bell System Technical Journal, 48(7):2059–2069, 1969.
- [2] A. Z. Subramanian, E. Ryckeboer, A. Dhakal, F. Peyskens, A. Malik, B. Kuyken, H. Zhao, S. Pathak, A. Ruocco, A. De Groote, P. Wuytens, D. Martens, F. Leo, W. Xie, U. D. Dave, M. Muneeb, P. Van Dorpe, J. Van Campenhout, W. Bogaerts, P. Bienstman, N. Le Thomas, D. Van Thourhout, Z. Hens, G. Roelkens, and R. Baets. *Silicon and silicon nitride photonic circuits for spectroscopic sensing on-a-chip [Invited]*. Photonics Res., 3(5):B47, oct 2015.
- [3] Z. L. Newman, V. Maurice, T. Drake, J. R. Stone, T. C. Briles, D. T. Spencer, C. Fredrick, Q. Li, D. Westly, B. R. Ilic, B. Shen, M.-G. Suh, K. Y. Yang, C. Johnson, D. M. S. Johnson, L. Hollberg, K. J. Vahala, K. Srinivasan, S. A. Diddams, J. Kitching, S. B. Papp, and M. T. Hummon. *Architecture for the photonic integration of an optical atomic clock*. Optica, 6(5):680, may 2019.
- [4] Intel. *Intel Demonstrates Industry-First Co-Packaged Optics Ethernet Switch*.
- [5] imec. *Silicon photonics technology for next-generation datacenter interconnects*.
- [6] A. Rahim, J. Goyvaerts, B. Szelag, J.-M. Fedeli, P. Absil, T. Aalto, M. Harjanne, C. Littlejohns, G. Reed, G. Winzer, S. Lischke, L. Zimmermann, D. Knoll, D. Geuzebroek, A. Leinse, M. Geiselmann, M. Zervas, H. Jans, A. Stassen, C. Dominguez, P. Munoz, D. Domenech, A. L. Giesecke, M. C. Lemme, and R. Baets. *Open-Access Silicon Photonics Platforms in Europe*. IEEE Journal of Selected Topics in Quantum Electronics, 25(5):1–18, sep 2019.
- [7] X. Ji, F. A. S. Barbosa, S. P. Roberts, A. Dutt, J. Cardenas, Y. Okawachi, A. Bryant, A. L. Gaeta, and M. Lipson. *Ultra-low-loss on-chip resonators with sub-milliwatt parametric oscillation threshold*. Optica, 4(6):619, jun 2017.
- [8] C. Wang, M. Zhang, X. Chen, M. Bertrand, A. Shams-Ansari, S. Chandrasekhar, P. Winzer, and M. Lončar. *Integrated lithium niobate electro-optic modulators operating at CMOS-compatible voltages*. Nature, 562(7725):101–104, 2018.

- [9] J. Wang, S. Paesani, Y. Ding, R. Santagati, P. Skrzypczyk, A. Salavrakos, J. Tura, R. Augusiak, L. Mančinska, D. Bacco, D. Bonneau, J. W. Silverstone, Q. Gong, A. Acín, K. Rottwitt, L. K. Oxenløwe, J. L. O'Brien, A. Laing, and M. G. Thompson. *Multidimensional quantum entanglement with large-scale integrated optics*. *Science*, 360(6386):285–291, apr 2018.
- [10] G. Roelkens, J. Van Campenhout, J. Brouckaert, D. Van Thourhout, R. Baets, P. R. Romeo, P. Regreny, A. Kazmierczak, C. Seassal, X. Letartre, G. Hollinger, J. M. Fedeli, L. Di Cioccio, and C. Lagahe-Blanchard. *III-V/Si photonics by die-to-wafer bonding*. *Materials Today*, 10(7-8):36–43, 2007.
- [11] J. Zhang, G. Muliuk, J. Juvert, S. Kumari, J. Goyvaerts, B. Haq, C. Op De Beeck, B. Kuyken, G. Morthier, D. Van Thourhout, R. Baets, G. Lepage, P. Verheyen, J. Van Campenhout, A. Gocalinska, J. O'Callaghan, E. Pelucchi, K. Thomas, B. Corbett, A. J. Trindade, and G. Roelkens. *III-V-on-Si photonic integrated circuits realized using micro-transfer-printing*. *APL Photonics*, 4(11):110803, 2019.
- [12] H. Ishikawa, H. Imai, T. Tanahashi, Y. Nishitani, M. Takusagawa, and K. Takahei. *V-grooved substrate buried heterostructure InGaAsP/InP laser*. *Electronics Letters*, 17(13):465, 1981.
- [13] R. N. Hall, G. E. Fenner, J. D. Kingsley, T. J. Soltys, and R. O. Carlson. *Coherent light emission from GaAs junctions*. *Physical Review Letters*, 9(9):366–368, 1962.
- [14] S. Nakamura and G. Fasol. *The blue laser diode: GaN based light emitters and lasers*. Springer Science & Business Media, 2013.
- [15] L. Jiang, J.-P. Liu, A. Tian, Y. Cheng, Z. Li, L. Zhang, S. Zhang, D. Li, M. Ikeda, and H. Yang. *GaN-based green laser diodes*. *Journal of Semiconductors*, 37(11):111001, nov 2016.
- [16] K. Kobayashi, S. Kawata, A. Gomyo, I. Hino, and T. Suzuki. *Room-temperature CW operation of AlGaInP double-heterostructure visible lasers*. *Electronics Letters*, 21(20):931, 1985.
- [17] T. Photonics. *TOPTICA's cutting edge laser systems*.
- [18] M. D. Tessier, D. Dupont, K. De Nolf, J. De Roo, and Z. Hens. *Economic and Size-Tunable Synthesis of InP/ZnE (E = S, Se) Colloidal Quantum Dots*. *Chemistry of Materials*, 27(13):4893–4898, jul 2015.

- [19] G. Niu, A. Ruditskiy, M. Vara, and Y. Xia. *Toward continuous and scalable production of colloidal nanocrystals by switching from batch to droplet reactors*. *Chemical Society Reviews*, 44(16):5806–5820, 2015.
- [20] M. Nasilowski, P. Spinicelli, G. Patriarche, and B. Dubertret. *Gradient CdSe/CdS Quantum Dots with Room Temperature Biexciton Unity Quantum Yield*. *Nano Letters*, 15(6):3953–3958, jun 2015.
- [21] Y. Li, X. Hou, X. Dai, Z. Yao, L. Lv, Y. Jin, and X. Peng. *Stoichiometry-Controlled InP-Based Quantum Dots: Synthesis, Photoluminescence, and Electroluminescence*. *Journal of the American Chemical Society*, 141(16):6448–6452, apr 2019.
- [22] J. Maes, N. Castro, K. De Nolf, W. Walravens, B. Abécassis, and Z. Hens. *Size and Concentration Determination of Colloidal Nanocrystals by Small-Angle X-Ray Scattering*. *Chemistry of Materials*, 30:32, 2018.
- [23] J. Jasieniak, L. Smith, J. van Embden, P. Mulvaney, and M. Califano. *Re-examination of the Size-Dependent Absorption Properties of CdSe Quantum Dots*. *The Journal of Physical Chemistry C*, 113(45):19468–19474, nov 2009.
- [24] P. Yu, M. C. Beard, R. J. Ellingson, S. Ferrere, C. Curtis, J. Drexler, F. Luiszer, and A. J. Nozik. *Absorption Cross-Section and Related Optical Properties of Colloidal InAs Quantum Dots*. *The Journal of Physical Chemistry B*, 109(15):7084–7087, apr 2005.
- [25] H. V. Demir, S. Nizamoglu, T. Erdem, E. Mutlugun, N. Gaponik, and A. Eychmüller. *Quantum dot integrated LEDs using photonic and excitonic color conversion*. *Nano Today*, 6(6):632–647, dec 2011.
- [26] Y. Shirasaki, G. J. Supran, M. G. Bawendi, and V. Bulović. *Emergence of colloidal quantum-dot light-emitting technologies*. *Nat. Photonics*, 7(1):13–23, jan 2013.
- [27] D. R. Larson, W. R. Zipfel, R. M. Williams, S. W. Clark, M. P. Bruchez, F. W. Wise, and W. W. Webb. *Water-soluble quantum dots for multiphoton fluorescence imaging in vivo*. *Science*, 300(5624):1434–1436, may 2003.
- [28] G. Konstantatos and E. H. Sargent. *Colloidal quantum dot photodetectors*. *Infrared Physics & Technology*, 54(3):278–282, may 2011.
- [29] J. Bao and M. G. Bawendi. *A colloidal quantum dot spectrometer*. *Nature*, 523(7558):67–70, jul 2015.

- [30] C. Dang, J. Lee, C. Breen, J. S. Steckel, S. Coe-Sullivan, and A. Nurmikko. *Red, green and blue lasing enabled by single-exciton gain in colloidal quantum dot films*. Nat. Nanotechnol., 7(5):335–339, may 2012.
- [31] C. Dang, J. Lee, K. Roh, H. Kim, S. Ahn, H. Jeon, C. Breen, J. S. Steckel, S. Coe-Sullivan, and A. Nurmikko. *Highly efficient, spatially coherent distributed feedback lasers from dense colloidal quantum dot films*. Appl. Phys. Lett., 103(17):171104, oct 2013.
- [32] Y. Zhu, W. Xie, S. Bisschop, T. Aubert, E. Brainis, P. Geiregat, Z. Hens, and D. Van Thourhout. *On-Chip Single-Mode Distributed Feedback Colloidal Quantum Dot Laser under Nanosecond Pumping*. ACS Photonics, 4(10):2446–2452, oct 2017.
- [33] M. M. Adachi, F. Fan, D. P. Sellan, S. Hoogland, O. Voznyy, A. J. Houtepen, K. D. Parrish, P. Kanjanaboos, J. A. Malen, and E. H. Sargent. *Microsecond-sustained lasing from colloidal quantum dot solids*. Nat. Commun., 6(1):8694, dec 2015.
- [34] F. Fan, O. Voznyy, R. P. Sabatini, K. T. Bicanic, M. M. Adachi, J. R. McBride, K. R. Reid, Y.-S. Park, X. Li, A. Jain, R. Quintero-Bermudez, M. Saravanapavanantham, M. Liu, M. Korkusinski, P. Hawrylak, V. I. Klimov, S. J. Rosenthal, S. Hoogland, and E. H. Sargent. *Continuous-wave lasing in colloidal quantum dot solids enabled by facet-selective epitaxy*. Nature, 544(7648):75–79, 2017.
- [35] Z. Yang, M. Pelton, I. Fedin, D. V. Talapin, and E. Waks. *A room temperature continuous-wave nanolaser using colloidal quantum wells*. Nature Communications, 8(1), 2017.
- [36] J. Lim, Y.-S. Park, and V. I. Klimov. *Optical gain in colloidal quantum dots achieved with direct-current electrical pumping*. Nat. Mater., 17(1):42–49, jan 2018.
- [37] W. Xie, T. Stöferle, G. Rainò, T. Aubert, S. Bisschop, Y. Zhu, R. F. Mahrt, P. Geiregat, E. Brainis, Z. Hens, and D. Van Thourhout. *On-Chip Integrated Quantum-Dot-Silicon-Nitride Microdisk Lasers*. Adv. Mater., 29(16):1604866, apr 2017.
- [38] V. I. Klimov. *Nanocrystal Quantum Dots*. CRC Press, 2010.
- [39] G. Konstantatos and E. H. Sargent. *Colloidal quantum dot optoelectronics and photovoltaics*. Cambridge University Press, 2013.

- [40] A. I. Ekimov and A. A. Onushchenko. *Quantum size effect in three-dimensional microscopic semiconductor crystals*. *Jetp Lett*, 34(6):345–349, 1981.
- [41] A. L. Efros and A. L. Efros. *Interband absorption of light in a semiconductor sphere*. *Soviet Physics Semiconductors-Ussr*, 16(7):772–775, 1982.
- [42] C. Murray, D. J. Norris, and M. G. Bawendi. *Synthesis and characterization of nearly monodisperse CdE (E= sulfur, selenium, tellurium) semiconductor nanocrystalites*. *Journal of the American Chemical Society*, 115(19):8706–8715, 1993.
- [43] A. L. Efros and D. J. Nesbitt. *Origin and control of blinking in quantum dots*. *Nature Nanotechnology*, 11(8):661–671, 2016.
- [44] M. A. Hines and P. Guyot-Sionnest. *Synthesis and Characterization of Strongly Luminescing ZnS-Capped CdSe Nanocrystals*. *The Journal of Physical Chemistry*, 100(2):468–471, jan 1996.
- [45] X. Peng, M. C. Schlamp, A. V. Kadavanich, and A. P. Alivisatos. *Epitaxial Growth of Highly Luminescent CdSe/CdS Core/Shell Nanocrystals with Photostability and Electronic Accessibility*. *Journal of the American Chemical Society*, 119(30):7019–7029, jul 1997.
- [46] L. E. Brus. *Electron–electron and electron-hole interactions in small semiconductor crystallites: The size dependence of the lowest excited electronic state*. *The Journal of chemical physics*, 80(9):4403–4409, 1984.
- [47] M. Nirmal, D. J. Norris, M. Kuno, M. G. Bawendi, A. L. Efros, and M. Rosen. *Observation of the "Dark Exciton" in CdSe Quantum Dots*. *Physical Review Letters*, 75(20):3728–3731, nov 1995.
- [48] A. L. Efros, M. Rosen, M. Kuno, M. Nirmal, D. J. Norris, and M. Bawendi. *Band-edge exciton in quantum dots of semiconductors with a degenerate valence band: Dark and bright exciton states*. *Physical Review B*, 54(7):4843–4856, aug 1996.
- [49] P. C. Sercel and A. L. Efros. *Band-Edge Exciton in CdSe and Other II-VI and III-V Compound Semiconductor Nanocrystals - Revisited*. *Nano Letters*, 18(7):4061–4068, jul 2018.
- [50] J. M. Luttinger and W. Kohn. *Motion of Electrons and Holes in Perturbed Periodic Fields*. *Physical Review*, 97(4):869–883, feb 1955.

-
- [51] A. F. van Driel, G. Allan, C. Delerue, P. Lodahl, W. L. Vos, and D. Vanmaekelbergh. *Frequency-Dependent Spontaneous Emission Rate from CdSe and CdTe Nanocrystals: Influence of Dark States*. Physical Review Letters, 95(23):236804, dec 2005.
- [52] C. de Mello Donegá and R. Koole. *Size Dependence of the Spontaneous Emission Rate and Absorption Cross Section of CdSe and CdTe Quantum Dots*. The Journal of Physical Chemistry C, 113(16):6511–6520, apr 2009.
- [53] V. I. Klimov, A. A. Mikhailovsky, D. W. McBranch, C. A. Leatherdale, and M. G. Bawendi. *Quantization of multiparticle Auger rates in semiconductor quantum dots*. Science, 287(5455):1011–1014, feb 2000.
- [54] P. P. Jha and P. Guyot-Sionnest. *Trion Decay in Colloidal Quantum Dots*. ACS Nano, 3(4):1011–1015, apr 2009.
- [55] G. E. Cragg and A. L. Efros. *Suppression of Auger Processes in Confined Structures*. Nano Letters, 10(1):313–317, jan 2010.
- [56] W. K. Bae, L. A. Padilha, Y.-S. Park, H. McDaniel, I. Robel, J. M. Pietryga, and V. I. Klimov. *Controlled Alloying of the Core-Shell Interface in CdSe/CdS Quantum Dots for Suppression of Auger Recombination*. ACS Nano, 7(4):3411–3419, apr 2013.
- [57] W. K. Bae, Y.-S. Park, J. Lim, D. Lee, L. A. Padilha, H. McDaniel, I. Robel, C. Lee, J. M. Pietryga, and V. I. Klimov. *Controlling the influence of Auger recombination on the performance of quantum-dot light-emitting diodes*. Nature Communications, 4(1):2661, dec 2013.
- [58] K. Wu, Y.-S. Park, J. Lim, and V. I. Klimov. *Towards zero-threshold optical gain using charged semiconductor quantum dots*. Nature Nanotechnology, 12(12):1140–1147, dec 2017.
- [59] O. V. Kozlov, Y.-S. Park, J. Roh, I. Fedin, T. Nakotte, and V. I. Klimov. *Sub-single-exciton lasing using charged quantum dots coupled to a distributed feedback cavity*. Science, 365(6454):672–675, aug 2019.

Chapter 2

Nano-patterned colloidal quantum dot light emitting diodes

Due to their large confinement potential, colloidal quantum dots (QDs) can be efficient room-temperature single-photon emitters. Here, we developed a nano-patterned QD light emitting diode, with the aim of achieving single-photon emission from dc electrical pumping, instead of commonly used optical excitation. We observed electroluminescence (EL) emission from few CdSe/CdS QDs, patterned in a rectangular array. But it was not possible to measure the anti-bunching characteristics of single-photon emission, due to a weak signal. Investigating the device physics, we found negative trion emission to significantly impair the EL quantum yield and present possible remedies to benefit future devices. As an alternative application of the developed techniques, we further explored devices with engineered emission directionality. The results presented in this chapter have in part been published in reference [1] and [2].

2.1 Introduction

Single-photon sources are indispensable building blocks for many emerging quantum-optical technologies. [3] For a long time, the most commonly used single-photon sources were based on spontaneous parametric down-conversion. By utilizing a heralding process, this technique offers pure and indistinguishable single photons, however at random points in time. [4] Moving from probabilistic single-photon emission to more practical deterministic emitters has been a considerable challenge. Only recently, epitax-

ial quantum dots have reached a sufficient maturity level as single-photon emitters, [5] enabling applications in several quantum photonic technologies. [6–8] However, due to their relatively shallow confinement potential, these QD sources have to be operated at cryogenic temperatures. For practical applications it would be beneficial, to develop alternative single-photon sources which are deterministic, but can also be operated without expensive cryostats.

Among other promising room-temperature emitters, [3] colloidal QDs are especially interesting due to recent improvements of their single-photon emission purity and stability, [9, 10] while solution processing allows for a flexible integration. [11] The aim of the work presented here was to show single-photon emission from colloidal QDs using electrical excitation. However, in course of the project we became aware of a publication from another research group, which demonstrates our research objective, [12] using a similar approach. Yet, while the researchers also employ a colloidal QD light emitting diode (QD-LED), their approach is completely random, without any control over the position of the emitter. Using the nano-patterning technique presented here, in contrast, individual QDs can be placed at a predetermined position of the sample.

In Table 2.1 we compare the results presented in reference [12] with other electrically driven single-photon sources operated at room temperature. Compared to neutral nitrogen-vacancy centers (NV^0) in diamond [13] and optically active defects in silicon carbide [14], colloidal CdSe/CdS exhibit a high single-photon purity, characterized by a second-order autocorrelation function $g^2(t=0)$ close to zero. In contrast, the relatively long radiative lifetime τ reduces the attainable single-photon rate and for practical applications, pulsed operation as shown in [14] is advantageous.

	CdSe/CdS QDs [12]	NV^0 in diamond [13]	defects in SiC [14]
$g^2(t=0)$	0.05 (dc)	0.45 (dc)	0.2 (pulsed)
τ (ns)	40	13	3
λ (nm)	625	575	745

Table 2.1: Comparison of different room-temperature single-photon emitters under electrical excitation.

The demonstration of single-photon emission from a QD-LED in reference [12] shows the viability of our approach and future research could be aimed at reducing the radiative lifetime, e.g. by means of Purcell enhancement as demonstrated in Chapter 4. However, due to persistent issues with

parts of the fabrication process performed by a collaborating research group and the reduced scientific impact, we shifted the focus to other research objectives. In this chapter we discuss process developments for nano-patterned QD-LEDs, which formed the foundation for further research presented in Chapter 3 and 4. Also, the investigation of the QD-LED properties provided a basis for the waveguide-coupled devices presented in Chapter 3.

2.2 Single-photon emission from colloidal CdSe/CdS QDs

For colloidal CdSe/ZnS QDs it was first shown, that they emit single photons at room temperature, upon non-resonant excitation with a pump laser. [15, 16] The fact that efficient Auger recombination suppresses the bi-excitation emission, allows for high count rates, while preserving the single-photon characteristics of the emission.

Here, we used colloidal CdSe/CdS QDs with reduced photoluminescence intermittency instead, [17] which were synthesized¹ according to literature procedures [18, 19] and have an inhomogeneously broadened photoluminescence (PL) spectrum as shown in Figure 2.1a. Details on the QD synthesis can be found in Appendix A.2. To characterize the single-photon emission properties of the CdSe/CdS QD sample, we spin-coated a dilute solution on a quartz substrate. Using a home-built microscope set-up with a high-resolution immersion objective (x100 magnification) and a 400 nm pump laser, we recorded the PL emission of an individual QD. As can be seen in Figure 2.1a, the emission of a single dot is homogeneously broadened with a full width at half maximum (FWHM) of 20 nm. The inhomogeneously broadened ensemble PL spectrum on the other hand has a FWHM of 45 nm. While the spectrum of an individual QD can be accurately represented by a Gaussian fit, the ensemble spectrum features a characteristic red tail.

We then used a Hanbury-Brown-Twiss experiment [20] as sketched in Figure 2.1b to record the second-order auto-correlation function

$$g^2(t) = \frac{\langle I(t^*)I(t^* + t) \rangle}{\langle I(t^*) \rangle^2}, \quad (2.1)$$

where $I(t)$ is the intensity of the emitter recorded at a time t . The so-called anti-bunching of $g^2(t)$ at $t = 0$ is indicative of a single-photon source (SPS), with the value of $g^2(0)$ determining the purity of the single-photon emission. Due to the finite dead time of single-photon resolving avalanche photo-diode

¹The CdSe/CdS QD synthesis was performed by Dr. Emile Drijvers, at the time associated with the physics and chemistry of nanocrystals (PCN) research group of Ghent University.

(APD) detectors, it is necessary to split the emission from the SPS and use two detectors to resolve short time-delays t . We used time-correlated single-photon counting (TCSPC) electronics (Picoquant Hydraharp) with an electronic delay to record the time-binned data in Figure 2.1c and d. Note that with suitable detectors characteristics, it is also possible to record the auto-correlation function with a single detector [21].

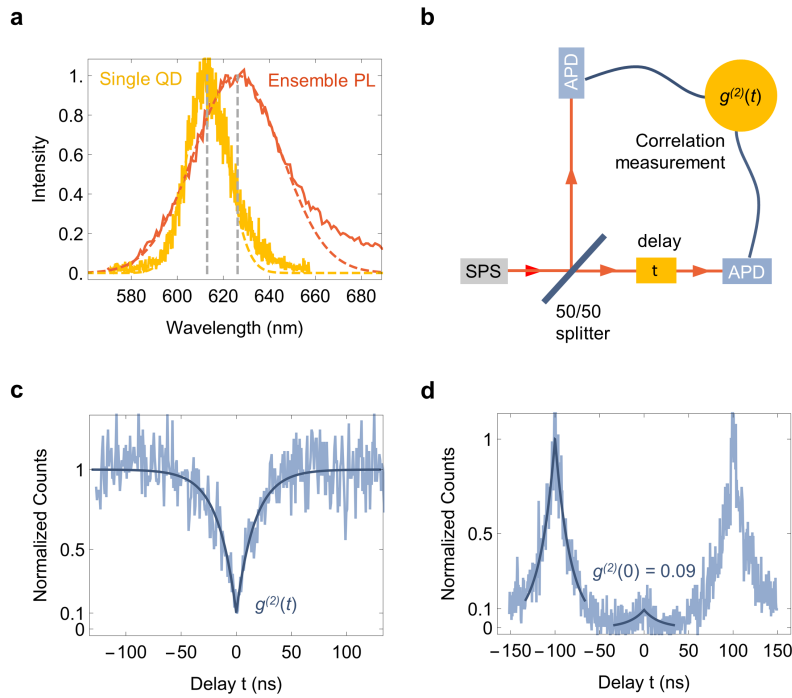


Figure 2.1: Properties of individual CdSe/CdS QDs. (a) Comparison of the PL emission spectrum of a single QD with an ensemble of QDs, exhibiting inhomogeneous broadening. (b) Sketch of a Hanbury-Brown-Twiss set-up used for the characterization of the second-order auto-correlation function $g^2(t)$, comprising a single-photon source (SPS) and two avalanche photo-diode detectors (APDs). Unlike the sketch indicating a delay in the optical path, we used an electrical delay in the experimental implementation. (c) Second-order auto-correlation function for an individual CdSe/CdS QD, measured using CW and (d) pulsed excitation.

Using continuous-wave (CW) excitation, for a two-level system $g^2(t)$ can be approximated as

$$g^2(t) = 1 - c e^{-(r+\tau^{-1})|t|}, \quad (2.2)$$

where r is the excitation rate and τ is the radiative lifetime of the system. For low excitation powers $r \rightarrow 0$ this turns into

$$g^2(t) = 1 - ce^{-|t|\tau^{-1}}, \quad (2.3)$$

which we used to fit the normalized data recorded for an individual CdSe/CdS QD in Figure 2.1c. Without any background subtraction, we obtained a value of $g^2(0) = 0.09 \pm 0.01$, which is in agreement with values reported in reference [12]. As a PL lifetime of the CdSe/CdS QD we extracted $\tau = 17$ ns. Using pulsed excitation, we further recorded the trace in Figure 2.1d, which was normalized by fitting the side-peak at $t_0 = -100$ ns with

$$g^2(t) = ce^{-|t-t_0|\tau^{-1}}. \quad (2.4)$$

Also fitting the central peak with Equation 2.4, we then extracted $g^2(0) = 0.09 \pm 0.02$ and $\tau = 17$ ns, in good agreement with the measurement using CW excitation. The confirmation of a high single-photon purity for the PL emission from individual CdSe/CdS QDs was a promising starting point for developing an electrical excitation scheme.

2.3 Nano-patterning of a QD layer

Next to pure single-photon emission, for practical applications a method to position the emitters on a substrate is highly desirable. Previously, a process has been developed to nano-pattern a QD layer down to a single-dot level. [11] Based on this work, we developed a process to work in conjunction with a QD-LED, as will be shown in Section 2.5.

First, we implemented the process outlined in reference [11] using a 50 kV e-beam lithography system (Raith Voyager) and optimized the QD patterning on a silicon substrate. We therefore coated a ~ 30 nm thin positive resist (ZEP 520A, Zeon Chemicals) on the sample, exposed it with an area dose of $120 \mu\text{C}/\text{cm}^2$, followed by a 30 s development in n-amyl acetate. A subsequent 5 s dry etch of the resist in O_2 plasma was found to improve the quality of the QD patterning. Langmuir-Blodgett (LB) deposition [22] (Nima 312D LB trough) was used to coat the sample with a dense monolayer of CdSe/CdS QDs (see Figure 2.2a). The deposition technique relies on the fact that due to oleic acid ligands on the surface of the QDs, a monolayer is formed on top of a polar solvent (de-ionized water). Pressure control (25 mN/m) allows to compress QDs, to form a dense monolayer. Pulling the substrate slowly out of the solvent, two samples can be coated with a QD monolayer at the same time, when mounting them back-to-back. To achieve a dense QD monolayer as shown in Figure 2.2b, it is essential that

the QD sample possesses a high size-uniformity, suppressing island formation with larger QDs in the center and smaller ones on the outside. Besides, to avoid the formation of incomplete layers, excess ligands have to be removed from the QD sample dispersed in toluene, prior to the deposition. Also, the solvent for the deposition has to be chosen carefully, to prevent excessive ligand stripping. The lift-off was performed in a 1:4 mixture of acetone and toluene, aided by ultrasonic agitation and followed by a prolonged rinse with isopropyl alcohol (IPA), to avoid the re-deposition of QDs. Figure 2.2b shows CdSe/CdS QDs patterned in the shape of the Ghent University Department of Information Technology logo. Structures with a feature size down to ~ 20 nm can be successfully resolved, with the limiting line edge roughness being determined by the QD diameter of ~ 10 nm.

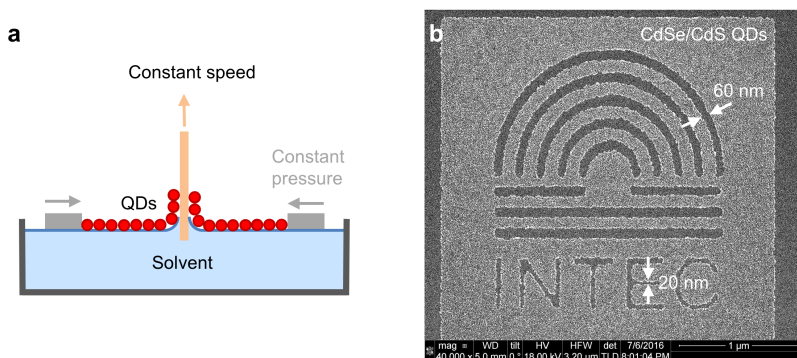


Figure 2.2: Nano-patterning of a colloidal QD monolayer. (a) Sketch of the Langmuir-Blodgett deposition technique, which allows to coat uniform QD monolayers on both sides of a sample. (b) SEM top-view of a nano-patterned layer of monodisperse CdSe/CdS QDs, showing the logo of the Ghent University Department of Information Technology. The technique allows to reliably pattern feature sizes down to 20 nm, with a limiting line edge roughness determined by the size of the QDs.

As shown in reference [11], the same process can also be used to place individual QDs in a defined pattern on a substrate. Using a dot dose of 0.5 fC and otherwise the same process parameters as described above, we deposited single CdSe/CdS QDs on a silicon substrate with a probability of $\sim 40\%$ as shown in Figure 2.3. High-resolution SEM images (Figure 2.3a) can be used to count the number of QDs, the resulting patterning probabilities (Figure 2.3b) are best described by a binomial fit. [11] Due to non-deterministic elements in the deposition process, the single-dot patterning probability

is limited to $\sim 40\%$ with the method. To overcome this limitation, the processing would have to be modified, e.g. using electrostatic self-assembly techniques. However, the techniques reported in literature [23, 24] make use of large dielectric silica shells enclosing the QDs, consequently rendering it impossible to electrically inject charge carriers into the QDs. Thus, methods relying on a silica encapsulation are not suitable for a nano-patterned QD-LED.

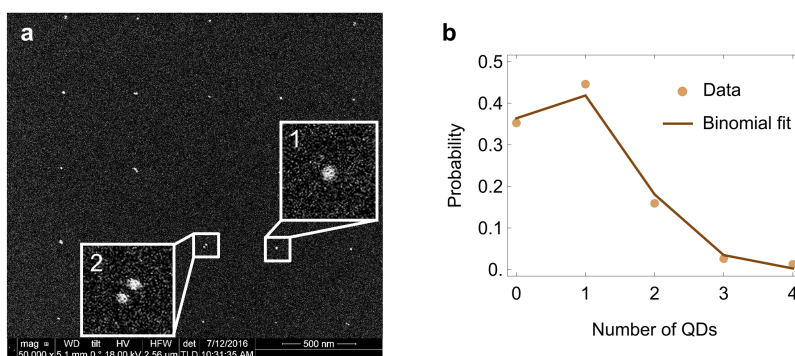


Figure 2.3: Single-dot patterning of colloidal CdSe/CdS QDs. (a) SEM top-view of an array with individual patterned QDs with magnified insets showing (1) a single QD and (2) two QDs. (b) Patterning statistics showing a probability of 40% for patterning of single QDs and a corresponding fit with a binomial distribution.

The presented technique employing LB deposition has the advantage that it can provide a QD monolayer, regardless of the patterned shape. However, to achieve a uniform layer, the QD sample has to be mono-disperse and ligands must not be removed from the QD surface in the polar solvent used for the deposition. In addition, while it is possible to also coat multiple layers using Langmuir-Blodgett deposition, it is more intricate and time-consuming than spin-coating QDs. For that reason, we developed an alternative lift-off process for nano-patterning colloidal QDs using spin-coating. We therefore used a positive e-beam resist (AR-P 617.09, Allresist), with a thickness depending on the desired QD thickness. A 10 min soft-bake at 200°C , an exposure dose adjusted to the pattern density and development in a dedicated developer (AR 600-55, Allresist) resulted in a high-resolution resist pattern. QDs were spin-coated from toluene, with concentration and spin-speed determining the resulting QD layer thickness. Lift-off in acetone produced a well-defined QD pattern, with only minimal re-deposition of QDs, as can be seen from the SEM images in Figure 2.4. The nano-

patterned CdSe/CdS QD film in Figure 2.4a also shows a drawback of the method though. While a uniform layer can be achieved for a large-area pattern, the bright areas of charged QDs indicate a thicker layer next to resist sidewalls, which were removed during the lift-off. This result is typical for spin-coated materials and might preclude the patterning technique for some applications, but in a lot of cases this effect can be compensated, when properly accounted for. For example, the array of nano-patterned pillars of PbS/CdS QDs in Figure 2.4b is highly uniform and individual pillars with a diameter of only 75 nm were well-resolved. Besides being less sensitive to the size dispersion of the QD sample, the QD nano-patterning using spin-coating also works for samples with a moderate surface profile. LB deposition on the other hand requires a planar surface for a high-resolution pattern, which can present a major limitation for more evolved device processing. For the device applications presented in this thesis we used both techniques, based on their respective advantages.

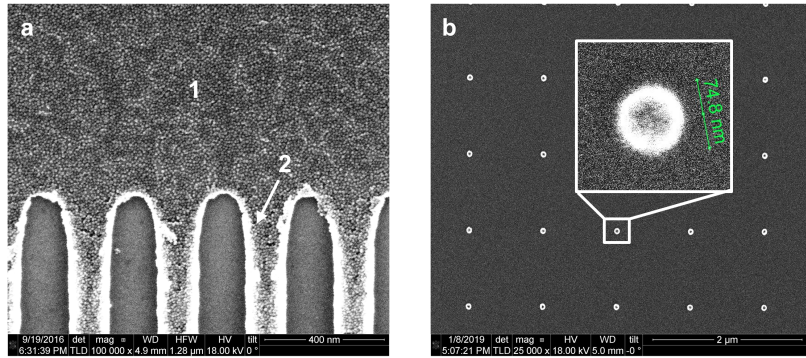


Figure 2.4: Nano-patterning of QDs using spin-coating. (a) SEM top-view of a patterned CdSe/CdS QD structure with two different feature sizes. (1) Large area with a uniform QD layer. (2) Nano-patterned grating of QDs, the bright regions originate from pronounced charging of the QDs and indicate areas with a thicker QD layer. (b) Array of nano-patterned PbS/CdS QDs, with the inset showing an individual 75 nm diameter QD pillar.

2.4 Colloidal QD light emitting diodes

Since the first demonstration of electroluminescence (EL) from colloidal QDs, [25] tremendous progress has been made to improve brightness and quantum efficiency of colloidal quantum dot light emitting diodes (QD-

LEDs), bringing display and solid-state lighting applications within reach. High-performance devices have been reported for different device architectures, in particular hybrid devices employing a combination of organic and inorganic charge transport layers have proven successful. [26] Internal quantum efficiencies approaching 100% have been reported for different layer stacks. [27, 28]

We based our QD-LED design on a so-called inverted² layer stack, [27] where electrons are injected from the side of the glass substrate coated with a transparent conductive oxide. Figure 2.5b shows the theoretical band alignment of the different layers. We used sputter-deposited indium tin oxide (ITO) on a glass slide as a common n-contact electrode and a thin layer of ZnO for efficient electron injection into the QDs. However, instead of solution-processed ZnO nanocrystals typically employed in literature, [26–28] we used atomic layer deposition (ALD) to coat a dense ZnO layer, ensuring compatibility with the nano-patterning process outlined in the next section.

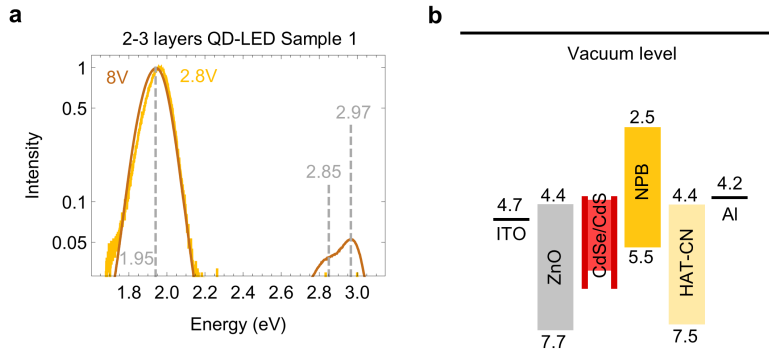


Figure 2.5: (a) Emission energies of the QD-LED device for different bias voltages on a logarithmic scale. (b) Theoretical band alignment of the different layers in the QD-LED stack with reference to the vacuum level and energy levels denoted in units of eV.

The 20 nm thin ZnO layer was deposited using an ALD process adapted from literature, [29] based on thermal ALD with diethylezinc (DEZ) used as a precursor and distilled water vapor as reactant.³ Additional details on the ALD process can be found in Appendix A.4. Literature suggests that

²The term “inverted” originates from the fact that, in the first QD-LED devices, holes were injected from the side of the transparent conductive oxide. Hence, a stack using electron injection from ITO instead, is considered inverted.

³ALD was performed by Dr. Jakob Kuhs, at the time associated with the Conformal Coating of Nanomaterials research group of Ghent University

the conductivity of a ZnO layer deposited by thermal ALD can be adjusted through the deposition temperature. [30, 31] We could reproduce this observation and obtained a conductive layer with a resistivity on the order of $10^{-2} \Omega \text{ cm}$ (measured with a 4-point probe) for a deposition temperature of 220°C , which is in good agreement with literature reports. [30] The observed n-type conductivity in ZnO due to native oxygen vacancy defects [32] can be spoiled when the thin films are simultaneously exposed to O_2 plasma and elevated temperatures, as for example in a common plasma cleaning tool (Tepla 600). Exposure to O_2 plasma at room-temperature in a reactive ion etch (RIE) chamber on the other hand, only had a minor effect on the conductivity. The ZnO layer deposited on a silicon sample was poly-crystalline with a preferential c-axis orientation, as can be seen from x-ray diffraction (XRD) measurements (2-theta scan in Figure 2.6a). We further used ellipsometry, to extract the complex refractive index of the layer, which is displayed in Figure 2.6b. The observed onset of an increasing absorption for a wavelength of 375 nm is in good agreement with the theoretical ZnO band gap of 3.3 eV. Note that these measurements were performed for ZnO deposited on a silicon substrate, while in the actual devices ZnO was coated onto ITO.

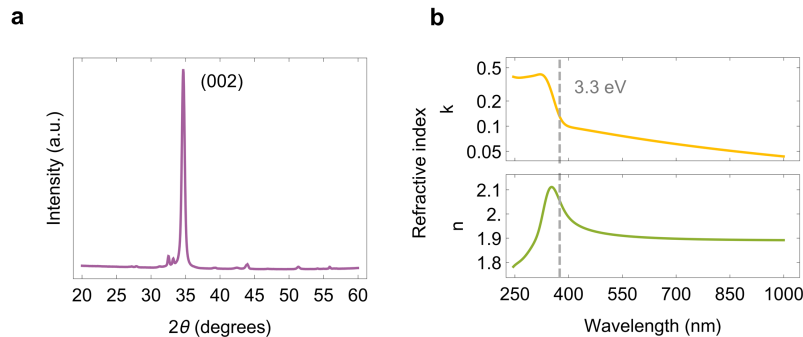


Figure 2.6: (a) 2-Theta XRD scan revealing the preferential c-axis orientation of the deposited ZnO layer. (b) Complex refractive index (n,k) from ellipsometry measurements with the dashed line indicating the ZnO band gap at 3.3 eV.

After patterning of the ZnO layer using optical contact lithography (TI-35E, Microchemicals) and an inductively coupled plasma (ICP) dry-etch in CH_4 and H_2 chemistry, we spin-coated a layer of CdSe/CdS QDs comprising 2-3 monolayers. Subsequently, small molecule organic layers for hole injection were deposited by thermal evaporation in a dedicated depo-

sition chamber (Trovato) connected to a glovebox.⁴ The layers, consisting of 65 nm NPB and 15 nm HAT-CN (sublimed grade, Lumtec), were capped by a 100 nm aluminum p-contact metal, evaporated with a separate shadow mask. To avoid degradation of the organic layers, due to oxygen and moisture outside of the glovebox environment, we further encapsulated the samples with a glass cover plate and an UV-curable glue incorporating additional getter material.

Figure 2.7 shows bright and uniform emission from a QD-LED device for a bias voltage of 7 V, observed under ambient lighting. The emissive area had a size of approximately 2 mm \times 3 mm and the sample was mounted on a microscopy glass slide to ease the handling. Figure 2.5a shows the corresponding emission spectrum recorded with an Ocean Optics spectrometer. For a bias voltage of 8 V, there is a main peak for an energy 1.95 eV, which originates from the electroluminescence of the CdSe/CdS QDs. The additional emission peaks at 2.97 eV and 2.85 eV, amounting to approximately 5% of the QD emission intensity, we assign to emission from the organic charge transport layers. For a bias of 2.8 V on the other hand, no emission from the organic layers can be observed, as can be expected, considering respective emission energies determined by the separation of HOMO and LUMO levels in NPB and HAT-CN (see Figure 2.5b).

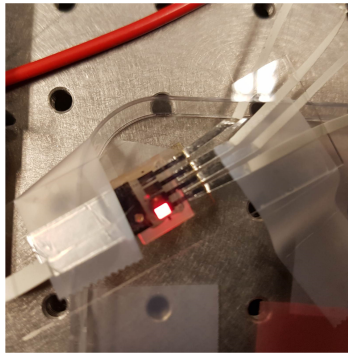


Figure 2.7: Bright and uniform emission from a QD-LED device for a bias of 7 V observed under ambient light. The emissive area has a size of approximately 2 mm \times 3 mm and the sample was mounted on a microscopy glass slide to ease the handling.

The turn-on behavior of the QD-LED is reported in Figure 2.8. Com-

⁴Organics and p-metal evaporation was performed by Dr. Michiel Callens, at the time associated with the Liquid Crystals and Photonics research group of Ghent University.

pared to the photoluminescence (PL) recorded using a 365 nm UV LED to pump the QDs, the EL emission spectrum for a bias of 2.8 V is slightly red-shifted and broadened. We used Gaussian fits (see Figure 2.8a) to determine a central wavelength λ_c of 631 nm (634 nm) and a corresponding FWHM of 41 nm (44 nm). The recorded normalized intensity, integrated over the whole emission spectrum, in Figure 2.8c shows an optical turn-on for a voltage of 2.1 V. Unfortunately, the electrical turn-on behavior in Figure 2.8b was obscured by a parasitic leakage due to issues with the patterning of the ZnO layer. We extracted a respective resistance of 4.1 k Ω from a linear fit of the current for bias voltages from 0-2 V.

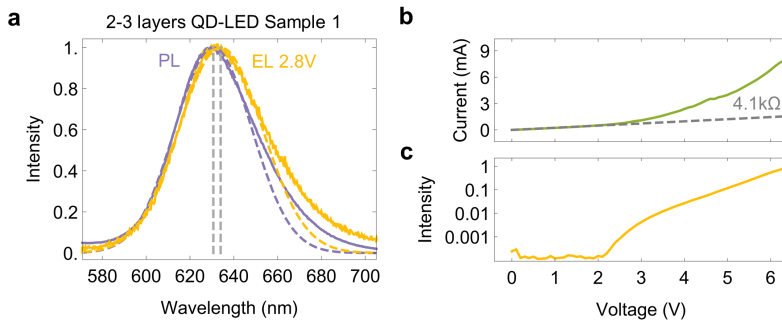


Figure 2.8: Turn-on behavior of the QD-LED. (a) Comparison of the photoluminescence (PL) emission spectrum and electroluminescence (EL) for a bias voltage of 2.8 V. Dashed lines indicate Gaussian fits and the extracted central wavelengths. (b) Electrical turn-on behavior, obscured by a leakage current due to issues with the processing of the electrodes. A resistance of 4.1 k Ω was extracted for the parasitic channel, through a linear fit of the current for a bias voltage up to 2 V. (c) Optical turn-on behavior of the QD-LED.

For a different QD-LED sample, we further investigated the spectral shift of the emission for increasing bias voltages. Figure 2.9a shows a shift and broadening of the EL spectrum, when increasing the bias voltage from 3 V to 7 V. The central wavelength λ_c shifts from 630 nm to 636 nm, with a corresponding increase of the FWHM from 38 nm to 47 nm. Figure 2.9b shows the equivalent peak energies as a function of the bias voltage, which can be translated into an applied electric field, assuming a uniform voltage drop across the 100 nm thin device. The respective values for the FWHM can be found in Figure 2.9c and we compared these values to the PL spectrum of a monolayer (ML) of the same CdSe/CdS QD sample deposited on a glass substrate.

We hypothesise, that the observed red-shift and spectral broadening of

the emission for increasing forward bias voltages is due to the quantum confined Stark effect (QCSE), as previously observed for colloidal CdSe based QDs. [33, 34] For a layer of randomly oriented CdSe/CdS QDs, this would imply a quadratic dependence of the peak energy on the applied electric field. Note that while in conventional optoelectronic devices an increasing forward bias would not be across the active layer, organic ligands covering the colloidal QDs present an additional barrier. This may justify the assumption of a uniform electric field, when forward biasing the QD-LEDs. The order of magnitude of the dependence extracted from a quadratic fit to the data in Figure 2.9b is in good agreement with values reported for individual QDs. [33]. However, the fit of the EL data fails to accurately predict the PL of a QD monolayer on a glass substrate. In addition, the extracted FWHM displayed in Figure 2.9c for a forward bias of 3V is less than for the PL of a monolayer on a glass substrate, which points to additional effects influencing the QD EL spectrum. It should be noted that issues with the Gaussian fit due to the pronounced red tail of the emission spectrum might be in part responsible for the observed effect. As suggested in reference [34], for a QD-LED structure similar to our devices, the electric field affecting the QDs might not be linear with the applied bias voltage, causing a further deviation from the quadratic behavior expected for a QCSE shift.

An alternative explanation for the red-shift could be an increase of the temperature in QD layer due to Joule heating and non-radiative recombination occurring in the active layer. This has been investigated for structurally similar organic light emitting diodes (OLEDs), for which temperatures of up to 60°C have been measured at the diode junction. [35] However, due to the large heat capacity of the whole sample this effect should be slow, on the order of one minute. [36] In contrast, the spectral shifts measured for our QD-LED samples were quasi-instantaneous, with the acquisition of the spectrum only taking a few seconds. Nevertheless, to provide conclusive evidence that heating effects on the emission of the QDs are negligible, [37] measurements of the PL emission spectrum under reverse bias of the QD-LED, as performed in reference [34] would have been helpful.

2.5 Nano-patterned QD-LED

Based on the results obtained for a large-area QD-LEDs presented above, we aimed to fabricate nano-patterned QD-LEDs. Simply applying the nano-patterning techniques presented in Section 2.3 would however result in a large leakage current. We therefore adapted the process, including a patterned dielectric layer.

Figure 2.10 outlines the main processing steps necessary to fabricate a

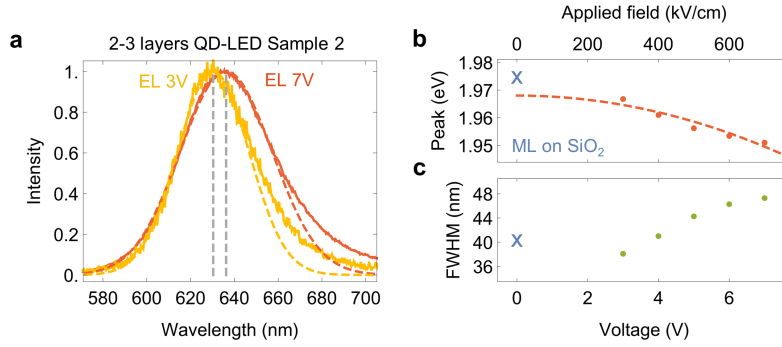


Figure 2.9: Shift of the QD-LED emission spectrum for larger bias voltages. (a) Comparison of the EL emission spectrum for a bias voltage of 3 V and 7 V. Dashed lines indicate Gaussian fits and the extracted central wavelengths. (b) Shift of the emission peak energy (quadratic fit represented by the dashed line) and (c) the full width at half-maximum (FWHM) extracted from Gaussian fits. Reference values in (b) and (c) were measured on a monolayer (ML) of the same QD sample deposited on SiO₂.

nano-patterned QD-LED. We again started from a glass substrate, coated with sputter deposited ITO and a ZnO ALD layer, on which we deposited an additional 5 nm Al₂O₃ layer, serving as a dielectric spacer. The Al₂O₃ was deposited by thermal (220°C) ALD according to a literature process, [38] employing trimethylaluminum and distilled water vapor as precursors. Details can be found in Appendix A.4. Using optical contact lithography and an ICP etch in CH₄ and H₂ chemistry, we then patterned the ITO and ALD layers to form large-area contacts. Subsequently, we spin-coated a 50 nm thin positive e-beam resist (ZEP520A, Zeon Chemicals) as well as a 50 nm conductive polymer (AR-PC 5091, Allresist). With an exposure dose of 120 $\mu\text{C}/\text{cm}^2$ in a 50 kV e-beam system (Raith Voyager) and 30 s development in n-amyl acetate we achieved a high-resolution pattern (Figure 2.10a). After a 5 s O₂ plasma exposure, we used dilute KOH (pH 12) heated to 50°C to selectively etch the dielectric Al₂O₃ layer (Figure 2.10b and Figure 2.11a). Employing Langmuir-Blodgett deposition, as introduced in Section 2.3, we coated the sample with a monolayer of CdSe/CdS QDs (Figure 2.10c). After lift-off in a 1:4 mixture of toluene and acetone, aided by ultrasonic agitation, we achieved a self-aligned pattern of QDs on ZnO, where the dielectric Al₂O₃ spacer was etched (Figure 2.10d and Figure 2.11b). Eventually, we finalized the samples with the evaporation of organic hole injection layers and an aluminum p-contact as described previously in Section 2.4. Figure 2.11 shows SEM micrographs of the sample after critical processing

steps.

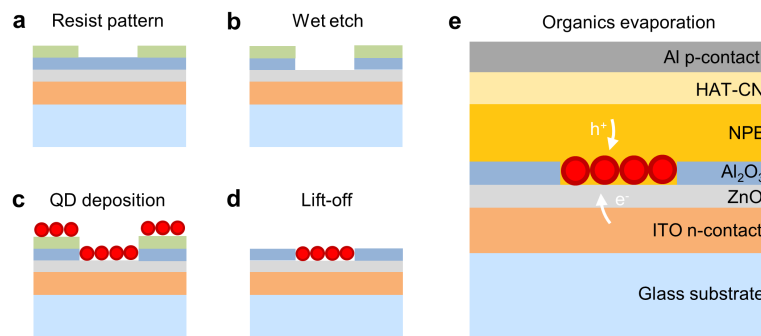


Figure 2.10: Main processing steps to fabricate nano-patterned QD-LEDs. (a) E-beam lithography with a thin positive resist on a glass sample coated with a sputtered ITO n-contact and an ALD layer of ZnO and Al_2O_3 . (b) Selective wet-etch of the dielectric Al_2O_3 layer. (c) Langmuir-Blodgett deposition of a monolayer of CdSe/CdS QDs. (d) Lift-off results in QDs selectively deposited in the etched areas. (e) Thermal evaporation of organic layers for hole transport (NPB) and hole generation (HAT-CN), as well as an aluminum p-contact.

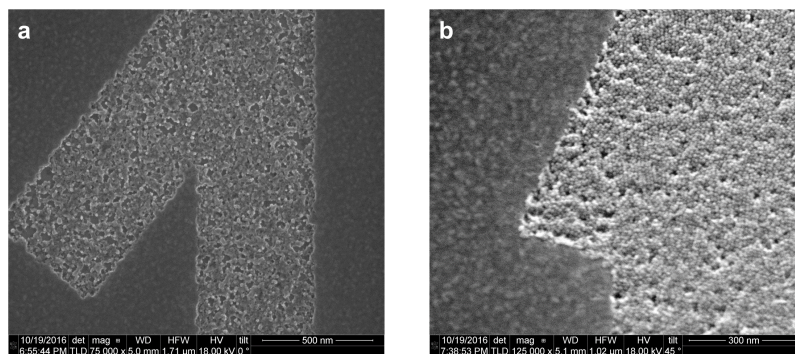


Figure 2.11: SEM micrographs of a dummy sample on a silicon substrate after different processing steps. (a) Top-view after the wet-etch of the dielectric Al_2O_3 ALD layer. (b) Angled view showing the self-aligned deposition of a CdSe/CdS QD monolayer in the etched area.

Figure 2.12a displays a schematic layout of the sample consisting of four separate devices, that can be electrically contacted with a common ITO n-

contact and individual aluminum p-contacts. As mentioned in Section 2.4, the active device area was encapsulated using a cover glass and UV-curable glue incorporating getter materials. To be able to image the nano-patterned QD-LED samples with a high-resolution oil immersion objective (see the schematic cross-section in Figure 2.12b), we had to match the thickness of the glass substrate to the short working distance of the objective. One possibility to achieve that, was to do the whole fabrication on $150\ \mu\text{m}$ thin glass substrates, which poses a challenge for the processing, since the samples are brittle and can break quite easily. Another option, which allowed to use thicker glass samples, pre-coated with ITO, was to thin down the samples only after completing the first processing steps, using chemical-mechanical polishing (CMP) to achieve a polished surface.

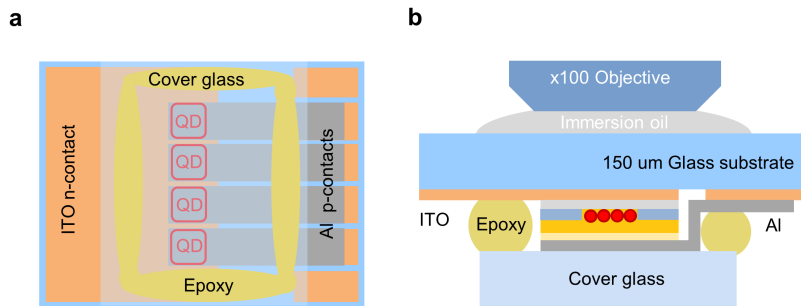


Figure 2.12: (a) Schematic layout of the nano-patterned QD-LED sample, showing a common ITO n-contact and four individual Al p-contacts for different areas containing patterned QDs. The active device area was encapsulated using a cover glass and UV-curable epoxy resin incorporating getter materials. (b) Schematic cross-section outlining the device characterization using a high-resolution oil immersion objective lens.

We then characterized the nano-patterned QD-LED sample, applying a voltage bias with a source measurement unit (Keithly 2450). Figure 2.13a shows the emission recorded for a bias voltage of 7 V and 10-fold magnification of an optical microscope (Olympus), revealing the electroluminescence of μm -size features. The spectrum in Figure 2.13b, recorded with an Ocean Optics spectrometer, reveals that for a bias voltage of 5 V, CdSe/CdS QDs (1.93 eV) are the sole sources of emission. However, for a bias voltage of 7 V, additional emission peaks at 2.82 eV and 2.97 eV appear, which we assign to the organic charge transport layers. The emission of the organic layers amounts to approximately 10% of the recorded intensity, which is

double than what we reported for conventional QD-LEDs in Section 2.4. This observation could be linked to the different active layer thickness. The nano-patterned QD-LEDs only comprise a QD monolayer, whereas there are 2-3 layers in the devices presented previously.

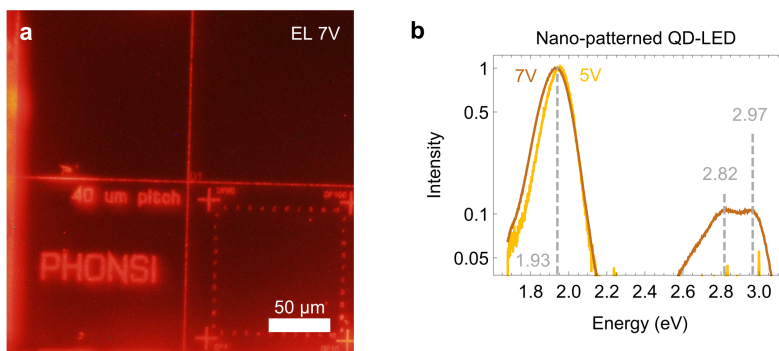


Figure 2.13: Emission from a nano-patterned QD-LED. (a) Large-area emission observed with an optical microscope with low magnification and a large working distance for a bias voltage of 7 V. (b) Emission energies plotted on a logarithmic scale for different forward bias voltages.

The electro-optic characterization of the nano-patterned QD-LED revealed an optical turn-on for a voltage bias around 3.5 V (Figure 2.14b). The electrical turn-on (Figure 2.14c) was again obscured by a leakage current. Fitting the measured current for voltages from 0-2 V, we extracted a resistance of 330 Ω . Similar to the leakage current reported in Section 2.4, we attribute this to issues with patterning of the electrodes. But also an incomplete QD layer, due to problems with the Langmuir-Blodgett deposition, can cause additional leakage channels. In addition, also the nano-patterned QD-LEDs display a distinct red-shift and broadening of the emission spectrum for increasing forward bias, as shown in Figure 2.14a. From Gaussian fits of the EL spectrum for a 5 V (7 V) bias we extracted a central wavelength of 636 nm (642 nm) and a FWHM of 46 nm (54 nm).

With a high-resolution microscope (Nikon Ti Eclipse) we investigated the EL emission of the nano-patterned QD-LEDs in more detail. Using a first objective with a 50-fold magnification and biasing the sample at 5 V, to avoid emission from the organic layers, we obtained the micrographs shown in Figure 2.15. The patterned structures providing orientation on the sample can clearly be distinguished from the dark areas, comprising the dielectric Al_2O_3 spacer. Yet, the emission from the nano-patterned structures was

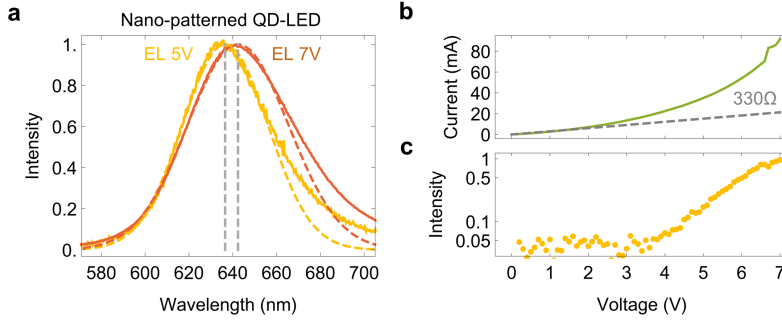


Figure 2.14: Turn-on behavior of the nano-patterned QD-LED. (a) Comparison of the emission spectrum for a bias voltages of 5 V and 7V. Dashed lines indicate Gaussian fits and the extracted central wavelengths. (b) Electrical turn-on behavior, obscured by a leakage current. A resistance of $330\ \Omega$ was extracted for the parasitic channel, through a linear fit of the current for a bias voltage up to 2 V. (c) Optical turn-on behavior of the QD-LED.

not uniform and multiple brightly and dark spots can be distinguished. The bright spots were fluctuating in time, as can be seen from the micrographs in Figure 2.15a and b, which were taken a few seconds apart under the same conditions. Comparing the indicated spot, a clear on/off blinking behavior can be observed. It is however unclear, how many CdSe/CdS QDs are involved in this blinking behavior. Since a pronounced fluorescence intermittency is an effect commonly observed in single-dot spectroscopy, [39] one might suspect that the EL blinking in our nano-patterned QD-LEDs would also point to emission from individual emitters. However, the patterned orientation marks are relatively large, comprising thousands of QDs (see Figure 2.11a), suggesting that the blinking might originate from charging and de-charging of an ensemble of QDs instead.

Increasing the integration time and enhancing the contrast and brightness, we recorded the images of PL and EL emission in Figure 2.16, for the same sector of the sample. For the photoluminescence image in Figure 2.16a, next to the orientation pattern, emission from randomly positioned re-deposited CdSe/CdS QDs can be seen in the center of the square. For the EL emission in Figure 2.16b on the other hand, a well-defined array of emission spots appeared, with a spacing of $5\ \mu\text{m}$ defined by lithography. From SEM images of nano-patterned dummy samples we could estimate that some of the spots might originate from individual CdSe/CdS QDs. Counting QDs on the actual nano-patterned QD-LED sample was unfortu-

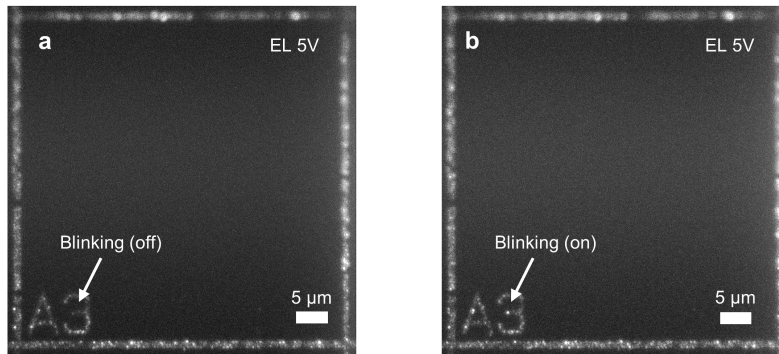


Figure 2.15: EL blinking observed with a high-resolution (x50) objective. (a) Emission for a bias voltage of 5 V showing part of the nano-patterned QD-LED in a low-emission (off) state. (b) Same part of the device a few seconds later in a high-emission (on) state.

nately not possible, due to pronounced charging hindering the acquisition of high-resolution SEM images.

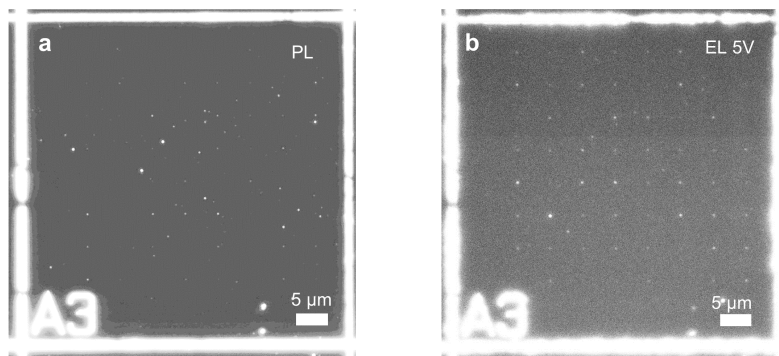


Figure 2.16: Comparison of the PL and EL emission of a nano-patterned QD-LED, observed with a high-resolution (x50) objective. (a) Photoluminescence of patterned CdSe/CdS QDs used for orientation as well as emission from re-deposited emitters in the center of the square. (b) Electroluminescence for a 5 V bias from the same device area, revealing emitters patterned on a 5 μm grid.

To investigate, whether the nano-patterned QD-LED structure shown in Figure 2.16b actually comprises individual single-photon emitters, we con-

ducted further experiments,⁵ recording the second-order auto-correlation function $g^2(t)$ as explained in Section 2.2. Unfortunately, it turned out that there was too much background from the orientation markers of the QD-LED sample, making it impossible to obtain anti-bunching for the QD electroluminescence. For any future samples it would be highly beneficial to either increase the distance between the markers and the individual QDs, or to implement separate contacts. That way, the emission from the markers could be switched off, while recording the autocorrelation function for an individual emitter. Adding a spatial filter in the form of a pin-hole to the home-built microscope set-up helped to limit the background, but also then we did not observe a dip in the second-order autocorrelation function. We further tried to look for individual QD emitters using optical excitation with a 400 nm pulsed laser, which was also unsuccessful. Comparing the recorded trace in Figure 2.17a to the PL anti-bunching of an individual CdSe/CdS QD on a SiO₂ substrate (Figure 2.17b), a strikingly different photoluminescence lifetime becomes apparent. Fitting the peak with a single exponential according to Equation 2.4, a PL lifetime of $\tau = 2$ ns can be extracted for the emitters in a nano-patterned QD-LED. For the individual CdSe/CdS QDs on a glass substrate the extracted lifetime was 17 ns instead. One possible explanation for the discrepancy could be a largely different excitation power, causing the formation of bi-excitons for the case of the nano-patterned QD-LED. Since varying the power of the excitation laser did not change the observed behavior, this seems unlikely. We therefore suspected, that an additional non-radiative decay channel reduces the PL lifetime and quantum yield for the QDs in the nano-patterned LED.

To gain more insight into the device physics, without relying on the rather intricate nano-patterning process, we then compared the PL lifetime for a monolayer and a multilayer QD-LED. To record the PL decay, we used a 400 nm pulsed excitation laser, a single-photon resolving APD detector and time-correlated single-photon counting (TCSPC) electronics. Figure 2.18 displays the normalized data after background subtraction, comparing different QD-LED devices without any applied voltage bias. To fit the data we used a stretched exponential

$$c(t) = a e^{-\left(\frac{t}{\tau_K}\right)^\beta}. \quad (2.5)$$

This accounts for a distribution of decay times for $\beta < 1$ and turns into a single-exponential decay for $\beta = 1$. We then extracted the mean lifetime $\bar{\tau}$

⁵The Hanbury-Brown-Twiss experiments on the nano-patterned QD-LEDs were performed in the course of a secondment at the IBM research center in Rueschlikon, Switzerland, together with Dr. Michael Becker and under the supervision of Dr. Thilo Stoeferle and Dr. Rainer Mahrt.

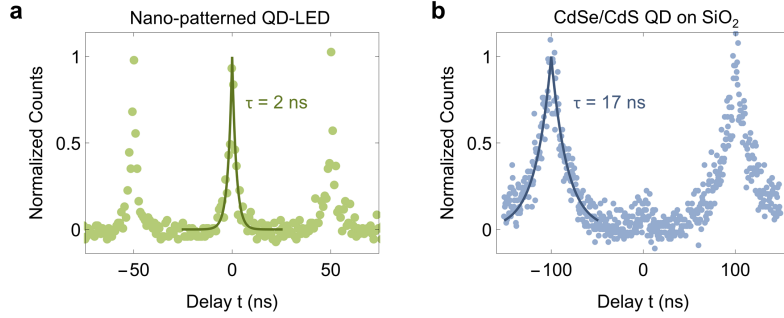


Figure 2.17: Comparison of the of the PL second-order auto-correlation function under pulsed excitation for (a) CdSe/CdS QD emission from the nano-patterned QD-LED and (b) an individual CdSe/CdS QD on a SiO₂ substrate. The lifetimes were extracted by a single-exponential fit of the respective peaks.

from the fitted parameters according to

$$\bar{\tau} = \frac{\tau_K}{\beta} \Gamma\left(\frac{1}{\beta}\right), \quad (2.6)$$

using the gamma function Γ . Already from the PL decay curves in Figure 2.18 it is obvious that the monolayer and the multilayer QD-LED show a strikingly different behavior.

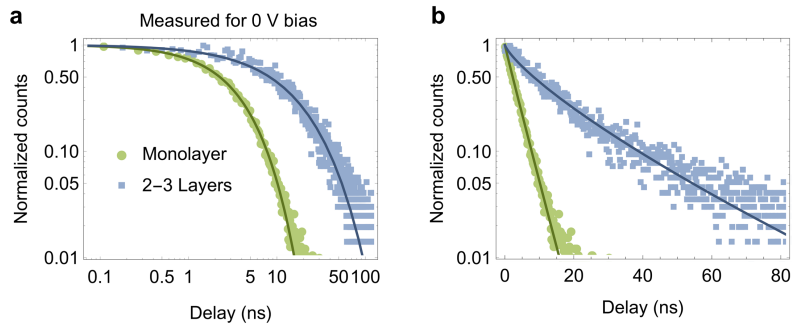


Figure 2.18: Photoluminescence decay measured for two different unbiased QD-LEDs, plotted on a (a) double-logarithmic and (b) the commonly used semi-logarithmic scale. The QD-LED comprising 2-3 layers of CdSe/CdS QDs clearly exhibits a slower PL decay than the monolayer QD-LED.

In Figure 2.19 we compared the parameters extracted from the fit for

the different devices under different biasing conditions. Note that the electroluminescence observed for a forward bias above the turn-on around 2 V only adds to the background of the measurement, which was subtracted from the data prior to the fit. For the monolayer QD-LED, the extracted mean lifetime (Figure 2.19a) was around 3 ns and largely independent of the bias voltage. For the QD-LED comprising 2-3 layers of CdSe/CdS QDs (Figure 2.19b) on the other hand, the extracted lifetime was longest (15 ns) for the case of a 0 V bias. With increasing forward bias, the extracted mean PL lifetime continuously dropped, with a minimum value of 10 ns for a forward bias of 7 V. Under reverse bias, a clear trend is less evident. There is an initial drop for a voltage of -1 V and a subsequent recovery of the mean lifetime to a value of 14 ns, for a maximum reverse bias voltage of -8 V. We suspect that this is an artefact induced by first measuring the device with a forward bias. Assuming that the QD-LED takes some time to recover its initial state, measuring with a bias of -1 V right after the 7 V bias can explain the observed behavior. Concurrently, the stretching exponent β decreases from a value 0.78 to 0.64 for the multilayer QD-LED, when changing the bias from 0 V to 7 V, indicating a broader distribution of lifetimes (Figure 2.19c). For the case of the monolayer QD-LED in contrast, the stretching exponent is close to one, regardless of the biasing conditions (Figure 2.19d).

From these results we deduct that the CdSe/CdS QDs comprising the first monolayer are in a different emissive state, characterized by a single-exponential decay with a lifetime of ~ 3 ns. This is in good agreement with the 2 ns lifetime extracted for the nano-patterned QD-LED in Figure 2.17a. It further appears that the biasing condition of the QD-LED only has a minor influence on the QDs in the first monolayer. The PL decay extracted for a multilayer QD-LED is multi-exponential, pointing to the presence of at least a second fraction of emitters with a longer PL lifetime. The fact that for increasing forward bias the extracted average lifetime is reduced, indicates that more QDs transition to the state with a short lifetime. Hence, we reason that the first monolayer of CdSe/CdS QDs is negatively charged. The extracted lifetime of 3 ns is in agreement with previous studies of the negative trion T^- emission for colloidal CdSe/CdS QDs using electrochemical charging. [40] In literature, there are reports for inverted QD-LEDs using ZnO nanocrystals as electron injection layer, which also assign the PL lifetime reduction for a thin CdSe/CdS QD layer (1-2 monolayers) to negative trions. [41] In other reports, the authors reason that positive trions are involved instead. [27] While the lifetime of positive trions can be similar, as observed in single-particle studies, [42] we argue that the lifetime reduction for a large forward bias in Figure 2.19d clearly points to negative trions for

the case of our nano-patterned QD-LEDs.

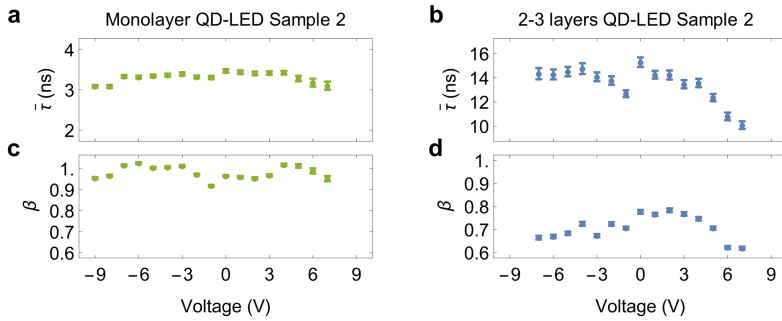


Figure 2.19: Parameters extracted from a stretched exponential fit of the PL decay for two different QD-LED samples, depending on the applied bias voltage. Mean lifetime (a) for the monolayer QD-LED and (b) the sample comprising 2-3 layers of QDs. Stretching exponent β for (a) monolayer and (b) multilayer QD-LED.

The emission from negative trions should still exhibit anti-bunching of the second-order autocorrelation function, characteristic for single-photon emission. However, since the PL quantum yield is significantly reduced, due to fast non-radiative Auger recombination, the measurement becomes more difficult and we reason that the results presented in Figure 2.17a were recorded for an ensemble of weakly emitting charged CdSe/CdS QDs. In light of the observation that emission of the nano-patterned QD-LED is mostly from the negative trion state, also the EL blinking in Figure 2.15 can be explained. We conjecture that the appearance of a bright emissive spot arises from the de-charging of one or more CdSe/CdS QDs in the device, resulting in bright neutral exciton emission lasting for a few seconds.

In literature, multiple approaches have been discussed to mitigate the effect of QD charging on the emission quantum yield of QD-LEDs. [41, 43–46] In Section 2.8 we compare several possibilities that would be compatible with the nano-patterning process we developed. Unfortunately, we were not able to implement any of these methods due to prolonged issues with the deposition of the organic layers and the subsequent abandonment of the project.

2.6 Properties of QD monolayers

In the following study of QD monolayers, we explored the possibility of limiting QD charging using an additional ZnS shell. We therefore coated two

different QD samples (CdSe/CdS and CdSe/CdS/ZnS) on SiO₂ and also on a substrate coated with a ZnO ALD layer, recording the photoluminescence spectra and lifetimes, as shown in Figure 2.20 and Figure 2.21. Since the set-up used for the experiments was not designed to handle thin-film samples, it was not possible to reliably compare intensity values between different samples, hence we only study the normalized data hereinafter.

Figure 2.20 compares the wavelength-resolved PL decay of the CdSe/CdS QD sample used for the nano-patterned QD-LED presented above. There is a clear difference between the traces recorded for a monolayer deposited on bare SiO₂ in Figure 2.20a and b and for a substrate comprising a 20 nm ZnO layer in Figure 2.20c and d, suggesting that the QDs already get at least partially charged when deposited on ZnO. Same as before, we used a stretched exponential fit (Equation 2.5) to extract a mean lifetime $\bar{\tau}$ and the stretching exponent β . The instrument response function (IRF) was measured by reflecting the 400 nm pulsed excitation laser directly to the detector.

The extracted wavelength-resolved PL lifetimes and respective PL spectra in Figure 2.21 are consistent with negative trion emission from QD monolayers coated on top of an ALD ZnO layer. Figure 2.21a shows a 4 nm blue-shift of the emission spectrum, when coating CdSe/CdS QDs on ZnO. This blue-shift is expected for trion emission and originates from Coulomb repulsion for multicarrier states, which raises the energy compared to the approximation of non-interacting carriers. [47] For CdSe/CdS/ZnS QDs in Figure 2.21b the blue-shift is reduced to 2 nm, indicating a reduced charging with the additional ZnS shell. Figure 2.21c and d show the wavelength-resolved mean lifetimes, for clarity we additionally report the values for the central emission wavelength in Table 2.2. The data clearly shows that PL lifetime reduction is less severe for CdSe/CdS/ZnS on a ZnO substrate. Yet, the effect is still present, indicating that the ~ 1 nm thin ZnS shell cannot fully prevent tunneling of electrons from the ZnO layer into the QDs. The stretching exponent in Figure 2.21e and f further shows that, in contrast to the monolayer QD-LED reported above, for QD monolayers on a 20 nm ZnO layer the charging is incomplete. In particular, we observe a mean lifetime of 7 ns and $\beta \sim 0.5$ for the CdSe/CdS QDs on ZnO, while for the monolayer QD-LED the decay is single-exponential with $\tau \sim 3$ ns (Figure 2.19). Hence, the improvement for CdSe/CdS/ZnS QDs observed here, might be reduced when the QDs are incorporated in the full QD-LED stack.

Furthermore, the wavelength-resolved data in Figure 2.21 shows signatures of energy transfer within the QD monolayer. [48] For the CdSe/CdS/ZnS QDs on SiO₂ it is apparent that only for the red tail of the emission

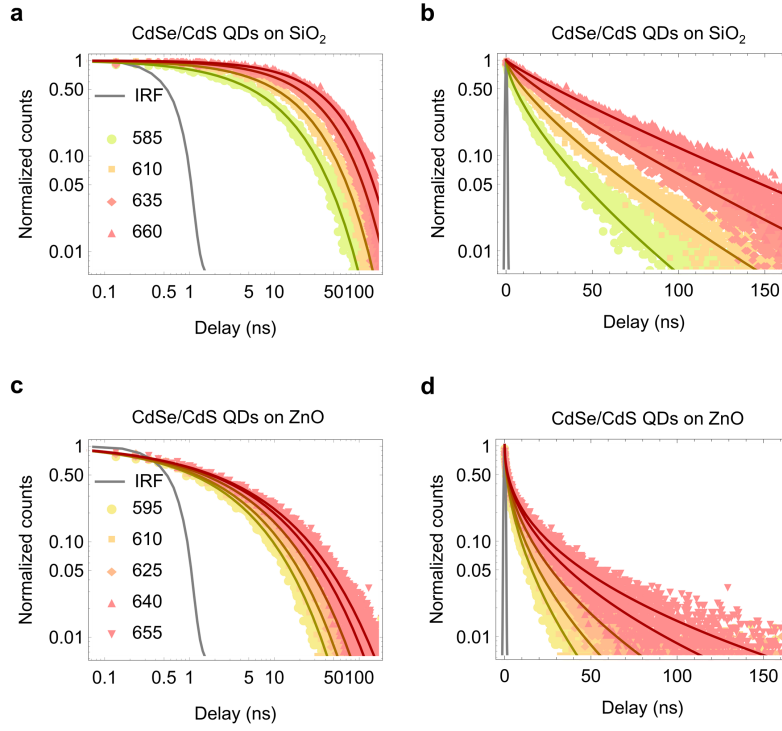


Figure 2.20: Wavelength-dependent PL decay of a CdSe/CdS QD monolayer on different surfaces. (a) Double-logarithmic and (b) semi-logarithmic plot for a SiO₂ substrate. (c) Double-logarithmic and (d) semi-logarithmic plot for the same QD sample on top of a thin layer of ALD ZnO. The data was fitted with stretched exponentials.

QD sample	Substrate	λ_c (nm)	β_{λ_c}	$\bar{\tau}_{\lambda_c}$ (ns)
CdSe/CdS	SiO ₂	628	0.82	30
	ZnO	624	0.49	7
CdSe/CdS/ZnS	SiO ₂	615	0.79	25
	ZnO	613	0.75	15

Table 2.2: Comparison of the extracted central wavelengths λ_c , stretching exponents β and mean PL lifetimes $\bar{\tau}$ for QD monolayers on different substrates.

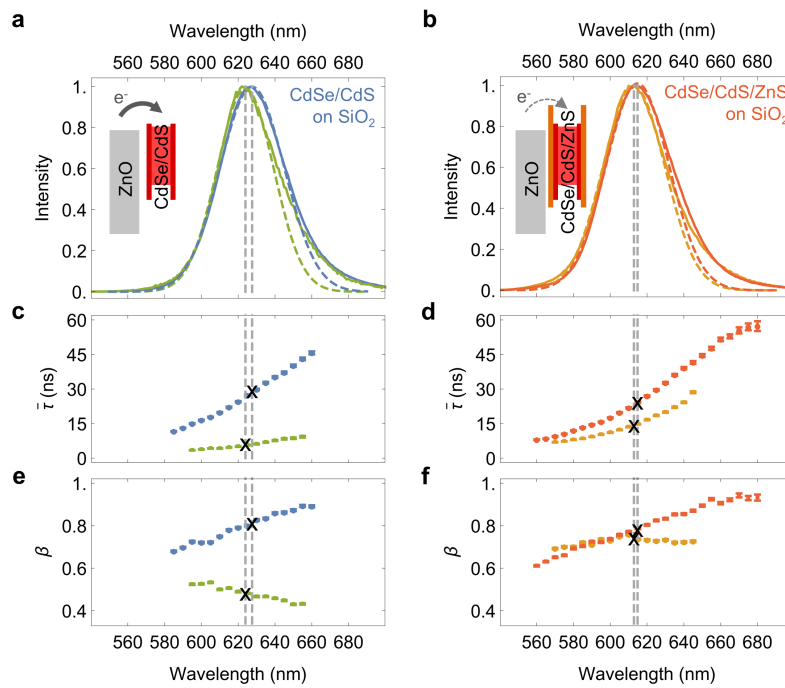


Figure 2.21: Spectroscopic analysis of the effect of QD shelling. (a) PL spectra of a dense CdSe/CdS QD monolayer on SiO₂ and on ZnO. The dashed lines represent a Gaussian fit and the extracted central wavelength. (b) Respective spectra for a CdSe/CdS/ZnS QD monolayer. (c) Mean lifetime extracted from a stretched exponential fit for the CdSe/CdS and (d) CdSe/CdS/ZnS QD sample. (e) Corresponding stretching exponent for the CdSe/CdS and (f) CdSe/CdS/ZnS QD sample.

around 680 nm, the PL decay is approximately single-exponential with a lifetime around 60 ns. This can be explained by the fact that for the largest QDs there are no lower-energy QDs available for Förster resonant energy transfer (FRET). For the smaller dots in the sample on the other hand, energy transfer to larger QDs is an additional loss channel, which lowers the observed PL lifetime. For larger dots, this energy transfer in return increases the PL lifetime. Additionally, the size-dispersion of these CdSe/CdS QDs, in particular shell thickness variations, can cause the same trend in the PL lifetime. [49] Due to the quasi type II band alignment of CdSe core and CdS shell, the hole is localized in the core, whereas the electron wavefunction spreads into the shell. Consequently, for a thicker shell the electron-hole wavefunction overlap is reduced, in turn reducing the radiative lifetime. While the wavelength-dependence of the stretching exponent $\beta < 1$ points to a pronounced influence of energy transfer, an additional study of the QD sample in solution would have been helpful to clearly separate these effects.

A similar PL lifetime reduction was observed, when a QD monolayer was coated with a layer of silicon nitride by plasma-enhanced chemical vapor deposition (PECVD), a technique which is commonly employed to integrate QDs in photonic devices. [50, 51] Figure 2.22a shows there is a red-shift of the emission spectrum, due to the SiN deposition. The SiN layer used for this study was only ~ 30 nm thin, ruling out any dielectric effects on the QD emission. We therefore interpreted the change in the emission spectrum as a consequence of smaller QDs being more likely damaged by the plasma exposure. [52] The corresponding decrease of the mean lifetime and stretching exponent displayed in Figure 2.22b and c respectively, can be explained assuming energy transfer in the QD monolayer. [48] The PECVD of SiN leads to an increased fraction of non-emissive dark QDs in the sample, hence energy transfer from bright to dark QDs introduces an additional non-radiative decay channel, which can be observed as a decrease of the mean PL lifetime.

2.7 Nano-patterned structures with directional PL

As an alternative application for the nano-patterning technique presented before, we further investigated the possibility of modifying the emission directionality of a QD-LED by patterning the QDs to form a bulls-eye grating. [53] Unfortunately, at the time, the organics deposition necessary to fabricate QD-LEDs, was not available. Therefore, we investigated the photoluminescence of devices instead, making use of an evaporated layer of Al_2O_3 (Leybold 560) to mimic the refractive index of the organic layers.

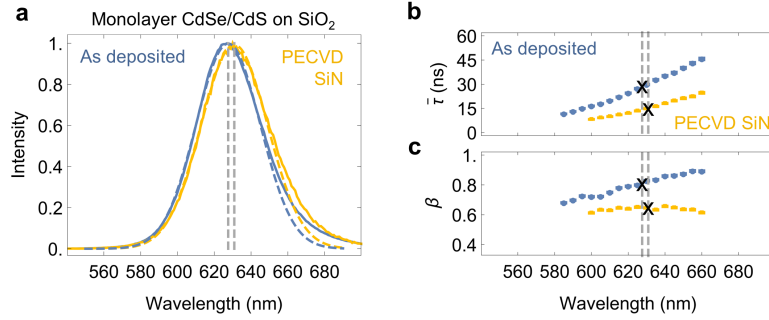


Figure 2.22: Influence of PECVD on a QD monolayer. (a) PL emission spectrum of a CdSe/CdS QD monolayer on a SiO₂ substrate, before and after the deposition of a 30 nm thin layer of PECVD SiN. (b) Wavelength-dependent mean lifetime of the CdSe/CdS QDs extracted from a stretched exponential fit of the PL decay and (c) corresponding stretching exponent.

Figure 2.23a shows a sketch of the fabricated structure. The emission angle θ is determined by the Bragg condition

$$\sin \theta = n_{eff} - \frac{m \lambda}{\Lambda}, \quad (2.7)$$

where Λ is the period of the patterned grating, λ is the emission wavelength of the CdSe/CdS QDs, m is the scattering order and n_{eff} is the effective index of the lateral waveguide mode. We further optimized the Al₂O₃ layer thickness t for maximum out-coupling efficiency using FDTD simulations (Lumerical).

To fabricate the grating structures we modified the self-aligned electron-beam lithography process presented in Section 2.5. Starting from a glass substrate coated with 20 nm ALD ZnO and 20 nm PECVD SiO₂, we used one lithography step, combining reactive ion etching (RIE) of the SiO₂ layer and a subsequent lift-off of spin-coated CdSe/CdS QDs (see Section 2.3). Figure 2.23b shows a FIB/SEM cross-section of the nano-patterned QD structure on a dummy sample, Figure 2.24a an angled top-view of a bullseye grating. The QDs were subsequently covered with a 100 nm Al₂O₃ layer and an aluminium mirror. For mass-production, more scalable nano-imprint lithography could be applied instead of the electron-beam lithography step. [53]

Since we fabricated the device with an Al₂O₃ layer instead of the organics necessary to obtain EL emission, we investigated the directionality of the PL emission only. Therefore, we excited the QDs with a UV-LED

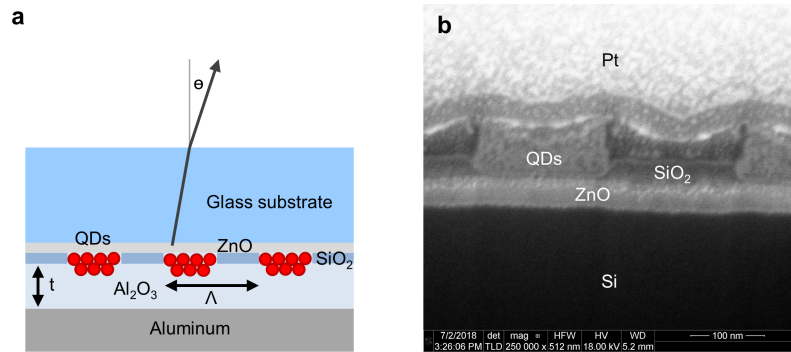


Figure 2.23: (a) Sketch of the device stack, resembling a QD-LED, but with an Al_2O_3 dielectric instead of the organic layers. (b) SEM micrograph of a FIB cross-section through a dummy sample revealing the nano-patterned QD layer on top of ZnO. The image in (b) is turned upside down with respect to the sketch in (a).

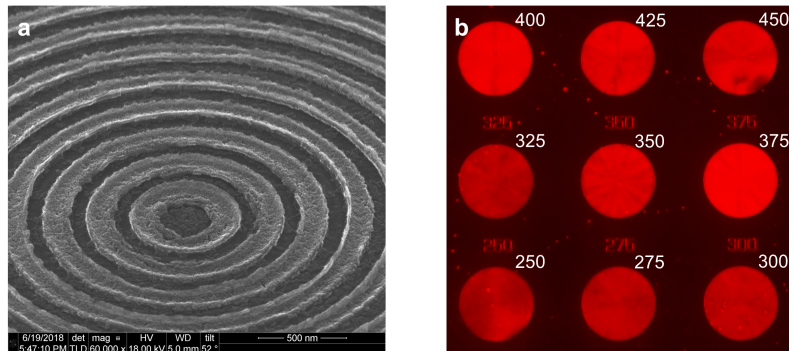


Figure 2.24: (a) Angled SEM top-view of CdSe/CdS QDs patterned in the form of a bulls eye grating. (b) The red color channel in the image plane visualized with a x10 objective shows an increased brightness of the structures with a grating period of 375 nm and 400 nm.

emitting around 405 nm. After passing a 500 nm short pass filter we used an objective with x50 magnification and a numerical aperture of 0.8 for excitation and collection of the QD emission. A 600 nm long pass filter was inserted to block the reflected excitation light before imaging the Fourier plane on a Thorlabs camera. Comparing the brightness of the emission for different grating periods in the image plane in Figure 2.24b suggests that a grating period between 375 nm and 400 nm should be ideal. Also, the corresponding unprocessed Fourier plane images in Figure 2.25a show an increased intensity for emission angles near $\theta = 0^\circ$.

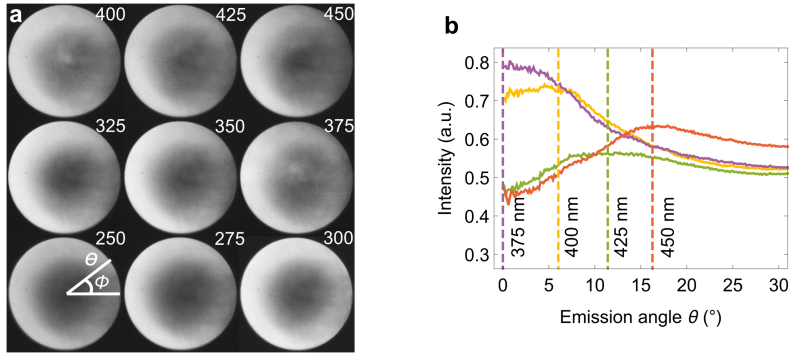


Figure 2.25: (a) Unprocessed Fourier plane images from a x50 0.8 NA objective for different grating periods (b) Angular dependence of the far field intensity $I(\theta)$ after correction for the transmission function of the microscope system and integration over $d\phi$.

After correcting for the microscope transmission function, using the Fourier plane image collected from a part of the sample where there was only the aluminium mirror and no QDs, the picture becomes even clearer. Figure 2.25b shows the angular dependence of the far field intensity $I(\theta)$ after integration over $d\phi$. Here, a period of 375 nm gave the highest intensity near $\theta = 0^\circ$. Also the emission directionality for the other grating periods is in good agreement with the predicted values from the Bragg condition (Equation 2.7), assuming an effective index of $n_{eff} = 1.68$ for the central emission wavelength $\lambda = 630$ nm of the CdSe/CdS QDs.

2.8 Conclusion and outlook

In summary, we fabricated and characterized nano-patterned QD-LEDs, which can be scaled down to single emitters for quantum-optics applications.

Alternatively, we showed that the technique can also be used to modify the emission directionality of QD-LEDs. While similar CdSe/CdS QDs have been shown to exhibit pure single-photon emission under electrical excitation, [12] we identified QD charging as a main hindrance to observe anti-bunching from our devices.

In literature, several possibilities have been discussed to overcome the detrimental effect of QD charging on the EL efficiency. For instance, it has been shown that smoothing the confinement potential in core-shell QDs by means of an alloyed shell can significantly slow down non-radiative Auger recombination. [54, 55] In reference [41], the authors show how this can be used to increase the EL quantum yield. However, reducing the Auger rate also increases the bi-exciton quantum yield, which in turn will reduce the purity of the single-photon emission. Therefore, alternative techniques, aimed to preserve the neutral charge state of the emitters in the QD-LED device are more suitable.

One possibility to balance the injection of positive and negative charges into the QD layer is to introduce a nanometer-thin insulating layer between the QDs and the ZnO electron-injection layer [12, 43]. This tunneling barrier slows down the efficient electron injection from ZnO, to a level which can be matched by the organic hole injection layers. Alternatively, modifying the conductivity and band alignment of the ZnO layer and introducing different QD shells can help to balance the charge-injection. [41, 44–46] These techniques have also enabled high-efficiency InP based QD-LEDs, [56] presenting a heavy metal free alternative to the CdSe based QDs used here.

In Section 2.6 we discussed the introduction of CdSe/CdS/ZnS QDs as a possible remedy to benefit future devices. Following up on the work presented in this chapter, it might be worthwhile to explore Purcell enhancement using plasmonic antennas as demonstrated in Chapter 4, in conjunction with electrical excitation. Reducing the relatively long radiative lifetime τ of colloidal quantum dots, could significantly increase the attainable single-photon rate.

References

- [1] L. Elsinger, M. Callens, J. Kuhs, V. Chandrasekaran, E. Drijvers, K. Neyts, C. Detavernier, E. Brainis, W. Xie, Z. Hens, et al. *Progress towards an electrically driven single photon source with colloidal quantum dots*. In 4th international workshop on Engineering of Quantum Emitter properties, Ireland, page 26, 2016.
- [2] L. Elsinger, T. Vandekerckhove, N. K. Zawacka, N. Le Thomas, Z. Hens, and D. Van Thourhout. *Nano-patterned quantum dot-LED structures with enhanced photoluminescence emission directionality*. In 23rd Annual symposium of the IEEE Photonics Benelux Chapter, 2018.
- [3] I. Aharonovich, D. Englund, and M. Toth. *Solid-state single-photon emitters*. Nature Photonics, 10(10):631–641, 2016.
- [4] D. C. Burnham and D. L. Weinberg. *Observation of Simultaneity in Parametric Production of Optical Photon Pairs*. Phys. Rev. Lett., 25(2):84–87, jul 1970.
- [5] P. Senellart, G. Solomon, and A. White. *High-performance semiconductor quantum-dot single-photon sources*. Nature Nanotechnology, 12(11):1026–1039, nov 2017.
- [6] I. Schwartz, D. Cogan, E. R. Schmidgall, Y. Don, L. Gantz, O. Kenneth, N. H. Lindner, and D. Gershoni. *Deterministic generation of a cluster state of entangled photons*. Science, 354(6311):434–437, oct 2016.
- [7] J. C. Loredo, M. A. Broome, P. Hilaire, O. Gazzano, I. Sagnes, A. Lemaitre, M. P. Almeida, P. Senellart, and A. G. White. *Boson Sampling with Single-Photon Fock States from a Bright Solid-State Source*. Phys. Rev. Lett., 118(13):130503, mar 2017.
- [8] M. Reindl, D. Huber, C. Schimpf, S. F. C. da Silva, M. B. Rota, H. Huang, V. Zwiller, K. D. Jöns, A. Rastelli, and R. Trotta. *All-photonic quantum teleportation using on-demand solid-state quantum emitters*. Sci. Adv., 4(12):eaau1255, dec 2018.
- [9] V. Chandrasekaran, M. D. Tessier, D. Dupont, P. Geiregat, Z. Hens, and E. Brainis. *Nearly Blinking-Free, High-Purity Single-Photon Emission by Colloidal InP/ZnSe Quantum Dots*. Nano Lett., 17(10):6104–6109, 2017.

- [10] Y.-S. Park, J. Lim, and V. I. Klimov. *Asymmetrically strained quantum dots with non-fluctuating single-dot emission spectra and subthermal room-temperature linewidths*. *Nature Materials*, 18(3):249–255, mar 2019.
- [11] W. Xie, R. Gomes, T. Aubert, S. Bisschop, Y. Zhu, Z. Hens, E. Brainis, and D. Van Thourhout. *Nanoscale and Single-Dot Patterning of Colloidal Quantum Dots*. *Nano Letters*, 15(11):7481–7487, nov 2015.
- [12] X. Lin, X. Dai, C. Pu, Y. Deng, Y. Niu, L. Tong, W. Fang, Y. Jin, and X. Peng. *Electrically-driven single-photon sources based on colloidal quantum dots with near-optimal antibunching at room temperature*. *Nature Communications*, 8(1):1132, 2017.
- [13] N. Mizuochi, T. Makino, H. Kato, D. Takeuchi, M. Ogura, H. Okushi, M. Nothhaft, P. Neumann, A. Gali, F. Jelezko, J. Wrachtrup, and S. Yamasaki. *Electrically driven single-photon source at room temperature in diamond*. *Nature Photonics*, 6(5):299–303, 2012.
- [14] A. Lohrmann, N. Iwamoto, Z. Bodrog, S. Castelletto, T. Ohshima, T. J. Karle, A. Gali, S. Prawer, J. C. McCallum, and B. C. Johnson. *Single-photon emitting diode in silicon carbide*. *Nature Communications*, 6, 2015.
- [15] B. Lounis, H. Bechtel, D. Gerion, P. Alivisatos, and W. Moerner. *Photon antibunching in single CdSe/ZnS quantum dot fluorescence*. *Chemical Physics Letters*, 329(5-6):399–404, oct 2000.
- [16] X. Brokmann, G. Messin, P. Desbiolles, E. Giacobino, M. Dahan, and J. P. Hermier. *Colloidal CdSe/ZnS quantum dots as single-photon sources*. *New Journal of Physics*, 6:99–99, jul 2004.
- [17] A. L. Efros and D. J. Nesbitt. *Origin and control of blinking in quantum dots*. *Nature Nanotechnology*, 11(8):661, 2016.
- [18] M. Cirillo, T. Aubert, R. Gomes, R. Van Deun, P. Emplit, A. Biermann, H. Lange, C. Thomsen, E. Brainis, and Z. Hens. *“Flash” Synthesis of CdSe/CdS Core–Shell Quantum Dots*. *Chem. Mater.*, 26(2):1154–1160, jan 2014.
- [19] E. Drijvers, J. De Roo, P. Geiregat, K. Fehér, Z. Hens, and T. Aubert. *Revisited Wurtzite CdSe Synthesis: A Gateway for the Versatile Flash Synthesis of Multishell Quantum Dots and Rods*. *Chem. Mater.*, 28(20):7311–7323, oct 2016.

- [20] R. Hanbury Brown and R. Q. Twiss. *A Test of a New Type of Stellar Interferometer on Sirius*. Nature, 178(4541):1046–1048, nov 1956.
- [21] G. A. Steudle, S. Schietinger, D. Höckel, S. N. Dorenbos, I. E. Zadeh, V. Zwiller, and O. Benson. *Measuring the quantum nature of light with a single source and a single detector*. Physical Review A, 86(5):053814, nov 2012.
- [22] K. Lambert, I. Moreels, D. V. Thourhout, and Z. Hens. *Quantum Dot Micropatterning on Si*. Langmuir, 24(11):5961–5966, jun 2008.
- [23] Q. Zhang, C. Dang, H. Urabe, J. Wang, S. Sun, and A. Nurmikko. *Large ordered arrays of single photon sources based on II–VI semiconductor colloidal quantum dot*. Optics Express, 16(24):19592, nov 2008.
- [24] M. Jiang, J. A. Kurvits, Y. Lu, A. V. Nurmikko, and R. Zia. *Reusable Inorganic Templates for Electrostatic Self-Assembly of Individual Quantum Dots, Nanodiamonds, and Lanthanide-Doped Nanoparticles*. Nano Letters, 15(8):5010–5016, aug 2015.
- [25] V. L. Colvin, M. C. Schlamp, and A. P. Alivisatos. *Light-emitting diodes made from cadmium selenide nanocrystals and a semiconducting polymer*. Nature, 370(6488):354–357, aug 1994.
- [26] Y. Shirasaki, G. J. Supran, M. G. Bawendi, and V. Bulović. *Emergence of colloidal quantum-dot light-emitting technologies*. Nature Photonics, 7(1):13–23, jan 2013.
- [27] B. S. Mashford, M. Stevenson, Z. Popovic, C. Hamilton, Z. Zhou, C. Breen, J. Steckel, V. Bulovic, M. Bawendi, S. Coe-Sullivan, and P. T. Kazlas. *High-efficiency quantum-dot light-emitting devices with enhanced charge injection*. Nat. Photonics, 7(5):407–412, 2013.
- [28] Y. Yang, Y. Zheng, W. Cao, A. Titov, J. Hyvonen, J. R. Manders, J. Xue, P. H. Holloway, and L. Qian. *High-efficiency light-emitting devices based on quantum dots with tailored nanostructures*. Nature Photonics, 9(4):259–266, apr 2015.
- [29] T. Tynell and M. Karppinen. *Atomic layer deposition of ZnO: a review*. Semiconductor Science and Technology, 29(4):043001, apr 2014.
- [30] D. Kim, H. Kang, J.-M. Kim, and H. Kim. *The properties of plasma-enhanced atomic layer deposition (ALD) ZnO thin films and comparison with thermal ALD*. Applied Surface Science, 257(8):3776–3779, feb 2011.

- [31] E. Guziewicz, M. Godlewski, L. Wachnicki, T. A. Krajewski, G. Luka, S. Gieraltowska, R. Jakiela, A. Stonert, W. Lisowski, M. Krawczyk, J. W. Sobczak, and A. Jablonski. *ALD grown zinc oxide with controllable electrical properties*. *Semiconductor Science and Technology*, 27(7):074011, 2012.
- [32] L. Liu, Z. Mei, A. Tang, A. Azarov, A. Kuznetsov, Q. K. Xue, and X. Du. *Oxygen vacancies: The origin of n-type conductivity in ZnO*. *Physical Review B*, 93(23):235305, 2016.
- [33] S. A. Empedocles. *Quantum-Confined Stark Effect in Single CdSe Nanocrystallite Quantum Dots*. *Science*, 278(5346):2114–2117, dec 1997.
- [34] Y. Shirasaki, G. J. Supran, W. A. Tisdale, and V. Bulović. *Origin of Efficiency Roll-Off in Colloidal Quantum-Dot Light-Emitting Diodes*. *Physical Review Letters*, 110(21):217403, may 2013.
- [35] L. Yang, B. Wei, and J. Zhang. *Transient thermal characterization of organic light-emitting diodes*. *Semiconductor Science and Technology*, 27(10):105011, oct 2012.
- [36] K. J. Bergemann, R. Krasny, and S. R. Forrest. *Thermal properties of organic light-emitting diodes*. *Organic Electronics*, 13(9):1565–1568, sep 2012.
- [37] D. Pugh-Thomas, B. M. Walsh, and M. C. Gupta. *CdSe(ZnS) nanocomposite luminescent high temperature sensor*. *Nanotechnology*, 22(18):185503, may 2011.
- [38] R. L. Puurunen. *Surface chemistry of atomic layer deposition: A case study for the trimethylaluminum/water process*. *Journal of Applied Physics*, 97(12):121301, jun 2005.
- [39] P. Frantsuzov, M. Kuno, B. Jankó, and R. A. Marcus. *Universal emission intermittency in quantum dots, nanorods and nanowires*. *Nature Physics*, 4(7):519–522, jul 2008.
- [40] P. P. Jha and P. Guyot-Sionnest. *Trion Decay in Colloidal Quantum Dots*. *ACS Nano*, 3(4):1011–1015, apr 2009.
- [41] W. K. Bae, Y.-S. Park, J. Lim, D. Lee, L. A. Padilha, H. McDaniel, I. Robel, C. Lee, J. M. Pietryga, and V. I. Klimov. *Controlling the influence of Auger recombination on the performance of quantum-dot light-emitting diodes*. *Nature Communications*, 4(1):2661, dec 2013.

- [42] D. E. Gómez, J. van Embden, P. Mulvaney, M. J. Fernée, and H. Rubinsztein-Dunlop. *Exciton-Trion Transitions in Single CdSe-CdS Core-Shell Nanocrystals*. ACS Nano, 3(8):2281–2287, aug 2009.
- [43] X. Dai, Z. Zhang, Y. Jin, Y. Niu, H. Cao, X. Liang, L. Chen, J. Wang, and X. Peng. *Solution-processed, high-performance light-emitting diodes based on quantum dots*. Nature, 515(7525):96–99, nov 2014.
- [44] J. Lim, Y.-S. Park, K. Wu, H. J. Yun, and V. I. Klimov. *Droop-Free Colloidal Quantum Dot Light-Emitting Diodes*. Nano Lett., 18(10):6645–6653, oct 2018.
- [45] Z. Zhang, Y. Ye, C. Pu, Y. Deng, X. Dai, X. Chen, D. Chen, X. Zheng, Y. Gao, W. Fang, X. Peng, and Y. Jin. *High-Performance, Solution-Processed, and Insulating-Layer-Free Light-Emitting Diodes Based on Colloidal Quantum Dots*. Adv. Mater., 30(28):1–8, 2018.
- [46] H. Shen, Q. Gao, Y. Zhang, Y. Lin, Q. Lin, Z. Li, L. Chen, Z. Zeng, X. Li, Y. Jia, S. Wang, Z. Du, L. S. Li, and Z. Zhang. *Visible quantum dot light-emitting diodes with simultaneous high brightness and efficiency*. Nature Photonics, 13(3):192–197, mar 2019.
- [47] V. I. Klimov, S. A. Ivanov, J. Nanda, M. Achermann, I. Bezel, J. A. McGuire, and A. Piryatinski. *Single-exciton optical gain in semiconductor nanocrystals*. Nature, 447(7143):441–446, may 2007.
- [48] C. R. Kagan, C. B. Murray, M. Nirmal, and M. G. Bawendi. *Electronic Energy Transfer in CdSe Quantum Dot Solids*. Physical Review Letters, 76(9):1517–1520, feb 1996.
- [49] S. Bisschop, P. Geiregat, T. Aubert, and Z. Hens. *The Impact of Core/Shell Sizes on the Optical Gain Characteristics of CdSe/CdS Quantum Dots*. ACS Nano, 12(9):9011–9021, sep 2018.
- [50] W. Xie, T. Stöferle, G. Rainò, T. Aubert, S. Bisschop, Y. Zhu, R. F. Mahrt, P. Geiregat, E. Brainis, Z. Hens, and D. Van Thourhout. *On-Chip Integrated Quantum-Dot-Silicon-Nitride Microdisk Lasers*. Adv. Mater., 29(16):1604866, apr 2017.
- [51] Y. Zhu, W. Xie, S. Bisschop, T. Aubert, E. Brainis, P. Geiregat, Z. Hens, and D. Van Thourhout. *On-Chip Single-Mode Distributed Feedback Colloidal Quantum Dot Laser under Nanosecond Pumping*. ACS Photonics, 4(10):2446–2452, oct 2017.

- [52] J. Kuhs, A. Werbrouck, N. Zawacka, E. Drijvers, P. F. Smet, Z. Hens, and C. Detavernier. *In Situ Photoluminescence of Colloidal Quantum Dots During Gas Exposure—The Role of Water and Reactive Atomic Layer Deposition Precursors*. ACS Applied Materials & Interfaces, 11(29):26277–26287, jul 2019.
- [53] F. Prins, D. K. Kim, J. Cui, E. De Leo, L. L. Spiegel, K. M. McPeak, and D. J. Norris. *Direct Patterning of Colloidal Quantum-Dot Thin Films for Enhanced and Spectrally Selective Out-Coupling of Emission*. Nano Letters, 17(3):1319–1325, 2017.
- [54] G. E. Cragg and A. L. Efros. *Suppression of Auger Processes in Confined Structures*. Nano Letters, 10(1):313–317, jan 2010.
- [55] W. K. Bae, L. A. Padilha, Y.-S. Park, H. McDaniel, I. Robel, J. M. Pietryga, and V. I. Klimov. *Controlled Alloying of the Core-Shell Interface in CdSe/CdS Quantum Dots for Suppression of Auger Recombination*. ACS Nano, 7(4):3411–3419, apr 2013.
- [56] Y.-H. Won, O. Cho, T. Kim, D.-Y. Chung, T. Kim, H. Chung, H. Jang, J. Lee, D. Kim, and E. Jang. *Highly efficient and stable InP/ZnSe/ZnS quantum dot light-emitting diodes*. Nature, 575, 2019.

Chapter 3

Waveguide-coupled colloidal quantum dot light emitting diodes and detectors on a silicon nitride platform

Colloidal quantum dots (QDs) have become an attractive light source for visible photonics, in particular their widely tunable emission wavelength, inexpensive wet-chemical synthesis and straight-forward hybrid integration can make the difference. Here, we demonstrate the first integrated light-emitting diodes based on CdSe/CdS QDs, with the emission directly coupled to a silicon nitride waveguide. We report a record current density of up to 100 A/cm^2 and a maximum on-chip power of almost 2 nW in a single-mode waveguide. Operated as detectors, the photodiodes have a low dark current of $1.5 \text{ }\mu\text{A/cm}^2$. We anticipate the devices to find an application in chip-based absorption spectroscopy and bio-sensing, as they can be post-processed on foundry-fabricated waveguide platforms, at a low cost. In addition, we believe that our approach provides the missing low-loss waveguide layer, necessary for building an electrically pumped laser using colloidal QDs. The results have in part been presented at a conference [1] and a full length journal paper has been submitted. In addition, a European patent application has been filed (EP20172462.2), based on the innovative device concept outlined in this chapter.

3.1 Introduction

Colloidal semiconductor nanocrystals or QDs are appealing gain materials for optical amplifiers and lasers. Especially in the case of optically pumped lasers, multiple studies have demonstrated the combined advantages of a tunable emission spectrum, high material gain and a suitability for solution-based processing. [2–4] In addition, reliable approaches to fabricate QD-based microlasers have been established [5, 6] and pathways identified to shift from femtosecond pulsed excitation to continuous-wave optical pumping, [7, 8] at power levels around 10 kW/cm^2 , compatible with cheap blue laser diodes. The demonstration of electrically pumped QD lasers, on the other hand, still remains a challenge. Building on the progress in colloidal QD light emitting diodes [9] (QD-LEDs), optical gain has been achieved with DC electrical pumping, by implementing a current focusing approach. [10] However, to attain lasing operation, LED designs that support the high current densities required to sustain population inversion must be integrated with a low-loss cavity. One approach to address this, is to use index confinement in the active material, combined with a patterned charge transport layer providing distributed feedback. [11] However, in such a device a sufficiently thick QD film is needed to support a confined optical mode. For thin QD layers, which can be inverted with the available current density, increasing passive optical losses strongly compromise lasing operation. As an alternative, we propose a novel design with a QD-LED structure in the evanescent field of a guided optical mode, allowing to significantly reduce passive optical losses for thin QD layers and enabling multiple means of optical feedback.

In this work, we demonstrate the first waveguide-coupled QD-LED, the basic building block for future laser designs. We therefore combined an adapted CdSe/CdS QD-LED structure with silicon nitride (SiN) integrated photonics. SiN recently emerged as a versatile platform for on-chip visible and infrared photonics, with applications in bio-sensing and spectroscopy. [12]. While SiN enables high performance passive components with propagation losses as low as 1 dB/m [13], the heterogeneous integration of active components is essential for advanced functionality. For example, fast Pockels modulators [14] and III-V amplifiers and lasers [15, 16] have been integrated on silicon nitride, as well as optically-pumped QD lasers. [5] To extend this work to integrated QD-LEDs, we started from an efficient so-called inverted QD-LED stack, [9, 17] consisting of a QD film in-between organic materials for hole injection and ZnO nanocrystals for electron injection. However, straightforward integration of this stack on top of a SiN waveguide would induce prohibitive propagation losses of several $\text{dB}/\mu\text{m}$.

A key to overcoming this issue, was developing a low-loss ZnO *n*-contact layer. In combination with the inherent current focusing architecture of our waveguide-coupled QD-LEDs, this enabled a record current density of 100 A/cm², while minimizing passive losses. Furthermore, the presented devices can also be operated as integrated photodiodes, making them a versatile building block to functionalize SiN integrated photonics. At the same time, our work constitutes a major step on the way to an electrically pumped QD laser.

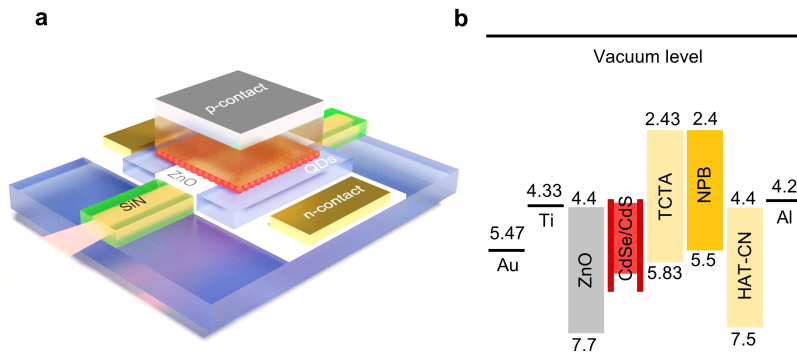


Figure 3.1: (a) Schematic model of the waveguide-coupled quantum dot light emitting diode (QD-LED), consisting of a silicon nitride waveguide covered with a low-loss ZnO electron transport and injection layer. Colloidal CdSe/CdS QDs are used as active material and organic layers for hole transport and injection. (b) Band alignment of the different layers used in the waveguide-coupled QDLED referenced to the vacuum level.

3.2 Design and simulation

Figure 3.2a shows the device cross-section, with an overlay of the fundamental transverse electric (TE) waveguide mode profile. The silicon nitride waveguide with width w and height h is overcoated with a 10 nm thin ZnO *n*-contact layer. Silicon oxide acts as a side-cladding of the waveguide, enabling the uniform deposition of a ~ 20 nm colloidal CdSe/CdS quantum dot layer. The QDs with a core/shell diameter of 3.7/7.5 nm were optimized for a high intrinsic gain and a low threshold. [18] Organic hole transport layers with a total thickness t and an aluminum *p*-contact complete the device. To optimize the geometry and find a suitable trade-off between coupling efficiency and propagation loss, we performed finite element (FE) and finite difference time domain (FDTD) simulations with a

commercial software package (Lumerical). The colloidal CdSe/CdS QDs can be approximated as isotropic dipole emitters, due to their random orientation in the device. [19] However, only one polarization couples efficiently to the fundamental TE waveguide mode. The average coupling efficiency β_{avg} , for quantum dots on top of the waveguide has a maximum for narrow single-mode waveguides, due to higher mode overlap compared to wider multi-mode waveguides. Yet, this does not mean that single-mode waveguides will perform better, since there will be more electrically contacted emitters on top of a wider waveguide. A more meaningful figure of merit is $w \times \beta_{avg}$, which is proportional to the total spontaneous emission coupled to the fundamental TE mode. Results for different geometries are displayed in Figure 3.2b, using a first-order interpolation between simulated values. The dashed black lines mark the onset of higher order TE modes for the simulation wavelength of 650 nm. It can be seen, that the coupled spontaneous emission depends weakly on the width and reaches a maximum for a height between 100 nm and 150 nm. For wider multi-mode waveguides, part of the spontaneous emission is coupled to the higher-order modes. However, for integrated photonics applications single-mode devices are preferred, to avoid spurious effects originating from mode mixing. All simulations were performed with refractive index values of the organic layers, ZnO and silicon nitride extracted from ellipsometry measurements. The values obtained for a wavelength of 650 nm were $n_{TCTA} = 1.74$, $n_{NPB} = 1.74$, $n_{HAT-CN} = 1.79$, $n_{ZnO} = 1.89$, $n_{SiN} = 1.94$. To accurately determine the loss of the optimized ZnO layer, we performed cut-back measurements, extracting an imaginary refractive index of $k_{ZnO} = 2.5 \times 10^{-4}$ (see Figure 3.5a).

Figure 3.2c visualizes the influence of the p-contact metal on the waveguide loss, for fixed dimensions of the silicon nitride waveguide ($w = 1 \mu\text{m}$, $h = 300 \text{ nm}$) and assuming loss-less organic layers. The metal loss component shows the expected dependence on the overlap with the evanescent field, resulting in an exponential decay of the loss with the thickness t . Only for a sufficient separation, determined by the thickness of the organic layers, reasonable loss can be achieved. For example, for an organic layer thickness of $t = 500 \text{ nm}$, simulations predict a metal loss of 4 dB/cm, which was confirmed by cut-back measurements. We therefore fabricated a sample according to the description in Section 3.3, but without depositing any QDs and a total thickness $t = 500 \text{ nm}$ of the organic layers. We then measured the waveguide transmission spectrum using a supercontinuum source (NKT Photonics, SuperK Extreme), coupling the broadband emission to the chip via a grating coupler (see Figure 3.3a) and an optical fiber (SM780) and recording the transmitted power with an optical spectrum analyzer (Advantest, 8381A). Figure 3.3b compares the transmission

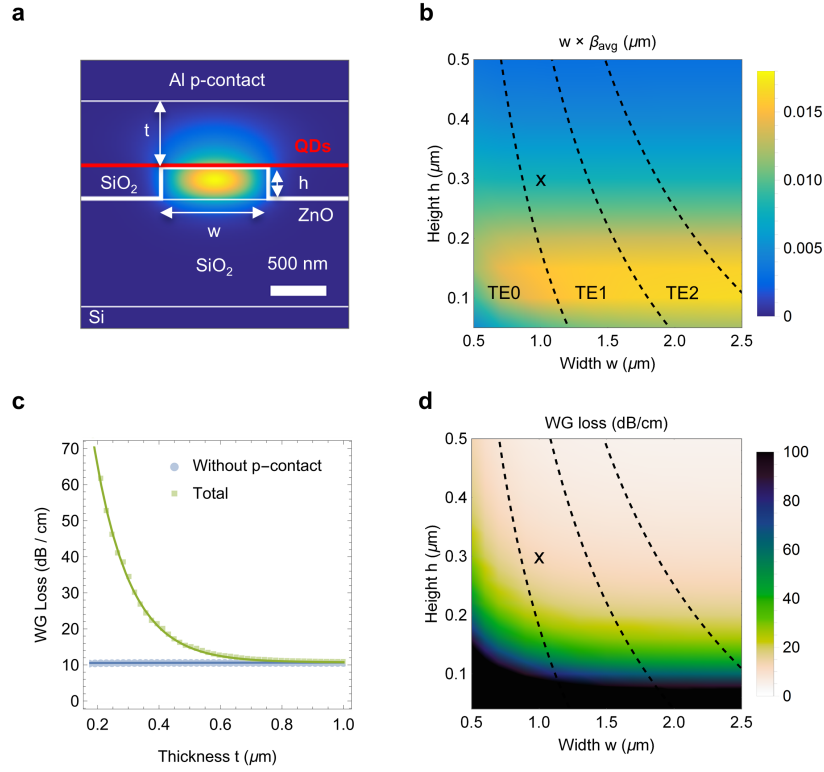


Figure 3.2: Simulation results of coupling efficiency and waveguide loss for different geometries. (a) Mode profile of the fundamental TE mode for the fabricated geometry and a simulation wavelength of 650 nm. (b) Figure of merit for the power coupled to the fundamental TE mode, for a given organics thickness of $t = 600$ nm. (c) Waveguide loss originating from the p-contact metal for a given width ($w = 1 \mu\text{m}$) and height ($h = 300$ nm) of the silicon nitride. (d) Dependence of the passive waveguide loss on the geometry, for a given organics thickness of $t = 600$ nm. First-order interpolation of the simulation results was used for the display in (b) and (d), the dashed lines represent the cut-on of higher order modes for the simulation wavelength.

measurements for different device lengths, from which we extracted an excess loss of 4 ± 3 dB/cm for the organic layers and p-contact metal using a linear fit.

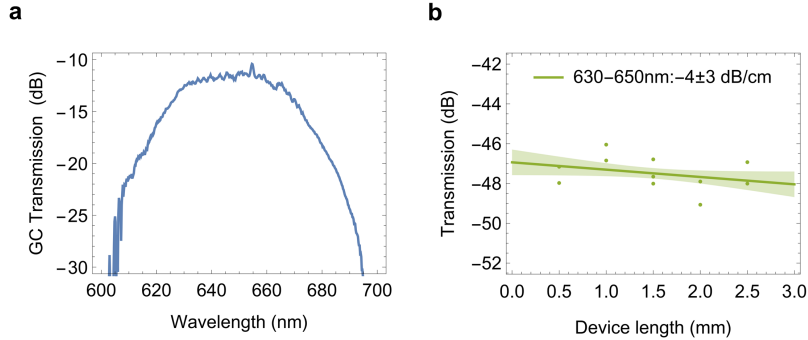


Figure 3.3: Extraction of the loss induced by the p-contact metal. (a) Grating coupler transmission spectrum. (b) Transmission measured for different device lengths.

The organic layers should also not be thicker than needed to suppress the loss from the p-contact metal, since this would unnecessarily increase the series resistance of the device. Also, there is a practical limitation of the material thickness, which can be deposited during one continuous evaporation step. Hence, we fixed the parameter at $t = 600$ nm. This corresponds to a simulated excess loss of 2 dB/cm due to the aluminum layer for $w = 1 \mu\text{m}$ and $h = 300$ nm. Figure 3.2d shows the dependence of the total waveguide loss on the width and height of the silicon nitride, for an organics thickness of $t = 600$ nm. Clearly, thin silicon nitride waveguides give rise to increasing losses, due to the larger mode overlap with the ZnO layer and the p-contact metal. A height of 300 nm provides a good trade-off between loss and coupling efficiency. Also, narrower single-mode waveguides show higher passive losses due to a larger mode overlap with the ZnO layer on the waveguide sidewalls and the unpumped quantum dots next to the waveguide, which were included in the simulation of passive losses, since they will only cause absorption. Table 3.1 summarizes the different loss contributions for the fundamental TE mode with the fabricated dimensions, including QDs on top of the waveguide as reported below. Transverse magnetic (TM) waveguide modes are strongly suppressed in the design, due to their larger overlap with the aluminum p-contact layer, resulting in simulated passive waveguide losses exceeding 180 dB/cm.

Wavelength (nm)	610 (band-edge)	642 (EL peak)	650
SiN (dB/cm)	≤ 1	≤ 1	≤ 1
ZnO (dB/cm)	9	9	9
Al p-contact (dB/cm)	1	2	2
QDs (dB/cm)	405	44	14
Total (dB/cm)	≤ 416	≤ 56	≤ 26

Table 3.1: Estimated waveguide loss contributions for the fundamental TE mode with the fabricated dimensions, assuming QD absorption in absence of electrical or optical pumping.

3.3 Fabrication process development

3.3.1 Silicon nitride waveguides

Based on the simulation results we targeted dimensions of $w = 1 \mu\text{m}$, $h = 300 \text{ nm}$ and $t = 600 \text{ nm}$ for the fabrication. We started from silicon samples cleaved from a 6" wafer, coated with a $1 \mu\text{m}$ thermal SiO_2 layer (Siegert Wafer) and deposited a 300 nm silicon nitride layer by plasma enhanced chemical vapor deposition (PECVD) at a substrate temperature of 270°C (Advanced Vacuum Vision 310 PECVD). In a first e-beam lithography step with our 50 kV system (Raith Voyager), we patterned metal markers using a positive resist (ARP-6200.09, Allresist), using an area dose of $200 \mu\text{C}/\text{cm}^2$ and development in n-amyl acetate. We then evaporated 50 nm Au on top of a sputtered 3 nm Ti adhesion layer (Leybold Univex) and performed a lift-off in a dedicated resist remover (AR 600-71, Allresist), using ultrasonic agitation. To pattern the waveguide layer, we again used a positive resist (ARP-6200.09, Allresist), an area dose of $160 \mu\text{C}/\text{cm}^2$ and development in n-amyl acetate. Reactive ion etching (RIE) in CF_4 and H_2 chemistry was followed by a resist strip in O_2 plasma (Advanced Vacuum Vision 320 RIE). Supplementary information on the fabrication of the SiN waveguides can be found in Appendix A.1. To ease the prototyping, the results presented here use in-house fabricated waveguides. But it would also be possible to do the following post-processing steps (see Figure 3.4c-i) on waveguides processed by a foundry, since 300 nm is a commonly available standard thickness for silicon nitride. [20]

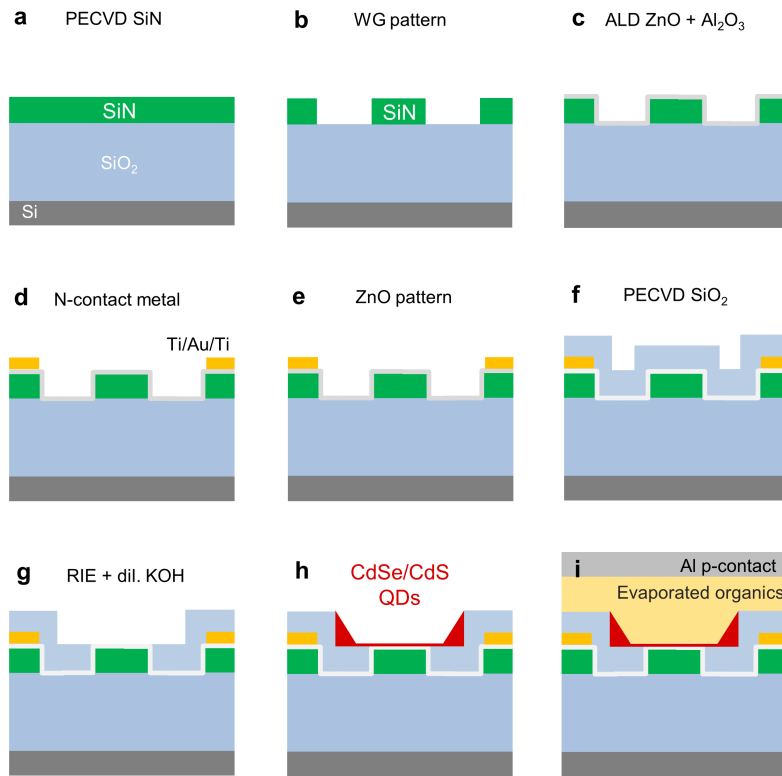


Figure 3.4: Main processing steps for fabricating waveguide-coupled QD-LEDs. (a) Low-frequency PECVD of a 300 nm SiN waveguide layer on a silicon sample with 1 μm thermal SiO₂. (b) Patterning of the waveguides using electron-beam lithography and a dry etch. (c) Atomic layer deposition (ALD) of the ZnO electron injection layer and Al₂O₃ passivation. (d) Local removal of Al₂O₃ and patterning of the Ti/Au/Ti n-contact metal using optical lithography and a lift-off process. (e) Patterning of the ZnO layer using optical lithography and a wet etch. (f) High-frequency PECVD of a 350 nm SiO₂ layer. (g) Local removal of SiO₂ using electron-beam lithography and a dry etch, wet removal of the Al₂O₃ layer to expose the ZnO electron injection layer. (h) Local deposition of CdSe/CdS colloidal quantum dots using a lift-off process. (i) Thermal evaporation of organic hole injection and hole transport layers, as well as an aluminum p-contact.

3.3.2 Atomic layer deposition of ZnO

Unlike conventional inverted LED designs found in literature, [9, 17] we do not use a combination of a transparent conductive oxide and ZnO nanocrystals for electron injection. Instead, to reduce passive optical losses, we employed atomic layer deposition¹ (ALD) to conformally coat the waveguides with a 10 nm thin layer of polycrystalline ZnO, serving as a electron transport and injection layer. Subsequently, we deposited a 15 nm Al₂O₃ ALD layer, acting as passivation and etch-stop layer. The ALD processes were adapted from established protocols found in literature [21, 22], using diethylezinc as a precursor for the ZnO deposition and trimethylaluminum for Al₂O₃. Distilled water vapor was used as reactant for both thermal ALD processes. Further details on the ALD process parameters can be found in Appendix A.4. The deposition was performed in the same home-built stainless steel pump-type reactor, that was used for the devices presented in Chapter 2. However, here we reduced the temperature of the sample holder to 150°C, resulting in a decreased intrinsic n-type conductivity of the ZnO layer and a correspondingly lower optical loss. After the ALD deposition, we performed a short annealing step, reaching a maximum temperature of 400°C for 30 s in N₂ and H₂ atmosphere.

To accurately determine the waveguide loss introduced by the 10 nm thin ZnO layer, we performed cut-back measurements for a ZnO coated waveguide ($w = 1 \mu\text{m}$, $h = 300 \text{ nm}$), covered with a $1 \mu\text{m}$ SiO₂ cladding. We therefore fabricated a separate sample that contained SiN spiral waveguides of different length and grating couplers (see Figure 3.3a). We measured the waveguide transmission using a supercontinuum source (NKT Photonics, SuperK Extreme), coupling the broadband emission to the chip via an optical fiber (SM780) and recording the transmitted power with an optical spectrum analyzer (Advantest, 8381A). Figure 3.5a compares the loss extracted for a sample before and after the rapid thermal annealing (RTA) step described above, for a wavelength of 640 nm. The annealing step significantly reduces the waveguide loss from $19.6 \pm 0.9 \text{ dB/cm}$ to $7.0 \pm 0.6 \text{ dB/cm}$. We then used finite element simulations (Lumerical Mode) to calculate the imaginary refractive index of $k = 2.5 \times 10^{-4}$ used for the simulations in Section 3.2, corresponding to a waveguide loss of 7 dB/cm.

The fabricated samples also included metal contacts with varying separation, for transfer length measurements (TLM), as shown in Figure 3.5b. Using DC probes and a source measurement unit (Keithly 2450) we obtained a sheet resistance of $1.2 \pm 0.1 \text{ k}\Omega/\square$ for typical samples after completing all processing steps. Although the ZnO layers are already conductive as-

¹Deposition of the ALD layers was performed by Robin Petit, associated with the Conformal Coating of Nanomaterials (CoCooN) research group of Ghent University.

deposited, we suspect that during the annealing step diffusion of Al from the Al_2O_3 passivation layer into the ZnO layer causes additional Al-doping [23] and therefore the observed reduction of the sheet resistance.

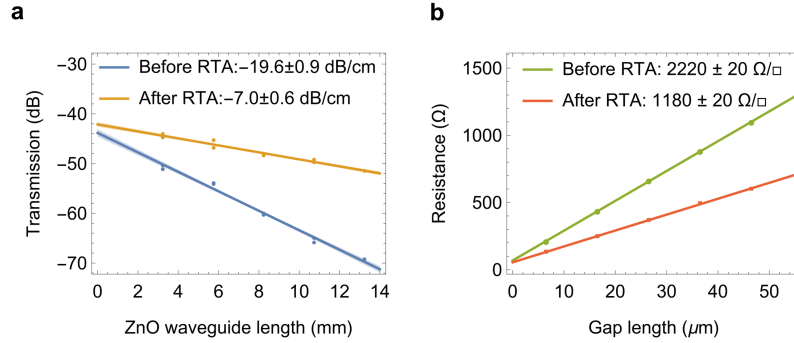


Figure 3.5: Material characterization of the optimized ZnO layer. (a) Cut-back measurements show a drastic reduction of the waveguide loss after the rapid thermal annealing (RTA) step. (b) Result of a typical transfer length measurement (TLM) to extract the sheet resistance of the 10 nm ZnO layer, before and after RTA.

3.3.3 Patterning of the n-contact metal and ZnO

To pattern the n-contact metal (20 nm Ti/100 nm Au/20 nm Ti) we used optical contact lithography (Karl Suss MA-6 mask aligner) and a lift-off process. To ease the processing, we made use of an image reversal resist (Ti-35E, Micro Chemicals), for which the developer also etches the Al_2O_3 passivation layer. To allow for a 4-5 min long development and simultaneous etching in dilute buffered KOH (AZ400K, Micro Chemicals), diluted 1:3 with de-ionized (DI) water, we had to adapt the standard recipe for the resist. We found that for a power density of $5 \text{ mW}/\text{cm}^2$ at 320 nm in our mask aligner, a first exposure of 100 s, a 3 min post-exposure bake on a hotplate set to 125°C and a subsequent 200 s flood exposure produced good results. The lift-off was performed in an acetone puddle, without ultrasonic agitation.

The first 20 nm Ti layer of the metal contact ensures a good band alignment and an Ohmic contact to the ZnO electron injection layer (see Figure 3.1b). From TLM we extracted a typical contact line resistance of $3.4 \Omega \text{ cm}$, as shown in Figure 3.5b. We found that due to the improved directionality, e-gun evaporation (Leybold 560) of the layer gives better results than sputter deposition, for which artifacts were found at the boundaries of

the metal contact. These artifacts, which originate from Ti being deposited on the resist sidewalls, caused pinholes in the p-contact metal deposited in the last fabrication step, in turn severely affecting the device performance outside of an inert atmosphere. The central 100 nm Au layer provides a high conductivity of the n-contact metal lines, while keeping the surface profile of the device low and the final 20 nm Ti layer ensures a good adhesion of the subsequently deposited SiO₂ layer.

Next, we patterned the ZnO electron injection layer using optical contact lithography with a positive resist (AZ5214, Micro Chemicals) and again making use of the over-development procedure described above to remove the Al₂O₃ passivation. Then we used a 30 s wet-etch in 37% hydrochloric acid (HCl), diluted 1:50 with DI water, to selectively remove all ZnO from the SiN waveguide structures. The high selectivity of this wet-etch process ensures that the original SiN device performance can be completely recovered. Figure 3.8a shows the resulting boundary between a ZnO covered waveguide and a section where the ALD layers were removed. To prepare the sample for the next processing step, we first removed the resist in acetone and any remaining residue during a 10 min O₂ plasma cleaning step (Advanced Vacuum Vision 320 RIE).

3.3.4 SiO₂ planarization etch and QD deposition

Serving as a dielectric barrier and side-cladding of the SiN waveguide, we deposited a 350 nm SiO₂ layer by PECVD, at a temperature of 150°C. Detailed parameters of the deposition process can be found in Appendix A.1.4. To provide the required overlay accuracy for the following planarization etch, we used electron-beam lithography with a positive resist (ARP-6200.13, Allresist), a dose of 160 $\mu\text{C}/\text{cm}^2$ and 90 s development in n-amyl acetate. Using a dry etch we locally removed the SiO₂, stopping at the Al₂O₃ etch-stop layer. Subsequently, the Al₂O₃ was removed using a wet-etch, exposing the ZnO electron injection layer.

It turned out that this planarization etch was one of the most critical processing steps in the device fabrication and quite a lot of effort went into finding a reliable procedure. For the reactive ion etch in CF₄, SF₆ and H₂ chemistry, we made use of an etch monitor (Intellemetrics LEP500). Figure 3.6 shows the recorded sample reflection during the etch, using the 980 nm laser installed in the tool. We therefore created openings of 200 $\mu\text{m} \times 200 \mu\text{m}$ in the resist, where we focused the laser beam. The signal displayed in Figure 3.6 shows the expected sinusoidal behaviour over time, indicating the removal of SiO₂ with a constant rate. A slight change in the slope can be observed when the etch reaches the Al₂O₃ etch-stop layer, at which point we manually terminated the etch. The use of the etch monitor

greatly simplifies the dry etch procedure, compensating for variations in the thickness of the deposited SiO_2 layer and in the etch rate.

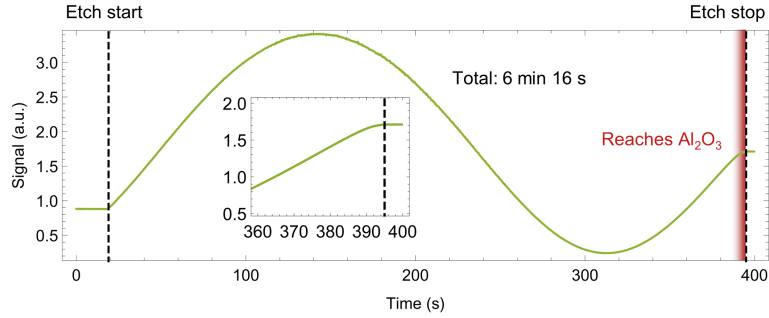


Figure 3.6: Reflected laser intensity recorded by the etch monitor during the removal of SiO_2 on top of the waveguide. A slight change in the slope indicates when the etch reaches the Al_2O_3 etch-stop layer.

To reduce the process variability and avoid the deposition of etch residue on the samples, it furthermore proved essential to start the etch with a well-conditioned RIE chamber. We therefore first performed a cleaning procedure, consisting of a 15 min SF_6 plasma step, followed by 15 min of O_2 plasma. Then we ran the SiO_2 etch recipe for 5 min without any sample in the chamber. Prior to the SiO_2 etch, we removed un-developed resist with a 20 second O_2 plasma step. After the etch we used a 10 min O_2 plasma exposure to remove the remaining resist mask and etch residue. Figure 3.7a shows the SEM top-view of a sample at this point in the fabrication process, with the exposed ALD layers appearing smooth and uniform, indicating a successful removal of the SiO_2 layer. For the sample in Figure 3.7b on the other hand, the SiO_2 etch was incomplete, resulting in visible residue on top of the SiN waveguide. In addition, it can be seen from Figure 3.7b, that for this sample the developed area of the resist was too wide, causing the SiO_2 cladding to be etched next to the waveguide as well.

We then used dilute buffered KOH (AZ400K diluted 1:3 with DI water) to remove the remaining Al_2O_3 etch-stop layer and expose the ZnO n-contact. Figure 3.7c shows a sample after this processing step, with the ZnO layer covering the SiN waveguide only showing minor imperfections. For the sample in Figure 3.7d in contrast, there are a multitude of holes in the ZnO layer, indicating a failed process due to poorly chosen parameters. Subsequently, we locally deposited a ~ 20 nm layer of CdSe/CdS quantum dots by spin-coating them from toluene, using a lift-off procedure with a

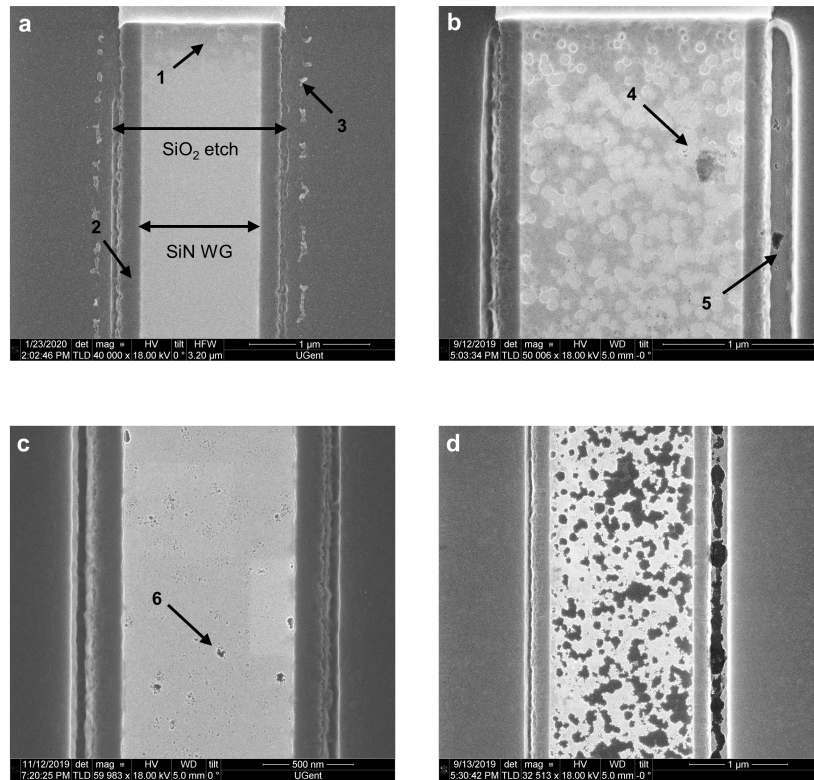


Figure 3.7: SEM top-view of different samples after the SiO_2 planarization etch. (a) Sample after successful RIE, before the Al_2O_3 wet-removal. The SiN waveguide appears bright due to the conformal ZnO coating and the etched area is aligned well to the underlying waveguide. (1) SiO_2 residue on top of the waveguide is only present near the edge of the etched area. (2) SiO_2 side-cladding next to the waveguide. (3) SiO_2 residue re-deposited next to the waveguide. (b) Sample after an incomplete RIE, before the Al_2O_3 wet-removal. The dark pattern on top of the waveguide indicates the presence of dielectric SiO_2 . (4) Etch residue likely due to insufficient chamber cleaning. (5) Etched SiO_2 side-cladding due to an overly wide developed area. (c) Sample after successful removal wet-removal of the Al_2O_3 etch-stop layer. (6) Only minor imperfections are present in the ZnO layer. (d) Sample after a failed SiO_2 planarization etch due to incorrect etch parameters. The ZnO layer exhibits many holes and likely a significantly reduced conductivity.

positive e-beam resist (AR 617.06, Allresist). The area dose for this process was $160 \mu\text{C}/\text{cm}^2$ and we used a dedicated developer (AR 600-55, Allresist) and lift-off in acetone, aided by ultrasonic agitation. Figure 3.8b shows a sample after this processing step, with a uniform layer of CdSe/CdS QDs covering the side-clad SiN waveguide.

As an alternative to patterning the QDs using an e-beam lithography step, we also explored the option of using optical contact lithography for that purpose. We therefore used an image reversal resist (TI-35E, Microchemicals) with the processing parameters described above, just after the SiO₂ RIE step. This way, the wet-removal of the Al₂O₃ etch-stop layer can be done just before the deposition of the QDs, ensuring a clean surface of the ZnO electron injection layer.

3.3.5 Organic layers and p-contact metal

For the deposition of the p-contact layers we used thermal evaporation in a dedicated deposition chamber (Trovato) with a base pressure of 1.5×10^{-6} mbar, connected to a glove box.² We rotated the sample holder with 12 rpm during shadow-mask evaporation of the organic layers, in order to obtain more uniform layers. The average deposition rate for the 70 nm TCTA layer (sublimed grade, Ossila) was $1.1 \text{ \AA}/\text{s}$, for the 500 nm NPB layer (sublimed grade, Ossila) $1.9 \text{ \AA}/\text{s}$ and for the 30 nm HAT-CN layer (sublimed grade, Ossila) $1.7 \text{ \AA}/\text{s}$. For the final 300 nm aluminum p-contact layer the average deposition rate was $2.3 \text{ \AA}/\text{s}$, without any rotation of the sample holder.

Figure 3.8c shows a focused ion-beam (FIB) cross-section of a device after the last processing step. The bright ZnO layer is clearly visible, conformally coating the SiN waveguide. To the left of the waveguide there is a smooth transition to the SiO₂ side-cladding, allowing a uniform deposition of the CdSe/CdS QD layer. However, to the right of the waveguide, a slight misalignment in the electron-beam lithography step prior to the SiO₂ planarization etch caused the SiO₂ side-cladding to be etched. In the subsequent QD deposition step the etched trench was partly filled. This illustrates a drawback of the planarization method used in this work, requiring the highest possible alignment accuracy. While the use of electron-beam lithography and a reduced fabrication yield is acceptable for small-scale prototyping, for the mass fabrication of devices, more reliable wafer-scale techniques employing chemical mechanical polishing (CMP) would be preferred. However, a small imperfection as shown in Figure 3.8c should not

²Deposition of the organic layers and p-contact metal was performed by Frederik Van Acker, associated with the Liquid Crystals and Photonics (LCP) research group of Ghent University.

significantly impact the device performance. Using finite element simulations (Lumerical Mode) we found that the impact of the QDs in the etched trench on the overall waveguide loss is negligible.

Another issue we encountered in the device fabrication was the formation of pinholes in the aluminum p-contact metal, visible in the FIB cross-section in Figure 3.8d. The step in the surface profile due to the SiN waveguide etch and the deposition of the n-contact metal directly translates to the p-contact metal, which appears to be cracked. This is a major issue for our devices, since the p-contact metal also serves as the only encapsulation of the devices during the characterization in an atmospheric environment. Pinholes in the layer lead to an ingress of atmospheric moisture and oxygen, quickly deteriorating the performance of the organic layers. For devices which suffer from pinholes in the p-contact metal, we observed a significant reduction of the attainable current density, compared to the values reported in the next section. We found that shifting the n-contact metal about $1\ \mu\text{m}$ away from the trench defining the SiN waveguide and using a large-area deposition of the CdSe/CdS QDs helped smoothing out the surface profile. Combined with a 300 nm thick aluminum layer, this significantly reduced the pinhole density, leading to a better device performance.

3.4 LED characterization

The SEM micrograph in Figure 3.9c shows a FIB cross-section of a waveguide-coupled QD-LED, with the annotated sketch next to it outlining the different layers. The large aluminum p-contact metal, covering an area of approximately $0.4\ \text{cm} \times 1\ \text{cm}$ of the fabricated chips, serves as the only encapsulation of the devices during the characterization in an atmospheric environment. The schematic top-view in Figure 3.9a shows that with our chip layout we were able to measure the waveguide transmission using grating couplers, while biasing the devices. For the devices presented here, we used one metal electrode to contact two waveguide-coupled QD-LEDs, increasing the number of devices on one chip. Figure 3.9b shows a corresponding SEM top-view of a finished device, detailing the device layout. In addition, each fabricated chip also contained two devices, which were contacted with two electrodes, one at each side of the waveguide. This way, we were able to monitor the effect of the Al_2O_3 removal etch on the conductivity of the underlying ZnO electron injection layer.

To evaluate the impact of asymmetries in the fabricated devices, we performed finite element simulations (Comsol Multiphysics), extracting the electric potential in the region of interest, as well as the current density in the organic layers. For the results displayed in Figure 3.10 we used the

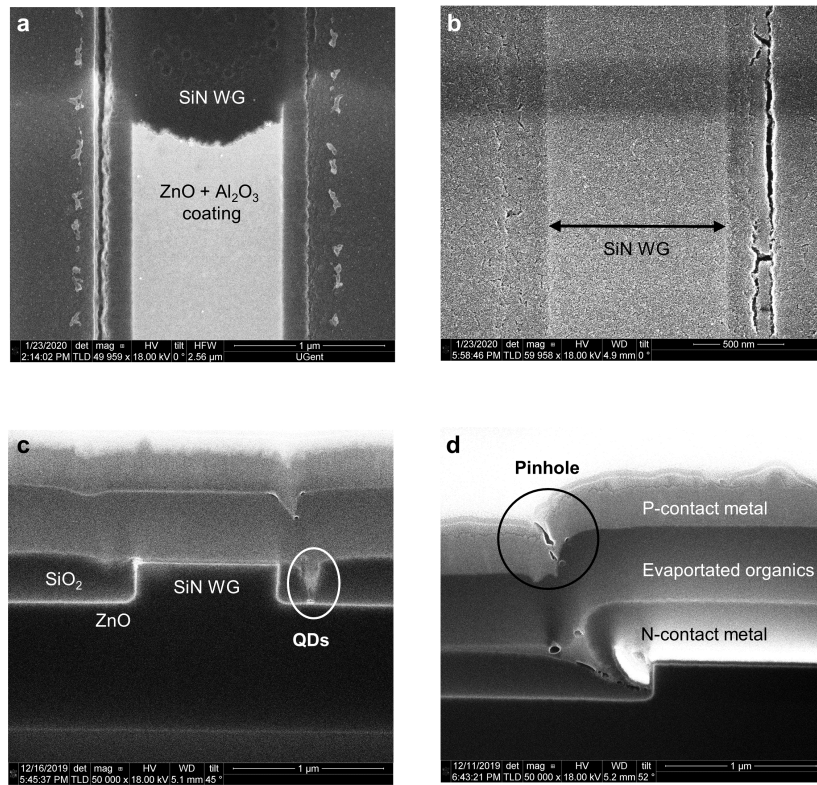


Figure 3.8: SEM images of the sample at different stages of the fabrication process. (a) Top-view of a SiN waveguide after the SiO₂ planarization etch, showing the boundary of the patterned ALD layers. The SiN waveguide appears damaged in the area, where it is not covered with ZnO and Al₂O₃. (b) Side-clad SiN waveguide covered with CdSe/CdS colloidal QDs. (c) Focused ion-beam (FIB) cross-section of a completed device showing the surroundings of the SiN waveguide. A slight misalignment in the electron-beam lithography step prior to the SiO₂ planarization etch caused the SiO₂ side-cladding to be etched next to the waveguide. In the subsequent QD deposition step the etched trench was partly filled. (d) FIB cross-section of the n-contact metal on a completed device. The step in the surface profile due to the SiN waveguide etch and the deposition of the n-contact metal directly translates to the p-contact metal, leading to pinholes in the evaporated aluminum layer.

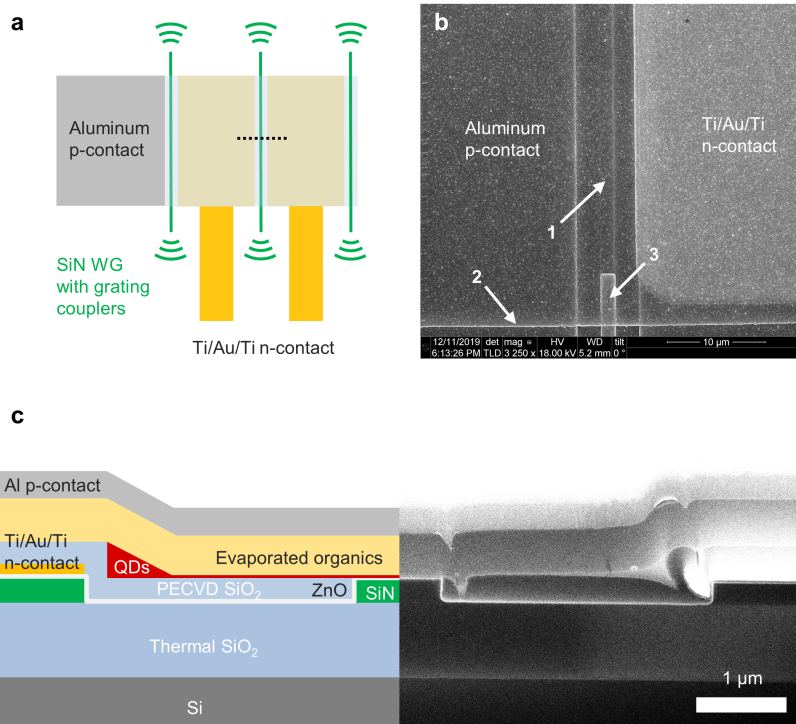


Figure 3.9: (a) Schematic top-view of the devices. (b) SEM top-view of a finished device showing the aluminum p-contact and the buried n-contact. (1) Part of the waveguide, where the SiO₂ top cladding was etched using the process described above. (2) Boundary of the large-area QD pattern. (3) Remaining SiO₂ on top of the SiN waveguide. (c) FIB cross-section of a finished device, outlining the different layers.

extracted ZnO conductivity, as shown above and an upper bound for the conductivity of the organic layers of $\rho = 0.01$ S/m found in literature. [24] The simulation results show, that due to the high conductivity of the thin ZnO electron transport layer, the largest part of the applied forward bias drops across the organic hole transport layers. In addition, while the ZnO layer was only grounded on one side of the simulation region, emulating a one-sided contact to the n-metal, we found that the geometric asymmetry of the electric field should be minimal.

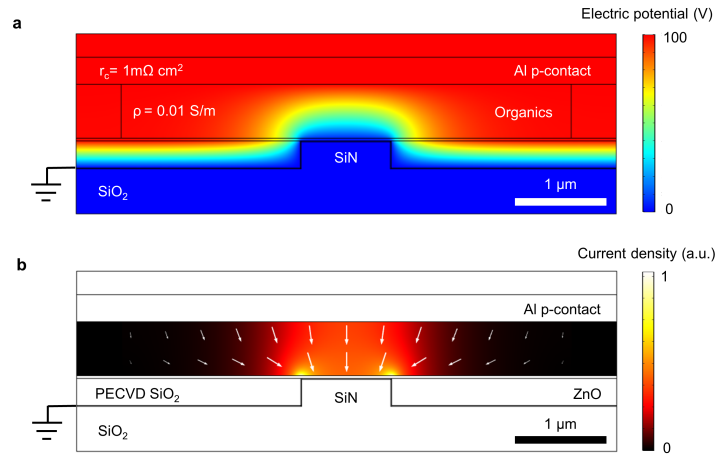


Figure 3.10: Finite element simulation of (a) the electric potential and (b) the current density in the organic layers for a forward bias voltage of 100 V.

To characterize the performance of the waveguide-coupled QD-LEDs, we used a source measurement unit (Keithley 2400) and DC probes to sweep the voltage and collect the grating coupler output with an optical fiber (SM780). Figure 3.11a shows the recorded current density for the device with the highest observed optical output power (Device 1), reaching 47 A/cm² at 100 V. The inset shows the electrical turn-on behavior of the device. Below a forward bias of 2 V we recorded a current noise of 2×10^{-6} A/cm² for the 2 mm long device, which was limited by the measurement range setting of the sources measurement unit. Figure 3.11b shows the electroluminescence (EL) spectrum, collected from the grating coupler output (measured with an Andor Shamrock SR-303i spectrometer). We observed a 2 nm red-shift of the peak emission wavelength for Device 1, when increasing the bias voltage from 40 V to 80 V, which we attribute to the quantum confined stark effect, due to the large bias voltage. [25] To test the capabilities of the waveguide-

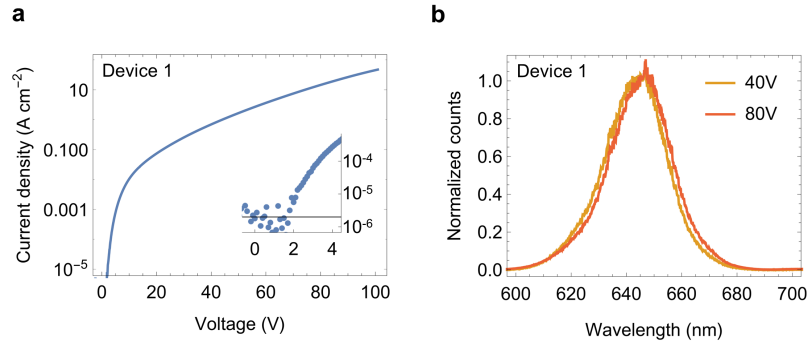


Figure 3.11: Waveguide-coupled QD-LED operated with a high bias voltage. (a) Current density recorded for the device with the highest optical output power, with an inset detailing the electrical turn-on behavior. (b) Normalized emission spectrum collected from the grating coupler output for different bias voltages.

coupled QD-LEDs we further increased the voltage for a different device on the same chip (Device 3). Figure 3.12 demonstrates a maximum current density of 100 A/cm^2 at 120 V bias, just before device failure. The SEM micrograph in Figure 3.12b shows visible damage to the device due to the overvoltage.

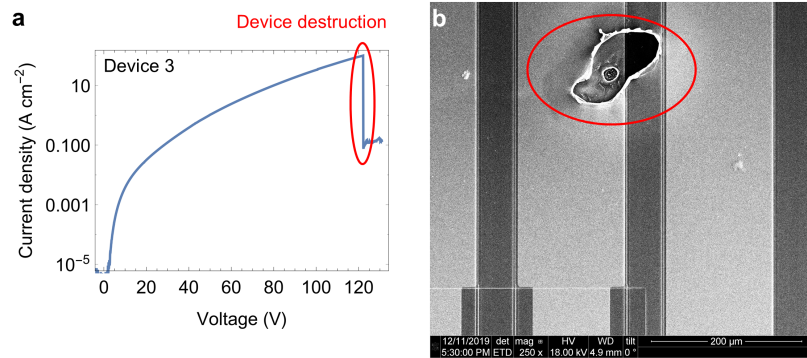


Figure 3.12: Bias voltage limitation for the waveguide-coupled QD-LED. (a) Irreversible destruction of the device was observed for a forward bias voltage above 120 V , with a reported maximum current density of 100 A/cm^2 . (b) SEM top-view showing the visibly damaged device.

The output measured with an optical power meter (HP8153A) for a

waveguide-coupled LED from a different chip (Device 2) is displayed in Figure 3.13a, indicating an optical turn-on at a voltage of 3 V. This measurement is limited by the noise floor of the optical power meter and we expect the actual value to be closer to the electrical turn-on at 2 V. Figure 3.13b shows the output spectrum of Device 2 at 5 V bias. As the efficiency of the grating coupler has a strong spectral dependence, we cleaved the chip for this measurement and collected the emission from the end facet with a multimode fiber. There is a 15 nm red-shift of the spectrum, compared to the photoluminescence (PL) emission of the same CdSe/CdS QD sample in solution, while the full width at half maximum (FWHM) remains approximately 35 nm. This is partly caused by short-range energy transfer from smaller to larger QDs, occurring in thin films. [26] Secondly, due to our device design, there is additional self-absorption of light propagating along the waveguide (see Figure 3.15b), limiting the output power of the LED (see Equation 3.2) and further shifting the electroluminescence (EL) emission peak.

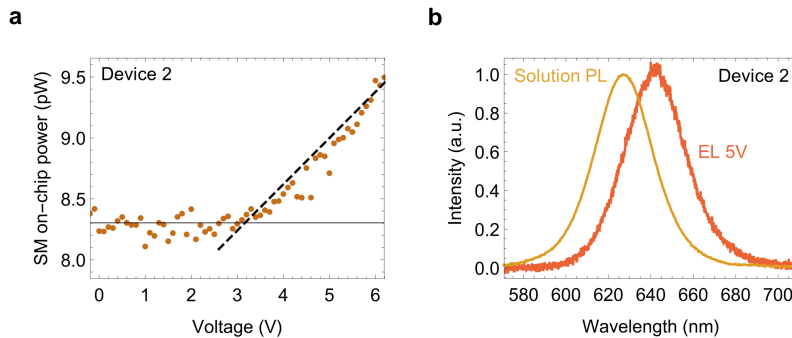


Figure 3.13: (a) Optical turn-on behavior of the waveguide-coupled QD-LED with the power collected from the grating coupler output. (b) Comparison of the EL emission collected from the end facet of a cleaved sample to the PL spectrum of the same CdSe/CdS QD sample in solution.

Using a separate measurement of the grating coupler transmission spectrum (see Figure 3.3a), we calculated an insertion loss of 13 dB, taking into account the QD emission spectrum. This allowed us to estimate the optical power in the silicon nitride waveguide. In addition, next to the 1 μm wide QD-LED section, the silicon nitride photonic chips include 400 μm long single-mode filter sections, with 450 nm wide waveguides. This ensures, that the optical power collected through the grating coupler is from the fundamental TE mode only. Figure 3.14a shows the on-chip power in

a single-mode waveguide, with a maximum of $P = 1.95$ nW for a current density of 47 A/cm², for the 2 mm long device. We used this power to calculate the quantum efficiency ϕ of the QD-LED. Figure 3.14b shows the normalized quantum efficiency, with a maximum for a current density of 0.04 A/cm² and a distinct roll-off behavior for higher current densities. A similar effect has been reported for many colloidal QD-LED devices in literature and is believed to originate from imperfect charge balance. It has been shown, that adjusting the barrier for electron injection into the dots, can help to overcome this issue. [27, 28]

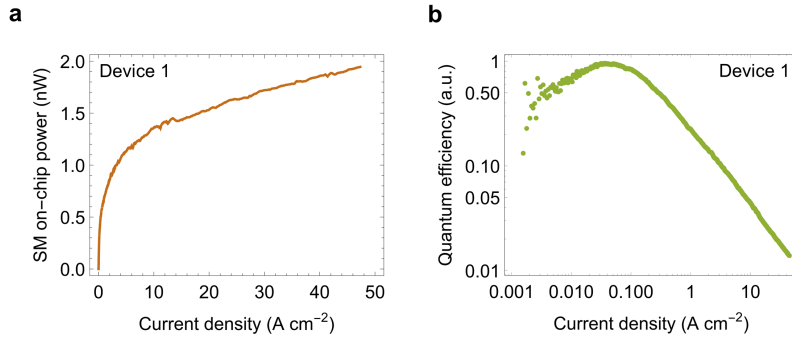


Figure 3.14: Saturation of the QD-LED output power. (a) Measured on-chip optical power in a single-mode waveguide and (b) normalized quantum efficiency as a function of the current density.

We calculated a maximum external quantum efficiency of $\phi_{ext} = 0.08\%$ for the device, according to

$$\phi_{ext} = \frac{P \lambda e}{I h c} \quad (3.1)$$

where e is the elementary charge, h the Planck constant, c the speed of light, I the device current and the EL emission peak wavelength of $\lambda = 642$ nm. The external quantum efficiency of our LEDs is low, compared to values reported for vertically emitting devices, [17] this is mainly due to the low average coupling efficiency β_{avg} to the fundamental TE mode. In addition, next to the short-range energy-transfer reducing the PL quantum yield in thin films, [26] self-absorption is also a major loss mechanism in our waveguide-coupled devices. Neglecting the unlikely re-emission into the waveguide mode after an absorption event, the output power of a LED with length l can be modeled as

$$P(l) = p \int_0^l e^{-\alpha x} dx, \quad (3.2)$$

where the constant p is the coupled power per unit length and α is the self-absorption coefficient. Therefore, the fraction of power reaching the output is

$$\gamma = \frac{1 - e^{-\alpha l}}{\alpha l}. \quad (3.3)$$

The coefficient α can be extracted from the QD absorption in Figure 3.15b, for the PL emission peak at $\lambda = 627$ nm we obtained $\alpha = 5.5$ mm⁻¹. We then calculated the internal quantum efficiency for the 2 mm long devices according to

$$\phi_{int} = \frac{\phi_{ext}}{\beta_{avg}\gamma}, \quad (3.4)$$

obtaining a maximum of $\phi_{int} = 11\%$, for $\beta_{avg} = 0.8\%$ extracted from the simulation results in Figure 3.2b. Comparing this to a PL quantum yield of 75% for the CdSe/CdS QD sample in solution, there is still room for improvement in the device processing and the band alignment of the different layers shown in Figure 3.1b.

3.5 Detector characterization

The same devices can also be operated as waveguide-coupled photo-detectors, using a moderate reverse bias. To characterize the detector performance, we first measured the transmission spectrum using the grating couplers for a device with and one without the QD layer (see Figure 3.15a). In Figure 3.15b we compare the extracted absorption to values calculated from the absorption spectrum of the CdSe/CdS QDs in solution. We used the material absorption of CdSe and CdS nanoparticles for a wavelength of 350 nm reported in literature, to calculate the absorption of our core/shell particles with an effective medium approach [29, 30] and re-scale the measured solution absorption. Assuming a QD fill-factor of 50% and a mode overlap of 3.6%, corresponding to a QD layer thickness of 22 nm, we observe a good agreement with the waveguide-based measurement.

For the detector characterization we used an external LED ($\lambda = 635$ nm) and estimated the power coupled into a single-mode waveguide from the transmission spectrum of a device without quantum dots (see Figure 3.16a). Figure 3.16b compares the current measured with a source measurement unit (Keithley Model 2450) for different optical input powers to the dark current for a 500 μ m long device. We then used the photo-current at a reverse bias of 7 V, subtracted the corresponding dark current of 1.5 μ A/cm² and fitted the detector response in Figure 3.17a with

$$I(P) = a P^b, \quad (3.5)$$

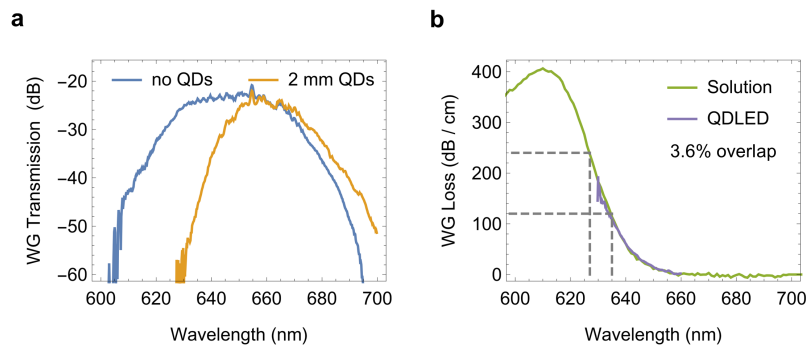


Figure 3.15: Waveguide loss induced by the CdSe/CdS QD layer. (a) Waveguide transmission measured for two different devices. (b) Extracted loss due to the QDs, compared to values calculated from a measurement of the CdSe/CdS QDs in solution.

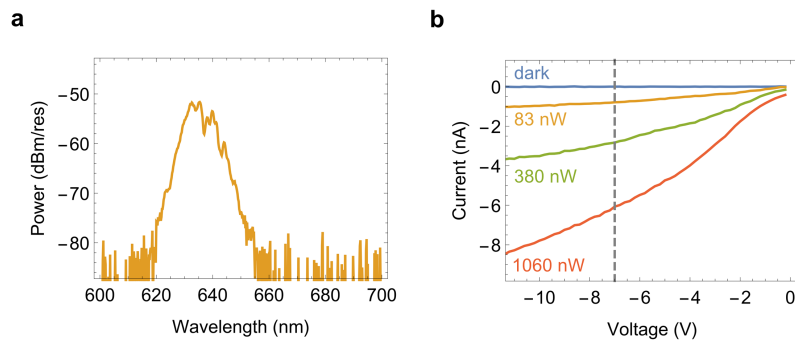


Figure 3.16: Detector characterization using an external LED. (a) Transmission spectrum of a device without QDs, used to estimate the power coupled into a single-mode waveguide. (b) Photo-current measured for different optical input powers for a 500 μm long device.

giving $a = 0.025$ A/W and $b = 0.8$. A possible explanation of the observed non-linear detector response might be the creation of trions and bi-excitons for larger input powers, for which we expect the charge extraction to become less efficient. However, the maximum power of $1 \mu\text{W}$, corresponding to a power density of 0.18 kW/cm^2 in the QD layer, only causes an excitation level of $\langle N \rangle \sim 0.01$, assuming a 15 ns average lifetime for the QD sample. [18] Therefore we reason that the non-linearity is caused by a different effect, possibly related to the deterioration of the organic layers, or a pronounced influence of the QD charging on the charge extraction efficiency, requiring a more detailed analysis in a future study. For a wavelength of $\lambda = 635 \text{ nm}$, it can be extracted from Figure 3.15b, that 75% of the incident power is absorbed in the detector, which limits the attainable detector quantum efficiency. Without any optimization of the devices, we extracted a detector quantum efficiency of $\phi_d = 6 \%$ for an input power of $P = 0.3 \text{ nW}$ (see Figure 3.17b) according to

$$\phi_d = \frac{I h c}{P \lambda e}, \quad (3.6)$$

where I is the measured photocurrent, h the Planck constant, c the speed of light and e the elementary charge. For the maximum input power of $1 \mu\text{W}$ used for the characterization, the detector quantum efficiency is reduced to 1%. With further improvements of the band alignment and device processing we expect to reach a detector performance, which is on par with similar planar devices reported in literature. [31]

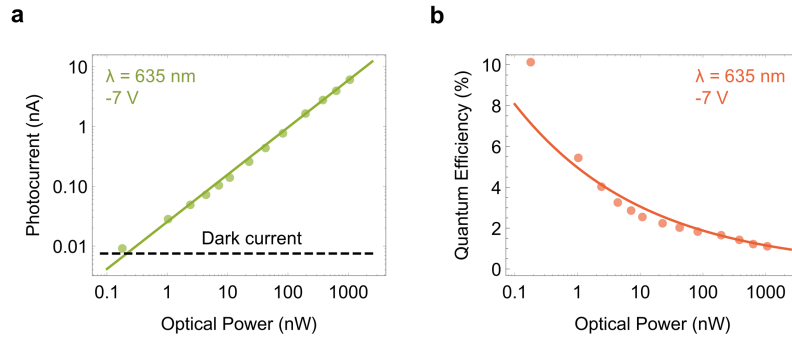


Figure 3.17: Detector performance of the waveguide-coupled QD-LED devices. (a) Photo-current after subtraction of the dark current and (b) detector quantum efficiency, for a reverse bias of 7 V and different optical input powers. Solid lines represent a fit of the data to Equation 3.5 and 3.6.

3.6 Estimation of the gain threshold

In literature, a saturation of the 1S-transition in colloidal QDs has been reported for a current density of 3.4 A/cm^2 , corresponding to an average exciton density of $\langle N \rangle = 1.4$, which in turn limits the output-power of QD-LEDs. [10] For our QD-LEDs, we used smaller CdSe/CdS QDs with a diameter of 7.5 nm, optimized for a high material gain. [18] To overcome the passive losses of 12 dB/cm in our devices, an intrinsic gain of $g_{i,th} = 880 \text{ cm}^{-1}$ is necessary, assuming a mode overlap of 3.6% and QD fill factor of 50% for 2-3 monolayers, as reported above. For a QD sample with the same core/shell volume fraction reported in the work of *Bisschop et al.*, [18] this intrinsic gain can be achieved with a power density of $200 \mu\text{J/cm}^2$ using femto-second pulsed excitation at $\lambda_p = 520 \text{ nm}$. With an absorption cross-section of $\sigma_{\lambda_p} = 3.96 \times 10^{-15} \text{ cm}^2$ reported for the same QD sample, [18] we can calculate a threshold excitation according to

$$\langle N \rangle_{th} = J_{ph} \times \sigma_{\lambda_p} \approx 2 \quad (3.7)$$

from the photon flux J_{ph} at the pump wavelength. In the work of *Lim et al.* [10] the authors report a excitation of $\langle N \rangle = 2$ for a current density of $\sim 6 \text{ A/cm}^2$ for QD-LED devices with 1-2 monolayers of QDs with a diameter of 19 nm. Taking into account the different QD size and layer thickness, we estimate a threshold current density of $j_{th} \sim 60 \text{ A/cm}^2$ for our devices. It should be noted, that this estimation does not take into account different Auger lifetimes of the QD samples, consequently the threshold current density might be higher for our CdSe/CdS QDs. Besides, the QD-LED output-power in Figure 3.14a already starts to saturate for a current density around 2 A/cm^2 . Hence we reason that a different effect causes the largest part of the observed saturation.

To characterize the gain spectrum of the CdSe/CdS QD sample in solution, we performed transient absorption (TA) measurements. The samples were therefore excited using 110 femtosecond pump pulses at 520 nm, the probe pulses were delayed relative to the pump using a delay stage with maximum delay of 3 ns. Details on the TA measurements can be found in Appendix B.1. Figure 3.18a shows the gain spectrum after 3 ps for different average number of excitons $\langle N \rangle$. Figure 3.18b shows the total absorption, measured at 650 nm, again for the same excitation levels $\langle N \rangle$. From these transient absorption experiments of QD sample in solution, we know gain should first appear around a wavelength of 650 nm. Therefore, we monitored the waveguide transmission with an external CW laser (see Figure 3.19a). But instead of the expected transparency we observed an excess loss with increasing forward bias, displayed in Figure 3.19b. We suspect, that this

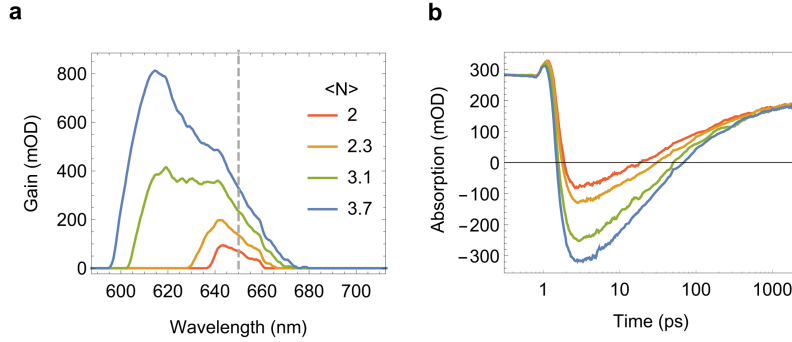


Figure 3.18: Transient absorption (TA) spectroscopy was used to characterize the CdSe/CdS QD sample in solution. (a) Gain spectrum after 3 ps, for different excitation $\langle N \rangle$ (b) Total absorption as a function of time, for a probe wavelength of 650 nm.

is partly caused by free carrier absorption in the ZnO layer and possibly the aforementioned quantum confined stark effect, also shifting the QD absorption spectrum. However, a large fraction of the original transmission can only be recovered after keeping the device at a moderate reverse bias for several minutes. Hence we hypothesize, that trapped charges in the ZnO n-contact and the QD layer might be involved. To prevent detrimental charge accumulation at high current densities in future devices, further investigations of the device physics are necessary to shed light on the involved processes. Possibly, strategies developed for planar QD-LEDs operating at much lower current densities [27, 28] can still be applied to our QD-LEDs to balance the injection of charge carriers of different polarity.

3.7 Including distributed feedback

To show that the thin layer of QDs on top of the ZnO covered SiN waveguide can indeed provide sufficient gain to overcome the passive losses, we fabricated a waveguide with a distributed feedback (DFB) grating. Enabling lasing action by means of a DFB grating is a widespread technique and especially suitable for low-threshold single-wavelength lasers. Previously, DFB lasers have been reported combining colloidal CdSe/CdS QDs with SiN waveguide gratings under nanosecond optical pumping. [6]

We implemented the grating as a sidewall corrugation of the SiN wave-

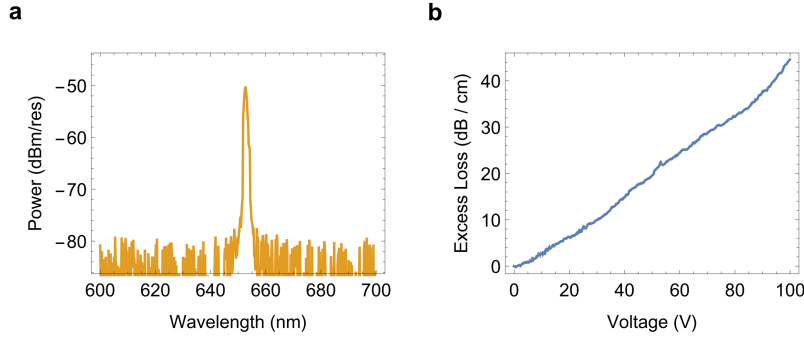


Figure 3.19: (a) Spectrum of the external laser used to monitor the waveguide transmission. (b) Excess loss for increasing forward bias extracted from a 2 mm long device.

guide, with a period Λ given by the Bragg condition

$$\Lambda = \frac{\lambda_{bragg}}{2n_{eff}}. \quad (3.8)$$

Figure 3.20a shows the fabricated structure after the SiO_2 planarization etch. The sidewall corrugation of the SiN waveguide is conformally covered by the ALD layers. Interestingly though, the PECVD SiO_2 acting as a side-cladding only grows on the grating teeth and not in the small gaps. This will in turn increase the grating strength κ compared to simulations assuming a uniform SiO_2 layer. Figure 3.20b shows the sidewall-corrugated waveguide, uniformly covered with an approximately 30 nm thin layer of CdSe/CdS QDs.

From the mode simulations presented in Figure 3.2 we learned that for a 1 μm wide waveguide, there are two TE modes in the SiN with a distinct effective index n_{eff} . Due to the reduced mode overlap with the sidewall corrugation, the fundamental TE mode will experience a lower grating strength κ . This puts a limit to the waveguide width, for which it is possible to ensure that the fundamental mode is lasing, since the higher order modes will always experience a higher grating strength. The fabricated samples consisted of a 500 μm long waveguide section with the sidewall corrugation. Figure 3.21a shows the transmission spectrum for a grating period of $\Lambda = 178$ nm, for a sample without ALD layers covering the SiN waveguide and a 350 nm PECVD SiO_2 top-cladding. The transmission dip at $\lambda_{bragg} = 638.2$ nm points to an effective index of $n_{eff} = 1.793$, which is in good agreement with the simulated value for the fundamental TE mode. For

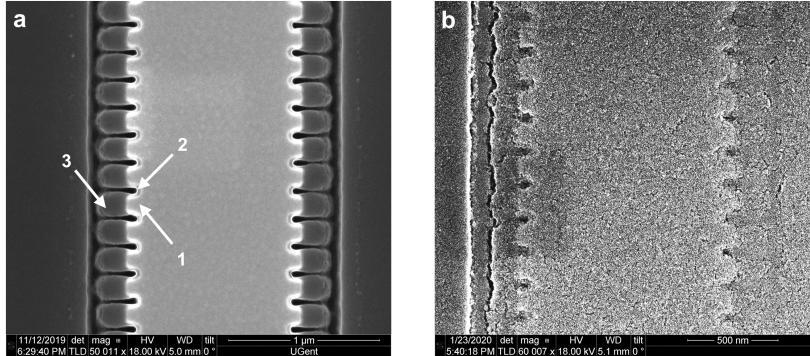


Figure 3.20: SEM top-view of structures with a grating for distributed feedback. (a) After the SiO_2 planarization etch. (1) Corrugated sidewalls of the SiN waveguide. (2) Conformal ZnO and Al_2O_3 ALD coating of the waveguide. (3) Selective growth of the PECVD SiO_2 used as a side-cladding. (b) Sidewall-corrugated waveguide after the deposition of a ~ 30 nm layer of CdSe/CdS QDs.

a second sample we went through the QD-LED fabrication steps described above, until the deposition of a ~ 30 nm layer of CdSe/CdS QDs, as shown in Figure 3.20b. We then cleaved the sample to be able to collect the waveguide output with a multimode fiber, while the sample was mounted vertically. To optically pump the QDs, we used a Q-switched frequency-doubled Nd:YAG laser (532 nm) with a 7 ns pulse width and a 938 Hz repetition rate. The pump laser was focused with a cylindrical lens, to pump the DFB section of the waveguide. Figure 3.21b shows the collected output spectrum (Thorlabs CCS100), with two distinct peaks centered around 631.1 nm. This corresponds to an effective index of $n_{eff} = 1.778$ for the sample without any top cladding, which was again confirmed by mode simulations. Since the DFB grating did not include a $\lambda/4$ defect, two lasing peaks, one at each side of the grating reflection are expected. This is exactly what we observe in Figure 3.21b and the separation of the peaks corresponds to the width of the transmission dip in Figure 3.21a. Note that the observed linewidth of the lasing peaks is limited by the spectrometer resolution. Therefore, we conclude that there is strong evidence that the observed emission peaks indeed are signs of QD lasing from the DFB cavity. Unfortunately, the sample was destroyed by an excessive pumping power, before we could do a detailed characterization, e.g. of the lasing threshold. Still, the experiment confirms that it is possible to attain sufficient gain for lasing with a thin CdSe/CdS QD layer on top of the lossy ZnO injection layer. Comparing

with the gain spectrum from TA measurements in Figure 3.18a, we reason that the nanosecond excitation of the QDs must have caused $\langle N \rangle > 2.3$, for sufficient gain to develop at a wavelength of 630 nm.

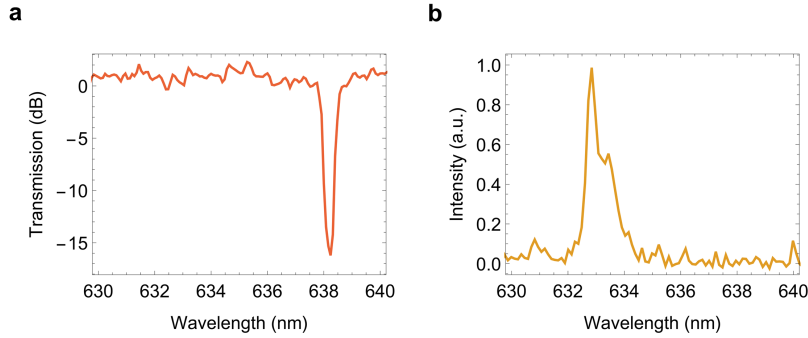


Figure 3.21: Sidewall-corrugation with a period of 178 nm. (a) Transmission spectrum of a SiN waveguide with a SiO₂ top- and side-cladding. (b) Lasing lines observed for a side-clad waveguide covered with ZnO and CdSe/CdS QDs, using ns-pulsed excitation at 520 nm.

3.8 Optimization for lasing

Besides distributed feedback, there are numerous alternatives to provide a spectrally narrow reflection for a single-mode laser cavity, which can be implemented using the SiN waveguides. This way, the gain section resembling a waveguide-coupled QD-LED presented above can also be designed with wider silicon nitride waveguides, overcoming the limitations of a DFB implementation with a sidewall-corrugated waveguide.

Instead of the average coupling efficiency β_{avg} , crucial for the coupling of spontaneous emission in a LED, the mode overlap with the active material or confinement factor is the decisive parameter for a laser. We therefore adapted our finite element simulations (Lumerical Mode) and report the mode overlap for a 20 nm QD layer in Figure 3.22b. Similar to the simulations in Figure 3.2, we varied the width w and height h of the SiN waveguide, while keeping the total thickness of the organic layers constant at $t = 600$ nm. The contour plot shows, that a maximum mode overlap of 6% can be obtained for a waveguide height of $h = 130$ nm and a width larger than $2 \mu\text{m}$. On the other hand, the waveguide loss plotted on a linear scale in Figure 3.22a is prohibitively high for these dimensions, considering the maximum material gain available from colloidal CdSe/CdS particles. [18]

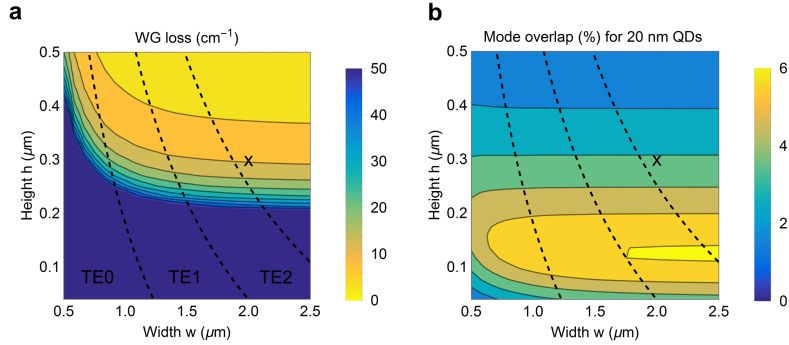


Figure 3.22: Finite element simulations for different width w and height h of the SiN waveguide and a constant thickness $t = 600$ nm of the organic layers. (a) Waveguide loss α on a linear scale. (b) Mode confinement Γ in a 20 nm QD layer on top of the SiN waveguide. The dashed black lines show the onset of higher order TE modes in the SiN waveguide.

As a figure of merit for the dimensions of an electrically pumped QD gain section, we calculated the modal gain g_{net} from the simulated passive waveguide loss α and the mode confinement in the QD layer Γ_{QD} according to

$$g_{\text{net}} = \eta g_i \Gamma_{\text{QD}} - \alpha. \quad (3.9)$$

We therefore assumed a QD packing fraction of $\eta = 50\%$ and varied the intrinsic material gain g_i of the CdSe/CdS QDs. Figures 3.23a-d show that depending on the material gain g_i , different waveguide dimensions will produce a maximum modal gain. For an intrinsic gain of only $g_i = 500 \text{ cm}^{-1}$ it is for instance not possible to obtain a positive net gain for a waveguide height of $h = 300$ nm, which was used for the QD-LEDs presented previously. Yet, CdSe/CdS QDs optimized for a high material gain [18] can provide $g_i = 1500 \text{ cm}^{-1}$ for a moderate excitation level $\langle N \rangle < 3$, which has previously been achieved by dc electrical pumping in the work of *Lim et al.* [10]. Figure 3.23d shows that assuming this higher material gain, a maximum modal gain of 15 cm^{-1} can be obtained for a waveguide height of $h = 300$ nm, for a width exceeding $2 \mu\text{m}$. This is low compared to a reported modal gain $212\text{-}350 \text{ cm}^{-1}$ for the optically pumped DFB lasers in the work of *Zhu et al.* [6]. However, a low modal gain can be compensated by designing a correspondingly longer gain section.

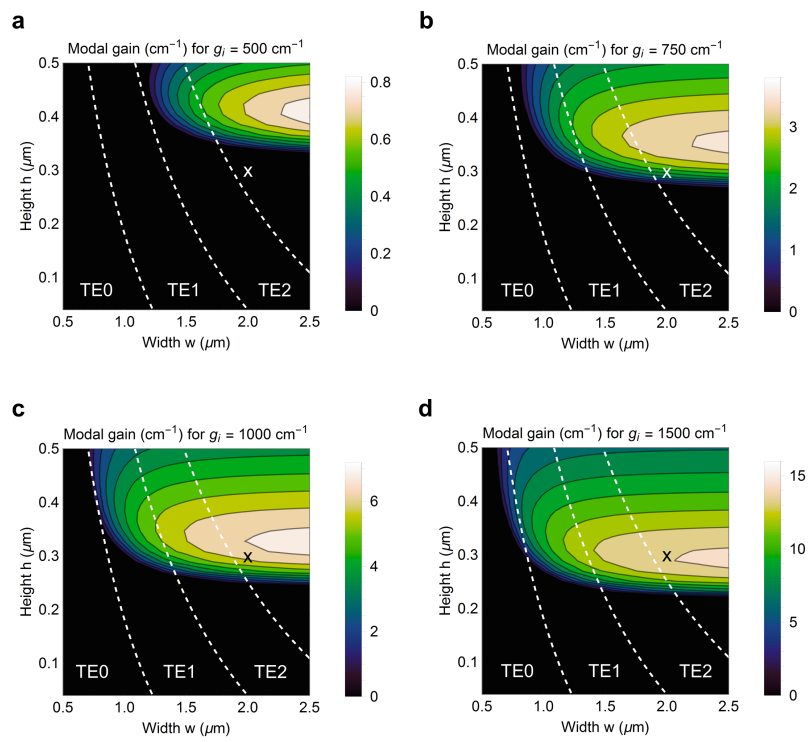


Figure 3.23: Figure of merit for a waveguide-coupled QD laser. (a) Modal gain calculated for a material gain of $g_i = 500 \text{ cm}^{-1}$ of a 20 nm QD layer with a fill-factor of 50%. (b) Modal gain for $g_i = 750 \text{ cm}^{-1}$. (c) Modal gain for $g_i = 1000 \text{ cm}^{-1}$. (d) Modal gain for $g_i = 1500 \text{ cm}^{-1}$.

3.9 Conclusion and outlook

In Summary, we have demonstrated waveguide-coupled colloidal quantum dot devices, which can be operated as detectors and LEDs. We anticipate that these devices can find applications in chip-based absorption spectroscopy, as they can be post-processed on foundry-fabricated waveguide platforms, at a low cost. For the LEDs we report a record current density of up to 100 A/cm^2 and a maximum on-chip power of almost 2 nW in a single-mode waveguide. The detectors have a low dark current of $1.5 \mu\text{A/cm}^2$ at a reverse bias of 7 V , but show a non-linear photocurrent response. We believe that with further progress in the process development, we can improve the internal quantum efficiency of both types of devices to reach the values reported in literature for planar designs. [17, 31]

The LED output power of 2 nW is mainly limited by the poor average coupling efficiency $\beta_{avg} = 0.8\%$, governing the process of spontaneous emission. However, for the reported current densities stimulated emission is within reach, [10] potentially enabling output powers in the μW range and a corresponding improvement of the external quantum efficiency. While the devices are currently still limited by adverse effects hampering the observation of optical transparency, we believe that our approach solves a key challenge in building an electrically pumped laser using colloidal QDs. In addition to inherent current-focusing built into our devices, the passive silicon nitride waveguide makes it possible to decouple the optical mode profile from the thickness of the QD layer. In combination with the low-loss n-contact layer, also thin QD layers, which can be inverted using an electrical bias, [10] are expected to provide sufficient gain for lasing to occur.

Lastly, we have observed indications of lasing for a thin CdSe/CdS QD layer on top of a ZnO coated silicon nitride waveguide from ns-optical pumping, confirming that the QDs can indeed provide sufficient gain to offset the passive optical loss from the charge injection layers.

References

- [1] L. Elsinger, I. Tanghe, F. V. Acker, N. K. Zawacka, R. Petit, K. Neyts, C. Detavernier, P. Geiregat, Z. Hens, and D. V. Thourhout. *A Waveguide-Coupled Colloidal Quantum Dot LED on a Silicon Nitride Platform*. In Conference on Lasers and Electro-Optics, page STh1J.8. Optical Society of America, 2020.
- [2] C. Dang, J. Lee, C. Breen, J. S. Steckel, S. Coe-Sullivan, and A. Nurmikko. *Red, green and blue lasing enabled by single-exciton gain in colloidal quantum dot films*. Nat. Nanotechnol., 7(5):335–339, may 2012.
- [3] C. Dang, J. Lee, K. Roh, H. Kim, S. Ahn, H. Jeon, C. Breen, J. S. Steckel, S. Coe-Sullivan, and A. Nurmikko. *Highly efficient, spatially coherent distributed feedback lasers from dense colloidal quantum dot films*. Appl. Phys. Lett., 103(17):171104, oct 2013.
- [4] M. M. Adachi, F. Fan, D. P. Sellan, S. Hoogland, O. Voznyy, A. J. Houtepen, K. D. Parrish, P. Kanjanaboos, J. A. Malen, and E. H. Sargent. *Microsecond-sustained lasing from colloidal quantum dot solids*. Nat. Commun., 6(1):8694, dec 2015.
- [5] W. Xie, T. Stöferle, G. Rainò, T. Aubert, S. Bisschop, Y. Zhu, R. F. Mahrt, P. Geiregat, E. Brainis, Z. Hens, and D. Van Thourhout. *On-Chip Integrated Quantum-Dot-Silicon-Nitride Microdisk Lasers*. Adv. Mater., 29(16):1604866, apr 2017.
- [6] Y. Zhu, W. Xie, S. Bisschop, T. Aubert, E. Brainis, P. Geiregat, Z. Hens, and D. Van Thourhout. *On-Chip Single-Mode Distributed Feedback Colloidal Quantum Dot Laser under Nanosecond Pumping*. ACS Photonics, 4(10):2446–2452, oct 2017.
- [7] F. Fan, O. Voznyy, R. P. Sabatini, K. T. Bicanic, M. M. Adachi, J. R. McBride, K. R. Reid, Y.-S. Park, X. Li, A. Jain, R. Quintero-Bermudez, M. Saravanapavanantham, M. Liu, M. Korkusinski, P. Hawrylak, V. I. Klimov, S. J. Rosenthal, S. Hoogland, and E. H. Sargent. *Continuous-wave lasing in colloidal quantum dot solids enabled by facet-selective epitaxy*. Nature, 544(7648):75–79, apr 2017.
- [8] Z. Yang, M. Pelton, I. Fedin, D. V. Talapin, and E. Waks. *A room temperature continuous-wave nanolaser using colloidal quantum wells*. Nat. Commun., 8(1):143, dec 2017.
- [9] Y. Shirasaki, G. J. Supran, M. G. Bawendi, and V. Bulović. *Emergence of colloidal quantum-dot light-emitting technologies*. Nat. Photonics, 7(1):13–23, jan 2013.

- [10] J. Lim, Y.-S. Park, and V. I. Klimov. *Optical gain in colloidal quantum dots achieved with direct-current electrical pumping*. Nat. Mater., 17(1):42–49, jan 2018.
- [11] J. Roh, Y.-S. Park, J. Lim, and V. I. Klimov. *Optically pumped colloidal-quantum-dot lasing in LED-like devices with an integrated optical cavity*. Nat. Commun., 11(1):271, dec 2020.
- [12] A. Z. Subramanian, E. Ryckeboer, A. Dhakal, F. Peyskens, A. Malik, B. Kuyken, H. Zhao, S. Pathak, A. Ruocco, A. De Groote, P. Wuytens, D. Martens, F. Leo, W. Xie, U. D. Dave, M. Muneeb, P. Van Dorpe, J. Van Campenhout, W. Bogaerts, P. Bienstman, N. Le Thomas, D. Van Thourhout, Z. Hens, G. Roelkens, and R. Baets. *Silicon and silicon nitride photonic circuits for spectroscopic sensing on-a-chip [Invited]*. Photonics Res., 3(5):B47, oct 2015.
- [13] X. Ji, F. A. S. Barbosa, S. P. Roberts, A. Dutt, J. Cardenas, Y. Okawachi, A. Bryant, A. L. Gaeta, and M. Lipson. *Ultra-low-loss on-chip resonators with sub-milliwatt parametric oscillation threshold*. Optica, 4(6):619, jun 2017.
- [14] K. Alexander, J. P. George, J. Verbist, K. Neyts, B. Kuyken, D. Van Thourhout, and J. Beeckman. *Nanophotonic Pockels modulators on a silicon nitride platform*. Nat. Commun., 9(1):3444, dec 2018.
- [15] C. O. de Beek, L. Elsinger, B. Haq, G. Roelkens, and B. Kuyken. *Heterogeneously Integrated Laser on a Silicon Nitride Platform via Micro-Transfer Printing*. In Frontiers in Optics + Laser Science APS/DLS, page FTu6B.1. Optical Society of America, 2019.
- [16] C. Xiang, W. Jin, J. Guo, J. D. Peters, M. J. Kennedy, J. Selvidge, P. A. Morton, and J. E. Bowers. *Narrow-linewidth III-V/Si/Si₃N₄ laser using multilayer heterogeneous integration*. Optica, 7(1):20, jan 2020.
- [17] B. S. Mashford, M. Stevenson, Z. Popovic, C. Hamilton, Z. Zhou, C. Breen, J. Steckel, V. Bulovic, M. Bawendi, S. Coe-Sullivan, and P. T. Kazlas. *High-efficiency quantum-dot light-emitting devices with enhanced charge injection*. Nat. Photonics, 7(5):407–412, 2013.
- [18] S. Bisschop, P. Geiregat, T. Aubert, and Z. Hens. *The Impact of Core/Shell Sizes on the Optical Gain Characteristics of CdSe/CdS Quantum Dots*. ACS Nano, 12(9):9011–9021, sep 2018.

- [19] Y. Y. Ussembayev, Z. Hens, and K. Neyts. *Contrasting Anisotropy of Light Absorption and Emission by Semiconductor Nanoparticles*. ACS Photonics, 6(5):1146–1152, may 2019.
- [20] A. Rahim, J. Goyvaerts, B. Szlag, J.-M. Fedeli, P. Absil, T. Aalto, M. Harjanne, C. Littlejohns, G. Reed, G. Winzer, S. Lischke, L. Zimmermann, D. Knoll, D. Geuzebroek, A. Leinse, M. Geiselmann, M. Zervas, H. Jans, A. Stassen, C. Dominguez, P. Munoz, D. Domenech, A. L. Giesecke, M. C. Lemme, and R. Baets. *Open-Access Silicon Photonics Platforms in Europe*. IEEE J. Sel. Top. Quantum Electron., 25(5):1–18, sep 2019.
- [21] R. L. Puurunen. *Surface chemistry of atomic layer deposition: A case study for the trimethylaluminum/water process*. Journal of Applied Physics, 97(12):121301, jun 2005.
- [22] T. Tynell and M. Karppinen. *Atomic layer deposition of ZnO: a review*. Semiconductor Science and Technology, 29(4):043001, apr 2014.
- [23] X. Jiang, F. L. Wong, M. K. Fung, and S. T. Lee. *Aluminum-doped zinc oxide films as transparent conductive electrode for organic light-emitting devices*. Applied Physics Letters, 83(9):1875–1877, sep 2003.
- [24] M. Lim, W. Yunus, Z. Talib, C. Dee, and A. Ismail. *Electrical and Optical Properties of N, N'-Bis (Inaphthyl)-N,N'-Diphenyl-1,1'-Biphenyl-4,4'-Diamine as Hole Transport Layer in Organic Light Emitting Devices*. Am. j. eng. appl. sci., 3(1):64–67, jan 2010.
- [25] S. A. Empedocles. *Quantum-Confined Stark Effect in Single CdSe Nanocrystallite Quantum Dots*. Science, 278(5346):2114–2117, dec 1997.
- [26] N. Kholmicheva, P. Moroz, H. Eckard, G. Jensen, and M. Zamkov. *Energy Transfer in Quantum Dot Solids*. ACS Energy Lett., 2(1):154–160, jan 2017.
- [27] Z. Zhang, Y. Ye, C. Pu, Y. Deng, X. Dai, X. Chen, D. Chen, X. Zheng, Y. Gao, W. Fang, X. Peng, and Y. Jin. *High-Performance, Solution-Processed, and Insulating-Layer-Free Light-Emitting Diodes Based on Colloidal Quantum Dots*. Adv. Mater., 30(28):1–8, 2018.
- [28] J. Lim, Y.-S. Park, K. Wu, H. J. Yun, and V. I. Klimov. *Droop-Free Colloidal Quantum Dot Light-Emitting Diodes*. Nano Lett., 18(10):6645–6653, oct 2018.

-
- [29] Z. Hens and I. Moreels. *Light absorption by colloidal semiconductor quantum dots*. J. Phys. Chem., 22(21):10406, 2012.
- [30] Y. Justo, P. Geiregat, K. V. Hoecke, F. Vanhaecke, C. De Mello Donega, and Z. Hens. *Optical properties of PbS/CdS Core/shell quantum dots*. J. Phys. Chem. C, 117(39):20171–20177, 2013.
- [31] P. Malinowski, E. Georgitzikis, J. Maes, I. Vamvaka, F. Frazzica, J. Van Olmen, P. De Moor, P. Heremans, Z. Hens, and D. Cheyns. *Thin-Film Quantum Dot Photodiode for Monolithic Infrared Image Sensors*. Sensors, 17(12):2867, dec 2017.

Chapter 4

Integration of colloidal PbS/CdS quantum dots with plasmonic antennas and superconducting detectors on a silicon nitride photonic platform

Single-photon sources and detectors are indispensable building blocks for integrated quantum photonics, a research field that is seeing ever increasing interest for numerous applications. Here, we implemented essential components for a Quantum Key Distribution (QKD) transceiver on a single photonic chip. Plasmonic antennas on top of silicon nitride waveguides provide Purcell enhancement with a concurrent increase of the count rate, speeding up the microsecond radiative lifetime of IR-emitting colloidal PbS/CdS Quantum Dots (QDs). The use of low-fluorescence silicon nitride with a waveguide loss smaller than 1 dB/cm, made it possible to implement high extinction ratio optical filters and low insertion loss spectrometers. Waveguide-coupled Superconducting Nanowire Single-Photon Detectors (SNSPDs) allow for low time-jitter single-photon detection. To showcase the performance of the components, we demonstrate on-chip lifetime spectroscopy of PbS/CdS QDs. The method developed in this chapter is predicted to scale down to single QDs and newly developed emitters can be readily integrated on the chip-based platform.

The work presented here is the result of a close collaboration with Ronan Gourgues, associated with Single Quantum, a company specialized on SNSPDs and partner in the PHONSI consortium. Ronan realized the experiments at cryogenic temperatures and designed the required experimental set-up. It was my task to design the photonic circuits, process silicon nitride waveguides, including plasmonic antennas and quantum dots, perform the passive characterizations and analyze the results of all experiments. The material presented in this chapter has in part been published as a journal paper [1] and several conference contributions [2–4]. Earlier results on the incorporation of colloidal QDs in the gap of plasmonic bowtie antennas have been published in reference [5].

4.1 Introduction

Most applications of single-photon sources in quantum optical technology have very stringent requirements on single-photon properties such as purity and indistinguishability [6]. Therefore, for a long time the most commonly used single-photon sources were based on spontaneous parametric down-conversion, which offers pure and indistinguishable heralded single-photon emission, but is probabilistic in nature [7]. Recently, epitaxial QDs have reached a high maturity level as deterministic single-photon emitters [8] enabling applications in several quantum photonic technologies. [9–11]

The unrivaled performance of SNSPDs in terms of system detection efficiency, dark count rate and temporal resolution [12–14] has made them indispensable for many quantum optics experiments. In addition, SNSPDs can be integrated with different photonic platforms while maintaining a small footprint [15–18]. Progress has been made in integrating epitaxial QDs with SNSPDs on the same chip [19], but the rather large waveguide loss is a main hindrance to the development of more complex photonic circuits. Hybrid integration approaches with epitaxial QDs [20–24] make use of the low waveguide loss of silicon photonics to be compliant with the requirements of quantum optics protocols.

Among other promising single photon emitters [6], colloidal QDs are especially interesting due to recent improvements of their single-photon emission purity and stability, [25–27] while solution processing allows for a flexible integration [28]. By looking at the current performance metrics, only the application with the lowest requirements on single-photon purity and indistinguishability, Quantum Key Distribution (QKD) [6] seems to be within reach. The original BB84 QKD protocol requires single-photon sources in its security proof [29]. However, modern decoy state protocols are also provably secure using attenuated lasers as sources, although at the cost of

reduced key generation rate [30–32]. QD single-photon emitters reaching the maximum average photon number per pulse of $\langle n \rangle = 1$ may outperform laser sources and have been employed for long-range QKD [33]. A chip-level implementation of QKD has been achieved with integrated lasers, [34] but remains elusive for true single-photon emitters. Key properties to be competitive with state-of-the-art decoy state protocols [32] are a fast source in the GHz range at a telecom wavelength where optical fiber losses are minimal and a narrow emission linewidth to enable Wavelength Division Multiplexing (WDM) and thus further enhance the key generation rate. Also, low-loss photonic waveguides, filters and spectrometers that retain a high average photon number $\langle n \rangle$ during the encoding and highly efficient single-photon detectors for telecom wavelengths are essential, as well as a low detector dark count rate to minimize the QKD error rate.

In this work we present a silicon nitride photonic platform that implements several of those components, as shown in Figure 4.1. A single chip contains colloidal QD emitters placed in the gap of plasmonic antennas that were fabricated on top of silicon nitride waveguides (I), sidewall corrugated grating filters for pump rejection (II) and a Planar Concave Grating (PCG) spectrometer (III) of which four channels are connected to waveguide-coupled SNSPDs (IV). All components were connected by low-loss photonic waveguides surrounded by metal strips to suppress stray light coupling (V).

For QKD fast sources are required, therefore a short radiative lifetime of QD emitters is crucial to be competitive compared to state-of-the-art implementations with attenuated pulsed lasers, achieving a repetition rate around 1 GHz. [34] Purcell enhancement of emitters placed in dielectric cavities or in the high local density of states (LDOS) field of plasmonic antennas is a common way to reduce the radiative lifetime without the need for engineering the emitter itself. [35–38] Here, we used the widely studied plasmonic gap antenna in a bowtie shape [39] (30 nm evaporated gold and a gap width of 25 nm) to improve the microsecond radiative lifetime of IR-emitting colloidal PbS/CdS QDs, coupling the emission directly to silicon nitride waveguides and measuring the photoluminescence (PL) decay trace with SNSPDs located on the same chip. For reference measurements we also fabricated isolated pillars of QDs on the same waveguides.

4.2 Antenna design and simulation

The effect of a plasmonic antenna on an emitter is most conveniently expressed in terms of the LDOS and commonly referred to as Purcell enhancement. Due to the metal losses of the antenna, there is a nonradiative

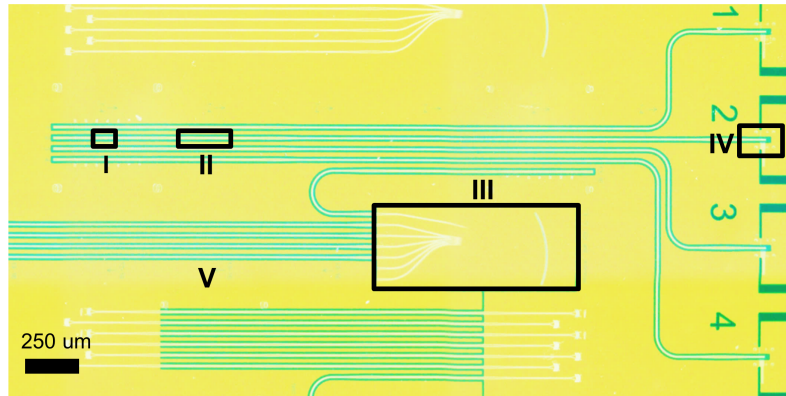


Figure 4.1: Optical microscope image of the SiN photonic chip. There are areas with colloidal QD emitters and plasmonic antennas (I), filters for pump rejection (II), a Planar Concave Grating (PCG) spectrometer (III) of which four channels are connected to waveguide-coupled SNSPD detectors (III). All components are connected by waveguides which are surrounded by metal strips to suppress stray light coupling (V). For measurements with SNSPDs the chip was cooled down in a helium bath cryostat to a temperature of 4.2 K.

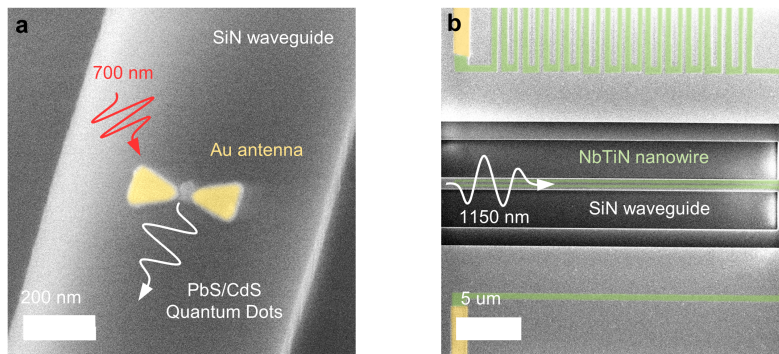


Figure 4.2: False-color SEM pictures of the main components. (a) SiN waveguide with a plasmonic bowtie antenna and a patch of colloidal QDs patterned on top of it. (b) The QD emission was detected by U-shaped superconducting detectors placed underneath the SiN waveguides.

contribution in addition to the radiative local density of states (LRDOS), leading to a nonradiative and radiative part of the PL decay rate [37]

$$\gamma_{ant} = \gamma_{0,nr} + \gamma_{0,r} (\text{LDOS} - \text{LRDOS}) + \gamma_{0,r} \text{LRDOS}, \quad (4.1)$$

where $\gamma_{0,nr}$ and $\gamma_{0,r}$ are the nonradiative and radiative decay rate of the emitter in absence of the antenna. We therefore first simulated the decay rate of a classical dipole emitter with a displacement vector \mathbf{d} in the direction of the antenna axis using a commercial Finite Difference Time Domain (FDTD) solver (Lumerical) and extracted LDOS and LRDOS, normalizing the values to a homogeneous background medium in the absence of the antenna. For the LRDOS map in Figure 4.3a, the in-plane position of the dipole emitter was swept and the values were recorded for the center wavelength of the PbS/CdS QD emission at $\lambda = 1150$ nm. The false-color SEM picture of a fabricated structure in Figure 4.3b shows a small pillar of QDs deterministically positioned in the gap of the antenna. The simulated LDOS(λ) for a dipole emitter in the center of the gap in Figure 4.3d shows a broad antenna resonance that matches the PbS/CdS QD photoluminescence emission spectrum in Figure 4.3c. Figure 4.3d also shows a reduction and red-shift of the LRDOS(λ), when including the pillar of QDs in the simulation with refractive index data from ellipsometry measurements. Taking this into account and sweeping the position of the dipole emitter within the volume of the QD pillar, gave an average LRDOS of 150. A slight misalignment of the QD pillar 20 nm off the antenna center perpendicular to the dipole moment, as can be observed in Figure 4.3b reduces this value to 100, for a larger misalignment of 50 nm, the enhancement factor drops to 6. The fraction of LRDOS(λ)/LDOS(λ) gives an antenna efficiency $>70\%$ for most of the QD emission spectrum and the respective map for the center wavelength can be found in Figure 4.4b. For the simulation, the position of the dipole emitter was swept in x- and y-direction and the total and radiative rate were recorded for a wavelength of 1150 nm using two sets of power monitors, one enclosing only the dipole emitter and the second the whole antenna. Second-order interpolation of the data points (spacing of 3 nm around antenna gap, 10 nm for the remaining area) was used to generate the plot, while only simulating one quarter and making use of the mirror symmetry of the geometry. For all Purcell enhancement simulations we used a cubic simulation volume of $0.6 \times 0.6 \times 0.6 \mu\text{m}^3$ terminated with Perfectly Matched Layer (PML) boundaries and a mesh refinement to 1 nm^3 surrounding the plasmonic antenna. The simulation was terminated after the total energy in the simulation volume had decreased to 10^{-5} times its initial value or a simulation time of 500 fs. Convergence of the simulations was further confirmed by varying the simulated volume and mesh size. The

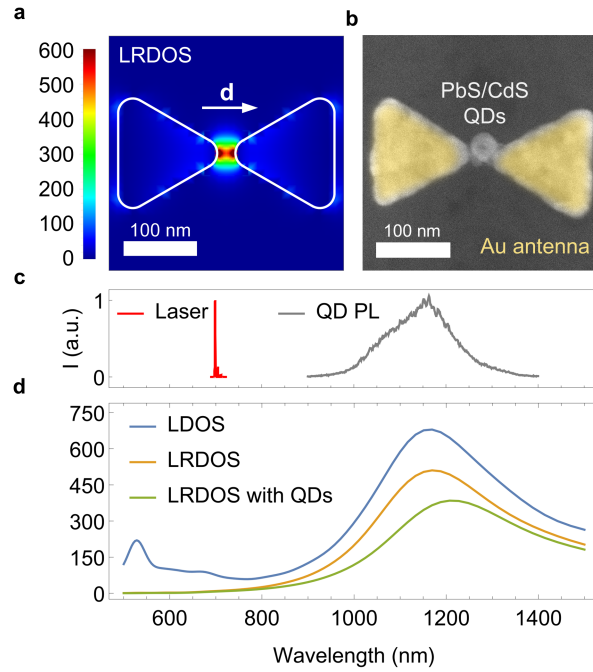


Figure 4.3: The map of the LRDOS in (a) results from Finite Difference Time Domain (FDTD) simulation of a dipole emitter with displacement vector \mathbf{d} . The SEM micrograph of the fabricated bowtie antenna with a small patch of PbS/CdS QDs deterministically positioned in the antenna gap (b) was colored to highlight the different materials. (c) Spectrum of the excitation laser and the QD PL emission at 4.2 K. (d) Comparison of the simulated LDOS for an emitter in the center of the antenna gap and the LRDOS for an empty antenna as well as for an antenna with a QD pillar placed in the gap.

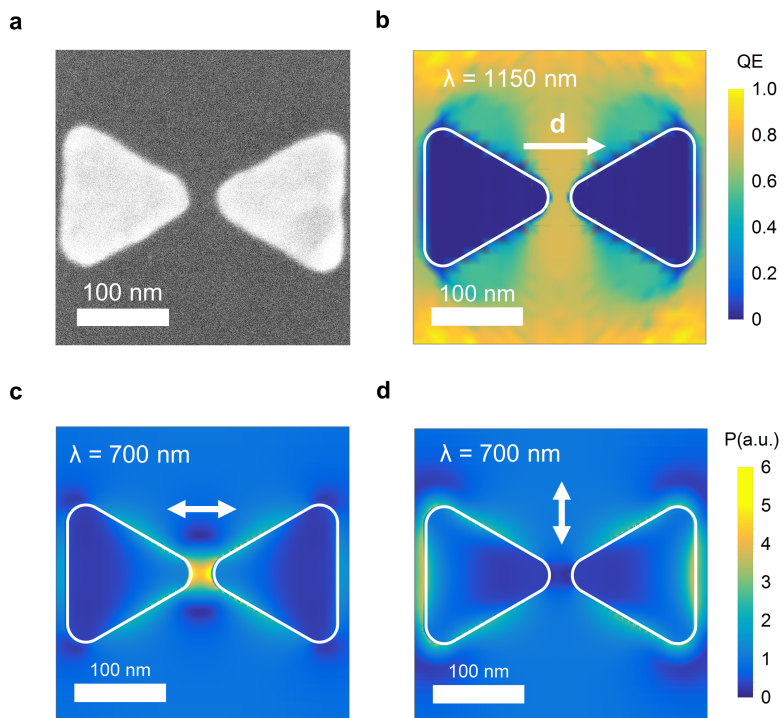


Figure 4.4: FDTD simulation of the plasmonic bowtie antenna. (a) SEM top-view of a fabricated antenna (30 nm evaporated gold and a gap width of 25 nm). (b) Simulated antenna quantum efficiency $QE = LRDOS/LDOS$ for the center wavelength of the QD emission. (c) Polarization dependent excitation enhancement for a pump wavelength of 700 nm, parallel and (d) perpendicular to the antenna dipole axis.

SEM top-view of a fabricated bowtie antenna in Figure 4.4a shows, that the size, gap width and the corner radius used in the simulations are realistic approximations, which can be achieved in practice.

The bowtie antenna also has a small resonance at the pump laser wavelength of 700 nm, which can be seen from the polarization dependent excitation enhancement maps displayed in Figure 4.4c-d. For the simulation of the excitation enhancement we used a Gaussian beam source with different polarization orientation, which was incident on an antenna placed on top of a silicon nitride waveguide. The electromagnetic field power was recorded for a wavelength of 700 nm and normalized using a separate simulation without the plasmonic antenna. Clearly, there is only a significant excitation enhancement in the antenna gap for a pump laser polarization parallel to the antenna axis. A polarization perpendicular to the antenna axis even causes a slight reduction of the excitation power, compared to a plain SiN waveguide. To reduce the scattering of the pump laser we used the perpendicular polarization for the experiments described below.

To measure the resonance of the plasmonic bowtie antennas we fabricated an array with a pitch of 300 nm on a quartz coated glass substrate using the procedure described below. The transmission referenced to a plain substrate was measured in a PerkinElmer Lambda 950 spectrometer. For the comparison with the transmission from FDTD simulation in Figure 4.5a the measured value had to be rescaled, since the size of the illuminated spot was much larger than the array of antennas. There is good agreement of the width and position of the antenna resonance between measurement and simulation. This finding supports the validity of the FDTD antenna simulations presented here.

We further used an extended FDTD simulation region to extract the coupling efficiency to the TE and TM waveguide mode for the case of an antenna and compare this to the case of an isolated pillar of QDs. Calculating the mode overlap using dedicated power monitors and extracting the emission in a single direction we arrived at the values displayed in Figure 4.5b. For the antenna we assumed exclusively TE polarized emission and report a coupling efficiency of $\beta_{ant} \sim 12\%$ to the fundamental TE mode. In absence of the antenna there is a larger variation of the coupling efficiency depending on the distance of the emitter from waveguide surface and we arrive at an average value of $\sim 11\%$ within the volume of the QD pillar, for both TE and TM polarization. For a polarization direction along the waveguide there is no appreciable coupling to a guided mode and therefore the overall coupling efficiency amounts to

$$\beta_0 = \frac{1}{3} (\beta_{0,TE} + \beta_{0,TM}). \quad (4.2)$$

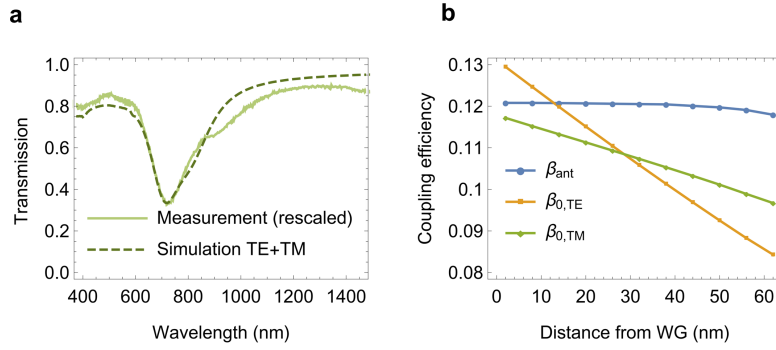


Figure 4.5: (a) Transmission spectrum of an array of plasmonic bowtie antennas fabricated on a glass substrate. (b) Simulation of the coupling efficiency to the TE and TM waveguide mode for an emitter in the gap of a plasmonic antenna.

4.3 Waveguide-coupled nanowire detectors

An extensive discussion of the superconducting nanowire single-photon detectors (SNSPDs) used in this work can be found in reference [40]. In this section we only estimate the relevant performance metrics for the on-chip experiments, in particular the detector quantum efficiency for the emission wavelength of the PbS/CdS QDs at cryogenic temperatures.

The detectors were implemented as U-shaped 9.5 nm thin and 70 nm wide NbTiN nanowires, with 300 nm thick SiN waveguides fabricated directly above (see SEM top-view in Figure 4.2b and Figure 4.7b). Therefore, the detector quantum efficiency is the product of the probability that a photon in the SiN waveguide mode will get absorbed by the nanowire and the probability that this absorption event will lead to a detector count. To evaluate the detector efficiency, we first simulated the optical absorption of the nanowire with a FDTD solver (Lumerical), using complex refractive index values obtained from ellipsometry. In the simulation, we launched the TE(TM) polarized fundamental waveguide mode into the structure and recorded the transmitted power after introducing the NbTiN nanowire below the waveguide, as well as the total scattered and reflected power. With a scattered power of 1.1%(1.5%) for TE(TM) polarization, the simulations suggest that the reduction of the detection efficiency due to light scattering and back-reflection is minor. In practice, fabrication imperfections might lead to an increased contribution. The corresponding mode profiles of the fundamental TE(TM) mode of the 1 μm wide and 300 nm high SiN waveguide on top of a nanowire are displayed in Figure 4.6a-b. Note that due to

the fabrication process a ~ 20 nm thin layer of HSQ electron-beam resist remained on top of the NbTiN, which was included in the simulations. Fig-

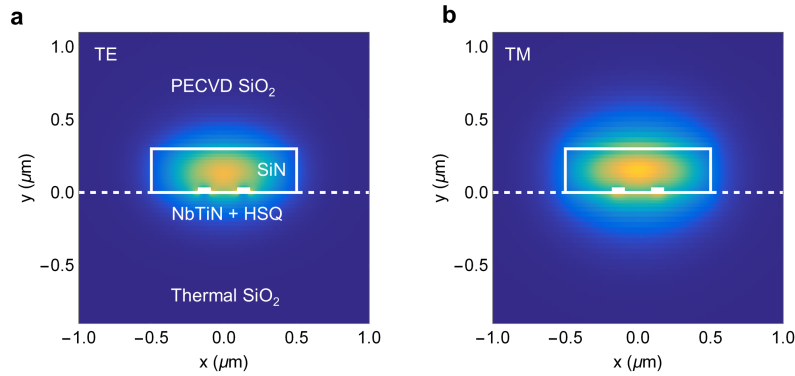


Figure 4.6: Mode profile for an oxide-clad SiN waveguide on top of superconducting NbTiN wires. (a) The fundamental transverse electric (TE) and (b) the fundamental transverse magnetic (TM) mode.

Figure 4.7a shows the simulated absorption for TE and TM polarization, overlaid with an exponential fit of the data points. For the fabricated nanowire length of $25 \mu\text{m}$, the absorption reaches 98%(82%) for the TE(TM) mode respectively. The SEM top-view of a fabricated waveguide-coupled SNSPD in Figure 4.7b, before the deposition of the top oxide, clearly shows the U-shaped outline of the hidden nanowire visible on the surface of the SiN waveguide. The patterned NbTiN nanowire and remaining HSQ resist on top have a total thickness of ~ 30 nm, which is translated to a respective profile on top of the SiN waveguide, providing the contrast in the SEM micrograph. Next to that, a slight misalignment of the nanowire and the waveguide can be observed in Figure 4.7b. Both effects however, were found to have a negligible effect on the nanowire absorption in FDTD simulations.

As a second step we estimated the internal efficiency of the SNSPDs, which is defined as the probability to generate a detection event after the absorption of a photon by the nanowire. The detectors were characterized at 4.2 K in a liquid helium bath cryostat using two attenuated lasers with wavelengths of 1050 nm and 1300 nm, enclosing the QD emission (see Figure 4.3c). The SNSPDs were biased with a tuneable current source and the detection events were registered by a high-speed counter after being amplified with a two-stage low noise RF amplifier. As shown in Figure 4.8a, detector 1 presents unity internal efficiency for 1050 nm resulting in a saturation of the Photon Count Rate (PCR) whilst increasing the bias current.

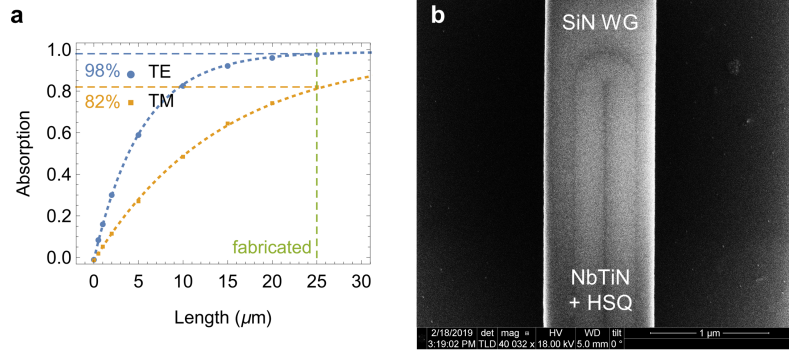


Figure 4.7: Simulated absorption of the waveguide-coupled SNSPD. (a) Absorption from FDTD simulations for the fundamental TE and TM mode of a $1 \mu\text{m}$ wide and 300 nm high SiN waveguide. (b) SEM top-view of a fabricated structure, showing a slight misalignment of the U-shaped nanowire and the SiN waveguide.

Even though the saturation regime was not reached for all detectors and wavelengths, we were still able to estimate the internal detection efficiency based on theories for narrow superconducting nanowires. Recent publications on SNSPDs optical detection mechanism [41] attribute the shape of the PCR curve as function of bias current for low energy photons, to Fano fluctuations. In this model, a detection event for a certain bias current is produced if enough quasi-particles are generated. As a consequence, a sigmoidal shape is expected, and we used an error function to fit the data. The fitted coefficient was used to normalize the data displayed in Figure 4.8. For the PL lifetime measurements, the bias current of the detectors was chosen to obtain a DCR of ~ 150 cps, the respective current is marked for the two different SNSPDs in Figure 4.8a and b. Using this method the internal efficiency of the first detector could be estimated to be between 95% and 99% for wavelengths between 1300 nm and 1050 nm , for the second detector the values were 70% and 95% respectively. The characterisations were conducted for a multitude of different detectors and the results presented here can be seen as a typical "good" and "still usable" detector for the PL lifetime experiments.

Timing jitter and dead time are also important performance metrics for SNSPDs. The timing jitter is the variation in time between the absorption of a photon along the superconducting nanowire and the generation of an electrical output pulse. The probability of the arrival time uncertainty follows a Gaussian distribution and the timing jitter is defined as the full

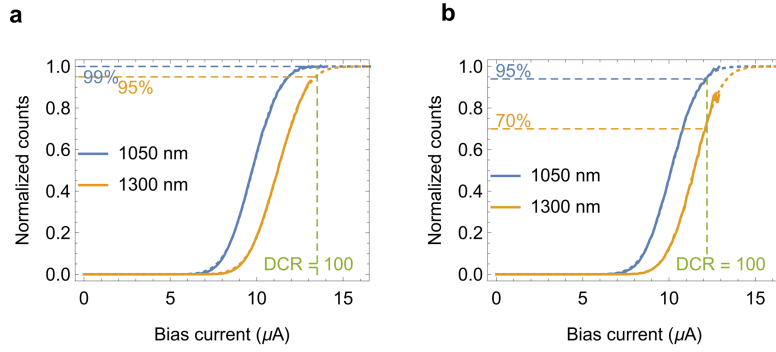


Figure 4.8: Estimation of the SNSPD internal detection efficiency for two different nanowires in (a) and (b). The dark counts were subtracted from the counts observed with illumination and an error function was fitted for the normalization where the saturation regime could not be reached. For a bias current corresponding to a Dark Count Rate (DCR) of 100 cps the extracted internal detection efficiency for the first detector in (a) is between 95% and 99% for the wavelength range of interest. The second detector in (b) has a significantly lower internal efficiency between 70% and 95%.

width at half-maximum (FWHM). The integrated arrival time difference of electrical pulses from a 86 MHz picosecond pulsed laser (Coherent Mira 900) and the superconducting detector was registered with a fast digital oscilloscope (LeCroy Waverunner 640Zi 4 GHz, 40 GS/s). As result we obtained a histogram as shown in Figure 4.9a and by using a Gaussian fit we calculated the temporal resolution of the selected device, which gave a timing jitter of 43 ± 3 ps. For our experiments the main source of the timing jitter was electrical noise.

The dead time is the time during which the bias current, i.e. the detection efficiency, is fully restored in the detector after absorbing a photon. Figure 4.9b shows the electrical output pulse of a selected SNSPD registered with a fast digital oscilloscope (LeCroy). From the exponential decay of the detection pulse we extracted a recovery time of $\tau_{exp} \sim 9$ ns. This value is in good agreement with the theoretical value calculated from the fraction of kinetic inductance of the superconducting nanowire (~ 500 nH) and the load resistance (50Ω), $\tau_{theory} \sim 10$ ns.

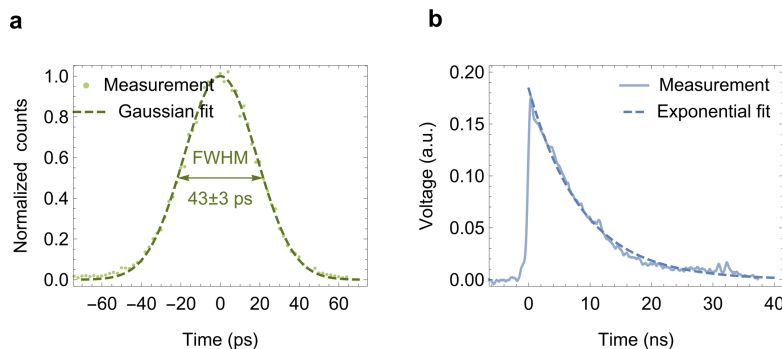


Figure 4.9: For the extraction of the SNSPD time jitter the binned data was fitted with a Gaussian for the normalization (a). The decay pulse in (b) was fitted with an exponential to extract the recovery time of the detector.

4.4 Colloidal PbS/CdS QDs

The IR-emitting colloidal PbS/CdS QDs used for the experiments presented in the following sections, were synthesised¹ according to literature procedures [42], with details reported in the Appendix A.3. Figure 4.10 compares the PL spectrum of the QD sample in solution with the emission from thin films at room temperature and in a liquid helium cryostat at 4 K. While the solution spectrum is well-represented by a Gaussian fit, the emission from the drop-casted film appears quite noisy. Still, there is a clear red-shift of the emission for the thin film of approximately 50 nm (50 meV). In addition, the photoluminescence quantum yield, measured using an integrating sphere, [43] was reduced from 8.5% in solution to 2.5% for the thin film at room temperature. We reason that energy transfer to larger QDs caused the red-shift in the thin film, whereas energy transfer to non-emissive dots causes an additional non-radiative decay channel and in turn the observed reduction of the PL quantum yield. It can further be seen from Figure 4.10 that the inhomogeneously broadened emission spectrum of the thin film gets narrower at cryogenic temperature, with a corresponding reduction of the FWHM from 245 nm to 172 nm. We attribute this to the expected reduction of the linewidth of individual PbS/CdS QDs at cryogenic temperatures.

¹The PbS/CdS QD synthesis and basic characterization was performed by Jorick Maes, associated with the Physics and Chemistry of Nanocrystals (PCN) research group of Ghent University

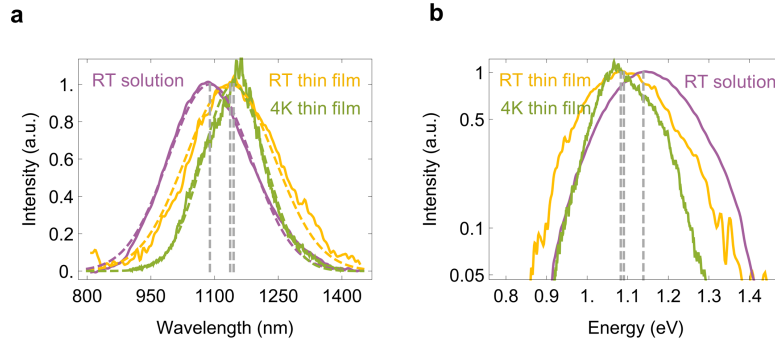


Figure 4.10: Comparison of the photoluminescence emission spectrum of the PbS/CdS QD sample in solution and a drop-casted film at room temperature and at cryogenic temperatures. Dashed lines represent Gaussian fits and the extracted central wavelengths.

4.5 Fabrication process

Fabrication started (see Figure 4.11) from a silicon wafer, which was thermally oxidized to form $3.6 \mu\text{m}$ of SiO_2 , which served as the bottom cladding for the photonic waveguides. Next, a 9.5 nm thin NbTiN layer was deposited using magnetron co-sputtering in an Ar and N_2 atmosphere.² Subsequently, Cr/Au contacts were formed using e-beam lithography, evaporation and lift-off. The nanowires were patterned on hydrogen silsesquioxane (HSQ) e-beam resist using a 100 kV lithography system, then the pattern was transferred to the NbTiN layer by dry etching using SF_6 and O_2 chemistry.³ For the purpose of prototyping, each chip housed 16 devices fabricated on a sample size of $1 \times 1 \text{ cm}^2$, which was limited by the range of the translation stages used for the experiments. The active part of the detector, shown in Figure 4.2b and Figure 4.7b, forms a U-shape with 70 nm wide nanowires separated by a 200 nm gap. To avoid latching due to the small kinetic inductance of the nanowire, a 2.5 mm long and 400 nm wide section serving as a series inductor was included.

By fabricating the SNSPDs first it was possible to test and pre-select the devices [40] before continuing the processing with the deposition of 300 nm silicon nitride using low-frequency plasma-enhanced chemical vapor depo-

²The deposition of the NbTiN layer was performed in the lab of Prof. Val Zwiller at Applied Physics department of KTH Stockholm, Sweden

³Patterning of the Cr/Au contacts and the NbTiN nanowires was performed by Dr. Iman E. Zadeh, associated with the Optics Research Group of Delft University of Technology, The Netherlands

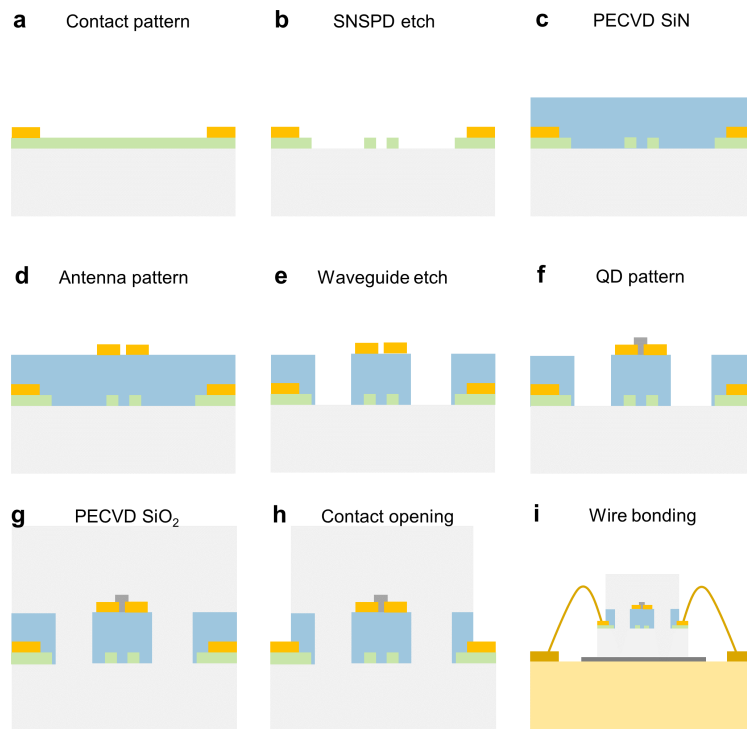


Figure 4.11: Main processing steps for the fabrication. (a) Patterning of Cr/Au contacts on top of a Si samples coated with thermal SiO₂ and a 9.5 nm layer of NbTiN. (b) Definition of the nanowires by e-beam lithography and RIE. (c) deposition of a 300 nm low-fluorescence PECVD SiN layer. (d) Patterning of plasmonic bowtie antennas using e-beam lithography and a lift-off process. (e) SiN waveguide definition with e-beam lithography and RIE. (f) Overlay of the PbS/CdS QDs in the antenna gap using e-beam lithography and a lift-off process. (g) Room-temperature PECVD of the SiO₂ top-cladding. (h) Creation of openings to access the metal contacts employing optical contact lithography and RIE. (i) The finalized sample is glued to a printed circuit board (PCB) with silver paste and electrically connected via wire bonds.

sition (PECVD). Atmospheric oxygen would oxidize the NbTiN SNSPDs if the sample was placed on the hot-plate at the deposition temperature of 270°C, so we lowered the temperature during loading, only ramping it back up for the deposition, once a sufficient vacuum was reached in the chamber. The specific SiN deposition process resulted in a low fluorescence background at cryogenic temperatures and low optical loss from visible wavelengths to the infrared, allowing the platform to be flexible to incorporate a multitude of different quantum emitters. By encapsulating the pre-fabricated SNSPDs, the silicon nitride serves a second purpose, protecting the detectors during the following fabrication steps.

Next, the plasmonic antennas, additional alignment markers and absorbing metal strips next to the waveguides were fabricated using a 50 kV e-beam lithography system (Raith Voyager), thermal evaporation and lift-off. AR-P 6200 (Allresist) positive resist was exposed with a dose of 180 $\mu\text{C}/\text{cm}^2$ and a 5 nm step size for the plasmonic antennas, development was done in n-amyl acetate. A short dry etch in oxygen plasma was used to clear resist residues from the developed areas and 3 nm of titanium was evaporated prior to a 35 nm gold layer for sufficient adhesion of the metal. Lift-off was aided by ultrasonic agitation to obtain clean edges of the metal. The plasmonic bowtie antennas fabricated according to this processes are shown in the SEM micrographs in Figure 4.3b and Figure 4.4a.

The silicon nitride photonic components were fabricated in another e-beam lithography step with AR-P 6200 positive resist, exposing 3 μm wide trenches around the waveguides with a dose of 160 $\mu\text{C}/\text{cm}^2$, using the fixed beam moving stage (FBMS) mode of the Raith Voyager system [44] to reduce the losses induced by write field stitching. For the connection to other photonic components and parts of the waveguides requiring high precision alignment, we tapered the width of the waveguides from 1 μm to 4 μm , to reduce the impact of stitching errors on the waveguide loss. The sidewall corrugated waveguide grating filters (see Figure 4.16) to reject the 700 nm pump laser, as well as the sharp taper tips (Figure 4.17c) and distributed Bragg reflectors (DBRs) (Figure 4.17b) of the planar concave grating (PCG) spectrometer were patterned with a step size of 5 nm and a dose of 160 $\mu\text{C}/\text{cm}^2$ in the regular exposure mode, to achieve the highest resolution possible. After development in n-amyl acetate, oxygen plasma was used to clear resist residues and smooth out the waveguide sidewalls prior to reactive ion etching (RIE) of the SiN photonic components in a CF_4 and H_2 chemistry. Additional information on the SiN waveguide fabrication can be found in Appendix A.1. The high precision alignment implemented in this lithography step to center the SNSPDs and plasmonic bowtie antennas with respect to the SiN waveguides used automatic image recognition and

the metal markers fabricated in the previous lithography steps. Figure 4.2b shows the resulting precise overlay of a $1\ \mu\text{m}$ wide SiN waveguide with the U-shaped SNSPD below. Oxygen plasma was used to remove the remaining resist and etch residue before the last e-beam lithography step.

To pattern the PbS/CdS QDs on top of the SiN waveguides and align them with the gap of the plasmonic bowtie antennas we used a lift-off process with AR-P 617 positive resist and again write field alignment with automatic marker recognition. In order to form small pillars of quantum dots, a dot dose of $2\ \text{fC}$, a dedicated developer (AR 600-55, Allresist) and a short oxygen plasma step were used to create high aspect ratio openings in the resist. Subsequently, a $7.5\ \mu\text{M}$ dispersion of PbS/CdS QDs in toluene was spin-coated on the sample for 60 s at 1000 rpm. For the lift-off, the sample was placed in acetone and slightly agitated until all the resist and the excess QDs were removed. Figure 4.2a and Figure 4.3b show QD pillars placed in the gap of the plasmonic bowtie antenna.

Finally, the chips were encapsulated with a $1\ \mu\text{m}$ thick SiO_2 top cladding deposited by high frequency PECVD at room temperature, to protect the photonic components from dust particles outside of the cleanroom environment. Optical contact lithography with TI-35 resist (Micro Chemicals) and RIE in CF_4 , SF_6 and H_2 chemistry was used to create access to the contact pads. Figure 4.1 shows an optical microscope image of the finished chip, highlighting the different photonic components. The sample was then mounted on a printed circuit board (PCB) with silver paste and wire bonded to allow for electrical biasing and readout of the detectors via RF coaxial cables suited for cryogenic environments. The PCB was then mounted on a dipstick which incorporated three axes piezo positioners (Attocube) and optical access from the top.

4.6 Measuring the antenna enhancement

The on-chip measurements were performed in a liquid helium bath cryostat (4.2 K base temperature), and we used a 700 nm diode laser that was controlled by a home-built driver, producing 3 ns long pulses at a repetition rate of $f_{rep} = 48\ \text{kHz}$. A quartz window at the top of the dip-stick allowed for optical access to image and localize areas of interest, and a microscope objective ($\text{NA} = 0.8$) was used to form an excitation spot measuring $\sim 1\ \mu\text{m}^2$. The power focused on this diffraction limited spot on top of the waveguide was measured outside the cryostat and the polarization orientation was controlled to be perpendicular to the antenna dipole axis in order to reduce the scattering of the pump laser. Time-correlated single photon counting (TCSPC) electronics (Picoquant Picoharp 300) were used

to record the PL decay traces, receiving the "start" event from the laser and "stop" event from the SNSPDs driver.

While this study focuses on PbS/CdS QDs emitting in the infrared, the same set-up also allows for the on-chip characterization of CdSe/CdS QDs at cryogenic temperatures, using a 400 nm pulsed laser for the excitation. This demonstrates the flexibility of our platform to incorporate different colloidal nanocrystal emitters, with varying emission wavelength and time response. Figure 4.12a compares the instrument response function (IRF), obtained by focusing the pump laser directly onto a SNSPD, with the normalized PL decay signal from CdSe/CdS QDs and PbS/CdS QDs on top of a SiN waveguide. The instrument response function is determined by the pulse shape of the excitation laser, as well as the time jitter of the detector and puts a limit to the shortest measurable time constant. Clearly, for the characterization of the PbS/CdS QDs with their rather long PL lifetime it is not a limiting factor.

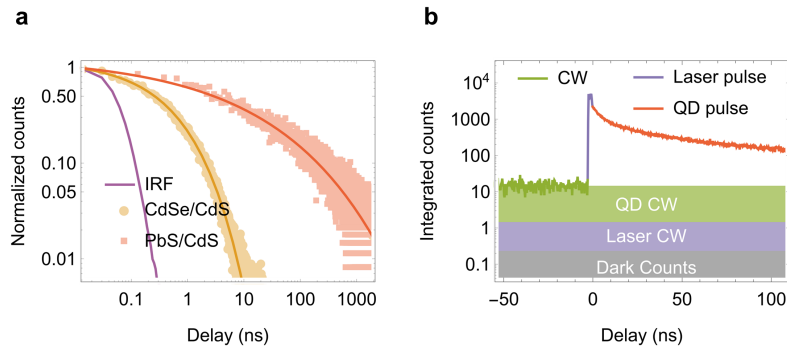


Figure 4.12: Instrument response function (IRF) and PL decay signal from CdSe/CdS QDs and PbS/CdS QDs on top of SiN waveguides. The normalized data was fitted with a stretched exponential after subtraction for the background. (b) Analysis of the countrate contributions for PbS/CdS QDs in the gap of a plasmonic bowtie antenna for an excitation power of $P_{ant} = 800$ nW.

Figure 4.12b displays a typical PL decay trace from PbS/CdS QDs placed in an antenna gap, after time-binning of the TCSPC data and before normalizing the integrated counts. The response of the PbS/CdS QDs can clearly be separated from the residual pump laser pulse. However, there also is a considerable continuous wave (CW) background. Detector dark counts only contribute 150 cps to the background, the remainder has to originate either from the pump laser or the QDs. From the instrument response recorded on an empty antenna we extracted that 80% of all laser counts

were CW and therefore assign the remainder of the background counts to the QDs. Using this reasoning, we estimate by integrating the counts in Figure 4.12b, that for a typical count rate of 24 kcps recorded with the SNSPD, 8% are residual counts from the pump laser, 1% are dark counts, 25% are from the QD pulse and 66% are CW counts from the QDs. We suspect that the large laser CW background originates from amplified spontaneous emission (ASE), when driving the laser diode very close to threshold in the off-periods.

For varying pump power the extracted count rates for the pulsed and CW contribution of the QD emission are displayed in Figure 4.13a. While the CW part shows a linear increase with the excitation power, the pulsed contribution saturates as a result of fast Auger recombination suppressing the emission from multi-exciton states. Fitting the count rate from pulsed emission c_{pulse} to the expected behavior for QDs emitting from a single-exciton state

$$c_{pulse}(P) = c_{sat}(1 - e^{-\rho P}), \quad (4.3)$$

yields an estimate for average number of excitations per QD in the antenna gap $\langle n \rangle_{ant} = 0.84 \pm 0.07$, for a pump power of $P_{ant} = 800$ nW.

Alternatively, the average number of excitons $\langle n \rangle$ can also be estimated from the QD absorption cross-section σ_i and the power density of the pump. We therefore calculated the mean number of photons per pulse $\langle p \rangle$ for the 700 nm pulsed laser with a 48 kHz repetition rate, starting from an average power of 800 nW recorded at the last mirror before reaching the optical access window of the dip-stick cryostat. First we assumed that only 20% of the laser power is in the pulse, which can be focused on a diffraction limited spot size of $1 \mu\text{m}^2$. Dividing by the repetition rate, we arrived at an energy density of $3.2 \times 10^{-12} \text{ J}\mu\text{m}^{-2}$. Using Planck's relation between energy and frequency $E = h\nu$ this translates into $\langle p \rangle = 12.5 \times 10^6 \mu\text{m}^{-2}$. We then estimated the intrinsic absorption cross-section of the PbS/CdS QDs by rescaling the value for an excitation wavelength of 400 nm from [42] of $\sigma_i(400 \text{ nm}) = 2 \times 10^5 \text{ cm}^{-1}$, using the solution absorption spectrum of the PbS/CdS QD sample, which gave $\sigma_i(700 \text{ nm}) = 2 \mu\text{m}^{-1}$. Scaling with the volume of an individual QD, we arrived at an average number of excitons $\langle n \rangle$ per QD

$$\langle n \rangle = \sigma_i(700 \text{ nm}) V_{QD} \langle p \rangle = 1.25 \quad (4.4)$$

Additional losses between the microscope objective lens and the focused spot on the sample, which are not taken into account in this calculation, can explain the difference compared to the estimation above, using the saturation of the count rate.

From the pulsed count rate of $c_{ant} = 6$ kcps it is further possible to estimate the average quantum yield ϕ_{ant} of the n_{QD} QDs in the antenna

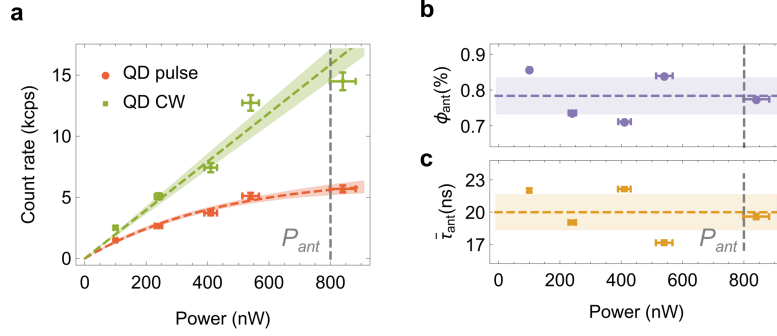


Figure 4.13: (a) Power dependence of the pulsed and CW contribution of the QD emission. The shaded areas show the 1- σ confidence intervals from the fit displayed as a dashed line. Excitation power dependence of the (b) estimated quantum efficiency and the (c) mean lifetime extracted from a stretched exponential fit.

gap to be

$$\phi_{ant} = \frac{c_{ant}}{f_{rep} n_{QD} \langle n \rangle_{ant} \beta_{ant} \xi \eta_{ant}}, \quad (4.5)$$

taking into account the waveguide coupling efficiency β_{ant} , the waveguide transmission ξ and the SNSPD detection efficiency η_{ant} .

To estimate the number of excited QDs in the experiments, we extracted the dimensions of the patterned QD pillars as well as the QD packing density from SEM micrographs (Figure 4.14). With a measured diameter of 35 nm and a cylinder height of 60 nm obtained for a 7.5 μM QD concentration and a mean smallest distance between dots of 6.6 nm, assuming a cubic packing fraction p_c , we obtained the number of QDs from

$$n_{QD} = \frac{p_c V_{pillar}}{V_{QD}}. \quad (4.6)$$

The pillar diameter is well defined due to the lithography, the height and the average distance between adjacent dots however have a larger uncertainty, so we estimate $n_{QD} = 200 \pm 50$. Generally, we found that pillars with an aspect ratio of 2:1 or lower will stay upright during the processing, whereas for a larger aspect ratio achieved by spin-coating QD dispersions with a higher concentration, the pillars tend to collapse as can be seen in Figure 4.14a.

Presuming that spherical PbS/CdS QDs show isotropic emission from their threefold degenerate bright exciton state [45] in a homogeneous environment, we argue that the high LRDOS in the antenna gap will force an emission polarization along the antenna dipole axis \mathbf{d} . FDTD simulations of the coupling to the transverse electric (TE) waveguide mode pre-

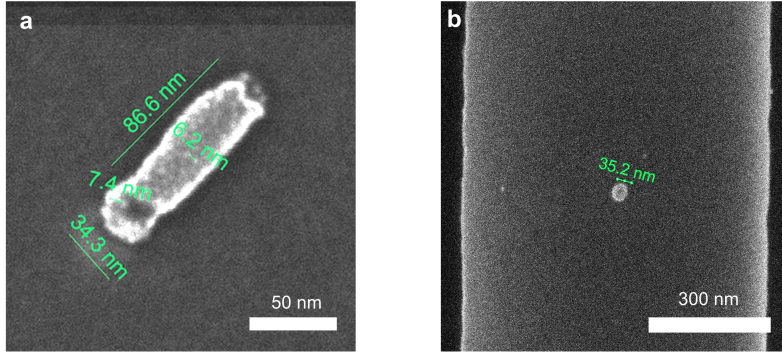


Figure 4.14: SEM micrographs of patterned colloidal PbS/CdS QDs used to estimate the number of excited dots in the experiments. The collapsed pillar in (a) was fabricated using $10 \mu\text{M}$ concentration of the QD dispersed in toluene. The QD pillar in (b) on top of a silicon nitride waveguide was fabricated with a $7.5 \mu\text{M}$ concentration and is still standing upright.

sented above (see Figure 4.5b) predict a nearly constant coupling efficiency of $\beta_{ant} = 0.12$ within the volume of the QD pillar. For the waveguide transmission we measured $\xi = 0.9$ for the 1 cm long waveguide connecting the antenna to the SNSPD, which has a detection efficiency of $\eta_{ant} = 0.9 \pm 0.1$ for the TE waveguide mode. Using these values we arrive at a quantum yield of $\phi_{ant} = 0.8 \pm 0.3\%$ for QDs in the antenna gap, which includes the metal losses from the antenna. Figure 4.13b shows the extracted quantum yield for various excitation powers, changing $\langle n \rangle$. Apart from variations, well within the error of the estimation, the extracted values are constant. We then used the same parameters to estimate the average number of excitations per QD due to the CW content of the pump laser and find an upper limit $\langle n \rangle_{CW} < 0.01$ based on the observed CW count rate from the QDs, under the assumption that an excitation lasts $1 \mu\text{s}$ on average. It can therefore be assured that the CW content of the laser does not unduly distort the extracted PL lifetimes.

In Figure 4.15d and e we compare the PL decay traces collected from an isolated pillar of QDs with QDs placed in the gap of an antenna on top of the same silicon nitride waveguide, assuring that a different detector behavior would not impede the results. The data was normalized and fitted with a stretched exponential

$$c(t) = a e^{-\left(\frac{t}{\tau_K}\right)^\zeta} \quad (4.7)$$

after subtraction of the background. This accounts for a distribution of

decay times for $\zeta < 1$ and turns into an single-exponential decay expected for a single-exciton emission at $\zeta = 1$. To judge the effect of the plasmonic antennas on the QD PL lifetime, we then extracted the mean lifetime $\bar{\tau}$ from the fitted parameters according to

$$\bar{\tau} = \frac{\tau_K}{\zeta} \Gamma\left(\frac{1}{\zeta}\right), \quad (4.8)$$

using the gamma function Γ . Averaging the values for fourteen different QD pillars collected with different SNSPDs we obtained an expectation value for the mean lifetime from the QDs on a waveguide $\langle \bar{\tau}_0 \rangle = 138 \pm 27$ ns (Figure 4.15a) and $\langle \bar{\tau}_{ant} \rangle = 30 \pm 9$ ns for QDs in the antenna gaps (Figure 4.15b). To minimize the effect of unintended excitation through scattered laser light, individual antennas and isolated pillars were separated by $20 \mu\text{m}$ on the waveguides. Figure 4.13c shows further that the measured lifetime does not depend on the excitation power, there is however a variation resulting from the fitting procedure.

FDTD simulations showed that for the chosen polarization direction of the laser perpendicular to the antenna dipole (see Figure 4.4d), the excitation enhancement of the antennas is negligible. For isolated QD pillars the polarization control of the pump laser was removed, leading to an increased excitation power $P_0 \sim 2P_{ant}$, which results in an average excitation number per QD $\langle n \rangle_0 \sim 1$. Due to an approximately isotropic emission in absence of the antenna the coupling efficiency reduces to $\beta_0 = \frac{1}{3} (\beta_{TE} + \beta_{TM})$ with average values of $\beta_{TE} = \beta_{TM} = 0.11$ obtained from FDTD simulations (see Figure 4.5b). Since the isolated pillar of QDs equally couples to the TE and TM mode of the waveguide the SNSPD detection efficiency further reduces to $\eta_0 = \frac{1}{2} (\eta_{TE} + \eta_{TM}) = 0.8 \pm 0.1$. Comparing QDs in an antenna gap and isolated pillars on the same waveguide the change in quantum yield can be estimated as

$$\frac{\phi_{ant}}{\phi_0} = \frac{c_{ant} \langle n \rangle_0 \beta_0 \eta_0}{c_0 \langle n \rangle_{ant} \beta_{ant} \eta_{ant}} \quad (4.9)$$

where c_0 is the pulsed count rate from an isolated QD pillar. The values reported in Figure 4.15c were corrected for the antenna absorption in case of multiple antennas on a single waveguide and correspond to the lifetimes at the same position in Figure 4.15b. For most antennas a short lifetime corresponds to a large enhancement of the quantum yield. Averaging over the reported data set we calculate $\langle \phi_{ant}/\phi_0 \rangle = 9.5 \pm 4.5$, the observed variation can be attributed to a misalignment of the QD pillar with respect to the antenna gap during the fabrication process. As a figure of merit for the antenna performance we finally calculate the radiative part of the local density of states

$$\text{LRDOS} = \frac{\tau_0}{\tau_{ant}} \frac{\phi_{ant}}{\phi_0} \quad (4.10)$$

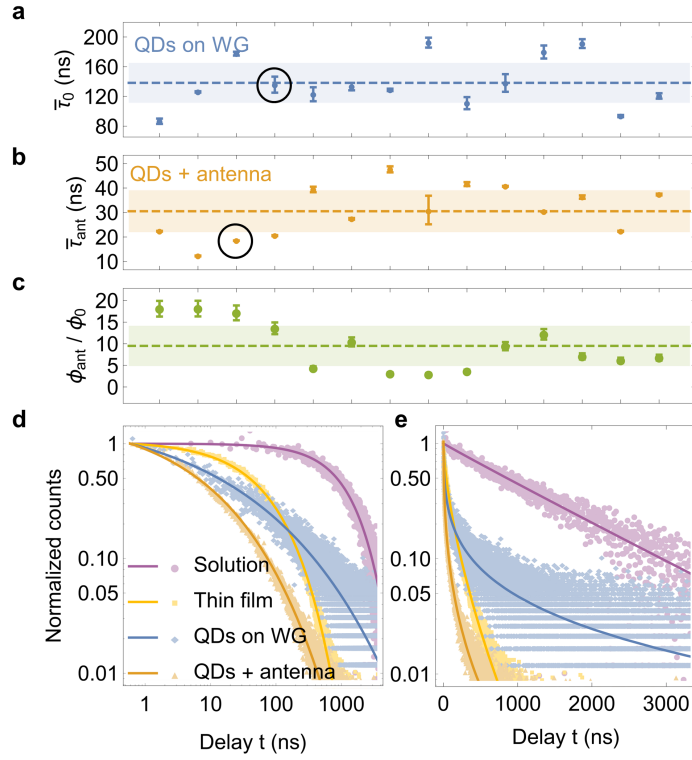


Figure 4.15: PL lifetime from different freestanding pillars of PbS/CdS QDs (a) and PbS/CdS QDs placed in the gap of plasmonic bowtie antennas (b) extracted from measurements with different SNSPDs. The quantum efficiency with an antenna ϕ_{ant} normalized to an isolated pillar ϕ_0 in (c) correspond to the lifetime measurements above. The dashed lines and shaded areas show the respective mean value and standard deviation, the displayed error bars are the $1-\sigma$ confidence intervals from the fit. The PL decay traces in (d) and (e) were normalized after subtraction of the background, the experimental data is overlaid with fitted stretched exponential functions. The circled data points in (a) and (b) were extracted from the respective decay traces in (d) and (e).

and obtain a mean value of $\langle \text{LRDOS} \rangle = 44 \pm 26$ and a maximum of 200 ± 50 , which is in good agreement with the results from FDTD simulations presented above.

To understand the multi-exponential decay from pillars of PbS/CdS QDs at cryogenic temperatures we performed additional lifetime measurements of the same QD sample at room temperature in solution and for a $1 \mu\text{m}$ thick drop-cast film. The results are reported in Figure 4.15d and e and it can be clearly seen that for the sample in solution with a quantum yield of 8.5%, the decay is nearly single-exponential. The fitting procedure yields $\zeta = 0.97 \pm 0.02$ and a lifetime of $\bar{\tau}_{sol} = 1260 \pm 50 \text{ ns}$, which is in line with PL lifetimes reported for similar QDs. [42] For the thin film at room temperature the lifetime drops to $\bar{\tau}_{TF} = 90 \pm 5 \text{ ns}$, accompanied by a reduction of the quantum yield to 2.5%. We hypothesize that is the result of a QD sample consisting of many dark dots and a subset of bright dots with a quantum yield close to 100%. While in solution the dots are sufficiently separated to suppress interaction, in thin films energy transfer between adjacent QDs will lead to the observed multi-exponential decay by introducing additional non-radiative decay channels for dots which are bright in solution. The extensive processing of the QDs measured with the photonic chip at cryogenic temperatures might further reduce the fraction of bright dots, leading to an even lower average quantum yield of $\langle \phi_0 \rangle = 0.05 \pm 0.03\%$ for isolated QD pillars on a waveguide.

4.7 Scaling to single emitters

The maximum LRDOS of 200 ± 50 measured on this integration platform shows its potential to reduce the lifetime of individual IR emitters. However, also the different count rate contributions are essential for targeting quantum applications. Based on the analysis above we estimate that using the antenna, 91% of the total counts on the detector were from the QDs, 7% from residual pump laser transmission through the waveguide, 1% from differently scattered laser light, while 1% were dark counts. This suggests that the corrugated sidewall grating filter in the current implementation (see Figure 4.16) with a pump suppression of 40 dB should be further improved to reach the limit of what is possible on a single chip [46].

Figure 4.16a shows the filter transmission for combined TE and TM transmission, measured on a cleaved sample, using a supercontinuum source (SuperK Extreme, NKT photonics) and an Advantest Q8381A spectrometer. We compare this to the pump laser spectrum measured with a Thorlabs spectrometer. The pump suppression at 700 nm reaches -40 dB, which corresponds to the noise floor of the measurement and the insertion loss at

the QD emission peak of 1150 nm is below 1 dB. The SEM top-view in Figure 4.16b shows part of the 400 μm long sidewall-corrugated waveguide before the deposition of the SiO_2 top-cladding. The grating has an indentation of ± 200 nm and consists of two sections with different periods of 225 nm and 230 nm, to effectively suppress both the fundamental TE and TM mode as well as higher order modes at the wavelength of the pump laser. Next to the waveguide trenches, the top-view further shows the absorbing metal lines aimed to suppress stray light coupling.

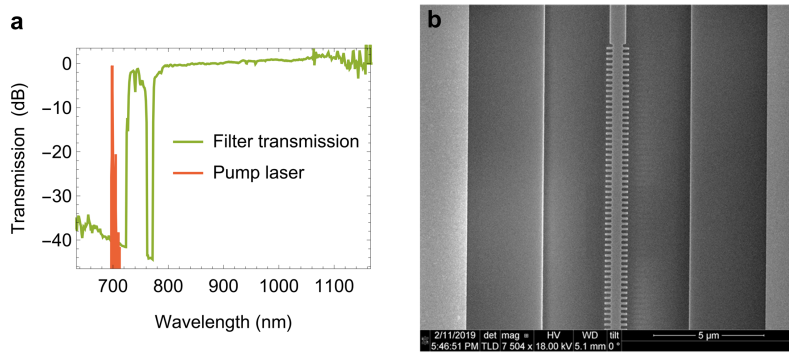


Figure 4.16: Corrugated sidewall grating filter designed to reject the 700 nm pump laser. (a) Transmission spectrum measured for a cleaved sample, compared to the spectrum of the pump laser. (b) SEM top-view of the sidewall-corrugated waveguide, with absorbing metal lines next to the trenches.

In the previous section we estimated a quantum yield of $\phi_{ant} = 0.8 \pm 0.3\%$ for a pillar consisting of $n_{QD} = 200 \pm 50$ PbS/CdS QDs, accurately placed in the gap of a plasmonic antenna. Due to the low index contrast of the SiN waveguides and the SiO_2 cladding material, the coupling of the QD emission to the waveguide mode is only 12%, a value that could be readily increased by adding DBR mirrors, incorporating the QDs inside the waveguide [28] and partially removing the cladding material [47]. This means that by using brighter emitters and minor changes in the design, the integration platform presented here should allow to scale down to one emitter per antenna and thereby achieve single-photon emission. It can also be expected to obtain improved emission enhancement for ideally placed individual QDs. There has been some recent progress on single-photon emission from colloidal QDs emitting in the visible [26, 27], but improved emitters in the IR suitable for QKD with narrower linewidth and faster initial radiative decay have yet to become available.

4.8 On-chip lifetime spectroscopy

Wavelength division multiplexing (WDM) can increase the key generation rate for QKD and it is already widely used for conventional optical telecommunication. To multiplex and de-multiplex the signal from several sources to a single transmission channel and back to several detectors, arrayed waveguide gratings (AWG) are the photonic component of choice. AWGs allow for a narrow channel spacing while keeping the device footprint small and have been successfully integrated with SNSPDs [48]. An alternative component is a planar concave grating (PCG), which can perform better in terms of cross-talk between the channels, but typically has a larger footprint for a small channel spacing [49]. However, the ensemble PL spectrum of the PbS/CdS QDs we used for this work was very broad (see Figure 4.3c), so we opted for a PCG spectrometer to perform a wavelength-resolved PL lifetime characterization of the emitters instead. The spectrometer sketched in Figure 4.17a was designed to have four channels connected to SNSPDs, which was the maximum number of detectors we were able to connect electrically in a single cool-down. An additional two channels of the PCG allowed for a passive characterization of the fabricated devices at room temperature, prior to the measurements at cryogenic temperatures.

The six spectrometer channels were designed with a spacing of 30 nm. To achieve a low insertion loss, distributed Bragg reflectors (DBRs) with a period of 370 nm were used as mirrors - see Figure 4.18a for the simulated TE reflection spectrum and Figure 4.17b for a SEM picture. The taper tips connecting to in- and output waveguides (see Figure 4.17c) were fabricated with a tip radius as small as 50 nm to minimize reflection losses. Due to the unavailability of a source that would span the whole spectrum, we used two different broadband sources for the characterization shown in Figure 4.18b. Channels 1-3 were measured with a SLED (Superlum), channels 4-6 with a supercontinuum source (SuperK Extreme, NKT Photonics), both in combination with a spectrum analyzer (Q8381A, Advantest). The transmission measurements show an insertion loss as low as 1.5 dB and a cross-talk below -20 dB for all channels, confirming the suitability of silicon nitride passive photonic components for quantum applications. The slight dip in the transmission of channel 1 might indicate that the DBR reflection spectrum was shifted compared to the simulation in Figure 4.18a, due to a shift of the effective index, possibly caused by a variation in the thickness of the PECVD SiN waveguide layer.

To obtain enough signal for the wavelength resolved measurements, the number of QDs was increased by covering a 100 μm long section of the single-mode waveguide with multiple layers of QDs, as shown in Figure 4.19b.

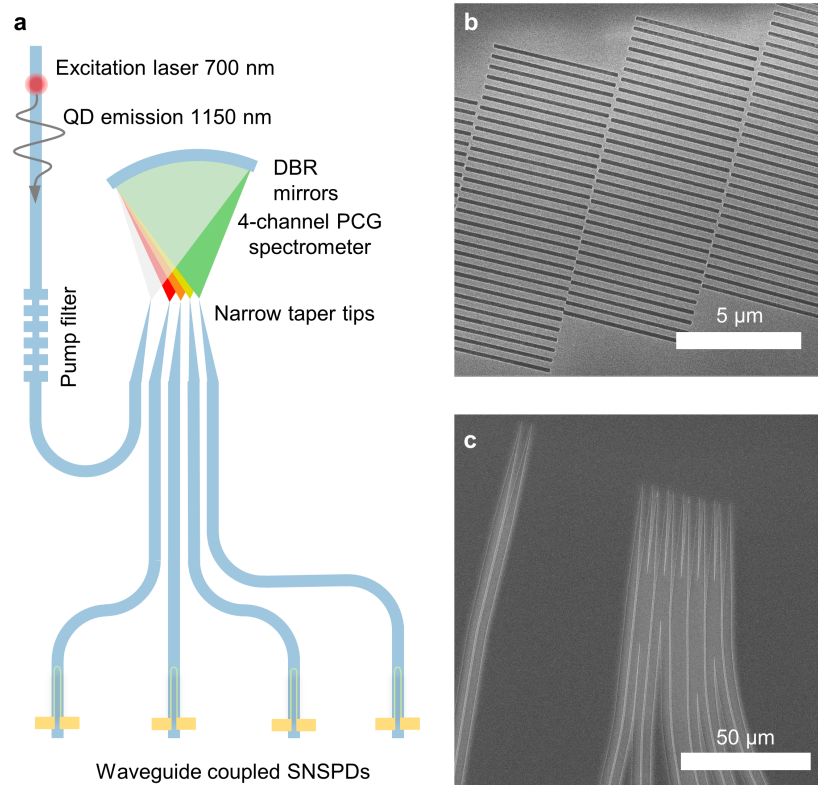


Figure 4.17: (a) Schematic chip layout for the on-chip lifetime spectroscopy experiment. PbS/CdS QDs were excited from the top by a 700 nm pulsed laser, the emission coupled to SiN waveguides. A corrugated sidewall grating filter rejects light from the pump laser. The planar concave grating (PCG) spectrometer with four output arms connected to waveguide-coupled SNSPDs allows for a wavelength-resolved characterization of the PL decay. (b) SEM micrograph of the distributed Bragg reflector (DBR) elements making up the blazed mirror grating of the spectrometer. (c) SEM micrograph of the in- and output waveguide tapers, interfacing the single-mode SiN waveguides with the slab mode section of the spectrometer.

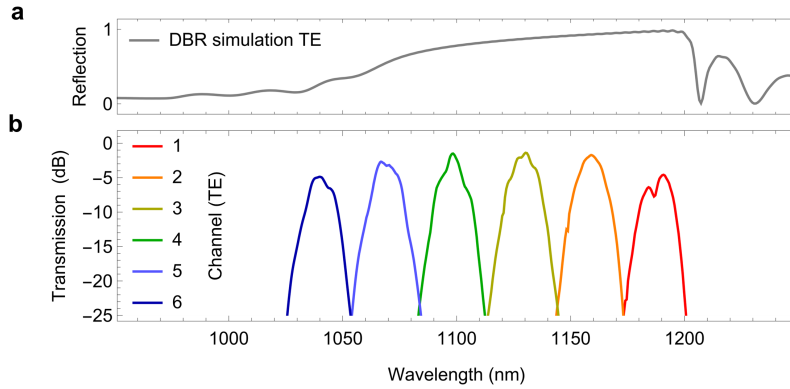


Figure 4.18: (a) Simulated TE reflection spectrum of the DBR mirror designed for the spectrometer. (b) Transmission measurements from all 6 channels. Channels 1-4 were connected to waveguide-coupled SNSPD. Channels 5 and 6 were used to characterize the fabricated spectrometers at room temperature, prior to the cool-down.

Measuring with a single SNSPD connected to the waveguide, we observed a saturation of the extracted lifetime with respect to the excitation position shown in Figure 4.19a, indicating some influence of self-absorption on the measurement. For the preferred excitation position giving a maximum count rate on the detector, an average lifetime of $\bar{\tau} = 200 \pm 5$ ns was obtained.

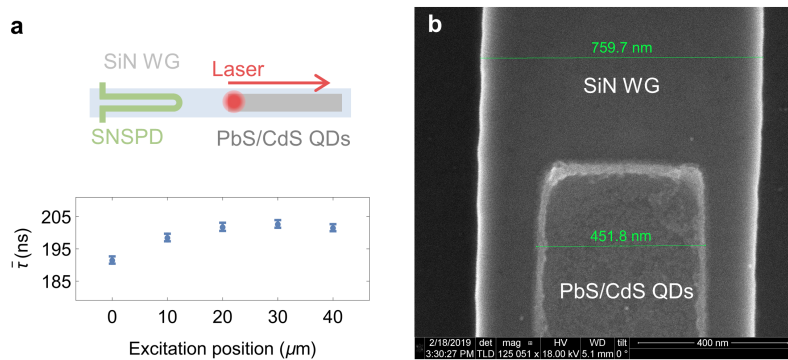


Figure 4.19: (a) Position dependence of the lifetime extracted from a stretched exponential fit, measured with a single SNSPD. (b) SEM top-view of part of a single-mode SiN waveguide covered with multiple layers of PbS/CdS QDs, before the deposition of the SiO₂ top-cladding.

Using the spectrometer and four different SNSPDs, the mean lifetime values in Figure 4.20b were extracted from the PL decay traces in Figure 4.20a. A clear increase of the mean lifetime with increasing wavelength was observed. Figure 4.20c again shows the Pb/CdS QD emission spectrum at 4.2K for comparison. This observation is in contrast with the behavior in solution at room temperature [42], but a very similar spectral dependence of the PL lifetime of PbS/CdS QD thin films has been observed at cryogenic temperatures [50]. Again, the correlation between longer emission wavelengths and longer lifetimes could reflect the influence of energy transfer on the emission of QDs in a close-packed thin film. To also collect a valid intensity spectrum of the QDs with the on-chip PCG, it would be necessary to calibrate for different detector efficiencies prior to any measurements, which was not possible due to the limitations of the set-up.

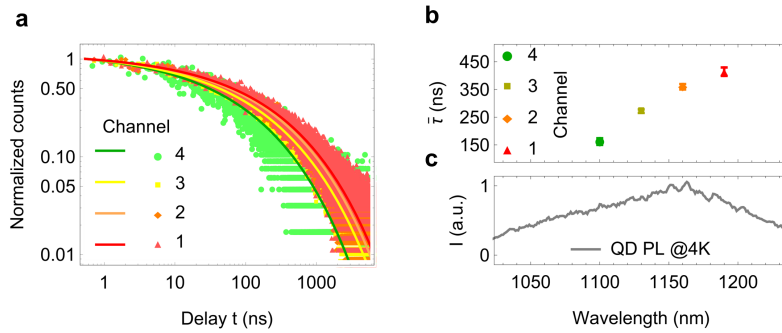


Figure 4.20: On-chip lifetime spectroscopy of PbS/CdS QDs. (a) The PL decay traces measured with SNSPDs connected to the spectrometer channels, fitted with a stretched exponential. (b) Extracted lifetimes for the respective spectrometer channels (c) The emission spectrum of an embedded layer of PbS/CdS QDs at 4.2 K.

4.9 Spectrally resolved antenna enhancement

Finally, we aimed to also perform a spectrally resolved measurement of the antenna enhancement using the planar concave grating spectrometer. Therefore, we increased the size of the QD patch deposited in the gap of the bowtie antenna, as shown in the inset of Figure 4.21b. While this increased the count-rate for the case of antennas, the signal was still too low to perform a reliable reference measurement with free-standing QD pillars of the same size. Hence, we again had to rely on larger QD patches, as shown in Figure 4.19b. This made it impossible to quantify the enhancement of the emitter quantum yield ϕ_{ant}/ϕ_0 in this experiment. Still, the fact that a signal could only be obtained for the QD pillars in the antenna gap, indicates a corresponding increase of the quantum efficiency.

Analyzing the mean lifetimes extracted from a stretched exponential fit using the 4-channel on-chip spectrometer in Figure 4.21c, we observed an opposite behavior for the QDs in the antenna gap and the reference measurement. While for the large patch of QDs the lifetime increases for larger wavelengths, as shown in the last section, for QDs in the antenna gap it decreases. From the mean lifetime values we extracted the rate enhancement γ_{ant}/γ_0 in Figure 4.21b. While for the spectrometer channel at 1100 nm there is barely any rate enhancement, there is a steady increase for the longer wavelengths. A maximum rate enhancement of 5 ± 1 is observed for the spectrometer channel centered at 1190 nm.

Comparing with FDTD simulations of $\text{LRDOS}(\lambda)$ in Figure 4.21a, the antenna enhancement shows a maximum at 1150 nm only for an empty antenna. When the larger QD pillar is included in the simulation, with a refractive index from ellipsometry measurements, the antenna resonance red-shifts and the maximum value of the LRDOS decreases. Comparing the larger QD pillar in the inset of Figure 4.21b with the LRDOS enhancement map in the inset of Figure 4.21a it is clear, that the overlap with the region of high enhancement is smaller than for the experiments presented earlier in Section 4.6. Hence, we also expect a decreased average LRDOS for the larger QD pillar with a diameter of ~ 100 nm. Yet, the value we obtained for the longest wavelength channel $\gamma_{ant}/\gamma_0(1190 \text{ nm}) = 5 \pm 1$ is comparable to the average rate enhancement $\langle \gamma_{ant}/\gamma_0 \rangle = 4.6$ calculated for a QD pillar with a diameter of ~ 35 nm presented before. Assuming a similar enhancement of the emitter quantum yield of $\langle \phi_{ant}/\phi_0 \rangle = 9.5 \pm 4.5$ as calculated in Section 4.6 and averaging the simulated LRDOS over the larger QD pillar, measurement and simulation can be matched. More importantly, the simulated $\text{LRDOS}(\lambda)$ and the measured rate enhancement γ_{ant}/γ_0 show a matching spectral behavior, as expected from Equation 4.10. This further

validates the results presented in this chapter.

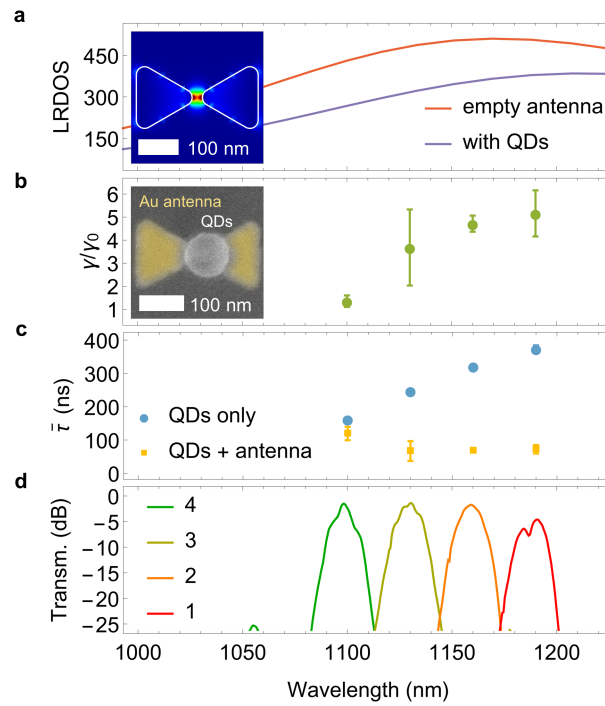


Figure 4.21: (a) Simulated radiative local density of states (LRDOS) in the gap of a plasmonic antenna with the inset showing a corresponding 2D map for a wavelength of $\lambda = 1150$ nm. (b) Rate enhancement measured using the four channels of an on-chip spectrometer and an inset showing a false-color SEM image of a fabricated structure. (c) Average lifetimes extracted from a stretched exponential fit of the PL decay. (d) Transmission measured through the four spectrometer channels connected to SNSPDs. Error bars represent $1-\sigma$ confidence intervals.

4.10 Conclusion and outlook

In summary, we developed a method to reliably integrate and test several components required for QKD at cryogenic temperatures, showing their combined operation on-chip. These are SNSPDs, plasmonic antennas to enhance the emission of IR-emitting colloidal PbS/CdS QDs and high-quality silicon nitride passive photonic components. Using these components we performed on-chip lifetime spectroscopy of PbS/CdS QDs at cryogenic temperatures and further demonstrated a maximum radiative local density of states (LRDOS) enhancement of 200 ± 50 for QDs deterministically placed in the antenna gap. The e-beam fabricated waveguides had a transmission loss below 1 dB/cm and the insertion loss of the spectrometer was 1.5 dB. The pump filter, achieving a suppression of -40 dB had an insertion loss below 1 dB. However, to realize a complete transceiver chip, further active photonic components are necessary to encode information either using path- or time-bin-encoding. Nanophotonic Pockels modulators [51] can achieve this functionality on a silicon nitride photonic platform. In addition, more suitable emitters than the colloidal PbS/CdS QDs in the current implementation, crucially with a higher ensemble PL quantum yield that would allow to work with individual single-photon emitters are necessary to be competitive with current on-chip implementations using attenuated lasers [34]. Importantly, the chip-based platform presented in this chapter is flexible to changes and newly developed solution-processed emitters can be readily integrated.

References

- [1] L. Elsinger, R. Gourgues, I. E. Zadeh, J. Maes, A. Guardiani, G. Bulgarini, S. F. Pereira, S. N. Dorenbos, V. Zwiller, Z. Hens, and D. Van Thourhout. *Integration of Colloidal PbS/CdS Quantum Dots with Plasmonic Antennas and Superconducting Detectors on a Silicon Nitride Photonic Platform*. Nano Letters, 19(8):5452–5458, aug 2019.
- [2] L. Elsinger, R. Gourgues, I. E. Zadeh, J. Maes, A. Guardiani, G. Bulgarini, S. F. Pereira, S. N. Dorenbos, V. Zwiller, Z. Hens, and D. Van Thourhout. *Wavelength-resolved Purcell enhancement of PbS/CdS quantum dots measured on a chip-based platform*. In Photonic and Phononic Properties of Engineered Nanostructures X, volume 11289, page 1128914. International Society for Optics and Photonics, 2020.
- [3] L. Elsinger, R. Gourgues, I. E. Zadeh, J. Maes, V. Chandrasekaran, G. Bulgarini, V. Zwiller, Z. Hens, and D. Van Thourhout. *On-chip Spectroscopy of PbS/CdS Colloidal QDs using Superconducting Nanowire Single Photon Detectors (SNSPDs) on a Silicon Nitride Photonic Platform*. Poster presented at nanoGe Fall Meeting in Torremolinos, Spain, 2018.
- [4] L. Elsinger, R. Gourgues, I. E. Zadeh, J. Maes, V. Chandrasekaran, G. Bulgarini, V. Zwiller, Z. Hens, and D. Van Thourhout. *Integration of colloidal QDs with plasmonics and superconducting nanowire detectors on a silicon photonic platform*. Poster presented at the Tenth International Conference on Quantum Dots in Toronto, Canada, 2018.
- [5] L. Elsinger, E. Drijvers, V. Chandrasekaran, W. Xie, Z. Hens, and D. Van Thourhout. *Incorporation of colloidal quantum dots into the gap of plasmonic bowtie antennas*. In Proceedings Symposium IEEE Photonics Society Benelux, pages 297–300, 2016.
- [6] I. Aharonovich, D. Englund, and M. Toth. *Solid-state single-photon emitters*. Nat. Photonics, 10(10):631–641, 2016.
- [7] D. C. Burnham and D. L. Weinberg. *Observation of Simultaneity in Parametric Production of Optical Photon Pairs*. Phys. Rev. Lett., 25(2):84–87, jul 1970.
- [8] P. Senellart, G. Solomon, and A. White. *High-performance semiconductor quantum-dot single-photon sources*. Nat. Nanotechnol., 12(11):1026–1039, 2017.

- [9] I. Schwartz, D. Cogan, E. R. Schmidgall, Y. Don, L. Gantz, O. Kenneth, N. H. Lindner, and D. Gershoni. *Deterministic generation of a cluster state of entangled photons*. Science, 354(6311):434–437, oct 2016.
- [10] J. C. Loredó, M. A. Broome, P. Hilaire, O. Gazzano, I. Sagnes, A. Lemaitre, M. P. Almeida, P. Senellart, and A. G. White. *Boson Sampling with Single-Photon Fock States from a Bright Solid-State Source*. Phys. Rev. Lett., 118(13):130503, mar 2017.
- [11] M. Reindl, D. Huber, C. Schimpf, S. F. C. da Silva, M. B. Rota, H. Huang, V. Zwiller, K. D. Jöns, A. Rastelli, and R. Trotta. *All-photonic quantum teleportation using on-demand solid-state quantum emitters*. Sci. Adv., 4(12):eaau1255, dec 2018.
- [12] F. Marsili, V. B. Verma, J. A. Stern, S. Harrington, A. E. Lita, T. Gerrits, I. Vayshenker, B. Baek, M. D. Shaw, R. P. Mirin, and S. W. Nam. *Detecting single infrared photons with 93% system efficiency*. Nat. Photonics, 7(3):210–214, mar 2013.
- [13] C. Schuck, W. H. P. Pernice, and H. X. Tang. *Waveguide integrated low noise NbTiN nanowire single-photon detectors with milli-Hz dark count rate*. Sci. Rep., 3(1):1893, dec 2013.
- [14] I. Esmaeil Zadeh, J. W. N. Los, R. B. M. Gourgues, V. Steinmetz, G. Bulgarini, S. M. Dobrovolskiy, V. Zwiller, and S. N. Dorenbos. *Single-photon detectors combining high efficiency, high detection rates, and ultra-high timing resolution*. APL Photonics, 2(11):111301, nov 2017.
- [15] W. Pernice, C. Schuck, O. Minaeva, M. Li, G. Goltsman, A. Sergienko, and H. Tang. *High-speed and high-efficiency travelling wave single-photon detectors embedded in nanophotonic circuits*. Nat. Commun., 3(1):1325, jan 2012.
- [16] C. Schuck, W. H. P. Pernice, and H. X. Tang. *NbTiN superconducting nanowire detectors for visible and telecom wavelengths single photon counting on Si₃N₄ photonic circuits*. Appl. Phys. Lett., 102(5):051101, feb 2013.
- [17] G. Reithmaier, S. Lichtmannecker, T. Reichert, P. Hasch, K. Müller, M. Bichler, R. Gross, and J. J. Finley. *On-chip time resolved detection of quantum dot emission using integrated superconducting single photon detectors*. Sci. Rep., 3(1):1901, dec 2013.

- [18] P. Rath, O. Kahl, S. Ferrari, F. Sproll, G. Lewes-Malandrakis, D. Brink, K. Ilin, M. Siegel, C. Nebel, and W. Pernice. *Superconducting single-photon detectors integrated with diamond nanophotonic circuits*. *Light Sci. Appl.*, 4(10):e338–e338, oct 2015.
- [19] M. Schwartz, E. Schmidt, U. Rengstl, F. Hornung, S. Hepp, S. L. Portalupi, K. Llin, M. Jetter, M. Siegel, and P. Michler. *Fully On-Chip Single-Photon Hanbury-Brown and Twiss Experiment on a Monolithic Semiconductor-Superconductor Platform*. *Nano Lett.*, 18(11):6892–6897, nov 2018.
- [20] I. E. Zadeh, A. W. Elshaari, K. D. Jöns, A. Fognini, D. Dalacu, P. J. Poole, M. E. Reimer, and V. Zwiller. *Deterministic Integration of Single Photon Sources in Silicon Based Photonic Circuits*. *Nano Lett.*, 16(4):2289–2294, 2016.
- [21] J.-H. Kim, S. Aghaeimeibodi, C. J. K. Richardson, R. P. Leavitt, D. Englund, and E. Waks. *Hybrid Integration of Solid-State Quantum Emitters on a Silicon Photonic Chip*. *Nano Lett.*, 17(12):7394–7400, dec 2017.
- [22] A. W. Elshaari, I. E. Zadeh, A. Fognini, M. E. Reimer, D. Dalacu, P. J. Poole, V. Zwiller, and K. D. Jöns. *On-chip single photon filtering and multiplexing in hybrid quantum photonic circuits*. *Nat. Commun.*, 8(1):379, dec 2017.
- [23] M. Davanco, J. Liu, L. Sapienza, C.-Z. Zhang, J. V. De Miranda Cardoso, V. Verma, R. Mirin, S. W. Nam, L. Liu, and K. Srinivasan. *Heterogeneous integration for on-chip quantum photonic circuits with single quantum dot devices*. *Nat. Commun.*, 8(1):889, dec 2017.
- [24] R. Katsumi, Y. Ota, M. Kakuda, S. Iwamoto, and Y. Arakawa. *Transfer-printed single-photon sources coupled to wire waveguides*. *Optica*, 5(6):691, jun 2018.
- [25] R. E. Correa, E. A. Dauler, G. Nair, S. H. Pan, D. Rosenberg, A. J. Kerman, R. J. Molnar, X. Hu, F. Marsili, V. Anant, K. K. Berggren, and M. G. Bawendi. *Single photon counting from individual nanocrystals in the infrared*. *Nano Lett.*, 12(6):2953–2958, 2012.
- [26] V. Chandrasekaran, M. D. Tessier, D. Dupont, P. Geiregat, Z. Hens, and E. Brainis. *Nearly Blinking-Free, High-Purity Single-Photon Emission by Colloidal InP/ZnSe Quantum Dots*. *Nano Lett.*, 17(10):6104–6109, 2017.

- [27] Y.-S. Park, J. Lim, and V. I. Klimov. *Asymmetrically strained quantum dots with non-fluctuating single-dot emission spectra and subthermal room-temperature linewidths*. *Nature Materials*, 18(3):249–255, mar 2019.
- [28] W. Xie, R. Gomes, T. Aubert, S. Bisschop, Y. Zhu, Z. Hens, E. Brainis, and D. Van Thourhout. *Nanoscale and Single-Dot Patterning of Colloidal Quantum Dots*. *Nano Lett.*, 15(11):7481–7487, nov 2015.
- [29] J. Preskill and P. W. Shor. *Simple Proof of Security of the BB84 Quantum Key Distribution Protocol*. *Phys. Rev. Lett.*, 85(2):441–444, 2000.
- [30] H.-K. Lo, X. Ma, and K. Chen. *Decoy State Quantum Key Distribution*. *Phys. Rev. Lett.*, 94(23):230504, jun 2005.
- [31] H.-K. Lo, M. Curty, and K. Tamaki. *Secure quantum key distribution*. *Nat. Photonics*, 8(8):595–604, aug 2014.
- [32] A. Boaron, G. Boso, D. Rusca, C. Vulliez, C. Autebert, M. Caloz, M. Perrenoud, G. Gras, F. Bussi eres, M.-J. Li, D. Nolan, A. Martin, and H. Zbinden. *Secure Quantum Key Distribution over 421 km of Optical Fiber*. *Phys. Rev. Lett.*, 121(19):190502, nov 2018.
- [33] K. Takemoto, Y. Nambu, T. Miyazawa, Y. Sakuma, T. Yamamoto, S. Yorozu, and Y. Arakawa. *Quantum key distribution over 120 km using ultrahigh purity single-photon source and superconducting single-photon detectors*. *Sci. Rep.*, 5(1):14383, nov 2015.
- [34] P. Sibson, C. Erven, M. Godfrey, S. Miki, T. Yamashita, M. Fujiwara, M. Sasaki, H. Terai, M. G. Tanner, C. M. Natarajan, R. H. Hadfield, J. L. O’Brien, and M. G. Thompson. *Chip-based quantum key distribution*. *Nat. Commun.*, 8:13984, feb 2017.
- [35] G. M. Akselrod, M. C. Weidman, Y. Li, C. Argyropoulos, W. A. Tisdale, and M. H. Mikkelsen. *Efficient Nanosecond Photoluminescence from Infrared PbS Quantum Dots Coupled to Plasmonic Nanoantennas*. *ACS Photonics*, 3(10):1741–1746, 2016.
- [36] T. B. Hoang, G. M. Akselrod, and M. H. Mikkelsen. *Ultrafast Room-Temperature Single Photon Emission from Quantum Dots Coupled to Plasmonic Nanocavities*. *Nano Lett.*, 16(1):270–275, 2016.
- [37] A. F. Koenderink. *Single-Photon Nanoantennas*. *ACS Photonics*, 4(4):710–722, 2017.

- [38] Y. Chen, A. Ryou, M. R. Friedfeld, T. Fryett, J. Whitehead, B. M. Cossairt, and A. Majumdar. *Deterministic Positioning of Colloidal Quantum Dots on Silicon Nitride Nanobeam Cavities*. *Nano Lett.*, 18(10):6404–6410, oct 2018.
- [39] A. Kinkhabwala, Z. Yu, S. Fan, Y. Avlasevich, K. Müllen, and W. E. Moerner. *Large single-molecule fluorescence enhancements produced by a bowtie nanoantenna*. *Nat. Photonics*, 3(11):654–657, 2009.
- [40] R. Gourgues, I. E. Zadeh, A. W. Elshaari, G. Bulgarini, J. W. N. Los, J. Zichi, D. Dalacu, P. J. Poole, S. N. Dorenbos, and V. Zwiller. *Controlled integration of selected detectors and emitters in photonic integrated circuits*. *Opt. Express*, 27(3):3710, feb 2019.
- [41] M. Caloz, B. Korzh, N. Timoney, M. Weiss, S. Gariglio, R. J. Warburton, C. Schönenberger, J. Renema, H. Zbinden, and F. Bussièeres. *Optically probing the detection mechanism in a molybdenum silicide superconducting nanowire single-photon detector*. *Appl. Phys. Lett.*, 110(8):083106, feb 2017.
- [42] Y. Justo, P. Geiregat, K. V. Hoecke, F. Vanhaecke, C. De Mello Donega, and Z. Hens. *Optical properties of PbS/CdS Core/shell quantum dots*. *J. Phys. Chem. C*, 117(39):20171–20177, 2013.
- [43] J. C. de Mello, H. F. Wittmann, and R. H. Friend. *An improved experimental determination of external photoluminescence quantum efficiency*. *Adv. Mater.*, 9(3):230–232, mar 1997.
- [44] I. Khodadad, N. Nelson-Fitzpatrick, K. Burcham, A. Hajian, and S. S. Saini. *Electron beam lithography using fixed beam moving stage*. *J. Vac. Sci. Technol. B*, 35(5):051601, sep 2017.
- [45] J. M. An, A. Franceschetti, and A. Zunger. *The Excitonic Exchange Splitting and Radiative Lifetime in PbSe Quantum Dots*. *Nano Lett.*, 7(7):2129–2135, jul 2007.
- [46] M. Piekarek, D. Bonneau, S. Miki, T. Yamashita, M. Fujiwara, M. Sasaki, H. Terai, M. G. Tanner, C. M. Natarajan, R. H. Hadfield, J. L. O’Brien, and M. G. Thompson. *High-extinction ratio integrated photonic filters for silicon quantum photonics*. *Opt. Lett.*, 42(4):815, feb 2017.
- [47] S. Bisschop, A. Guille, D. Van Thourhout, Z. Hens, and E. Brainis. *Broadband enhancement of single photon emission and polarization dependent coupling in silicon nitride waveguides*. *Opt. Express*, 23(11):13713, jun 2015.

- [48] O. Kahl, S. Ferrari, V. Kovalyuk, A. Vetter, G. Lewes-Malandrakis, C. Nebel, A. Korneev, G. Goltsman, and W. Pernice. *Spectrally multiplexed single-photon detection with hybrid superconducting nanophotonic circuits*. *Optica*, 4(5):557, 2017.
- [49] A. Rahim, E. Ryckeboer, A. Z. Subramanian, S. Clemmen, B. Kuyken, A. Dhakal, A. Raza, A. Hermans, M. Muneeb, S. Dhoore, Y. Li, U. Dave, P. Bienstman, N. Le Thomas, G. Roelkens, D. Van Thourhout, P. Helin, S. Severi, X. Rottenberg, and R. Baets. *Expanding the Silicon Photonics Portfolio with Silicon Nitride Photonic Integrated Circuits*. *J. Light. Technol.*, 35(4):639–649, 2017.
- [50] *Temperature-Dependent Optical Properties of PbS/CdS Core/Shell Quantum Dot Thin Films: Probing the Wave Function Delocalization*. *J. Phys. Chem. C*, 119(30):17480–17486, 2015.
- [51] K. Alexander, J. P. George, J. Verbist, K. Neyts, B. Kuyken, D. Van Thourhout, and J. Beeckman. *Nanophotonic Pockels modulators on a silicon nitride platform*. *Nat. Commun.*, 9(1):3444, dec 2018.

Chapter 5

Conclusions and perspectives

5.1 Optoelectronic devices

In this thesis several novel optoelectronic device concepts employing colloidal nanocrystals have been developed. The nano-patterned colloidal QD-LEDs presented in Chapter 2 were aimed at demonstrating single-photon emission from electrical pumping. While this goal was not reached, the demonstration of the objective by a competing research group [1] showed the viability of the approach. In addition, the techniques developed in Chapter 2 enabled the development of waveguide-coupled QD-LEDs and photodetectors presented in Chapter 3. We anticipate that, provided that future improvements are going to lead to a leap in performance, these devices will find an application in chip-based absorption spectroscopy and bio-sensing, as they can be post-processed on foundry-fabricated waveguide platforms, at a low cost. Consequently, a European patent application has been filed to facilitate the valorization of colloidal nanocrystal technologies for integrated photonics applications.

While we demonstrated waveguide-coupled QD-LEDs and detectors, the ultimate goal of this work has been to achieve lasing from electrically pumped colloidal QDs, which has long been sought after by the research community. The recent demonstration of optical gain from dc electrical bias reported in literature [2] has shown the theoretical feasibility. Yet, it has proven difficult to engineer a low-loss optical cavity around established QD-LED stacks, developed for next-generation display applications. [3] Previous attempts of other research groups have used index confinement in the active material, combined with a patterned charge transport layer providing

distributed feedback. [4] However, this approach suffers from a fundamental limitation of efficient hybrid inorganic/organic QD-LED concepts. Due to the use of organic hole transport materials, the attainable current density is limited to approximately 1 A/cm^2 in planar devices. [3] Moderate current focusing is necessary to observe optical gain from an electrical bias, with a previously reported maximum of 20 A/cm^2 . [2] While it is possible to invert only thin QD layers with the available current density, a thick QD film is needed to support a confined optical mode. Consequently, devices employing index confinement in thin QD layers suffer from increasing passive optical losses, which strongly compromise lasing operation. [4]

As an alternative, we developed a novel design with a QD-LED structure in the evanescent field of a guided optical mode, allowing to significantly reduce passive optical losses for thin QD layers and enabling multiple means of optical feedback. Figure 5.1 outlines the device concept based on a 300 nm thick silicon nitride waveguide, which was conformally coated with a 10 nm thin ZnO layer for electron transport and injection. Optimisation of the ZnO deposition parameters resulted in a suitable trade-off between optical loss and electrical conductivity. The n-contact metal was patterned next to the waveguides, to contact the devices without adding any loss. We further made use of a planarization etch, to allow for the uniform deposition of a thin layer of CdSe/CdS QDs. Evaporated small molecule organic hole transport layers and an aluminum p-contact layer completed the device. Owing to

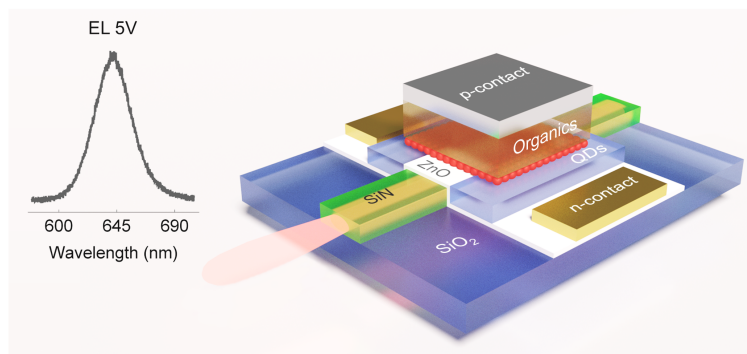


Figure 5.1: Schematic rendering of the waveguide-coupled colloidal QD light emitting diode developed in Chapter 3 and the emission spectrum collected for a voltage bias of 5 V.

the more pronounced current focusing, inherent to this device architecture, we were able to achieve a record current density of up to 100 A/cm^2 for the

QD-LEDs, putting stimulated emission from colloidal nanocrystals within reach. It should be noted that while this current density is a record for QD-LEDs, it is still more than an order of magnitude lower than the current density commonly achieved in conventional III-V stacks. [5] Still, in the reported devices the observation of transparency and gain from colloidal CdSe/CdS QDs was hindered by adverse effects leading to an increased waveguide absorption when forward biasing the devices. We believe that additional research aimed at solving this issue will lead to a leap in LED device performance and eventually enable the demonstration of electrically pumped lasing from colloidal QDs.

Currently, for the first generation of functional QD-LEDs, the recorded maximum power in a single-mode waveguide was only 2 nW, which is still several orders of magnitude too low for practical applications. The output power could be significantly increased through further research aimed at improving the internal quantum efficiency, which was drastically decreased at higher bias currents in our devices, as shown in Chapter 3. Techniques developed to balance the charge injection in planar QD-LEDs have led to devices with an internal quantum efficiency approaching 100% reported in literature. [6–8] One approach, that could be easily implemented is the use of QDs with an additional ZnS shell, as discussed in Chapter 2. The band alignment of CdSe/CdS/ZnS QDs helps to impede charging of the QD monolayer adjacent to the ZnO electron injection layer and thereby ensures efficient emission from the neutral exciton state. However, ultimately the external efficiency of waveguide-coupled QD-LEDs is limited by the low coupling efficiency β , governing the process of spontaneous emission and self-absorption along the waveguide. The use of waveguides with a higher refractive index might be a possible remedy, for example TiO₂ with a refractive index of $n = 2.4$ could serve as an alternative material of the waveguide core. [9] Still, with a refractive index of the organic hole injection materials close to $n = 1.7$, only a medium index contrast can be achieved, limiting the maximum coupling efficiency. Reaching the threshold for stimulated emission on the other hand, could potentially enable output powers in the μW range, since the device performance is no longer limited by β . Instead, for SLED and laser devices the mode confinement in the active material could be adjusted to find a suitable trade-off between threshold current and saturation power, similar to heterogeneously integrated III-V on silicon devices. [5]

As discussed in Chapter 1, due to the two-fold degeneracy of the band-edge exciton state in CdSe based nanocrystals, an average excitation level $\langle N \rangle > 1$ is required for optical gain in neutral QDs. It has been shown in literature, that in negatively charged QDs the lasing threshold can be sig-

nificantly reduced, since two extra charges in the conduction band turn the quantum dot into an effective 3-level system. [10] While solution based transient absorption spectroscopy can be used to identify suitable nanocrystal gain materials, [11] the exact charge state and injection mechanism of the emitters in our waveguide-coupled QD-LEDs remains unexplored. Photoluminescence lifetime spectroscopy at previously unavailable current densities could be a valuable tool to discern the QD charging and identify a suitable operation regime for an electrically pumped colloidal QD laser. Future experiments, similar to the study of different QD layer thicknesses described in Chapter 2, investigating the combined electrical and optical excitation of a single QD, could offer unique insight into the physical mechanisms of charge injection in a QD-LED. [12]

Further improvements to the presented waveguide-coupled QD-LED devices could be made by studying the properties of the ZnO electron injection layer in more detail. In course of the process development we empirically found a deposition and annealing procedure, which resulted in layers with a suitable optical loss and electrical conductivity. Yet, a physical understanding of the annealing process is lacking. It could be worthwhile to characterize the carrier concentration and mobility of the deposited layers and explore the limitation of optical loss by free carrier absorption. Additionally, the use of organic hole injection materials makes QD-LEDs quite susceptible to moisture and oxygen present outside of a glovebox environment. For the measurements presented in Chapter 3 of this thesis, the large aluminum p-contact served as the only encapsulation for our devices. To improve the long-term stability of the QD-LEDs, further research is necessary to develop a more reliable encapsulation procedure, which can prevent the ingress of atmospheric oxygen and water vapor.

Next to developments aimed at building a laser, we also demonstrated photodetection for the waveguide-coupled devices reported in Chapter 3. Importantly, already the first generation of devices showed a low dark current of 1.5×10^{-6} A/cm². The non-linear detector behavior and maximum detector quantum efficiency below 10% however still leave room for improvement. Planar colloidal QD photodiode designs reported in literature have been shown to exhibit a linear behavior and higher responsivity in the infrared. [13, 14] With further optimization of the waveguide-coupled detectors, aimed at improving the charge extraction efficiency, we believe that values reported in literature can be matched. Subject to these improvements, colloidal QD photodiode detectors could be an attractive post-processing option for low-cost passive only waveguide platforms. The use of organic charge transport materials limits the frequency response of the devices, yet it should be sufficient for applications in spectroscopy and bio-sensing. The

flexibility to incorporate different solution-processable nanocrystals with a tailored absorption spectrum stands out as a key benefit of the device concept. One could for example envision a multitude of detectors with different absorption spectrum post-processed on top of a single waveguide, achieving spectroscopic detection.

The processes developed in this thesis could also benefit other research directions. Combining low-loss passive waveguides with thin charge transport layers and colloidal nanocrystal gain materials, could enable optically pumped lasers with an electrically controlled charge state of the QDs. Compared to the first demonstration of a reduced lasing threshold from charged QDs reported in literature, [10] this could potentially enable continuous wave operation of an integrated device, at pump power levels well below 10 kW/cm^2 , compatible with cheap blue laser diodes. The low-loss ZnO charge transport layer presented in Chapter 3 could also be a valuable addition to other waveguide platforms based on amorphous materials. These lack the possibility to change the material conductivity through the incorporation of dopants, which is a powerful tool in silicon and native III-V platforms. Instead, metal contacts have to be placed close to the waveguides to apply strong electric fields, which is detrimental in terms of optical loss. A possible device application could for example be an electro-optic modulator that uses a highly nonlinear organic material in the gap of a silicon nitride slot waveguide. [15]

5.2 Quantum photonic applications

In Chapter 4 we successfully integrated colloidal QDs, plasmonic antennas and superconducting nanowire single-photon detectors (SNSPDs) with high-quality passive components on a silicon nitride platform and showed the combined operation at cryogenic temperatures. We performed on-chip lifetime spectroscopy of the IR-emitting PbS/CdS QDs and further demonstrated a maximum radiative local density of states (LRDOS) enhancement of 200 ± 50 , for QDs deterministically placed in the antenna gap. However, more suitable emitters than the colloidal PbS/CdS QDs in the present implementation, crucially with a higher PL quantum yield would be needed to work with individual single-photon emitters.

Provided that adequate nanocrystal single-photon emitters can be found, one could imagine future research to focus on a chip-based platform that combines the nano-patterned QD-LED devices presented in Chapter 2 with the antenna enhancement from Chapter 4 on top of silicon nitride waveguides. Purcell-enhanced electroluminescence from individual QDs could be coupled to low-loss silicon nitride components, manipulated and detected

on the same chip. Electrical excitation has the advantage that it eliminates the need for an effective suppression of the pump laser, [16] which otherwise is a major hurdle for quantum optics on a single chip. Only recently, a Hanbury-Brown-Twiss experiment using resonantly pumped epitaxial QDs and SNSPDs on the same chip has been demonstrated. [17] Large-scale quantum photonic experiments using parametric down-conversion sources, which rely on an intense pump laser, usually require off-chip detection to be able to sufficiently suppress the excitation laser. [18]

To date, while significant progress has been made on the emission purity and stability of colloidal QD single-photon emitters, [19–21] quantum photonic applications that go beyond QKD, for which the requirements can also be fulfilled by attenuated lasers, [22] are still out of reach. The main limitation is that the emission is usually lacking the required indistinguishability. While the room-temperature emission of an individual CdSe/CdS QD shown in Chapter 2 is significantly broadened by phonon interactions, also at cryogenic temperatures the emission linewidth is far from being Fourier transform limited. [23] Generally, the large dark-bright splitting of the band-edge exciton, leading to an increased excited state lifetime of colloidal nanocrystals at low temperatures, is a major hindrance. [24] Transient four wave mixing studies of InP/ZnS QDs, which feature pure single photon emission, [20] have for example revealed short dephasing times, compared to the excited state lifetime. [25] This precludes most colloidal emitters from a use for quantum photonic applications, the only exception might be lead-halide perovskite nanocrystals, for which it was recently proposed that the lowest energy state is a bright triplet, leading to fast emission at low temperatures. [26] Photon-correlation Fourier spectroscopy has been used to reveal dephasing times on the order of the radiative lifetime for these particles, which enables coherent single-photon emission. [27]

Still, while these recent results for perovskite nanocrystals are promising, [27] compared to established epitaxial QD sources [28] colloidal nanocrystals fall short when it comes to quantum photonic applications. [29] For practical reasons it would be beneficial to develop components for quantum applications, which can be operated at room temperature. However, high-performance single-photon detectors (see Chapter 4) also need to be operated at cryogenic temperatures and besides for most solid-state emitters, phonon induced dephasing is a major limitation for the single-photon indistinguishability at room temperature. [29] Therefore, we reason that integrated quantum photonic experiments with sources, modulators and detectors combined on the same chip will most likely require low-temperature operation in any case. Figure 5.2 sketches an envisioned integration concept, based on transfer printing of epitaxial QDs, [30] a technique which

has also been successfully used to integrate III-V lasers on a silicon nitride platform. [31] While previous quantum photonic experiments have used in-

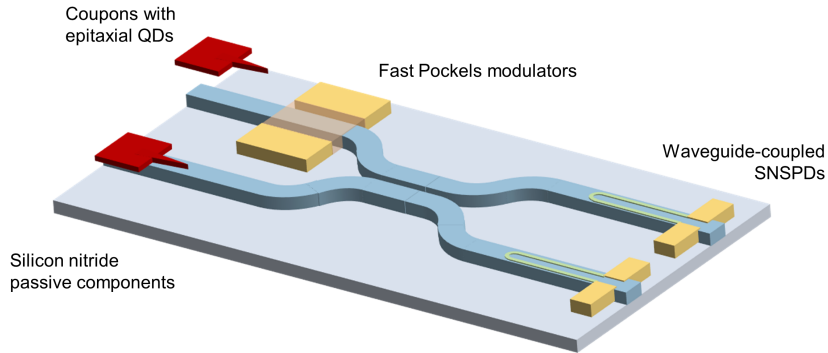


Figure 5.2: Sketch of an integration scheme for further work on chip-based quantum photonics. Mature epitaxial quantum dots can be pre-selected and transfer printed on top of foundry processed SiN passives. Pure phase modulators should be compatible with operation at cryogenic temperatures, which are required for the high-performance waveguide-coupled SNSPDs.

distinguishable single photons from one QD, [32–34] it remains challenging to achieve mutual coherence of the emission from different emitters, which is a requirement for large-scale quantum photonic technologies. Quantum frequency conversion can be used to show Hong-Ou-Mandel interference from remote QD emitters, [35] another possibility is to use different tuning mechanisms, to directly modify the QD emission wavelength. [36] While temperature tuning has been heavily used in the past, [28] to integrate multiple emitters on the same chip, other techniques such as strain tuning [36, 37] or electrical tuning by the QCSE [38] have to be established for transfer-printed sources. To restrict the required tuning range, pre-selection of suitable QD emitters prior to the transfer process could be a powerful tool. A further advantage of epitaxial quantum dots embedded in high-index III-V materials is the near-unity coupling efficiency to a waveguide mode, which can be achieved due to the large index contrast. [39] Yet another challenge is the suppression of the resonant excitation laser, while simultaneously maintaining a high source efficiency. [40, 41]

Quantum photonic protocols have stringent requirements, not only on single-photon sources and detection efficiency, but also on the waveguide loss of passive components and require pure phase modulators. [29] Therefore, the relatively high waveguide losses of the native substrates epitaxial

QDs are grown on, are a major hindrance and heterogeneous integration on low-loss passive photonic waveguides is of the essence for large-scale circuits. [42, 43] A possible solution for pure phase modulators, which can be integrated with silicon nitride passive waveguides are nanophotonic Pockels modulators. [44] The performance of these modulators reported at room temperature however needs to be validated at cryogenic temperatures, which are required for QD emitters and SNSPDs.

In conclusion, even with established epitaxial QD single-photon sources, it is still a daunting task to create the envisioned large-scale circuits for linear optical quantum computing. [45] Therefore, we reason that future research should be focused on the most pressing tasks, like establishing mutual coherence between many individual sources, rather than trying to improve the performance of colloidal nanocrystals as single-photon sources. As explained in the beginning of this chapter, colloidal nanocrystals are attractive materials for other applications in integrated photonics and achieving lasing from electrically pumped colloidal emitters will be a disruptive technology, enabling many new applications.

References

- [1] X. Lin, X. Dai, C. Pu, Y. Deng, Y. Niu, L. Tong, W. Fang, Y. Jin, and X. Peng. *Electrically-driven single-photon sources based on colloidal quantum dots with near-optimal antibunching at room temperature*. Nature Communications, 8(1):1132, 2017.
- [2] J. Lim, Y.-S. Park, and V. I. Klimov. *Optical gain in colloidal quantum dots achieved with direct-current electrical pumping*. Nat. Mater., 17(1):42–49, jan 2018.
- [3] Y. Shirasaki, G. J. Supran, M. G. Bawendi, and V. Bulović. *Emergence of colloidal quantum-dot light-emitting technologies*. Nat. Photonics, 7(1):13–23, jan 2013.
- [4] J. Roh, Y.-S. Park, J. Lim, and V. I. Klimov. *Optically pumped colloidal-quantum-dot lasing in LED-like devices with an integrated optical cavity*. Nat. Commun., 11(1):271, dec 2020.
- [5] K. Van Gasse, R. Wang, and G. Roelkens. *27 dB gain III–V-on-silicon semiconductor optical amplifier with > 17 dBm output power*. Optics Express, 27(1):293, jan 2019.
- [6] J. Lim, Y.-S. Park, K. Wu, H. J. Yun, and V. I. Klimov. *Droop-Free Colloidal Quantum Dot Light-Emitting Diodes*. Nano Lett., 18(10):6645–6653, oct 2018.

- [7] Z. Zhang, Y. Ye, C. Pu, Y. Deng, X. Dai, X. Chen, D. Chen, X. Zheng, Y. Gao, W. Fang, X. Peng, and Y. Jin. *High-Performance, Solution-Processed, and Insulating-Layer-Free Light-Emitting Diodes Based on Colloidal Quantum Dots*. *Adv. Mater.*, 30(28):1–8, 2018.
- [8] Y.-H. Won, O. Cho, T. Kim, D.-Y. Chung, T. Kim, H. Chung, H. Jang, J. Lee, D. Kim, and E. Jang. *Highly efficient and stable InP/ZnSe/ZnS quantum dot light-emitting diodes*. *Nature*, 575, 2019.
- [9] A. Raza, S. Clemmen, P. Wuytens, M. de Goede, A. S. K. Tong, N. Le Thomas, C. Liu, J. Suntivich, A. G. Skirtach, S. M. Garcia-Blanco, D. J. Blumenthal, J. S. Wilkinson, and R. Baets. *High index contrast photonic platforms for on-chip Raman spectroscopy*. *Optics Express*, 27(16):23067, aug 2019.
- [10] O. V. Kozlov, Y.-S. Park, J. Roh, I. Fedin, T. Nakotte, and V. I. Klimov. *Sub-single-exciton lasing using charged quantum dots coupled to a distributed feedback cavity*. *Science*, 365(6454):672–675, aug 2019.
- [11] S. Bisschop, P. Geiregat, T. Aubert, and Z. Hens. *The Impact of Core/Shell Sizes on the Optical Gain Characteristics of CdSe/CdS Quantum Dots*. *ACS Nano*, 12(9):9011–9021, sep 2018.
- [12] Y. Deng, X. Lin, W. Fang, D. Di, L. Wang, R. H. Friend, X. Peng, and Y. Jin. *Deciphering exciton-generation processes in quantum-dot electroluminescence*. *Nature Communications*, 11(1):2309, dec 2020.
- [13] P. Malinowski, E. Georgitzikis, J. Maes, I. Vamvaka, F. Frazzica, J. Van Olmen, P. De Moor, P. Heremans, Z. Hens, and D. Cheyns. *Thin-Film Quantum Dot Photodiode for Monolithic Infrared Image Sensors*. *Sensors*, 17(12):2867, dec 2017.
- [14] E. Georgitzikis, P. E. Malinowski, J. Maes, A. Hadipour, Z. Hens, P. Heremans, and D. Cheyns. *Optimization of Charge Carrier Extraction in Colloidal Quantum Dots Short-Wave Infrared Photodiodes through Optical Engineering*. *Advanced Functional Materials*, 28(42):1804502, oct 2018.
- [15] L. Alloatti, R. Palmer, S. Diebold, K. P. Pahl, B. Chen, R. Dinu, M. Fournier, J. M. Fedeli, T. Zwick, W. Freude, C. Koos, and J. Leuthold. *100 GHz silicon-organic hybrid modulator*. *Light: Science and Applications*, 3(5):e173–e173, may 2014.
- [16] S. Khasminskaya, F. Pyatkov, K. Słowik, S. Ferrari, O. Kahl, V. Kovalyuk, P. Rath, A. Vetter, F. Hennrich, M. M. Kappes, G. Gol'tsman,

- A. Korneev, C. Rockstuhl, R. Krupke, and W. H. P. Pernice. *Fully integrated quantum photonic circuit with an electrically driven light source*. Nature Photonics, 10(11):727–732, nov 2016.
- [17] M. Schwartz, E. Schmidt, U. Rengstl, F. Hornung, S. Hepp, S. L. Portalupi, K. Llin, M. Jetter, M. Siegel, and P. Michler. *Fully On-Chip Single-Photon Hanbury-Brown and Twiss Experiment on a Monolithic Semiconductor–Superconductor Platform*. Nano Letters, 18(11):6892–6897, nov 2018.
- [18] J. Wang, S. Paesani, Y. Ding, R. Santagati, P. Skrzypczyk, A. Salavrakos, J. Tura, R. Augusiak, L. Mančinska, D. Bacco, D. Bonneau, J. W. Silverstone, Q. Gong, A. Acín, K. Rottwitt, L. K. Oxenløwe, J. L. O’Brien, A. Laing, and M. G. Thompson. *Multidimensional quantum entanglement with large-scale integrated optics*. Science, 360(6386):285–291, apr 2018.
- [19] R. E. Correa, E. A. Dauler, G. Nair, S. H. Pan, D. Rosenberg, A. J. Kerman, R. J. Molnar, X. Hu, F. Marsili, V. Anant, K. K. Berggren, and M. G. Bawendi. *Single photon counting from individual nanocrystals in the infrared*. Nano Lett., 12(6):2953–2958, 2012.
- [20] V. Chandrasekaran, M. D. Tessier, D. Dupont, P. Geiregat, Z. Hens, and E. Brainis. *Nearly Blinking-Free, High-Purity Single-Photon Emission by Colloidal InP/ZnSe Quantum Dots*. Nano Lett., 17(10):6104–6109, 2017.
- [21] Y.-S. Park, J. Lim, and V. I. Klimov. *Asymmetrically strained quantum dots with non-fluctuating single-dot emission spectra and subthermal room-temperature linewidths*. Nature Materials, 18(3):249–255, mar 2019.
- [22] J. Preskill and P. W. Shor. *Simple Proof of Security of the BB84 Quantum Key Distribution Protocol*. Phys. Rev. Lett., 85(2):441–444, 2000.
- [23] M. J. Fernée, P. Tamarat, and B. Lounis. *Cryogenic Single-Nanocrystal Spectroscopy: Reading the Spectral Fingerprint of Individual CdSe Quantum Dots*. The Journal of Physical Chemistry Letters, 4(4):609–618, feb 2013.
- [24] M. Nirmal, D. J. Norris, M. Kuno, M. G. Bawendi, A. L. Efros, and M. Rosen. *Observation of the "Dark Exciton" in CdSe Quantum Dots*. Physical Review Letters, 75(20):3728–3731, nov 1995.

- [25] V. Chandrasekaran. *Are the excitons in colloidal InP quantum dots suitable for quantum photonics?* PhD thesis, Ghent University, 2019.
- [26] M. A. Becker, R. Vaxenburg, G. Nedelcu, P. C. Sercel, A. Shabaev, M. J. Mehl, J. G. Michopoulos, S. G. Lambrakos, N. Bernstein, J. L. Lyons, T. Stöferle, R. F. Mahrt, M. V. Kovalenko, D. J. Norris, G. Rainò, and A. L. Efros. *Bright triplet excitons in caesium lead halide perovskites*. *Nature*, 553(7687):189–193, jan 2018.
- [27] H. Utzat, W. Sun, A. E. K. Kaplan, F. Krieg, M. Ginterseder, B. Spokoiny, N. D. Klein, K. E. Shulenberger, C. F. Perkinson, M. V. Kovalenko, and M. G. Bawendi. *Coherent single-photon emission from colloidal lead halide perovskite quantum dots*. *Science*, 363(6431):1068–1072, mar 2019.
- [28] P. Senellart, G. Solomon, and A. White. *High-performance semiconductor quantum-dot single-photon sources*. *Nat. Nanotechnol.*, 12(11):1026–1039, 2017.
- [29] I. Aharonovich, D. Englund, and M. Toth. *Solid-state single-photon emitters*. *Nat. Photonics*, 10(10):631–641, 2016.
- [30] R. Katsumi, Y. Ota, M. Kakuda, S. Iwamoto, and Y. Arakawa. *Transfer-printed single-photon sources coupled to wire waveguides*. *Optica*, 5(6):691, jun 2018.
- [31] C. O. de Beeck, L. Elsinger, B. Haq, G. Roelkens, and B. Kuyken. *Heterogeneously Integrated Laser on a Silicon Nitride Platform via Micro-Transfer Printing*. In *Frontiers in Optics + Laser Science APS/DLS*, page FTu6B.1. Optical Society of America, 2019.
- [32] I. Schwartz, D. Cogan, E. R. Schmidgall, Y. Don, L. Gantz, O. Kenneth, N. H. Lindner, and D. Gershoni. *Deterministic generation of a cluster state of entangled photons*. *Science*, 354(6311):434–437, oct 2016.
- [33] J. C. Loredo, M. A. Broome, P. Hilaire, O. Gazzano, I. Sagnes, A. Lemaitre, M. P. Almeida, P. Senellart, and A. G. White. *Boson Sampling with Single-Photon Fock States from a Bright Solid-State Source*. *Phys. Rev. Lett.*, 118(13):130503, mar 2017.
- [34] M. Reindl, D. Huber, C. Schimpf, S. F. C. da Silva, M. B. Rota, H. Huang, V. Zwiller, K. D. Jöns, A. Rastelli, and R. Trotta. *All-photon quantum teleportation using on-demand solid-state quantum emitters*. *Sci. Adv.*, 4(12):eaau1255, dec 2018.

- [35] J. H. Weber, B. Kambs, J. Kettler, S. Kern, J. Maisch, H. Vural, M. Jetter, S. L. Portalupi, C. Becher, and P. Michler. *Two-photon interference in the telecom C-band after frequency conversion of photons from remote quantum emitters*. *Nature Nanotechnology*, 14(1):23–26, jan 2019.
- [36] M. Reindl, K. D. Jöns, D. Huber, C. Schimpf, Y. Huo, V. Zwiller, A. Rastelli, and R. Trotta. *Phonon-Assisted Two-Photon Interference from Remote Quantum Emitters*. *Nano Letters*, 17(7):4090–4095, 2017.
- [37] A. W. Elshaari, E. Büyüközer, I. E. Zadeh, T. Lettner, P. Zhao, E. Schöll, S. Gyger, M. E. Reimer, D. Dalacu, P. J. Poole, K. D. Jöns, and V. Zwiller. *Strain-Tunable Quantum Integrated Photonics*. *Nano Letters*, 18(12):7969–7976, dec 2018.
- [38] A. J. Bennett, R. B. Patel, J. Skiba-Szymanska, C. A. Nicoll, I. Farrer, D. A. Ritchie, and A. J. Shields. *Giant Stark effect in the emission of single semiconductor quantum dots*. *Applied Physics Letters*, 97(3):031104, jul 2010.
- [39] M. Arcari, I. Söllner, A. Javadi, S. Lindskov Hansen, S. Mahmoodian, J. Liu, H. Thyrrestrup, E. H. Lee, J. D. Song, S. Stobbe, and P. Lodahl. *Near-Unity Coupling Efficiency of a Quantum Emitter to a Photonic Crystal Waveguide*. *Physical Review Letters*, 113(9):093603, aug 2014.
- [40] H. Wang, Y.-M. He, T.-H. Chung, H. Hu, Y. Yu, S. Chen, X. Ding, M.-C. Chen, J. Qin, X. Yang, R.-Z. Liu, Z.-C. Duan, J.-P. Li, S. Gerhard, K. Winkler, J. Jurkat, L.-J. Wang, N. Gregersen, Y.-H. Huo, Q. Dai, S. Yu, S. Höfling, C.-Y. Lu, and J.-W. Pan. *Towards optimal single-photon sources from polarized microcavities*. *Nature Photonics*, 13(11):770–775, nov 2019.
- [41] T. Huber, M. Davanco, M. Müller, Y. Shuai, O. Gazzano, and G. S. Solomon. *Filter-free single-photon quantum dot resonance fluorescence in an integrated cavity-waveguide device*. *Optica*, 7(5):380, may 2020.
- [42] J.-H. Kim, S. Aghaeimeibodi, J. Carolan, D. Englund, and E. Waks. *Hybrid integration methods for on-chip quantum photonics*. *Optica*, 7(4):291, apr 2020.
- [43] A. W. Elshaari, W. Pernice, K. Srinivasan, O. Benson, and V. Zwiller. *Hybrid integrated quantum photonic circuits*. *Nature Photonics*, 14(5):285–298, may 2020.

-
- [44] K. Alexander, J. P. George, J. Verbist, K. Neyts, B. Kuyken, D. Van Thourhout, and J. Beeckman. *Nanophotonic Pockels modulators on a silicon nitride platform*. Nat. Commun., 9(1):3444, dec 2018.
- [45] E. Knill, R. Laflamme, and G. J. Milburn. *A scheme for efficient quantum computation with linear optics*. Nature, 409(6816):46–52, jan 2001.

Appendix A

Detailed fabrication processes

A.1 E-beam fabricated SiN waveguides

This section outlines the fabrication details for silicon nitride (SiN) waveguides used in Chapter 3 and 3. The in-house fabrication using e-beam lithography started from cleaved silicon samples, coated with a thermal SiO₂ layer serving as a bottom cladding layer for the SiN waveguides.

A.1.1 Low-frequency PECVD SiN deposition

The SiN layers were deposited with a standard plasma-enhanced chemical vapor deposition (PECVD) system (Advanced Vacuum Vision 310 PECVD) operating at a temperature of 270°C. The recipe used a flow of 1960 sccm of N₂, 35 sccm of NH₃ and 40 sccm of SiH₄, at a chamber pressure of 650 mTorr and an RF bias of 50 W. The PECVD system was equipped with two RF frequency sources operating at, respectively, high frequency (13.56 MHz) and low frequency (100–460 kHz). All the SiN layers were prepared using the low RF frequency, resulting in a reduced material absorption. The thickness of the deposited layers was determined by reflectometry (Filmetrics F40).

A.1.2 E-beam lithography

In an optional first e-beam lithography step with our 50 kV system (Raith Voyager), we patterned metal markers using a positive resist (ARP-6200.09, Allresist). Spin-coating of the resist for 1 min at 4000 rpm (1000 rpm/s acceleration) resulted in a layer thickness of approximately 200 nm. Subsequent to a 1 min soft-bake on hot plate set to 150°C, we coated a conductive

polymer (AR-PC 5091, Allresist) to reduce charging-induced artifacts during the exposure. A spin-speed of 3000 rpm resulted in a layer thickness of approximately 60 nm after a 2 min soft-bake at 90°C. For the metal markers we used a step size of 5 nm and an area dose of 200 $\mu\text{A}/\text{cm}^2$ for the exposure to achieve an appropriate under-cut of the developed resist profile. The conductive polymer was removed prior to the development of the sample by a gentle rinse in DI water and subsequent drying of the sample with an N_2 gun. The development in n-amyl acetate under slight agitation lasted for 1 min and was stopped by submerging the sample in an IPA puddle for 30 seconds. The sample was dried with an N_2 gun and a 10 second exposure to O_2 plasma (Advanced Vacuum Vision 320 RIE) was used to clear undeveloped resist residue and improve the adhesion of the metal markers. We then evaporated 50 nm Au on top of a sputtered 3 nm Ti adhesion layer (Leybold Univex) and performed a lift-off in a dedicated resist remover (AR 600-71, Allresist), using ultrasonic agitation. After cleaning the sample in acetone and IPA, it was dried using an N_2 gun and exposed to O_2 plasma (PVA TePla 600) for 10 minutes. The metal markers were only patterned on the sample, in case the SiN waveguides had to be aligned to other structures on the sample.

To pattern the waveguide layer, we again used a positive resist (ARP-6200.09, Allresist) and a conductive polymer (AR-PC 5091, Allresist) with the same process parameters as described above. However, for 300 nm thick SiN layers the spin speed for the resist was 1500 rpm, resulting in a sufficient thickness of the resist mask for the RIE waveguide etch. High-resolution waveguide structures such as narrow tapers and DBR gratings described in Chapter 4 were patterned using a step size of 5 nm and an area dose of 160 $\mu\text{A}/\text{cm}^2$. The exposure mode was set to "concentric" and "outwards" for a uniform exposure. Long waveguide sections were exposed using the fixed beam moving stage (FBMS) mode of the Voyager system [1] to reduce the losses induced by write field stitching. For the 3 μm wide trenches around the waveguides we used a dose of 160 $\mu\text{C}/\text{cm}^2$ and a step size of 20 nm for a beam current of approximately 0.45 nA. To reduce the writing time, long waveguide sections were also exposed with a beam current of approximately 2.2 nA at times, resulting in a slightly larger waveguide loss. After 1 min development in n-amyl acetate and subsequent drying of the sample, a 20 second exposure to O_2 plasma (Advanced Vacuum Vision 320 RIE) was used to remove undeveloped resist residue and create smoother resist sidewalls. The corresponding shrinkage of the developed structures was accounted for in the design. Including the following RIE dry etch, the total shrinkage amounted to approximately 30 nm, with minor variations due to uncorrected proximity effects in the exposure.

A.1.3 SiN RIE recipe

Reactive ion etching for 4 min 30 seconds in CF_4 and H_2 chemistry was followed by a 10 min resist strip in O_2 plasma (Advanced Vacuum Vision 320 RIE) for 300 nm SiN waveguides. The SiN etch recipe used a gas flow of 80 sccm CF_4 and 4 sccm H_2 , at a chamber pressure of 20 mTorr and an RF bias of 210 W.

A.1.4 PECVD SiO_2 cladding layer

For the waveguides presented in Chapter 3 and 4 we deposited a PECVD (Advanced Vacuum Vision 310 PECVD) SiO_2 cladding layer at different temperatures (RT and 150°C), using otherwise the same process. The recipe used a flow of 1425 sccm of N_2O , 393 sccm of N_2 and 10 sccm of SiH_4 , at a chamber pressure of 700 mTorr and a high-frequency (13.56 MHz) RF bias with a power of 30 W.

A.1.5 SiO_2 RIE recipe

The SiO_2 RIE recipe (Advanced Vacuum Vision 320 RIE) used a gas flow of 80 sccm CF_4 , 3 sccm SF_6 and 7 sccm H_2 , at a chamber pressure of 20 mTorr and an RF bias of 210 W.

A.2 Synthesis of CdSe/CdS QDs

The CdSe/CdS QD samples used in this work consisted of oleate-capped core/shell QDs synthesized using a seeded-growth flash method as previously described in the literature. [2, 3] First, wurtzite CdSe cores were synthesized from injections of trioctylphosphine selenide into a hot solution of cadmium phosphonate in trioctylphosphine oxide, with the size of the QDs being controlled by the reaction time. Next, CdS shells were grown by injecting a mixture of the CdSe cores and trioctylphosphine sulfide into a hot solution of cadmium oleate in trioctylphosphine oxide. The thickness of the shell was controlled by changing the amounts of Cd and S in this second synthesis step. All samples were purified by means of centrifugation using toluene and methanol as solvent and nonsolvent, respectively, and were stored in toluene afterwards.

A.3 Synthesis of PbS/CdS QDs

For the synthesis of PbS/CdS QDs, toluene, ethanol, isopropanol and methanol were purchased from Fiers. Oleic acid (90 %), cadmium oxide (> 99.99 %

metals bases), phenyl isothiocyanate (99 %), n-dodecylamine (98 %), diethylene glycol dimethyl ether (diglyme, anhydrous, 99.5%), 1-octene (98%), trifluoroacetic acid (99 %), trifluoroacetic anhydride (> 99 %) and triethylamine (> 99 %) were purchased from Sigma-Aldrich; lead(II) oxide (Puratronic, 99.999 % (metals basis) was purchased from Alfa Aesar; n-dodecane (99 % for synthesis) was purchased from Merck; Acetone (water free, > 99.8 %) was purchased from VWR. All chemicals were used without further purification. Toluene, 1-octene and n-dodecane were dried with calcium hydride overnight, distilled and stored over molecular sieves in a nitrogen-filled glovebox.

Lead oleate was prepared from lead trifluoroacetate as previously reported. [4] N-dodecyl-N'-phenylthiourea was prepared from n-dodecylamine and phenyl isothiocyanate as previously reported. [4] Cadmium oleate was prepared by dissolving cadmium oxide (3 g) in oleic acid (18 mL) at 250 °C under nitrogen atmosphere.

Lead oleate (3.1 mmol, 2.387 g) and anhydrous 1-octene (20 mL) were added to a 50 mL three-neck flash and heated to 120°C under nitrogen atmosphere. In a nitrogen-filled glove box N-dodecyl-N'-phenylthiourea (2.07 mmol, 0.6635 g) was mixed with 1 mL anhydrous diethylene glycol dimethyl ether (diglyme) and taken outside in a vial equipped with a septum. After heating to 120°C, the thiourea solution was quickly inject into the lead oleate solution yielding to fast color change. The reaction was allowed to run for 10 min at 120°C after which it was cooled down to room temperature. This was followed by 4 purification steps under nitrogen atmosphere with toluene and acetone to be finally dispersed in 5 mL of anhydrous toluene.

2 mL of the PbS QD stock dispersion was diluted with anhydrous n-dodecane (25 mL) in a 50 mL three-neck flask and heated to 140°C under nitrogen atmosphere. Now, 10 mL of the cadmium oleate solution was added to trigger a cation exchange reaction towards CdS. The reaction was allowed to run for 2h to reach a shell thickness of 1.1 nm. The synthesis mixture was purified four times with toluene and ethanol to be finally dispersed in 2 mL of anhydrous toluene.

Absorption spectra in tetrachloroethylene were taken with a PerkinElmer Lambda 950 spectrometer. QD size and concentration determination of the PbS(/CdS) QDs was done according to Maes et al. [5] Photoluminescence measurements were done on an Edinburgh Instruments FLSP920 UV-Vis-NIR spectrofluorometer using a 450 W xenon lamp as the excitation source. An excitation wavelength of 800 nm was used for all steady-state emission spectra.

A.4 Atomic layer deposition

The thermal ALD processes used for the sample fabrication in Chapter 2 and 3 were adapted from established protocols found in literature [6, 7]. The deposition was performed in a home-built stainless steel pump-type reactor, equipped with a rotation pump and a turbomolecular pump, achieving a base pressure of 5×10^{-6} mbar. The chamber pressure was monitored using a combined Pirani gauge and cold cathode measuring system. The walls of the reactor were heated to a temperature of 100°C and the sample holder was kept at a deposition temperature of 150°C (220°C). Precursor and reactant materials were contained within stainless steel bottles, connected to the reactor via heated stainless steel tubes and the gas flow was controlled via pneumatic valves and adjusted to a pressure of 5×10^{-3} mbar using needle valves for all precursors and reactants. For the ZnO deposition we used diethylezinc ($>95\%$, Strem Chemicals, Inc.) as a precursor, for Al_2O_3 trimethylaluminum ($>98\%$, Strem Chemicals, Inc.). Distilled water vapor was used as reactant for both thermal ALD processes. Saturation of the surface reactions was obtained during the 5 s of precursor and reactant exposure. The growth per ALD cycle was determined to be 0.7 \AA for ZnO and 1.1 \AA for Al_2O_3 through x-ray reflection (XRR) measurements. Prior to the deposition, the samples were cleaned by an O_2 plasma exposure within the ALD chamber, which was equipped with a quartz tube wrapped with an RF coil on top of the reactor for that purpose.

Appendix B

Characterization details

B.1 Transient absorption spectroscopy

To characterize the gain spectrum of the CdSe/CdS QD sample in solution we performed transient absorption (TA) measurements. The samples were therefore excited using 110 femtosecond pump pulses at 520 nm, created from the 800 nm fundamental (Spitfire Ace, Spectra Physics) through non-linear conversion in an OPA (Light Conversion TOPAS). Probe pulses were generated in a thin CaF₂ crystal using the 800 nm fundamental. The pulses were delayed relative to the pump using a delay stage with maximum delay of 3 ns. The probe spectrum in our experiments covers the UV-VIS window from 350 nm up to 750 nm. CdSe/CdS quantum dots were dispersed in an optically transparent solvent (toluene) and continuously stirred to avoid charging or photo-degradation. The pump wavelength and sample concentration were chosen to obtain an optimal trade-off between having a good signal at the band-edge transitions, while still not having a too strong absorption at the pump-wavelength as to assure a uniform pumping of the sample. The average number of absorbed photons (or equivalently created excitons) at time zero, noted as $\langle N \rangle$, can be calculated from the photon flux J_{ph} , the cuvette length L and the nanocrystal absorption cross section at the pump wavelength σ_{λ_p} :

$$\langle N \rangle = J_{ph} \times \sigma_{\lambda_p} \times \frac{1 - e^{-\alpha_{0,\lambda_p} L}}{\alpha_{0,\lambda_p} L}. \quad (\text{B.1})$$

The photon flux is calculated from the beam area, obtained through a Thorlabs CCD beam profiler, and defined as $A_{beam} = 2\pi \times \sigma_x \sigma_y$ where σ_i is the standard deviation in the $i = x, y$ direction.

References

- [1] I. Khodadad, N. Nelson-Fitzpatrick, K. Burcham, A. Hajian, and S. S. Saini. *Electron beam lithography using fixed beam moving stage*. J. Vac. Sci. Technol. B, 35(5):051601, sep 2017.
- [2] M. Cirillo, T. Aubert, R. Gomes, R. Van Deun, P. Emplit, A. Biermann, H. Lange, C. Thomsen, E. Brainis, and Z. Hens. *“Flash” Synthesis of CdSe/CdS Core-Shell Quantum Dots*. Chem. Mater., 26(2):1154–1160, jan 2014.
- [3] E. Drijvers, J. De Roo, P. Geiregat, K. Fehér, Z. Hens, and T. Aubert. *Revisited Wurtzite CdSe Synthesis: A Gateway for the Versatile Flash Synthesis of Multishell Quantum Dots and Rods*. Chem. Mater., 28(20):7311–7323, oct 2016.
- [4] M. P. Hendricks, M. P. Campos, G. T. Cleveland, I. Jen-La Plante, and J. S. Owen. *A tunable library of substituted thiourea precursors to metal sulfide nanocrystals*. Science, 348(6240):1226–1230, jun 2015.
- [5] J. Maes, N. Castro, K. De Nolf, W. Walravens, B. Abécassis, and Z. Hens. *Size and Concentration Determination of Colloidal Nanocrystals by Small-Angle X-Ray Scattering*. Chem. Mater., 30:32, 2018.
- [6] R. L. Puurunen. *Surface chemistry of atomic layer deposition: A case study for the trimethylaluminum/water process*. Journal of Applied Physics, 97(12):121301, jun 2005.
- [7] T. Tynell and M. Karppinen. *Atomic layer deposition of ZnO: a review*. Semiconductor Science and Technology, 29(4):043001, apr 2014.

